THE ACCELEROMETER AS

AN END-POINT CONTROL SENSOR FOR THE BASIC OXYGEN STEELMAKING PROCESS

by

KEVIN E. O'LEARY

A Thesis Submitted to the Faculty of Graduate Studies and Research in Partial Fulfilment of the Requirements for the Degree of Master of Engineering

Department of Mining and Metallurgical Engineering McGill University
Montreal, Canada

@April 1990

To my wife, Brenda,
whose constant encouragement
was a source of great inspiration.

Abstract

The present work attempts to determine the feasibility of the accelerometer as an end-point control sensor for the basic oxygen steelmaking process. In this study, two series of laboratory scale BOF simulations were performed. In the first series, the accelerometer was sampled at low frequency to obtain an amplitude-time relation that can be related to the rate of decarburization during the oxygen blow. In contrast, the accelerometer was sampled at high frequency in the second series in order to discern the presence of specific vibrational frequencies that can be related to the process. As a final aspect of the research work, several high frequency simulations were terminated prematurely in an attempt to elucidate the carbon content of the bath at the point in time when the accelerometer can clearly detect the final change in the rate of decarburization.

In both series, it was found that the variance of the accelerometer signal over time clearly followed the ideal path of decarburization during the oxygen blow, and, more importantly, was able to detect deviations from this path. The final change in the equation governing the rate of decarburization was easily detected as a significant drop in the variance of the accelerometer's signal; indicating a decrease in the intensity of the vibrations as the volume of CO_{gas} produced also decreases during this period.

In the high frequency series, it was noted that specific vibrational frequencies can be related to the steelmaking process. Moreover, a

significant change in the pattern of these frequencies occurs when the carbon reference point is passed and the rate of decarburization decreases. However, it was found that the frequency characteristics of the accelerometer's signal was highly sensitive to changes to the steelmaking vessel.

Furthermore, results indicate that the carbon content of the bath when the accelerometer is able to detect the decay in the decarburization rate is between 0.40 and 0.44 %C. The application of the accelerometer appears to be well suited to the production of medium and low carbon steels whose end-point carbon is less than 0.44 %C.

Résumé

Ce travail tente de déterminer si l'utilisation de l'accéléromètre comme point de contrôle pour les convertisseurs à l'oxgène est possible. Dans le cadre de cette étude, deux séries de simulations sur les convertisseur à l'oxygène ont eté exécutées en laporatoire. Dans la première série, l'accéléromètre était ajusté à basse fréquence afin d'obtenir une relation amplitude-temps qui peut être relié au taux de décarburisation durant le soufflage d'oxygène. Par contre, l'accéléromètre était ajusté à haute fréquence durant la deuxième série de façon à discerner la présence de certaines fréquence de vibration qui peuvent être reliées au procédé.

Comme aspect final du travail de recherche, plusieurs simulations à haute iréquence ont été arrétées prématurément dans le but de déterminer le pourcentage de carbone dans le bain au moment où l'accéléromètre dètecte clairement détecter le changement final du taux de décarburisation.

Dans les deux séries de sumulations, il a été trouvé que la variation du signal de l'accéléromètre en fonction du temps suit clairement le courbe idéale de décarburisation durant le soufflage d'oxygène, et, de surcroît, étaiet capable de détecter les déviations par rapport a cette course. Le changement final dans l'équation gouvernant 'e taux de décarburisation étaiet facilement détecté par une chute importante dans la variation du signal de l'accéléromètre; ceci indiquait une diminution de l'intensité des vibrations car le volume de CO₄₁₂ produit

décroît aussi durant cette période.

Dans la série à haute fréquence, il a été noté que cartaines fréquences de vibrations peuvent être reliées au procédé sidérugique. De surcroît, un changement significatif dans la courbe pour ces réquences survient lorsque le pourcentage de carbone de référence est dépassé et que le taux de décarburisation diminue. Cependant, il a été trouvé que les caractéristiques des fréquences des signaux de l'accéléromètre sont très sensibles aux changements se produisant au convertisseur.

De plus, les résultats indiquent que le pourcentage de carbone dans le bain, lorsque l'àccéléromètre détecte la baisse drastique du taux de décarburisation, est entre 0.40 et 0.44 %C. L'application de l'accéléromètre apparaît très prometteur pour la production d'acier moyen et bas carbone dont le pourcentage de carbone est plus petit que 0.44%C.

Acknowledgements

The author wishes to extend his sincere gratitude to Dr. F.A. Mucciard, director of this research work, for his confidence, guidance, helpful suggestions, and the countless hours of discussion on the present work.

The author would also like to thank Mr. R. Paquette for his assistance in conducting the experiments, Messrs M. Knoepfel and B. Grondin for their advice and assistance in the design and fabrication of the oxygen lance and ancillary equipment, and the staff and graduate students of the department of Mining and Metallurgical Engineering for making my graduate studies a most enriching experience. In addition, the author wishes to acknowledge the encouragement given by Mr. K.W. Heyer to complete this thesis.

Finally, the author wishes to thank the Natural Sciences and Engineering Research Council of Canada for their financial support.

Table of Contents

į

Content	<u>s</u>		Page
Abstrac	t		i
Resume			iii
Acknowl	edgen	nents	v
List of	Figu	ires	ix
List of	Tabl	es	xx
List of	Appe	endices	xxi
Chapter	1.	Introduction	1.1
Chapter	2.1 2.2 2.3	Oxygen Steelmaking Process Introduction General Description of the Oxygen Steelmaking Process 2.2.1 BOF/LD/LD-AC Oxygen Steelmaking	2.1 2.3 2.3 2.3 2.6 2.13 2.20 2.26 2.26 2.34 2.44 2.58
Chapter	3.1 3.2	Accelerometer Transducers Introduction General Description of Accelerometers Piezoelectric Acceleration Transducers 3.3.1 Crystal Materials 3.3.2 Designs 3.3.3 Signal Conditioning 3.3.4 Sources of Error 3.3.5 PCB 308B02 Quartz Accelerometer	3.1 3.2 3.7 3.8 3.9 3.11 3.12 3.12
Chapter		Control of the Oxygen Steelmaking Process Introduction Static Control 4.2.1 Introduction 4.2.2 Predictive Models 4.2.3 Statistical Models 4.2.4 Predictive-Adaptive Models 4.2.5 Limitations of Static Models	4.1 4.4 4.4 4.8 4.10 4.11

Contents Cont'd		<u>Paqe</u>	
	4.3	Dynamic End-Point Control 4.3.1 Introduction 4.3.2 Periodic Measurement of Variables 4.3.3 Continuous Measurement of Variables 4.3.3.1 Introduction 4.3.3.2 Off-gas Analysis 4.3.3.3 Fume Temperature 4.3.3.4 Acoustic Analysis 4.3.3.5 Vibrational Analysis	4.14 4.18 4.26 4.26 4.26 4.33 4.36 4.40
Chapter	5.1 5.2 5.3	Application of the Accelerometer in Metallurgy Introduction Mechanical Applications 5.2.1 Predictive Maintenance Programmes 5.2.2 Accelerometer Application in a Down Coiler Multi-Phase Mixing Applications 5.3.1 Introduction 5.3.2 Rimming Steels 5.3.3 Ladle Metallurgy 5.3.4 Addition of Volatile Reagents in Ladle Metallurgy 5.3.5 Slag Detection Continuous Casting	5.1 5.3 5.3 5.6 5.10 5.10 5.11 5.13 5.21 5.21
Chapter	6.1 6.2 6.3 6.4	Experimental Introduction Laboratory Scale BOF Vessel 6.2.1 General 6.2.2 Oxygen Lance Sensors and Relays Data Acquisition and Control 6.4.1 Introduction 6.4.2 Low Frequency 6.4.3 High Frequency Experimental Procedure	6.1 6.2 6.2 6.2 6.9 6.12 6.12 6.13 6.17 6.21
Chapter	7.1 7.2 7.3	Introduction General Low Frequency High Frequency 7.4.1 Fourier Analysis Technique 7.4.2 Results of Frequency Analysis	/.1 / 1 / 2 /.6 / 19 / 33 7.3/ 7.50
Chapter	8.	Summary and Conclusions	8.1
Appendi	ces		A.1
Referen	ces		R.1

2.30

2.35

Fig. 2.14 Schematic of a Q-BOP tuvere [5].

Fig. 2.15 Types of combined blowing-oxygen

steelmaking processes[5].

	List of Figures	Page -ix-
Figure		Page
Fig. 2.16	Schematic of the LBE steelmaking process ^[5] .	2.35
Fig. 2.17	Profile of a porous element for the LBE process ^[16] .	2.36
Fig. 2.18	Initial LBE porous element configuration at USS Gary Works[14].	2.37
Fig. 2.19	Modified element configuration employed at Broken Hill Proprietary's Newcastle Works ^[15] .	2.38
Fig. 2.20	Dependence of LBE efficiency on thickness of bottom build-up ^[15] .	2.39
Fig. 2.21	Structure of the tubular element designed at BHP Newcastle Works [15].	2.40
Fig. 2.22	Location of the tubular elements in the furnace $bottom^{(15)}$.	2.41
Fig. 2.23	Schematic of a K-BOP oxygen steelmaking vessel $^{[5]}$.	2.42
Fig. 2.24	Overview of the KMS steelmaking process[17].	2.43
Fig. 2.25	Free energies of formation of oxides for the standard states; pure elements, pure oxides and oxygen at 1 atm of pressure.	2.47
Fig. 2.26	Change in the oxygen potential of the metal during BOF steelmaking[4].	2.48
Fig. 2.27	Comparison between calculated and determined oxygen content, different symbols are used for data from different sources ^[18] .	2.52
Fig. 2.28	Carbon-oxygen relationship in the BOH and BOF steelmaking processes compared with the equilibrium curve for 1 atm carbon monoxide gas at $1600^{\circ}C^{(4)}$.	2.54
Fig. 2.29	Removal of the major constituents from the metal bath during the BOF process ^[4] .	2.59

		<u>List of Figures</u>	Page -x-
Figur	e		Page
Fig.	2.30	Distribution of oxygen between steel, slag, and decarburization near the end of the blow[4].	2.59
Fig.	2.31	Typical decarburization rate curve for a BOF heat [4].	2.60
Fig.	2.32	Comparative geometry of the flow modes ^[21] . Legend: (1) nozzle body; (2) entrainment region of the original jet; (*3) entrainment region of the wall jet across the phase interface; (4) stagnation point of the wall jet; (6) two-phase exit flow.	2.62
Fig.	2.33	Nomograph for determining jet penetration in molten steel. Q is the blowing rate per nozzle in scfm, LH is the lance heigth in inches, D is the nozzle diameter in inches [24].	2.64
Fig.	2.34	Diagram showing the flow set up in a foaming slag by a gas jet from (a) a lance above the foam and (b) from a lance within the foam [4].	2.66
Fig.	2.35	Compositional change of slag in a BOF vessel with variable lance height during the blow [4].	2.68
Fig.	2.36	Decarburization rate curves taken during the critical slag formation period ^[25] .	2.70
Fig.	2.37	Comparison of decarburization rates for smooth and sloppy heats [25].	2.71
Fig.	2.38	Definition of conditions and terms used in analysis of scrap melting. C_{o} is the scrap carbon content and C_{b} is the bath bulk carbon content.	2.74
Fig.	2.39	Scrap carburization mechanism during scrap melting in the BOF process.	2.74
Fig.	3.1	Basic spring-mass system of an acceleration transducer.	3.1

	List of Figures	Page -xi-
Figure		Page
Fig. 3.2	Typical piezcelectric acceleration transducer designs showing; (k) crystal, (m) seismic mass, (k1, k2) secondary elastic members ^[26] .	3.10
Fig. 3.3	Schematic of the PCB 308B02 accelerometer from PCB Piezotronics ^[27] .	3.13
Fig. 4.1	Flow chart for charge calculation (after D.G. Boltz $^{[31]}$).	4.9
Fig. 4.2	Exponential decay characteristic exhibited by the decarburization rate curve[41].	4.16
Fig. 4.3	Schematic showing the relative location of the sublance $^{[41]}$.	4.20
Fig. 4.4	Early design of the sublance probe [40].	4.21
Fig. 4.5	Comparison between liquidus temperature and carbon content $^{[41]}$.	4.22
Fig. 4.6	Carbon error as a function of bath carbon [42].	4.24
Fig. 4.7	Schematic showing the general arrangement of sensors employed for off-gas analysis at the steel works of Cockerill-Chertal ⁽⁴⁹⁾ .	4.27
Fig. 4.8	Typical decarburization rate curve from waste gas analysis [42].	4.29
Fig. 4.9	Oxygen distribution principles as determined by off-gas analysis [50].	4.31
Fig. 4.10	Effect of full process control on liquid steel yield, vessel refractory life, and oxygen lance life ^[50] .	4.32
Fig. 4.11	Evolution of the off-gas temperature and of the decarburization rate as determined from off-gas analyzers [53].	4.34
Fig. 4.12	Decarburization model showing the trajectory of the rate of decarburization [53].	4.35

	List of Figures	Page -xii-
Figure		Page
Fig. 4.13	Previous testing locations of the sonic $meter^{[52]}$.	4.37
Fig. 4.14	Noise spectra at two different moments during the blow.	4.38
Fig. 4.15	Appearance of background noises in the spectra during the blow.	4.39
Fig. 4.16	Sound intensity-time trane during a typical blow.	4.40
Fig. 4.17	Schematic showing the vibration analysis system attached to a BOF vessel.	4.41
Fig. 4.18	Vertical vibrations of a 40 tonne BOF, showing both the overall vibration intensity and the intensity of the 1100 Hz frequency.	4.42
Fig. 4.19	Vertical vibrations of a 40 tonne BOF, showing both the overall vibration intensity and the intensity of the 1080 Hz frequency.	4.42
Fig. 4.20	Dynamic traces generated by the continuous weighing system.	4.44
Fig. 4.21	Relationship between turndown carbon and turndown activity.	4.45
Fig. 4.22	Histograms showing predictive turndown carbon performance of vessel weighing equipment.	4.46
Fig. 4.23	Schematic showing the application of two accelerometers for slag formation control on a 250 tonne BOF.	4.47
Fig. 4.24	Frequency spectrum of the composite lance vibration.	4.48
Fig. 4.25	Relation between acceleration of lance vibration and foaming slag height.	4.49
Fig. 4.26	Concept of the slag formation control scheme.	4.50

Figure	
Fig. 4.27 Example of automatic blowing control.	4.51
Fig. 4.28 Improvement of blowing results at Kawasaki's Mizushima No.2 BOF.	4.51
Fig. 4.29 Change of the vibrations of a K-BOP furnace during the refining period.	4.53
Fig. 4.30 Relation between Δt and [P] at blow-end.	4.53
Fig. 4.31 Relation between Δt and (T.Fe) in slag.	4.54
Fig. 5.1 Comparison of vibration signatures for identical fans, one running smoothly and one with a bad bearing.	5.5
Fig. 5.2 Strip overlying the leading edge makes a stepped portion in coil surface.	5.7
Fig. 5.3 Wrapper roll control system.	5.8
Fig. 5.4 Signal-time traces for the sensors of the tracking circuit.	5.8
Fig. 5.5 Wrapper roll withdraws in position control mode, then presses strip onto the mandrel in force control mode.	5.9
Fig. 5.6 Measurement of the rimming action of rimmed steel using an accelerometer[3].	5.11
Fig. 5.7 Experimental configuration for water system. All dimensions are in cm. (a: accelerometer, p: photocell, and L: light source) [7].	5.14
Fig. 5.8 Correlation of the transformed accelerometer signal as a function of the computed mixing power input for the water model study [7].	5.15
Fig. 5.9 Slopes of the integrated accelerometer signal at various flow rates in molten lead system [6].	5.17

List of Figures Page -xv-Figure Page Initial design of a water-cooled, oxygen Fig. 6.3 6.4 lance. 6.6 Fig. 6.4 Oxygen lance schematic showing final design. Photograph of the inlet and outlet surge 6.7 Fig. 6.5 tanks of the water-cooled oxygen lance. 6.10 Fig. 6.6 Oxygen control circuit. Microprocessor environment during low 6.14 Fig. 6.7 frequency experiments. Fig. 6.8 Accelerometer circuit used in the high 6.19 frequency experiments. Microprocessor environment during low 6.20 Fig. 6.9 frequency experiments. Fig. 6.10 Positioning of the accelerometer on the 6.23 induction furnace structure. 7.2 Condition of the steelmaking vessel, an Fig. 7.1 alumina crucible, afet a BOF simulation. Accelerometer signal during BOF simulation 7.8 Fig. 7.2 A/1. 7.8 Temperature of the cooling water at the Fig. 7.3 nozzle tip during BOF simulation A/1. 7.9 Fig. 7.4 Temperature of the cooling water at the exit surge tank during BOF simulation A/1. 7.9 Fig. 7.5 Accelerometer signal during BOF simulation A/2. 7.10 Fig. 7.6 Temperature of the cooling water at the nozzle tip during BOF simu ation A/2. 7.10 Fig. 7.7 Temperature of the cooling water at the exit surge tank during BOF simulation A/2. 7.11 Fig. 7.8 Accelerometer signal during BOF simulation A/3.

Figure		Page
Fig. 7.25	Temperature of the cooling water at the nozzle tip during BOF simulation B/6.	7.25
Fig. 7.26	Temperature of the cooling water at the exit surge tank during BOF simulation B/6.	7.25
Fig. 7.27	Intensity of the photocell signal during BOF simulation B/5.	7.26
Fig. 7.28	The mean of the accelerometer signal during BOF simulation C/1.	7.26
Fig. 7.29	Variation of the accelerometer signal during BOF simulation C/1.	7.27
Fig. 7.30	The mean of the accelerometer signal during BOF simulation C/2.	7.27
Fig. 7.31	Variation of the accelerometer signal during BOF simulation C/2.	7.28
Fig. 7.32	The mean of the accelerometer signal during BOF simulation C/3.	7.28
Fig. 7.33	Variation of the accelerometer signal during BOF simulation C/3.	7.29
Fig. 7.34	The mean of the accelerometer signal during BOF simulation C/4.	7.29
Fig. 7.35	Variation of the accelerometer signal during BOF simulation C/4.	7.30
Fig. 7.36	The mean of the accelerometer signal during BOF simulation C/5.	7.30
Fig. 7.37	Variation of the accelerometer signal during BOF simulation C/5.	7.31
Fig. 7.38	The mean of the accelerometer signal during BOF simulation C/6.	7.31
Fig. 7.39	Variation of the accelerometer signal during BOF simulation C/6.	7.32
Fig. 7.40	The power spectrum of the accelerometer signal at 65 seconds into simulation B/9.	7.38

Figure		Page
Fig. 7.41	The power spectrum of the accelerometer signal at 240 seconds into simulation B/9.	7.39
Fig. 7.42	The power spectrum of the accelerometer signal at 700 seconds into simulation B/9.	7.39
Fig. 7.43	The power spectrum of the accelerometer signal at 100 seconds into simulation C/3.	7.40
Fig. 7.44	The power spectrum of the accelerometer signal at 200 seconds into simulation C/3.	7.40
Fig. 7.45	The power spectrum of the accelerometer signal at 400 seconds into simulation C/3.	7.41
Fig. 7.46	The power spectrum of the accelerometer signal at £00 seconds into simulation C/3.	7.41
Fig. 7.47	The power spectrum of the accelerometer signal at 800 seconds into simulation C/3.	7.42
Fig. 7.48	The power spectrum of the accelerometer signal at 1000 seconds into simulation C/3.	7.42
Fig. 7.49	Relative contribution of three frequency band widths during simulation B/9.	7.45
Fig. 7.50	Relative contribution of three frequency band widths during simulation C/3.	7.50
Fig. 7.51	Relative contribution of three frequency band widths during simulation C/3.	7.47
Fig. 7.52	Relative contribution of two frequency band widths shown to be predominant before the start of simulation B/6.	7.49
Fig. 7.53	Relationship showing the carbon reference point as a function of the oxygen blowing rate (After Ichinoe $^{[78]}$).	7.53

List of Tables Page -xix-Table Page Table 2.1 Comparison of Refractory Consumption 2.29 Between the Q-BOP ar. the BOF Processes[9,10]. Table 4.1 End-Point Control Performance at Bethlehem's BOFs^[15]. 4.18 Table 4.2 End-Point Control Performance at 4.23 Bethlehem's BOFs[15]. Table 4.4 End-Point Control Results for Static 4.35 Inarge Model and a Dynamic Control Scheme Using Fume Temperature Measurements [27]. Table 7.1 Summary (the Operating Parameters of BOF 7.4 Simulations. 7.5 Table 7.2 Oxygen Jet Penetration During BOF Simulations. Table 7.3 Sampling Frequency of the Accelerometer 7.43 During High Frequency Simulations.

Appendix	Page
Appendix A	A.1

List of Appendices

Page -xx-

1. Introduction

As a result of recent economic conditions and market demands, steel producers must achieve higher productivity and quality levels, while simultaneously reducing operating and capital costs. The development of new secondary refining techniques and the implementation of continuous casting technologies are perhaps the most apparent avenues to achieve these goals. However, the integration of these technologies into an existing steelmaking shop imposes new constraints on the production of steel and, hence, increases the importance of control of the steelmaking process.

Dynamic control of pneumatic steelmaking processes has developed along two general paths, namely continuous monitoring of sensors which reflect the status of the process, and actual sampling of the metal bath. The sampling of the bath is facilitated by the sublance technology, and has achieved significant success.

The major disadvantage of implementing the sublance technology is its high capital and operating costs. Its implementation often requires extensive modifications to the shop structure itself, increasing the capital costs dramatically, which may explain why the cost of implementation varies greatly from plant to plant. In addition, high operating costs are often incurred in maintaining the sublance system operational.

Since the cost of implementing the sublance may be prohibitive to some

steelmaking shops, these shops must pursue other means of controlling the steelmaking process. Thus, various sensors must be developed that can reflect the status of the steel in the vessel. One such sensor is the accelerometer, a vibration-sensitive device. The application of the accelerometer, as a process control sensor, is facilitated by the inherent solid-liquid-gas interactions which cause the steelmaking vessel to vibrate during the process. An obvious factor affecting the magnitude of these interactions is the decarburization of the metal bath. The generation of CO_{qas} within the system imparts a mixing energy which causes the vessel to vibrate; the more COgas evolved, the greater Therefore, one would expect the intensity of the vibrations. similarities between the rate of decarburization and the accelerometer signal. Another major factor affecting the interactions is the slagmetal emulsion, which itself is influenced by the condition of the slag. These two factors are the rationale behind the application of the accelerometer in the dynamic control of the oxygen steelmaking process.

The present research work was undertaken to determine the feasibility of the accelerometer as an end-point carbon control sensor by measuring the vibrations of the steelmaking vessel during laboratory scale BOF simulations. Moreover, it attempted to elucidate three key points, (1) the major characteristics of the accelerometer signal during the oxygen blow, (2) the end-point carbon range or product mix for which the accelerometer can be applied, and (3) to suggest a simple control scheme for industrial applications.

The first part of the research work focused on obtaining a relationship between the amplitude of the accelerometer and the steelmaking process itself. Since one can think of vib-ations as a variation in acceleration and, therefore, in the accelerometer signal, the first series of simulations monitored the accelerometer signal at low frequency. On the other hand, the second series of simulations attempted to discern the presence of specific vibrational frequencies that can be related to the process. For this reason, the accelerometer was monitored at higher frequencies.

As a final aspect of the research work, the feasibility of the accelerometer for various product mixes essentially the carbon endpoint for the steel, was determined. This involved terminating several high frequency BOF simulations prematurely in an attempt 'o elucidate the maximum carbon content of the steel that the accelerometer can detect, i.e. the carbon reference point.

In this thesis, a thorough presentation of the basic oxygen steelmaking process, acceleration transducers, and the control of the basic oxygen steelmaking process are made in Chapters 2, 3, and 4, respectively. A review of existing applications of the accelerometer in the steel industry is presented in Chapter 5. These chapters may be omitted from a first reading of this thesis, since an extensive body of literature has been accumulated.

Hence, the present experimental work is described in Chapter 6 while

the results are presented and discussed in Chapter 7. Chapter 8 concludes this thesis with a summary and a list of conclusions and recommendations for future work.

2. Oxygen Steelmaking Process

2.1 Introduction

The main route of producing primary steel from iron oxide ore is the blast furnace followed by an oxygen steelmaking process. Iron oxide is reduced in the blast furnace to form a liquid iron saturated with carbon (~4.7 %C); metallurgical coke, a carbon source, is the reducing reagent. Present in the iron ore are gangue minerals, some of which are reduced to a certain extent (such as Si, and Mn) while others are not. Thus, the blast furnace produces an iron, referred to as hot metal, that must be refined in a subsequent step in the production of primary steel.

The basic oxygen steelmaking process provides a technique that rapidly refines the hot metal received from the blast furnace. The removal of the majority of impurities in the hot metal is accomplished by oxidation followed by separation of the oxides into a separate phase, either liquid slag or gas. The oxidizing atmosphere is provided by the injection of high purity oxygen without supplementary fuel to generate the required heat; this characteristic distinguishes the basic oxygen steelmaking process from other processes.

The various basic oxygen processes (BOP) existing today are typically categorized according to the oxygen delivery system, top or bottom oxygen blowing. Further classification is made with respect to operating practices and the presence of stirring gases, post combustion facilities and other minor differences. The basic oxygen furnace (BOF)

process, the most common type of BOP, delivers oxygen through a water cooled lance positioned above the melt, while the Q-BOP delivers oxygen through a set of tuyeres situated in the bottom of the vessel.

Regardless of the type of BOP, the refining process is carried out in a vessel in which a small portion of the furnace volume is taken up by the charge. The capacity of these vessels ranges from 100-400 tonnes of charge. The process is an extremely efficient method of making steel, regardless of furnace size. The charge normally consists of 70-80% hot metal and 20-30% scrap steel and/or iron. Variations in the scrap ratio from plant to plant are largely due to differences in operating philosophies and process type (ie., BOF vs. Q-BOP).

Basic oxygen steelmaking plants differ from one another largely with respect to equipment layout; this is primarily due to provisions for casting facilities and arrangements required to integrate existing plant facilities. The latter reason is a result of the relatively young age of the BOP, especially when compared to the blast furnace process. Plant equipment layout and subsequent logistics of material handling, such as the transfer of hot metal and liquid steel from one process step to another, plays a critical role in the performance of the basic oxygen steelmaking plant. However, the implication of such operational considerations is beyond the scope of this report.

In this chapter, a general description of the oxygen steelmaking process will be given followed by a review of the physical chemistry and kinetics of the oxygen steelmaking process.

2.2 General Description of the Oxygen Steelmaking Process

2.2.1 BOF/LD/LD-AC Oxygen Steelmaking

2.2.1.1 Introduction

The BOF process refines hot metal in a solid bottom, cylindrical vessel using a vertial water cooled oxygen lance entering from above. The vessel, lined with refractories, is mounted on a set of trunnions that facilitate charging and tapping of materials by tilting the vessel. The charge comprises of hot metal, scrap and fluxing reagents. Small quantities of iron ore may also be added. The product tapped from the vessel is liquid steel low in impurities, ranging in carbon from 1.0 %C to less than 0.05 %C.

Two major by-products are generated by the BOF: a liquid slag containing most of the impurities and an off-gas comprising of CO and CO₂, depending on various factors. The liquid slag is typically sent to a benefication plant to recover its iron and iron oxide content before being used in such applications as road fill. The off-gas is exploited for its heat content.

As was mentioned in the introduction, the unique aspect of the BOP is that the energy generated during the refining process is sufficient to bring the metal to its final temperature. The BOF, in fact, makes use of the heat generation to recycle approximately 30% by weight of scrap steel and/or iron without the use of supplementary fuels. Occasionally the heat balance may be altered to account for various factors, including supplementary fuels required to significantly increase the proportion of scrap charged.

The LD steelmaking process, named after Linz and Donawitz, was developed in 1952. The development of the LD was preceded by several years of experimentation, most notably by R. Durrer^[1,2]. Durrer's experiments were carried out on a pilot plant scale of 2.5 tons. The results obtained showed clearly that it was possible to refine iron by use of pure oxygen and to remove the impurities by the use of a basic slag. The experiments also indicated that a relatively large proportion of scrap could be added, nearly 50% of the charge in some cases.

Pilot plant scale work gradually evolved into a commercial plant with a 35 ton vessel in 1952. The scaling-up work was performed at Linz in association with VÖEST, an Austrian Iron and Steel producer^[3]. A technical group representing VÖEST management concluded that because of prior common knowledge, especially patents of Bessemer (1856) and Scharz (1931), the process was not patentable. However, patent applications were filed in Austria and the United States, US patent No. 2800631 was subsequently issued.

The US patent was the focal point of several law suits between the licensing agent and several US steelmakers. The US courts concurred with the VOEST technical group declaring the patent invalid because it did not meet the "substantive requirements of the Patent Laws". As a result of the conflict, North American steelmakers referred to the LD process as the BOF, hence, the reason for the two names.

The growth of the BOF process, outside of Austria, was concentrated in

North America. The earliest plants were sized mostly from 30 to 50 tons with the notable exception of Jones and Laughin's Aliquippa vessel rated at 80 tons. After these initial plants were proven successful, the number of installations and the size of the vessels continued to increase dramatically. Amazingly, ten years after the first commercial plant, Great Lakes Steel commissioned a 300 tons vessel at Escore Michigan, US⁽⁴⁾.

The initial growth rate in Europe, however, was limited primarily by a high phosphorous content in the hot metal. In England, France and Germany, the major process was the basic Bessemer or the Thomas process; these are based on a high-phosphorous hot metal and a two-slag practice. Initially, the LD process could not successfully remove phosphorous, thus, making the steel inferior. The problem was overcome by the development of the LD-AC and OLP processes, in Benelux and France, respectively. Both processes injected lime powder into the metal bath via the oxygen lance, using the oxygen as the carrier gas. In addition to the injection of lime, both processes, like their counterparts, employed a two slag practice.

As the the LD-AC and OLP processes were blossoming, many steel producers were abandoning native phosphoric ores in favour of the high-grade ores imported in large carriers. Within twenty years of the first BOF plant, the process had become the foremost steel process in the world. In addition to its awesome growth, vessel sizes often exceeded more than ten times its original size.

The remainder of this section is devoted to a detailed description of the BOF steelmaking practice. The description is divided into the following topics:

- · General Vessel Description
- · Oxygen Lance
- Operational Procedures

2.2.1.2 General Vessel Description

The design of the BOF vessel, particularly those in excess of 300 tons, required great engineering feats. As was mentioned earlier the BOF vessel is a solid bottom crucible. More specifically, the furnace can be described as having three sections; the bottom shell portion is usually a torispherical or torispherical-conical segment; the central portion, a cylindrical barrel; and the top portion, a truncated conical shell segment. A schematic diagram depicting the BOF vessel and its driving mechanism is shown in Fig. 2.1. A lower knuckle section is normally used as a transition from the spherical bottom to the cylindrical barrel section, although a short conical section is Similarly, an upper knuckle section is occasionally sometimes used. used between the barrel and the cone, although usually omitted in newer furnaces. A nose ring with a top lip ring plate is attached by bolting to the top cone at the mouth opening. A reinforcing stiffener band is usually welded to the end of the nose cone. The whole shell is protected internally by a safety layer and a working layer of refractory linings.

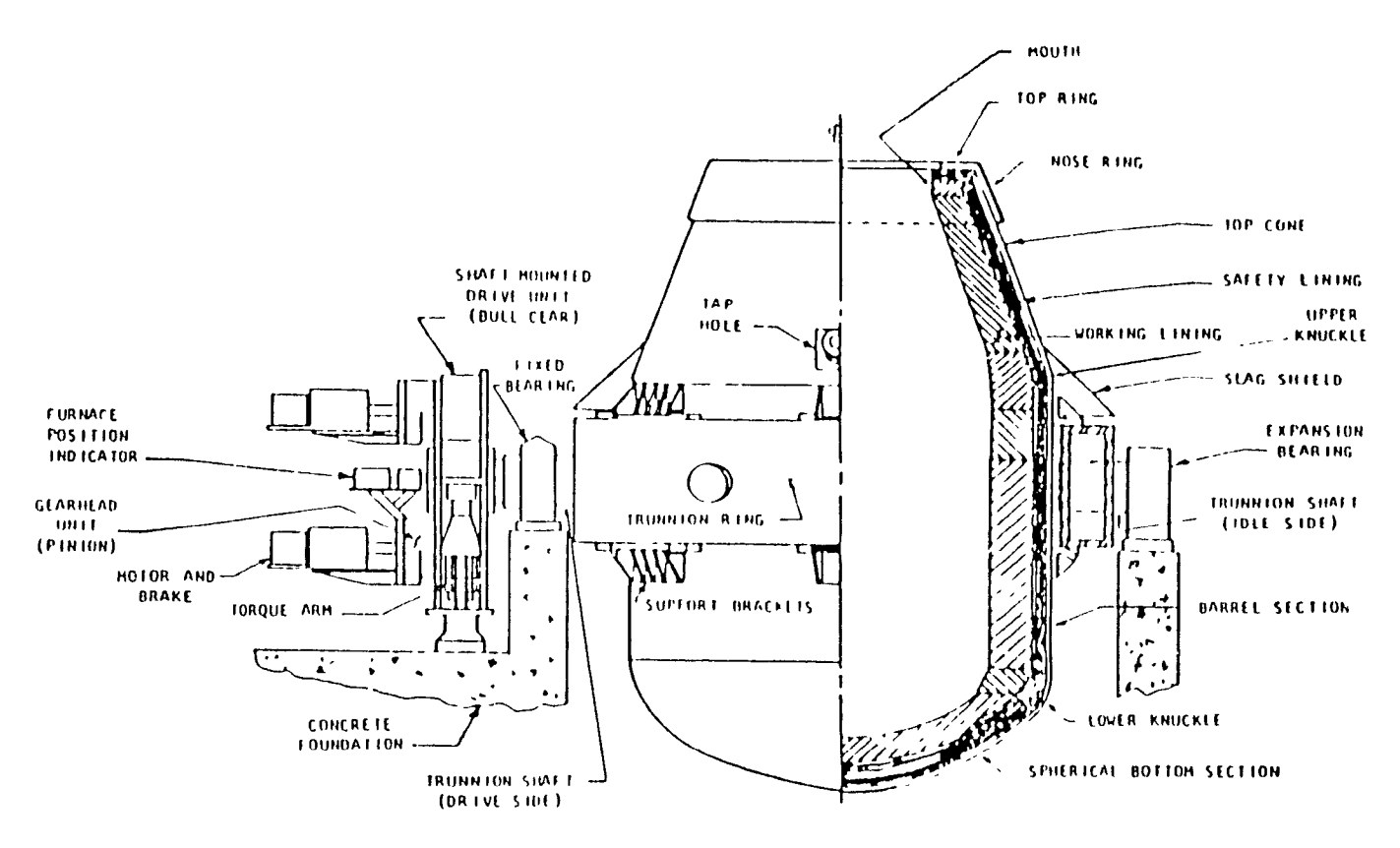


Fig. 2.1 Components of a typical BOF vessel [4].

The vessel shell, refractory linings and its charge are supported by a bracket or suspension system attached to the outside of the shell, which transmits the load to the trunnion ring, as shown in Fig. 2.1. The trunnion ring, in turn, is supported by trunnion shafts. This trunnion ring and shaft assembly is actually the main structural component used to transfer the total load of the vessel to the foundation. Typically only one of the two trunnion shafts is connected to the driving mechanism, hence, referred to as the driving side. The need for the free side to be equipped with a driving mechanism increases as the furnace capacity exceeds 250 tons. Both sides are

supported by bearings which ultimately transmit the load to the foundation while allowing the trunnion ring shafts to rotate. The trunnion shaft on the drive side is attached to a large diameter bull gear which is driven by pinions. Each pinion is driven by an independent motor and brake system.

The most common descriptive parameter of the BOF is the ratio of the furnace height to diameter. Through experience, it appears that a ratio of 1.5 to 1 obtains the optimum conditions, minimizing ejection of slag and steel from the vessel. In general, the sizing of the furnace is based largely on accumulated experience and the use of operating and dimensionless parameters.

The service life of the refractory linings of a BOF vessel depends on several operating, metallurgical and engineering principles. Figures 2.2 and 2.3 show the dimensions of the shell and refractory linings for 75 and 300 tons furnaces. As can be seen, the thickness of the refractory linings are approximately the same. In fact, if we considered the consumption of the working lining for several North American plants versus vessel size (heat size), as shown in Fig. 2.4, the overall trend indicates a reduced consumption with increasing vessel size. However, the large variation in the consumption does suggest that other factors are involved.

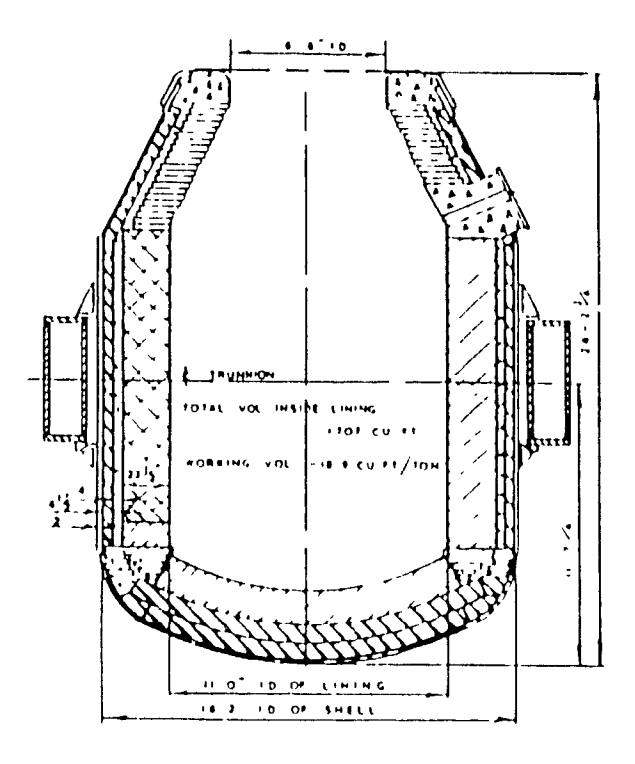


Fig. 2.2 Schematic of a 75 ton vessel showing the refractory linings $^{[4]}$.

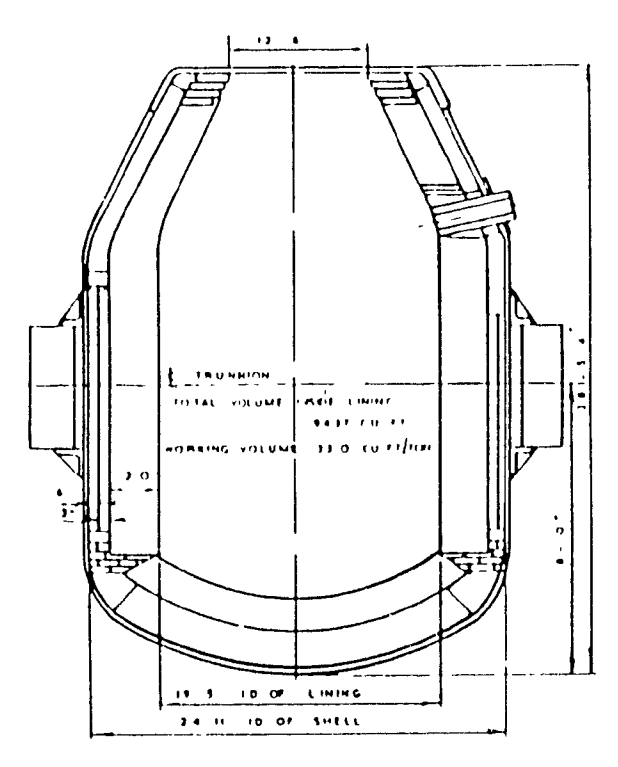


Fig. 2.3 Schematic of a 300 ton vessel showing the refractory linings $^{[4]}$.

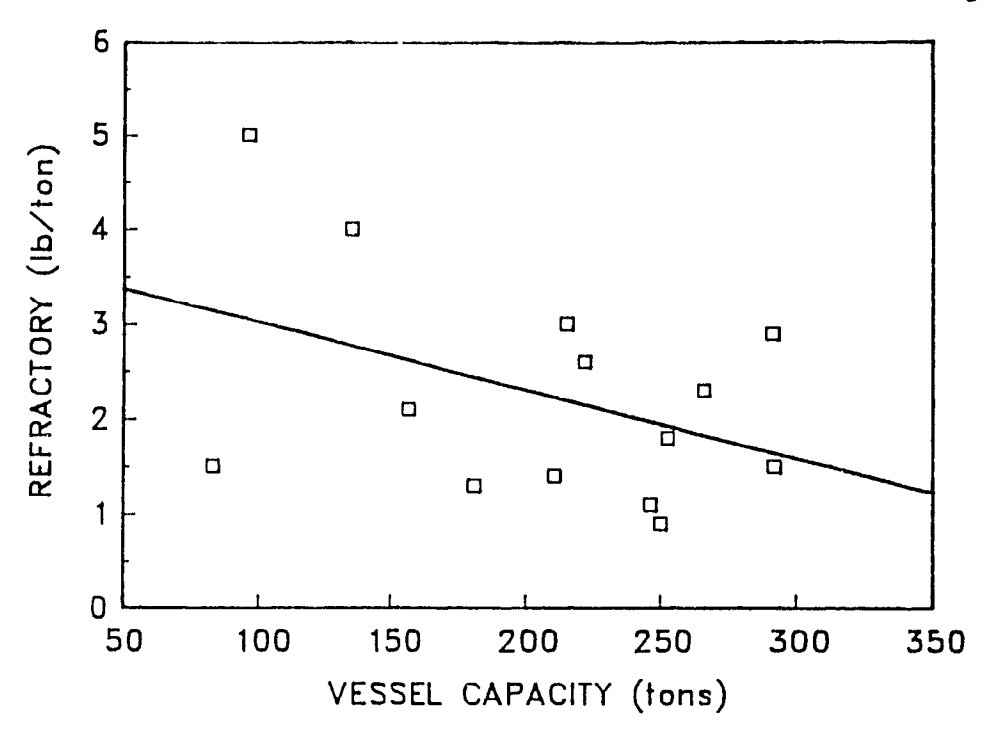


Fig. 2.4 Refractory lining consumption versus vessel heat size for several North American BOF plants.

Indeed, refractory costs represent a significant portion of the operating costs in a BOF plant. Common variables that affect the lining life are:

- slag analysis at tap
- hot metal analysis
- turndown temperature
- MgO content of the fluxes
- · quality of burned lime
- furnace gunning practice
- furnace design
- time from end of blow to tap

There are other variables that are not listed because of some interdependence with those variables listed above. For example, the number of reblows on a particular heat affects tap analysis; usually by increasing FeO content in the slag and, thus, reducing lining life.

Lower silicon content in the hot metal will improve the life of the refractories; however, the amount by which it can be reduced is limited. The manganese-silicon ratio must not exceed 5:1 in order to eliminate sparking. In addition, a reduction in the hot metal silicon reduces the quantity of scrap in the charge, as shown in Fig. 2.5. The main advantage of reduced hot metal silicon levels is a reduced slag volume in the BOF.

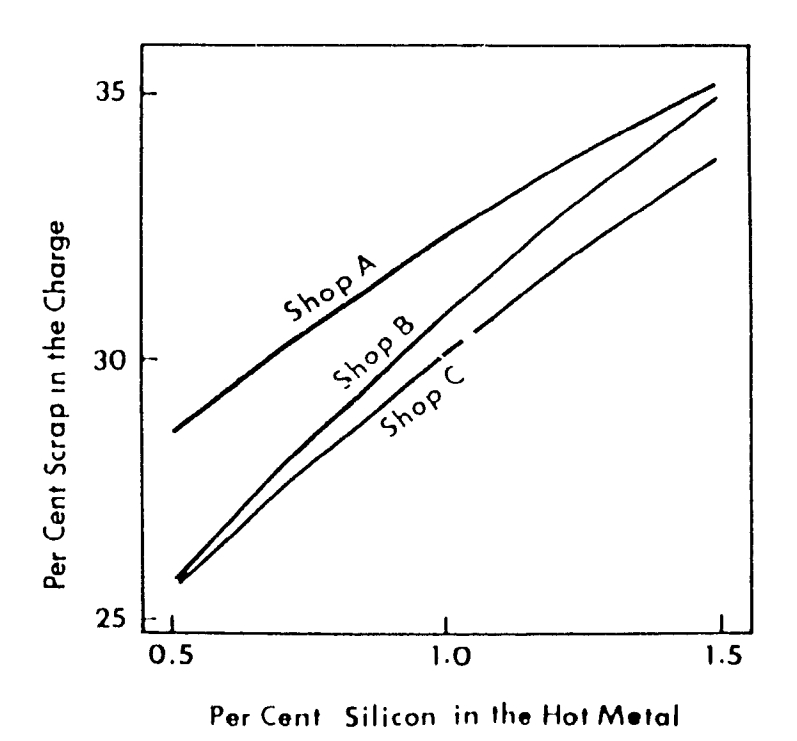


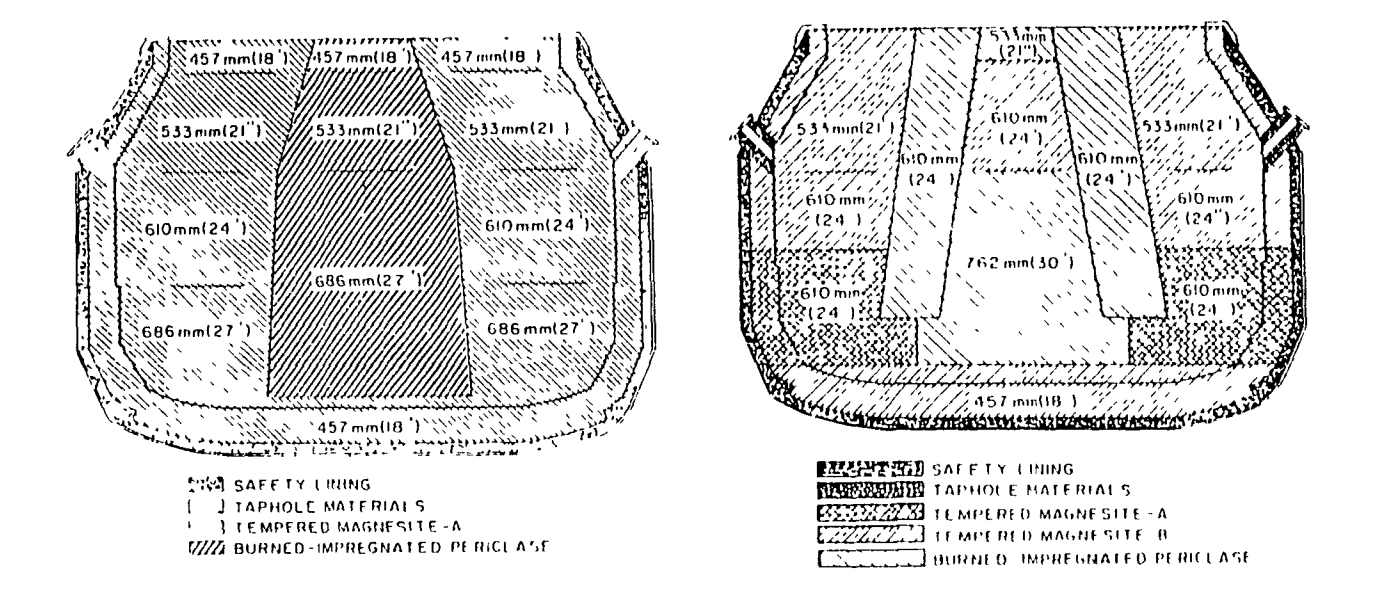
Fig. 2.5 Scrap charge as a function of silicon content of hot metal for three different BOF shops (aim carbon $\approx 0.05\%$) [5].

The tap temperatures are detrimental to the refractory service life. This became increasingly evident as the number of BOF shops supplying steel to continuous casting machines increased; higher tap temperatures are required for the extra processing time involved.

Dolomitic lime increases the MgO content and the viscosity of the slag and produces a less erosive slag. However, the viscosity of the slag is limited because of sampling difficulties incurred with viscous slags. The early formation of a fluid slag improves the operation of the process and vessel life.

Gunning a vessel with a high MgO refractory compound will usually increase vessel lining life; refractory linings are typically dolomitic (high MgO). The type of gunning practice adopted is determined primarily by economics.

The shorter the heat time in the furnace, the shorter the erosion time and, inevitably, the longer the lining life. Furthermore, it is the portion of time after the main blow and between the start of the tap, including reblows, that is the most detrimental to lining life. It is at this stage that the erosive slag attacks the refractory.



NOTE
NUMBERS INDICATE APPROXIMATE LINING THICKNESSES
LINING SHOWN AS FOLDOUT THROUGH TAPHOLE

Fig. 2.6 Simple (Left) and complex (Right) refractory lining patterns [5].

BOF linings are predominantly composed of magnesite brick bonded or impregnated with binding agents. Figure 2.6 shows both simple and complex refractory lining patterns; linings are installed in differing types and thicknesses in a zoned configuration to meet the specific demands of each area of the vessel. Ideally, the lining pattern is designed in such a manner as to have a minimum of refractory left in all locations after a campaign.

2.2.1.3 Oxygen Lance

The oxygen lance system of the BOF process is a critical component. Although considerable effort has been expanded on the development of reliable lance systems, duplication is a must. A general lance system is shown in Fig. 2.7. An oxygen lance system comprises of three main

components; an oxygen lance body serving as a conduit for gases and cooling water, a lance nozzle which forms the oxygen jet and a lance crive unit to move the lance vertically into the desired position.

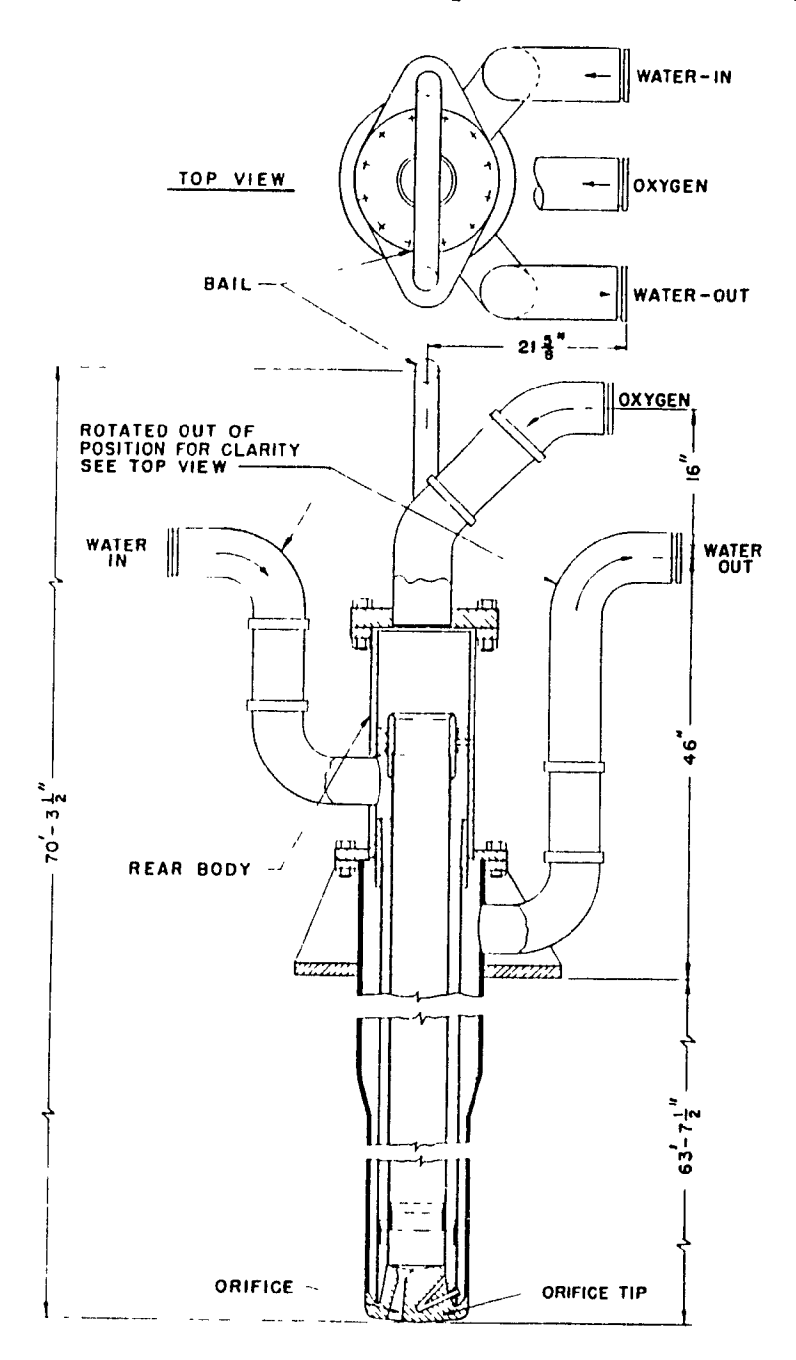


Fig. 2.7 Basic oxygen lance construction showing a multiport, converging-diverging nozzle [4].

The oxygen lance body comprises of a rear body, from which it hangs, and three eccentric pipes. The rear body may be of cast or fabricated construction with suitable connections for attaching the oxygen and cooling water service lines. Oxygen flows through the center pipe which is surrounded by inlet water moving down through the adjacent annular passage to the nozzle tip. After the cooling tip, the water returns through the outer annular passage to the rear body and discharge connection.

The outer pipe is securely fastened to the rear body and orifice tip. As a result of the construction, the inner pipes must be secured in a manner providing for differential expansion under operating conditions. At the upper end of the lance, the oxygen pipe is sealed by a pressure gasket arrangement that permits unrestrained endwise movement of the outer pipe. At the nozzle, the oxygen pipe is welded to the orifice tip. The middle pipe serves as a baffle between the inlet and outlet passages of the cooling water. The only requirements are that this pipe provide uniform clearance for the passage of water.

The most critical metallurgical parameter is the nozzle; the nozzle determines the maximum impingement force of the jet, the degree of post secondary combustion (CO + $^1/_2$ O₂ \rightarrow CO₂), the characteristics of the slag formation process and inevitably the refractory consumption. In the section below the general design of a nozzle and lance system is reviewed.

The early designs of BOF lance nozzles were typically straight, single

bore orifices. As vessel capacity increased, the single bore nozzles operated at proportionally higher oxygen flow rates. At the extreme, the high flow rate resulted in increased splashing, slopping and reduced yield. To overcome this problem a multi-orifice nozzle was developed.

The multiple-orifice lance head design was quickly accepted. The main advantages attributed to the multiple orifices are improved yield, less slopping, smoother blowing operations with higher blowing rates and improved oxygen efficiency. Detracting from the multi-hole design is the fact that the division of the total oxygen flow into smaller streams reduces the impingement forces. To compensate for this, multiple hole lances must operate closer to the bath than a single hole lance having the same capacity. The end result is increased lance erosion, ultimately leading to shorter lance life and increasing effective water cooling requirements. The acceptance of converging-diverging orifices alleviated this problem to some extent. A comparison of nozzle orifice types is made in Fig 2.8.

The theory of converging-diverging nozzles is discussed below in a concise manner; the discussion does not attempt to derive or develop the governing relationships from first principles. For an exhaustive presentation the reader is referred to Reference^[6]. Converging-diverging nozzles permit the oxygen jet to exceed sonic velocity, where sonic velocity represents the speed at which a pressure wave will travel through a compressible fluid and is expressed as:

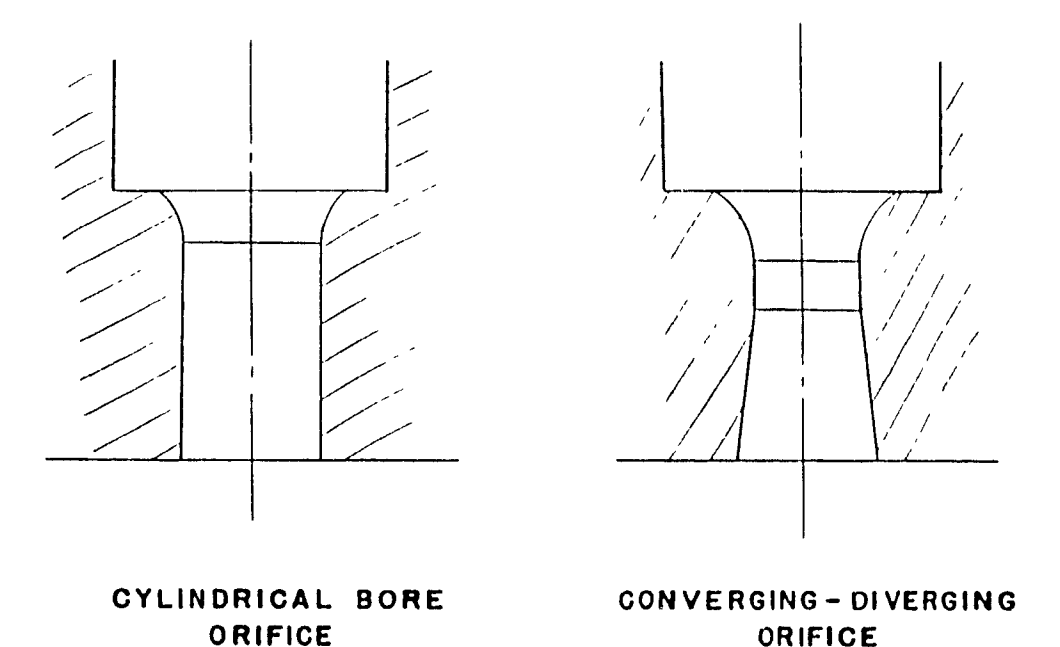


Fig. 2.8 Schematic presentation of the cylindrical, or straight-bore, and the converging-diverging nozzle.

$$c = \left\{ k \cdot R \cdot T \right\}^{-1/2} \tag{2.1}$$

where k is the isentropic exponent (C_p/C_v) , R is the gas constant and T is the absolute temperature. The mach number is a dimensionless ratio of the velocity of the fluid and the sonic velocity as shown below:

$$N_{\rm m} = \frac{V}{c} \tag{2.2}$$

where V is the velocity of the fluid. If $N_m<1$ the flow is said to be subsonic; if $N_m=1$, the flow is said to be sonic; if $N_m>1$, the flow is considered to be supersonic. The primary equation describing the conditions necessary for sonic or supersonic flow can be derived from the continuity equation and the Euler equation and is expressed as:

$$\frac{\partial A}{A} = (N_m^2 - 1) \frac{\partial V}{V}$$
 (2.3)

where ∂A is the change in cross sectional area in a one dimensional, cylindrical duct and ∂V is the change in velocity. From this equation several conclusions can be summarized as follows:

1. For subsonic flow $(N_m<1)$:

If
$$\frac{\partial V}{V} > 0$$
, $\frac{\partial A}{A} < 0$
If $\frac{\partial V}{V} < 0$, $\frac{\partial A}{A} > 0$

(area must decrease for increase in velocity)
(area must increase for decrease in velocity)

2. For supersonic flow $(N_n>1)$:

(area must increase if
velocity is to increase)
(area must decrease for a
decrease in velocity)

3. For sonic flow $(N_m=1)$:

$$\frac{\partial \mathbf{A}}{\mathbf{A}} = 0$$

Hence, it is apparent that to accelerate a flow at subsonic velocity, converging passage is required just as in the case of an incompressible fluid. To accelerate a flow at supersonic velocity, however, a diverging passage is required. This is explained by the fact that the decrease in fluid density exceeds the increase in flow velocity; therefore, to satisfy the expression of continuity, the passage must diverge.

For sonic velocity it is noted that $\partial A/A=0$. This condition occurs at the throat of a converging passage. The occurrence of sonic velocity in the throat of the passage requires a high pressure differential to accelerate the flow to sonic velocity. The velocity at the throat

will be a maximum, but not necessarily sonic. If the sonic velocity is attained in the throat, the flow will become supersonic if the converging passage is succeeded by a diverging passage. However, if the sonic velocity was not attained in the throat section, there would be a decrease in the velocity in the diverging passage that follows.

Thus, the design requirements for oxygen lance nozzles are such that a sonic velocity is attained in a converging section and maintained in the throat section followed by a diverging passage whereby the oxygen is accelerated to supersonic velocities.

The importance of water cooling in the operation of an oxygen lance is readily emphasized by the fact that the lance materials have melting points substantially lower than the maximum temperature generated with the BOF vessel. There are a large number of factors involved in maintaining the lance components at the appropriate operating temperatures. The major factors are lance size and exposed surface area as well as the condition of the cooling water itself.

With the introduction of multi-port nozzles, recommended cooling water flow rates increased by about 50%. This change is due primarily to the operation of the lance at lower lance heights and to a rather general observation that higher cooling water flow rates are conducive to longer lance life. The cooling water requirements for a typical BOF oxygen lance can be expressed in the following general equation:

```
where Q = cooling water flow rate (1/s)

k = \text{empirical constant } (4.1 \times 10^{-5} \text{ l} \cdot \text{s}^{-1} \cdot \text{m}^{-2})

D = nozzle diameter (m)

l = \text{lance length } (m)
```

The above formula assumes a maximum temperature rise of 15°C and high quality recirculating water (ie. minimal foul-up). The cooling water velocities are typically designed to avoid nucleate boiling on the hot faces of the lance; water cooling velocities of 12 to 15 m·s⁻¹ are common. It is interesting to note that the counter-current design supplies the colder water at the most critical area, the nozzle tip.

2.2.1.4 Process Operation

The BOF shop is a high productivity process, and the success of plant operators attaining the maximum productivity depends strongly on the efficiency of the operating practices employed. The average heat times, a traditional measure of productivity, have steadily decreased since its conception in 1952 until the 1980's were it appears that a limit has been reached. The average heat times for several North American steel producers are presented in Fig. 2.9. The large scatter in the data indicates that parameters unrelated to the BOF process are imposing limitations on the tap-to-tap times. These parameters include shop design and layout, and operating practices. Once a BOF shop is designed and built, the product mix usually being defined by existing finishing plants, the only tool available to steel producers to improve productivity is the development of efficient operating practices, short of investing large sums of capital. For this reason, the process operation or practice is briefly reviewed here.

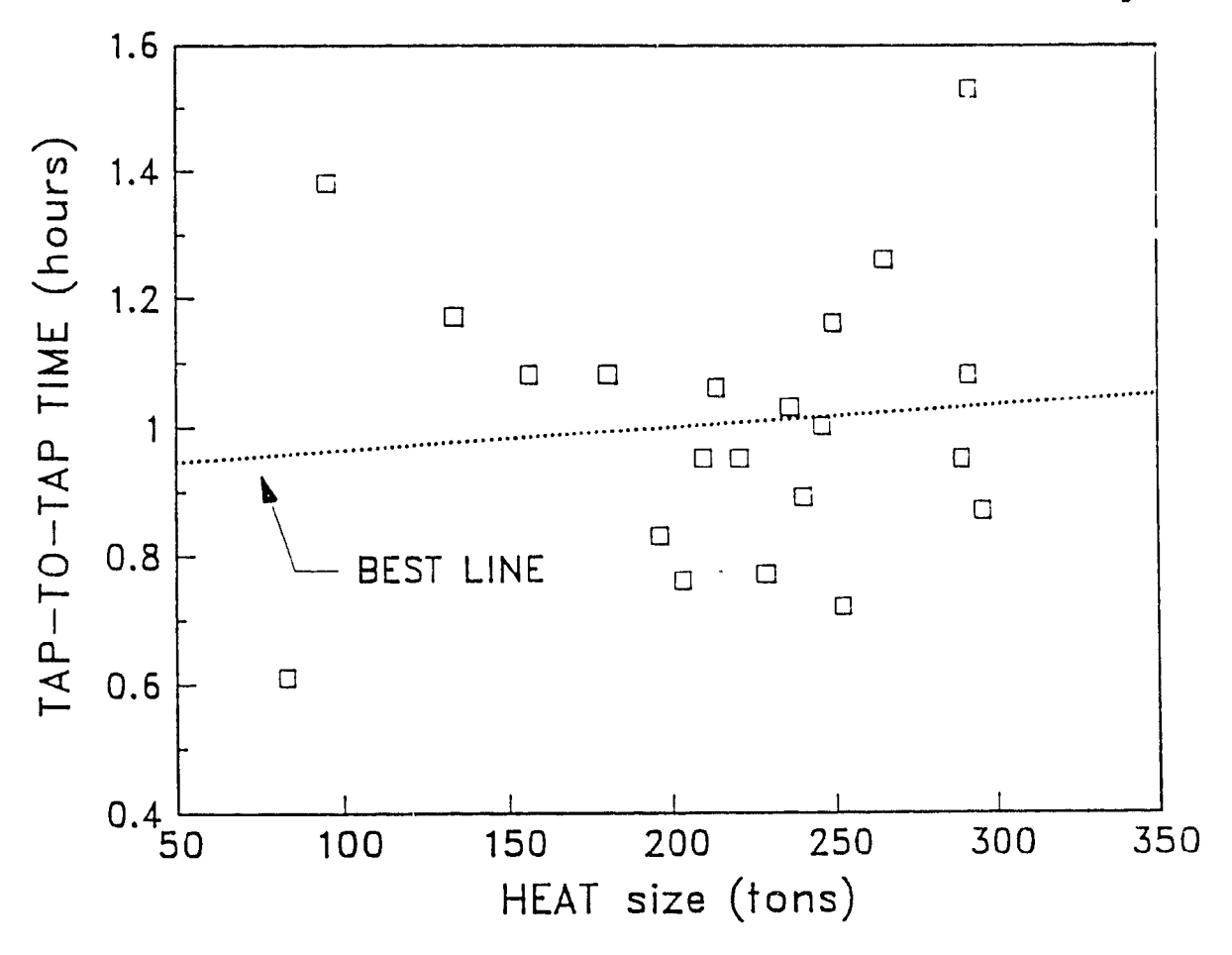


Fig. 2.9 Average tap-to-tap times for North American steel producers.

A typical BOF heat cycle generally begins with the hot metal order to the blast furnace, typically automated via scheduling programs. The cycle only begins in earnest when the hot metal charging ladle arrives at the hot metal pouring station. The charge calculation, a predictive-adaptive model, determines the weights of hot metal, cold pig iron, steel scrap, and flux materials required to produce a specified weight, temperature, and chemical analysis of steel at the end of the refining process. In many BOF shops, a predetermined weight of hot metal and scrap is weighed out and the final weights are obtained by trimming either or both after the charge calculation for the heat that has been completed for the actual weights received.

The hot metal and cold scrap are then transferred to the charging aisle, normally by transfer car. After the furnace has been tapped and the vessel emptied of any remaining slag from the previous heat, the vessel is rotated into position for the scrap charge. The scrap is charged from either a scrap charging machine, typically taking less than two minutes per charge. Following the scrap charge, the vessel is rocked to level the scrap in the furnace.

The vessel is then rotated back to the charging side to receive the hot metal which is poured into the furnace from a spouted transfer ladle using the charging crane, as shown in Fig. 2.10. The vessel is righted and the oxygen lance is lowered into position; oxygen flow is usually started while the lance is being lowered to avoid nozzle blockage. The ignition flame is normally achieved shortly after the lance is in position. Once ignition has occurred, flux materials such as burnt lime, dolomitic lime, fluorspar and possibly iron oxide are added to initiate the slag formation stage. Several different flux addition schedules are employed, however, those techniques which accelerate the formation of a good slag are preferred. The lance height and the oxygen blowing rate are occasionally varied during the heat by an operator or an automatic control program.

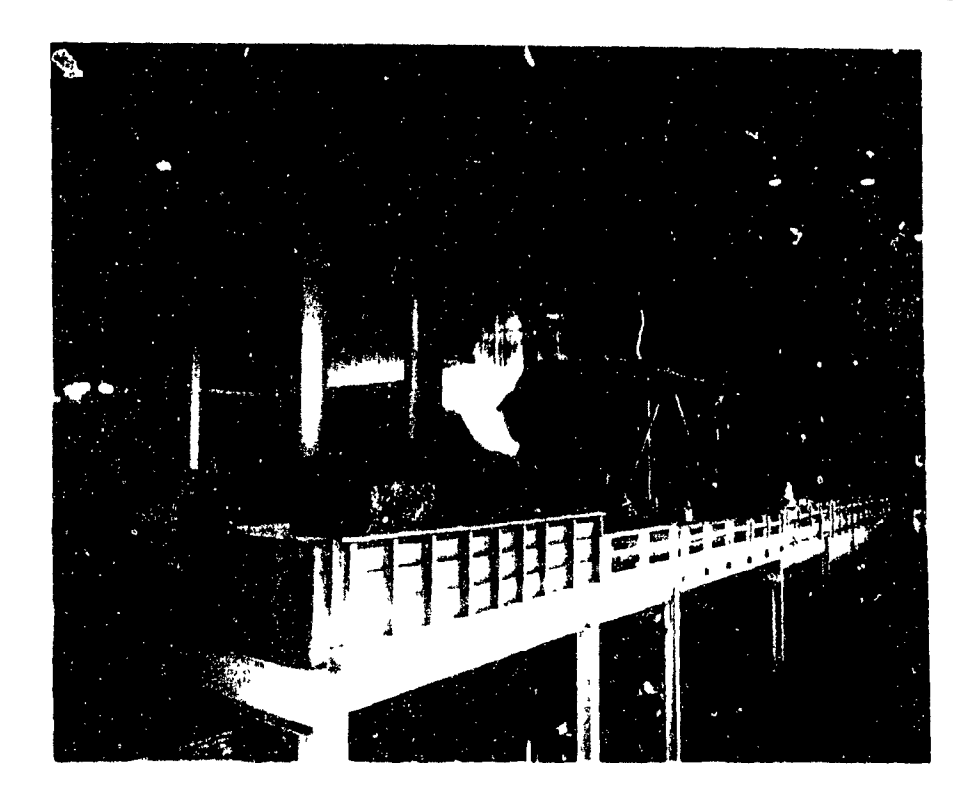


Fig. 2.10 Hot metal charging operation at Stelco Steel's Hilton Works.

The oxygen blow typically requires 15 to 30 minutes; determination of the correct time to terminate the oxygen blow is made by several methods. The accuracy of these methods often determines the duration of the heat. Methods for end-point control can be as simple to the visual flame drop method for low carbon steels or signif. The complex. These techniques are described in detail in Chapter 1.

After the main blow has terminated the vessel is rotated to the charging side for temperature and steel sampling, a step that is often avoided with the sublance technology. The steel bath temperature is usually measured first to confirm that the heat has obtained the minimum temperature, for the steel specifications. The temperature also provides an indication of the carbon content, and if nerow the minimum level, the heat is immediately reblown. The major exception

occurs when the steel temperature meets the requirements of another steel specification that must be produced. If the temperature of the bath exceed the minimum, the steel and the slag are sampled. Two types of steel samples are taken; the first sample is taken by immersing a disposable sampler and is used for laboratory analysis. The second sample is typically taken in a spoon; the steel in the spoon is subsequently poured into a special crucible. From the cooling curve generated by a thermocouple embedded in the bottom of the crucible, a reasonably accurate carbon analysis is made.

Based on the "quick" carbon test the heat may be reblown or left idle while operating personnel await the laboratory results. If the carbon, sulphur or phosphorous content of the steel is too high, the heat is normally reblown; a lime addition is often made to assist the desulphurization reactions. For most heats produced, the levels of manganese and silicon in the steel at tap time are well below the maximum levels permitted.

Once the steel specifications of temperature and chemistry have been obtained, the vessel is rotated to the tapping aisle and tapped into a ladle; the ladles are typically on transfer cars situated below the BOF vessel. The bulk of the alloy and deoxidation additions are made to the ladle during tapping, taking advantage of the mixing power of the steel stream. The compact tap stream is facilitated by a tap-hole in the upper sidewall of the vessel, this arrangement also minimizes slag carryover from the refining vessel. After completing the tapping operation, the vessel is rotated back to the charging aisle and the

slag is dumped into a slag pot under the vessel.

At this time the refractory lining of the vessel is inspected, and possibly measured and, if necessary, possible repair action is taken, normally by "gunning" a refractory slurry onto the lining. If no serious repair action is required, the furnace is positioned for the next scrap charge. This cycle may be repeated 20 or more times a day making the BOF an extremely productive process.

2.2.2 Other Oxygen Steelmaking Processes

2.2.2.1 Q-BOP/OBM Oxygen Steelmaking

The Q-BOP or bottom-blown oxygen steelmaking process was developed in the 1960's and early 1970's. Although the Q-BOP has many similarities to the top-blown process, there are several important differences. The obvious difference, as the name implies, is that the oxygen used for refining the hot metal is injected into the bottom of the vessel, improving the "mixing power" of the process. As a result, the primary advantage is that the Q-BOP operates much closer to equilibrium conditions between the metal and the slag and is, therefore, much lower in oxidation potential than the top-plown process. This characteristic manifests itself in lower iron losses, higher manganese recoveries, less slopping, etc.. In fact, vendors of the Q-BOP or OBM technology are quick to suggest that the Q in the process name represents the following:

- •Quick tap-to-tap
- ·Quiet blowing behaviour and
- •Quality product.

The first Q-BOP heat was produced in December, 1967, at the Sulzbach-Rosenberg Works, a modest heat size of 25 tons^[7]. In 1968, Maxhutte began to convert its Thomas converter plant to OBM/Q-BOP; the following year Maxhutte entered the field of licensing and technology transfer by selling the Q-BOP technology to Usinor and Neuves-Maisons of France as well as to Rochling-Burbach of West Germany. Efforts to introduce the Q-BOP technology to North American steel producers was facilitated by several tests showing its potential with low phosphorous hot metal in 1970. From that point on the application of the technology

increased rapidly until combined blowing techniques were introduced in the late 70's and early 80's. The production capacity of Q-BOP from 1967 to 1978 is shown in Fig. 2.11.

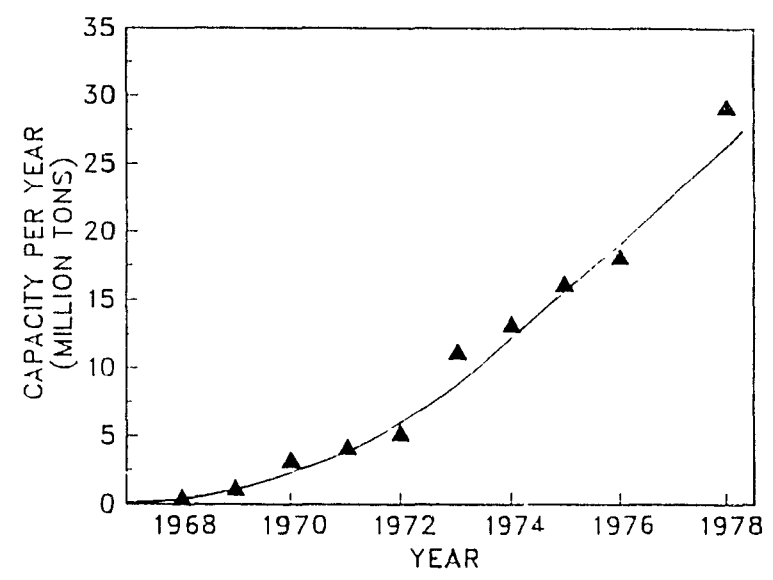


Fig. 2.11 Production capacity of the Q-BOP/OBM process from 1967 to $1978^{(11)}$.

The plant layout for a bottom-blown steelmaking shop is similar to that of a top-blown one. The major difference is that the required overall height for a Q-BOP shop is considerably less without an oxygen lance and, hence, represents a major capital cost reduction for a "greenfield" site. Furthermore, it is generally much easier to retrofit the bottom-blown process into an existing open-hearth shop. Other differences in the shop layout include provision for the process gases to be delivered to the bottom of the vessel where typically 16 or more tuyeres are set in the bottom's refractory lining⁽⁸⁾. Process gases are normally, but not necessarily, piped through the idle trunnion of the vessel to provide safe passage, a schematic of a Q-BOP is presented in Fig. 2.12.

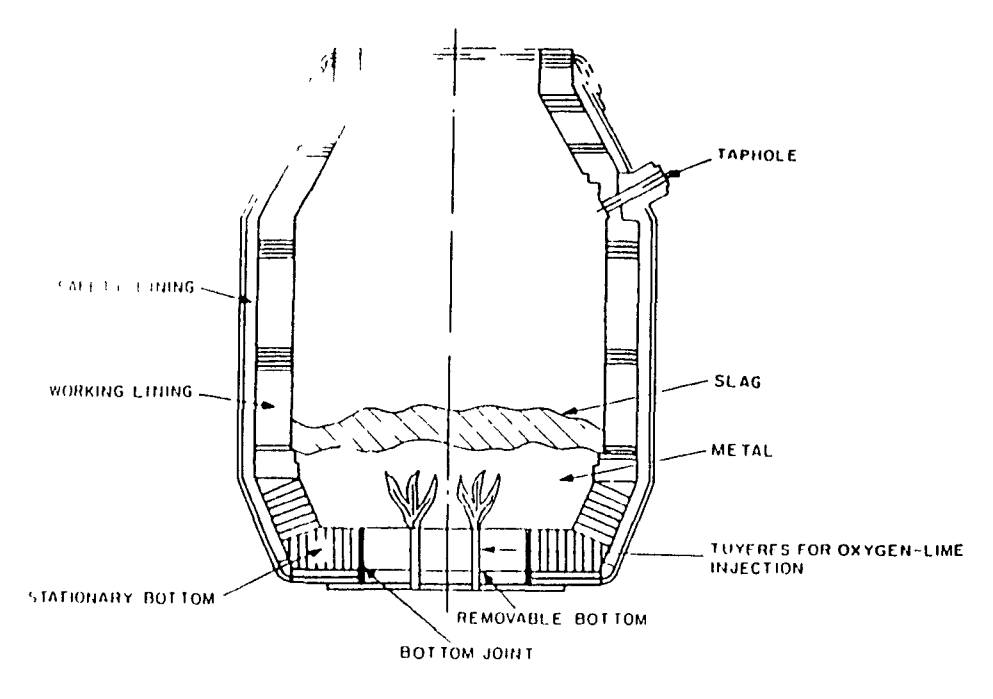


Fig. 2.12 A schematic of a Q-BOP vessel^[5].

Due to the high erosion rate of the bottom refractories and tuyeres, provisions are made in the vessel assembly and refractory lining to permit the quick replacement of the vessel bottom, including a complete set of tuyeres. An example of the refractory lining and the removable bottom is shown in Fig. 2.13. The service life of the vessel's barrel and cone section typically exceeds the bottom section by a factor of two to three. Since the service life of the barrel and cone of the Q-BOP are similar to that of the BOF process, these sections are lined in an identical manner. A comparison of refractory performance between the Q-BOP and the BOF is shown below in Table 2.1. As can be seen, the refractory system on the bottom section requires special precautions to avoid the rapid erosion of the tuyeres and refractory system. Erosion of the tuyeres is accelerated by the high operating temperatures and the motion of the liquid bath.

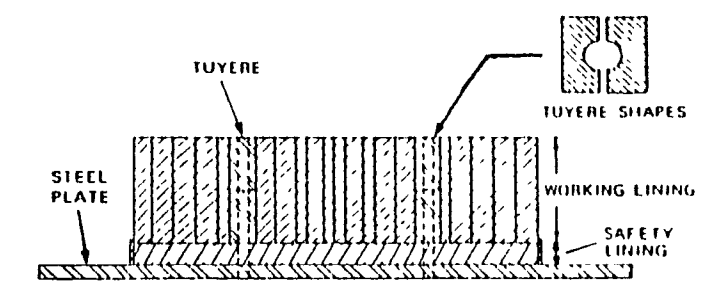


Fig. 2.13 Refractory lining of the removable bottom of a Q-BOP vessel $^{\text{[8]}}$.

Table 2.1 Comparison of Refractory Consumption Between the Q-BOP and the BOP Processes $^{\{9,10\}}$.

ITEM	Q-BOP	BOF
Lining Life, heats Side Wall Life Bottom Life	N/A 1400 450	1900 N/A N/A
Refractory Consumption. kg/tonne liquid steel		
Working Lining Safety Lining Bottoms	1.75 0.15 0.35	1.10 0.20 N/A
Gunning and Maintenance Materials	0.70	1.2
Total	2.95	2.5

Each tuyere, consists of two concentric pipes, the inner pipe delivering the oxygen while the outer pipe supplies a hydrocarbon, such as natural gas, propane, butane, etc. An example of a tuyere is shown schematically in Fig. 2.14. When the hydrocarbon comes near the molten bath, it decomposes endothermically absorbing enough energy, or heat, to essentially cool the region of the tuyere-metal interface. With this concentric tuyere design, pure oxygen can be introduced into the bath without excessive erosion of the bottom section. It is interesting to note that the Bessemer process, introduced in the 1860's, employed the nitrogen content of air as the "coolant" (albeit via a single pipe).

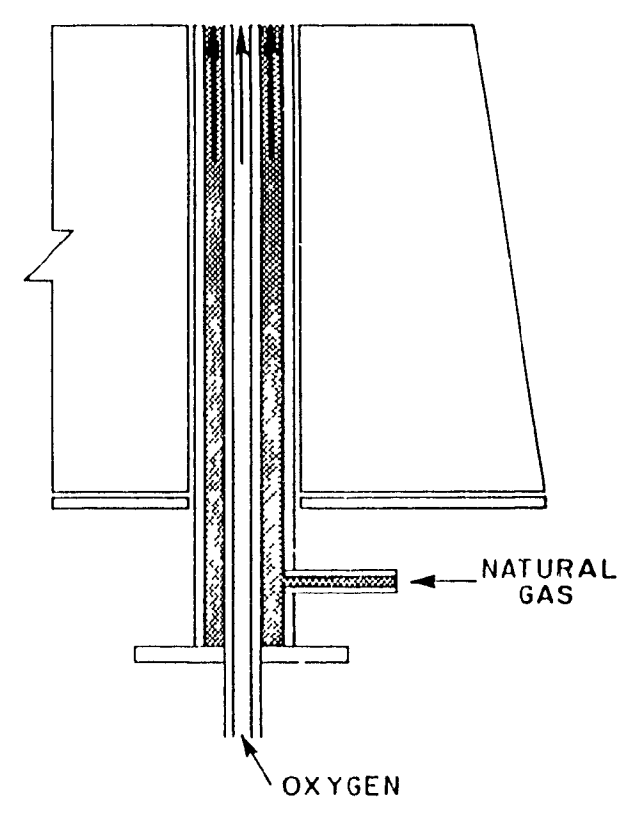


Fig. 2.14 Schematic of a Q-BOP tuyere [5].

The basic operation of the O-BOP shop is almost identical to the BOF shop. Major differences exist only because of the special precautions necessary to maintain high tuyere and refractory life of the bottom section and due to some of the advantages inherent in the process. The process description begins after the steel and slag from the previous heat have been removed from the furnace. At this point in time the vessel is tilted to a horizontal position and the furnace lining and tuyeres are inspected. If necessary, the furnace lining is repaired by gunning a refractory material onto the lining. Occasionally, a tuyere may not be sufficiently cooled by the hydrocarbon fluid and the tuyere will "burn back" too rapidly, typical burn back rates of ≈2.5mm/heat have been reported[10]. When the extent of the burn back endangers the safe operation of the process, the tuyere is removed from service by plugging it with refractory. During this maintenance period, a relatively small flow of nitrogen is maintained through the central and outer pipes of each tuyere to prevent the tuyere from being accidentally plugged by slag, metal or gunning material. nitrogen consumption for a Q-BOP varies from 15-20 Nm3/tonne; note that this is strongly influenced by specific shop practices.

Once the maintenance has been completed, the vessel is tilted to the scrap charging position. Again, the nitrogen purge is maintained to avoid blocking the tuyeres. Because of the improved mixing capabilities of the Q-BOP, it is able to melt larger pieces of scrap, including ingots, than the BOF. However, the potential to damage the tuyeres requires more prudent scrap charging practices.

After the scrap is charged, the flow rate of nitrogen is increased through the tuyeres and the hot metal is charged into the vessel. The vessel is then righted and the process gases are introduced. A uniform transition, with respect to the tuyere pressure, is required to avoid "sucking" hot metal into the tuyeres; the transition form the nitrogen purge to the process gases signals the start of the main blow. The oxygen flow rate for a 200 tonne Japanese Q-BOP is approximately 70°C Nm³/min., corresponding to a specific consumption of 44 Nm³/tonne(111,121). However, oxygen consumption as reported by other Q-BOPs suggests that specific consumption varies from 47 to 60 Nm³/tonne. Consumption of the hydrocarbon is considerably less, a consumption value of 1.4 Nm³/tonne (24 Nm³/min.) of propane was reported by Emi(111), while 3.6 Nm³/tonne of natural gas was reported by Brotzman(113).

Within about one minute lime is added to the oxygen being blown into the furnace. The addition of lime continues for most of the main blow. Specific lime consumptions of 35-45 kg/tonne have been reported by Pearce^[10]. Lime is injected to enhance the rapid formation of the slag phase and improve the metallurgical performance of the process. The injection of lime, typically in powder form, was successfully integrated into the Q-BOP process as early as 1976, and is now considered an essential aspect of the process.

Once the main oxygen blow has terminated, the process gases, oxygen and hydrocarbon, are switched to nitrogen or argon to provide a purge for the tuyeres. At this time the furnace is tilted for steel and temperature sampling. The oxygen blow is re-established and continued

until the steel specifications are achieved. During the entire process the tuyeres are continuously in use, either with a nitrogen purge or with the actual process gases. For the production of low nitrogen steels, the purging gas can be switched to argon. However, for the majority of steels produced, the nitrogen pickup attributable to the purging action does not warrant the extra production cost of argon, approximately a ten to one cost increase per unit volume. In addition to the production of nitrogen steels, an argon purge or rinse with about 1.6 Nm³/tonne at the end of the main blow can be used to reduce the hydrogen content of the steel [8].

2.2.2.2 Combination-Blown Oxygen Steelmaking

The rapid increase in new Q-BOP/OBM steelmaking facilities was surpassed by the successful introduction of the combination-blown oxygen steelmaking processes. In fact numerous existing Q-BOP as well as BOF shops were retrofitted for combined blowing processes. This, no doubt, was the result of several years of experience with the Q-BOP that concluded that the process had several serious downfalls such as lower scrap melting capacity, higher refractory costs and lower furnace availability than did its major competition, the BOF. These downfalls led to the conclusion that a process able to blend the advantages of both the Q-BOP and the BOF would provide for a superior steelmaking process. The logical solution was a combination of top and bottom blowing. Combined blowing practices are truly hybrids of the OBM and BOF processes. As a result, there are several types, as can be seen in Fig. 2.15.

The first combined blowing practice to be commercially accepted was the LBE, Lance Bubbling Equilibrium, developed by ARBE-IRSID^[12]. This process is much more closely related to the BOF process in that all the oxygen is supplied from a top lance. The combined blowing aspect is achieved by a set of porous elements installed in the bottom of the vessel through which argon or nitrogen is blown. A typical LBE vessel is shown in Fig. 2.16.

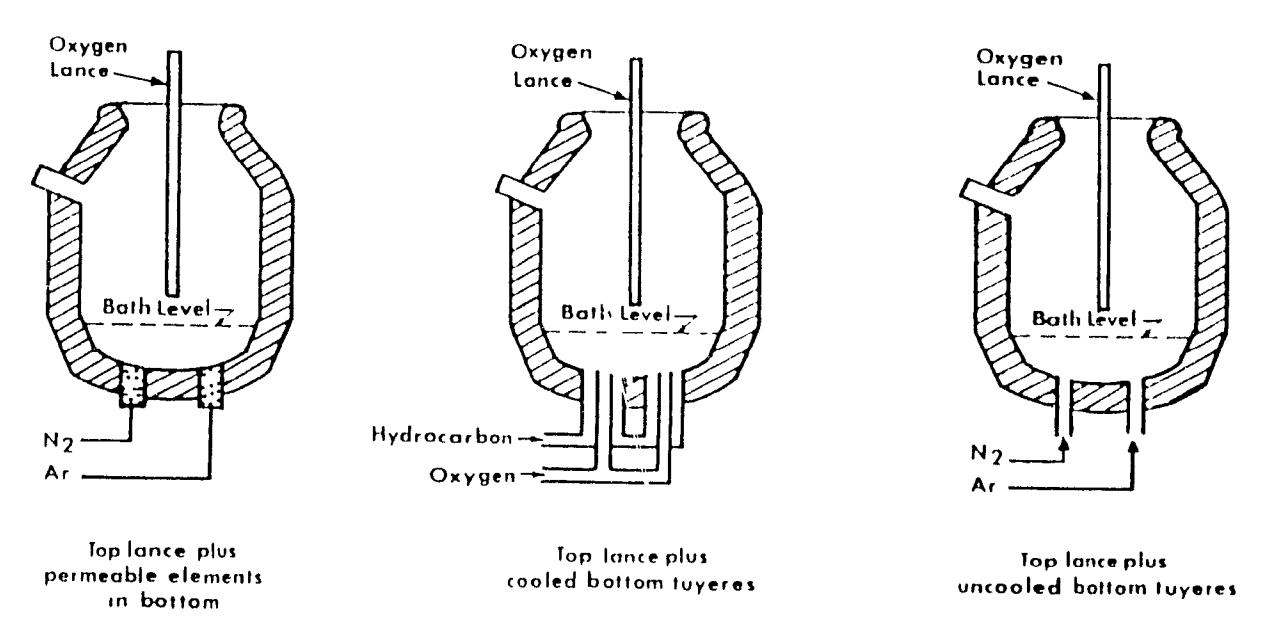


Fig. 2.15 Types of combined blowing-oxygen steelmaking processes[5].

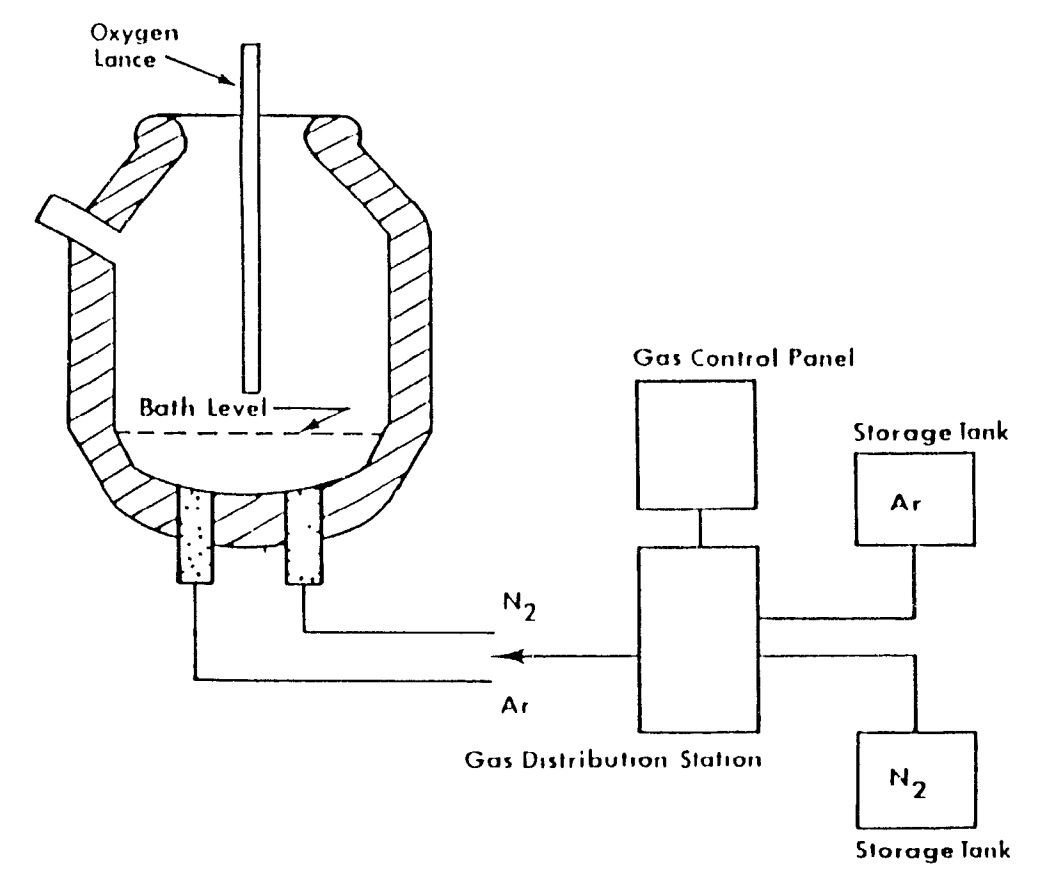
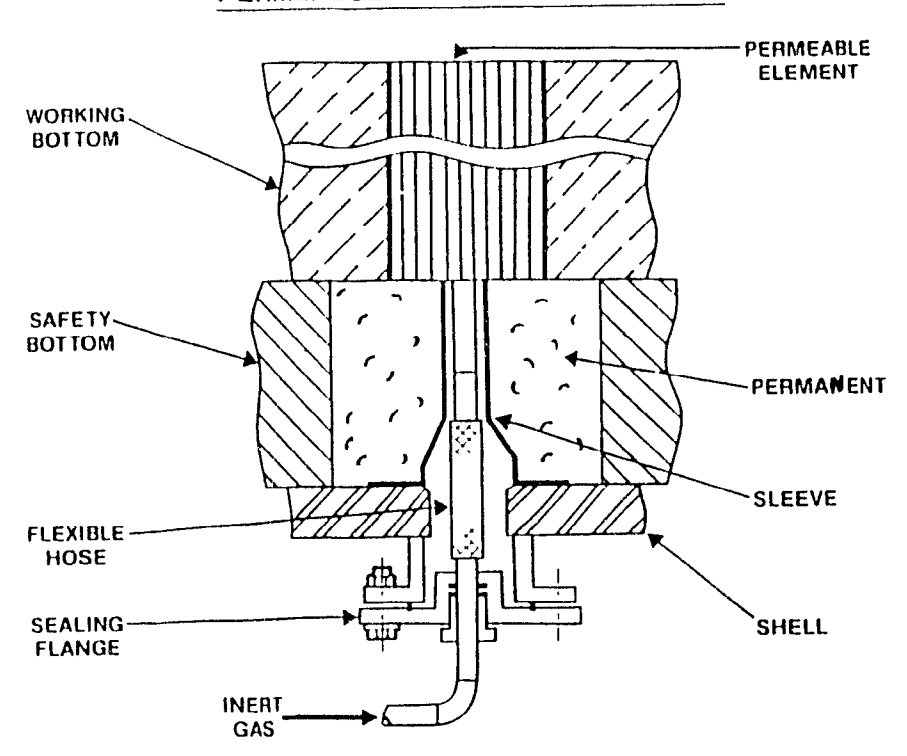


Fig. 2.16 Schematic of the LBE steelmaking process $^{[5]}$.

In brief, the theory of LBE is that by bubbling with inert gas a more intimate mixing of the bath and slag occurs throughout the blow. The inert gases used in the LBE are either nitrogen or argon, depending on process cycle. Typically, the nitrogen is used almost exclusively for the majority of the blow in the range of 3-11 Nm³/min. However, later in the blow when nitrogen absorption can create a problem, argon is selected as the stirring gas. In addition, argon is used almost exclusively as the inert gas for post-blow stirring; at this time the rate is increased to 10-17 Nm³/min.

PERMEABLE ELEMENT CONNECTION



F g. 2.17 Profile of a porous element for the LBE process[16].

The porous element, shown schematically in Fig. 2.17, typically consists of four bricks with machined longitudinal grooves on the broad faces. The refractory bricks are encased by a steel can and have steel plates between each brick. The refractory brick is not porous and, hence, the gas only flows through the machined faces. This element design has been quite successful for shorter campaign lives. However, as the refractory linings of the steelmaking vessel improved and vessel life increased significantly, an improved element design was required. Efforts in this area have concentrated on the application of copper channels in the grooved section.

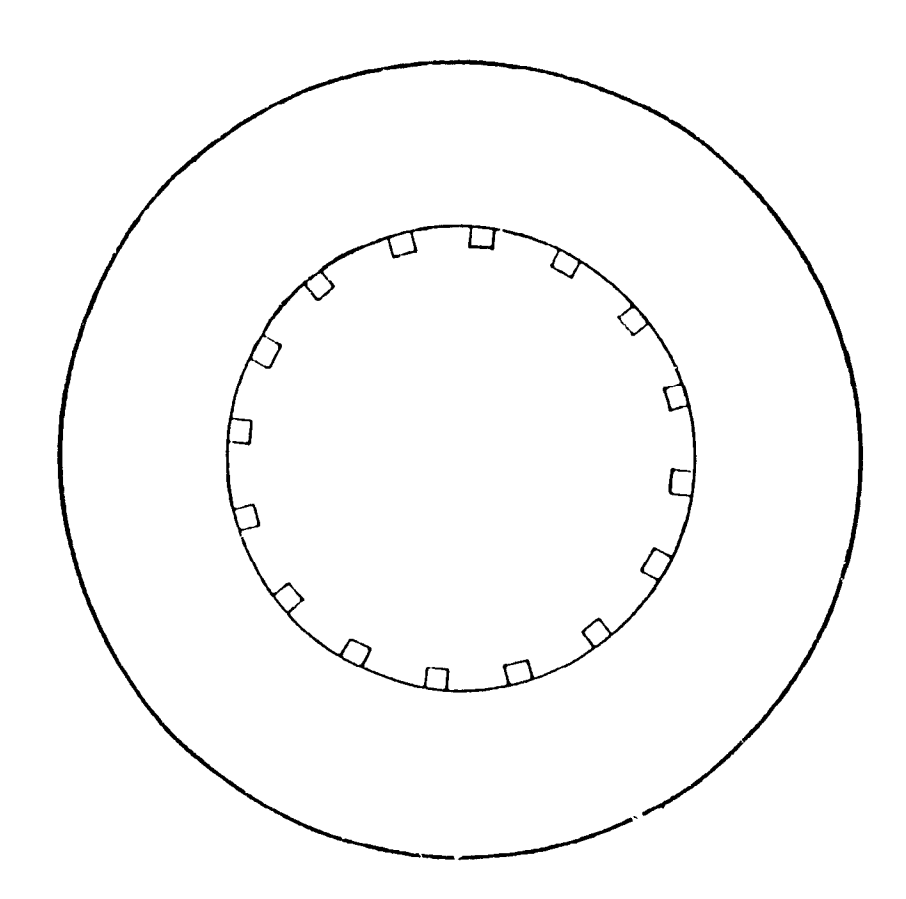


Fig. 2.18 Initial LBE porous element configuration at USS Gary Works^[14].

The geometric configurations of the LBE elements have developed from a simple circular configuration, consisting of typically 12 to 16 individual elements to more complex arrangements. The initial LBE element configuration at USS Gary Works is shown in Fig. 2.18. In subsequent campaigns, several elements were moved several brick courses closer to the center of the furnace to improve mixing and reduce bottom build-up⁽¹⁴⁾. This improvement in the element configuration was also adopted by Broken Hill Proprietary's Newcastle Works, as shown in Fig. 2.19. Other LBE operators have modified the configuration for other operational reasons, such as to avoid impact zones of the materials charged into the vessel.

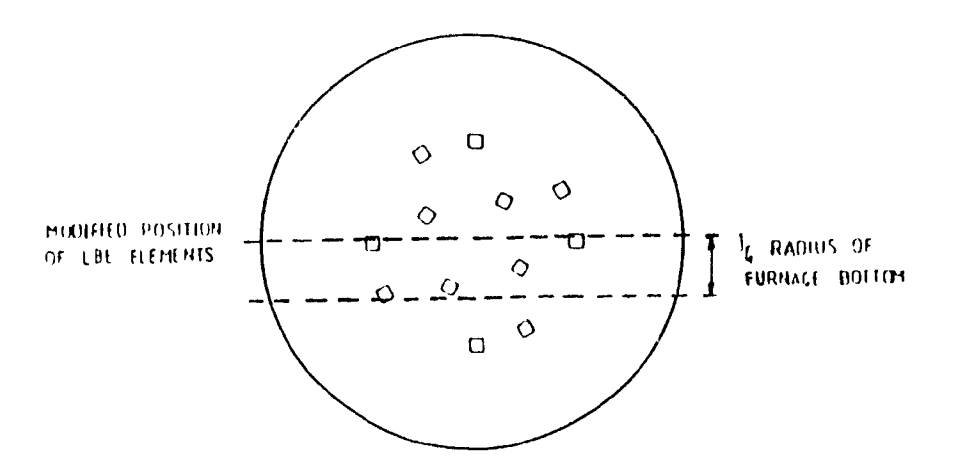


Fig. 2.19 Modified element configuration employed at Broken Hill Proprietary's Newcastle Works [15].

Operation of the LBE process is similar to that of the OBM in that special care must be taken to ensure the availability of the units installed in the bottom of the vessel. However, unlike the OBM process, the LBE process is concerned primarily with the build-up of

the bottom as opposed to erosion. Typically the state of the bottom is often controlled by coating the bottom with a slag to reduce the potential of erosion and, most often, a washing slag to reduce build-up of the bottom. Normally these processes can, to a large extent, be minimized by maintaining a constant basicity of the slag. A V-ratio, $[CaO]/[SiO_2]$, of 2.6-2.8 has been reported by Mullen et al^[16] to reduce build-up in conjunction with a reduced MgO slag content. The major danger to note about the washing is that it often affects the performance of the refractories in the knuckle area of the vessel; several LBE operators have experienced breakouts as a direct result of reducing bottom build-up[15,16]. In fact, bottom build-up and the subsequent loss of the porous element is the major problem associated with this process. Webster et al (15) showed that the efficiency of the LBE elements decrease rapidly as the bottom build-up covering the elements exceeded 50mm, Fig. 2.20.

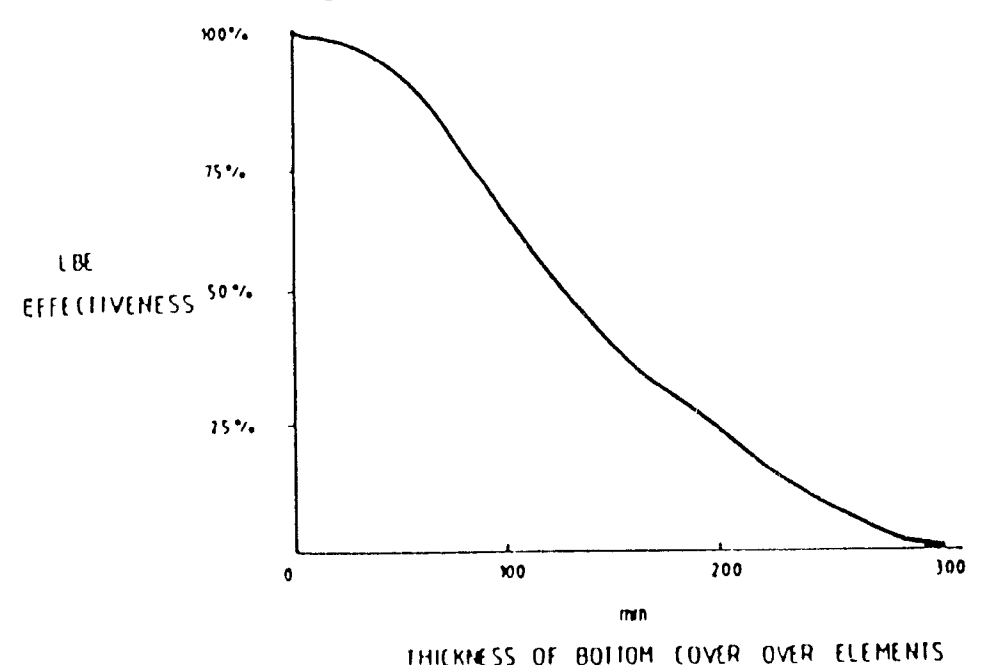


Fig. 2.20 Dependence of LBE efficiency on thickness of bottom build-up $^{\{15\}}$.

The difficulties in maintaining the LBE elements operational has led such steel producers as Newcastle Works of BHP to pursue the application of non-cooled tuyeres^[15]. In a similar manner, the oxygen is delivered via a top lance while the inert gas is introduced to the bath from the furnace bottom. The BHP tubular element design, shown in Fig. 2.21, consists of 6 small pipes set in a refractory matrix. Because of larger overall cross-sectional area available, higher gas flow rates are required to maintain the tuyeres operational. Therefore, the entire bottom blowing requirements of approximately 20 Nm³/min, for a 215 ton vessel, can be achieved by two elements. The location of the tubular elements in BHP's 215 ton vessel at Newcastle Works is shown in Fig. 2.22.

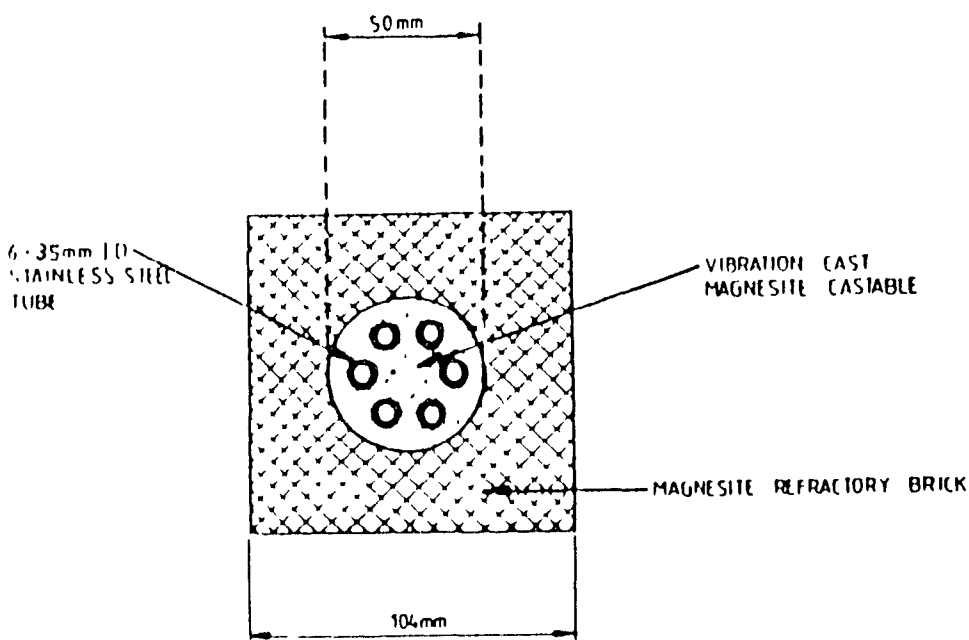


Fig. 2.21 Structure of the tubular element designed at BHP Newcastle Works $^{[15]}$.

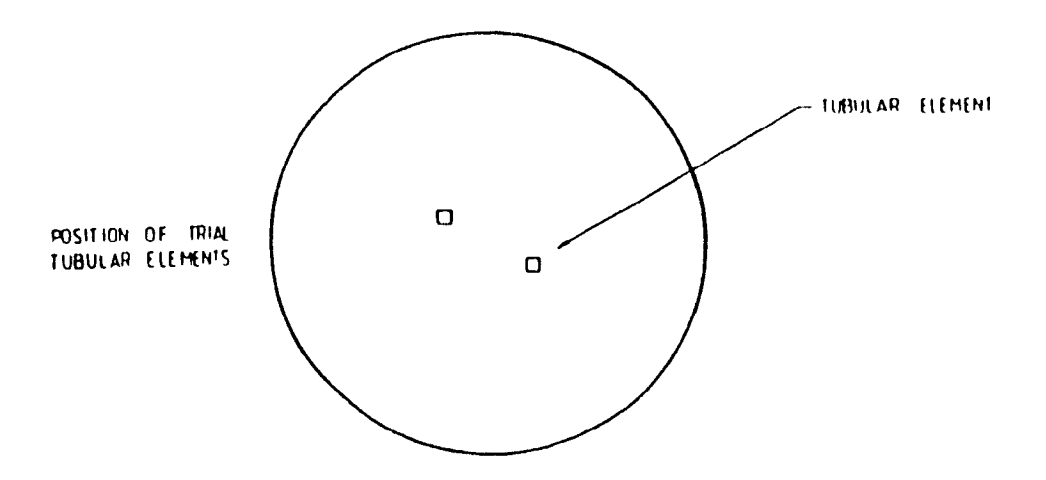


Fig. 2.22 Location of the tubular elements in the furnace bottom [15].

The benefits of this technique are similar to that of the LBE process. However, because of the excessive cooling, at the higher flow rates, improved metallurgical results at turndown are observed only in steels with carbon content greater than 0.06% when low flow rates are used^[5].

Top and Bottom Oxygen Blowing

Another system of combination blowing uses top and bottom oxygen blowing; a true offspring of the Q-BOP and the BOF processes. The most successful process was developed by Kawasaki Steel of Japan^[11] and is referred to as the K-BOP. In the K-BOP vessel, at least 20% of the total oxygen must be blown through the bottom tuyeres to obtain any metallurgical benefits associated with bottom blowing. In general, the higher the fraction of oxygen blown through the bottom tuyeres, the greater the metallurgical benefits. The fraction of bottom blown oxygen is limited because of metal ejection and reduced control of the

slag formation process. An example of a K-BOP vessel is shown in Fig.

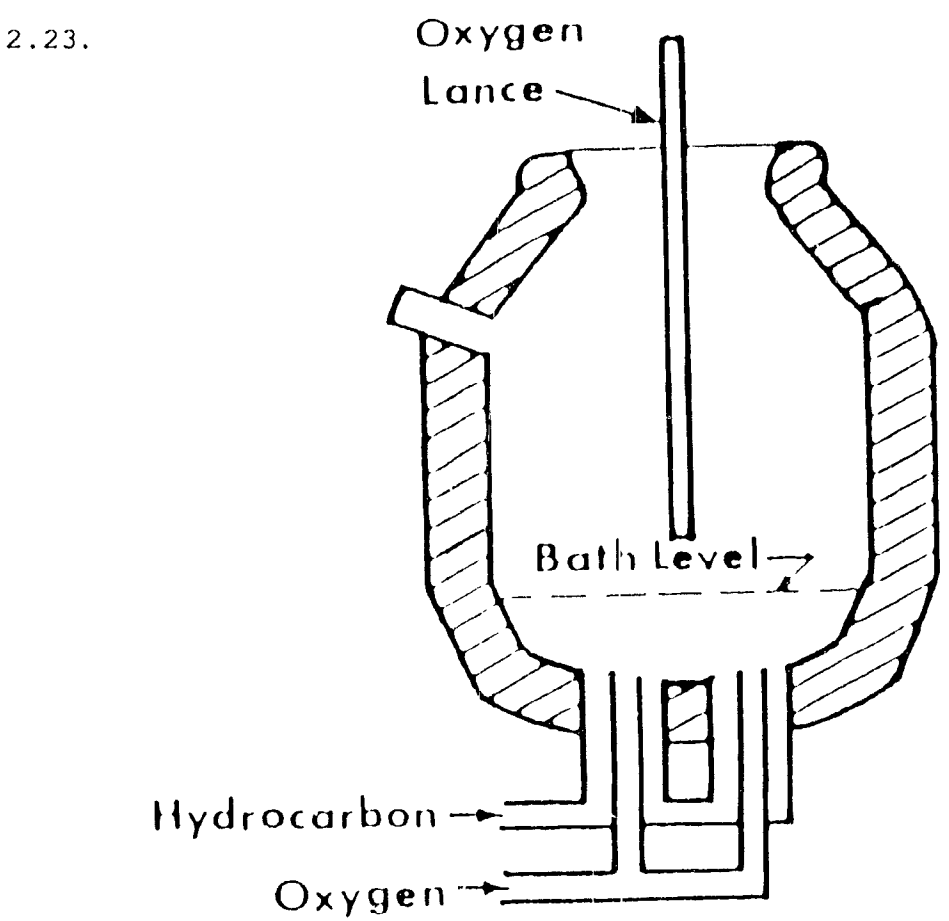


Fig. 2.23 Schematic of a K-BOP oxygen steelmaking vessel^[5].

Another example of a combined oxygen process is the KMS developed by Klockner Werke. Trials to develop this process started as early as 1978⁽¹⁾ and were focused primarily on the post-combustion of the converter gases by a top lance or a side tuyere in the upper part of the vessel, as can be seen in Fig. 2.24. The major difference is the potential to inject coal into the bottom of the bath. The coal can provide the thermal energy required to increase the scrap melting capacity beyond what is possible with the BOF process. In this case approximately 60% of the total oxygen blown is introduced via the

bottom tuyeres and an additional $5Nm^3/tonne$ of oxygen is consumed.

As can be seen by reviewing these processes, the more advanced steelmaking processes tend to be more complex in an attempt to provide the steelmaker with greater metallurgical benefits and flexibility.

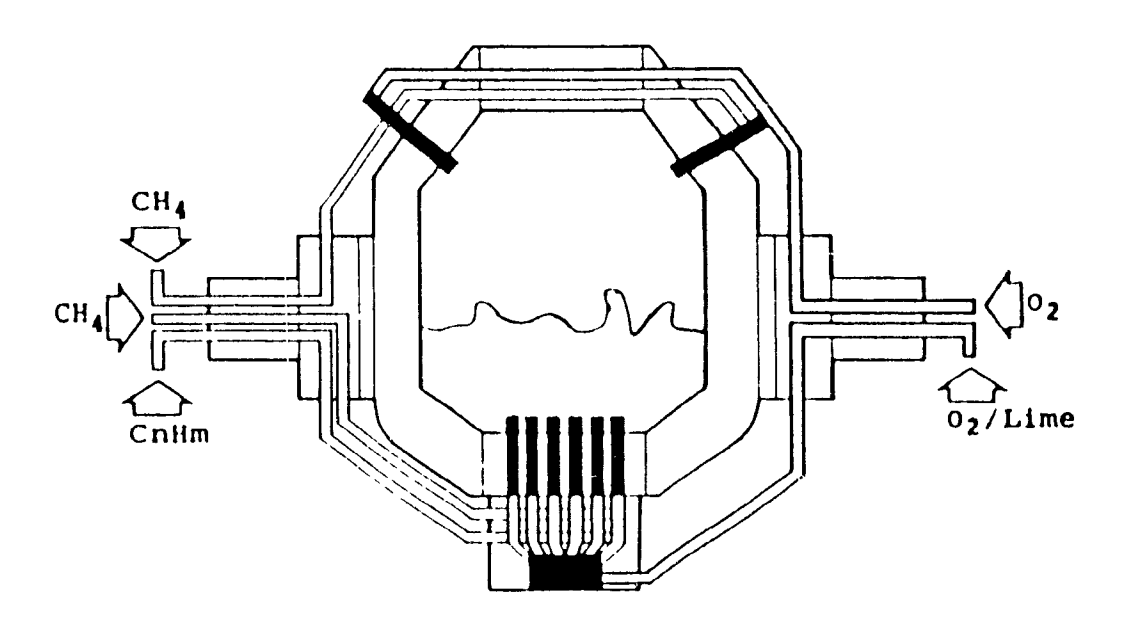


Fig. 2.24 Overview of the KMS steelmaking process $^{(17)}$.

2.3 Physical Chemistry of Oxygen Steelmaking

The physical chemistry of oxygen steelmaking can be considered as the foundation of our knowledge of the metallurgical behaviour of the pneumatic steelmaking processes. The reactions and their equilibria that are discussed in this section are common to all steelmaking processes, regardless of the type of vessel in which they are carried out. In fact the performance of various steelmaking processes are often measured in terms of deviation from equilibria, thereby providing an objective way to compare processes, as well as modifications. Although this discussion is limited to equilibrium conditions; it must be noted that these conditions rarely exist. Therefore, reaction rates, kinetics and mechanisms, will be discussed in a subsequent section.

As was mentioned earlier, the reactions occurring in a steelmaking process are essentially oxidation reactions. The carbon saturated hot metal produced by the blast furnace also contains a number of other impurities, namely Si,S,P,Mn, which together with carbon are removed by oxidation during the steelmaking operation. The steel produced is invariably over-oxidized and, therefore, final adjustments to the composition of the steel are made by adding suitable deoxidizers and alloying elements to satisfy the specifications of the steel requested by the customer.

In order to assess the feasibility of an oxidation reaction to occur, consideration must be first given to the free energy changes

accompanying the reaction at various temperatures and pressures. The reactions to be considered may be expressed in a general form as

where M and $M_{x}O_{y}$ are metal and metal oxide respectively. The equilibrium constant for the above reaction can be written as

$$K = \begin{pmatrix} a & 2^{2y} \\ \underline{M_{1}O_{y}} \\ (a_{M})^{2x/y} \cdot P_{O2} \end{pmatrix}$$
 (2.23)

where a represents the activities of the respective reactants and products. If M and M_xO_y are at unit activities, ie. pure metal and metal oxide, it follows from Eq(2.23) that the equilibrium constant for the reaction (2.22) is inversely proportional to the equilibrium partial pressure of oxygen in the system.

$$K = \frac{1}{P_{02}} \tag{2.24}$$

where P_{02} is in atmospheres and the standard state of oxygen is one atmosphere at the temperature under consideration. The standard free energy change, or the oxygen potential of the metal-metal oxide system is given by

$$\Delta G^{\circ} = -R T \ln (K) = R T \ln P_{O_2}$$
 (2.25)

where R represents the ideal gas constant and T represents the temperature under consideration. In terms of entropy and enthalpy changes the above equation can be expressed as

$$\Delta H^{\circ} - T \Delta S^{\circ} = R T \ln (P_{O})$$
 (2.26)

where ΔH^o and ΔS^o represent the changes in standard enthalpy and entropy respectively. The relationships described above are the basis

of the free energy diagrams or, more commonly, the Ellingham diagrams. In these diagrams the free energy of formation of oxides per mole of oxygen are plotted against temperature, as can be seen in Fig. 2.25. The advantages of constructing such diagrams is that one can predict the relative stability of the oxides, ie. what oxides can be reduced by which elements from relative positions of the oxygen potential lines. However, these diagrams are for their pure elements and their oxides, as already indicated. Due account must be taken of the activities of the reactants and products when they are dissolved in either liquid iron or slag. Nonetheless, it is possible to generalize some aspects of refining during steelmaking with such a diagram.

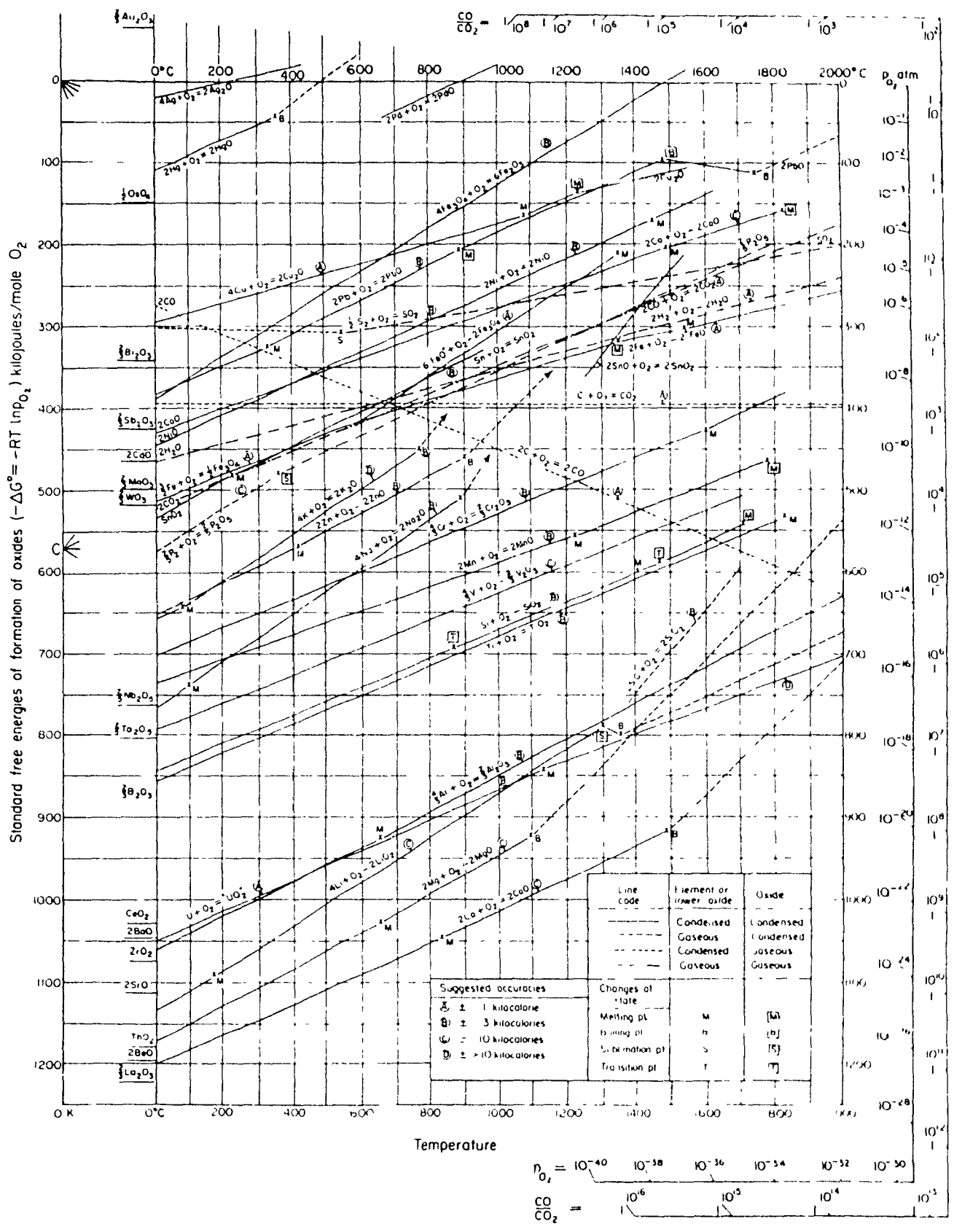


Fig. 2.25 Free energies of formation of oxides for the standard states; pure elements, pure oxides and oxygen at 1 atm of pressure 179,801 .

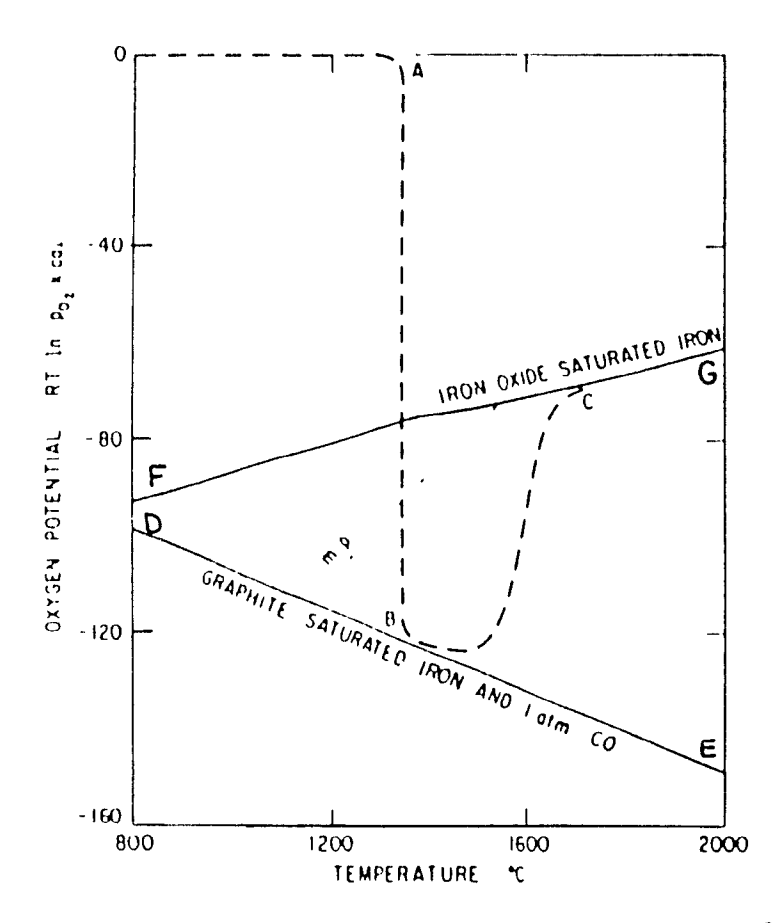


Fig. 2.26 Change in the oxygen potential of the metal during BOF steelmaking^[4].

The change in the oxygen potential of the liquid metal during oxygen steelmaking is shown in Fig. 2.26. The lower line, shown as D-E, is the oxygen potential of graphite saturated iron at $P_{co}=1$ and the upper line, F-G, is for iron saturated with iron oxide. The hot metal arriving from the blast furnace is at about $1350\,^{\circ}$ C and is saturated with graphite and therefore, its oxygen potential at $P_{co}=1$ atm is B, Fig. 2.26. The pressure of the carbon monoxide gas in the furnace is slightly greater than 1 atm, but for the purpose of this demonstration 1 atm will be assumed. At the beginning of the blow, the chemical potential of a unit of oxygen entering the bath is reduced from its standard state A to a value approaching that at point B as a result of

the reaction

$$2\underline{C} + O_{2(q)} \leftrightarrow 2 CO_{(q)} \tag{2.27}$$

Accompanying the oxidation of carbon is the oxidation of silicon and manganese. Since the oxidation of these impurities is exothermic, the temperature of the melt increases during the blow. The equilibrium organ partial pressure of the system increases with decreasing carbon content of the melt, as can be deduced from the equilibrium constant for the reaction (2.27)

$$K = \frac{(P_{co})^2}{a_c^2 \cdot P_{os}}$$
 (2.28)

Therefore, during blowing, the oxygen potential of the melt increases along the curve B-C in Fig. 2.26. When the carbon content of the liquid metal is below ≈0.02%C, the iron becomes saturated with iron oxide, therefore, further oxygen blowing results in excessive oxidation of iron. Referring to Fig. 2.25, the free energy lines for the oxides of Co, Ni, and Cu lie above that for iron - iron oxide, indicating that any of these elements present in the hot metal will not be oxidized and will remain in the iron phase.

Basic Steelmaking Slags

The importance of the slag phase during steelmaking cannot be over emphasized. In fact, many steelmakers claim that "if you take care of the slag, the steel will take care of itself". Its importance is readily understood when one considers that the majority of the impurities removed from the hot metal are oxidized and dissolved into the slag phase during the process.

The main ingredient in basic steelmaking slags is lime; a typical slag contains 40 to 50% CaO and 3 to 8% MgO and MnO. While other components depend largely on the composition of the hot metal, the major distinction being whether it is high or low phosphorous. In low phosphorous practice the silica content is in the range of 15 to 20%, whereas in the high phosphorous practice the silica content of the slag is in the range of 8 to 16% and 8 to 15 % P_2O_5 or higher. Other minor components can be Al_2O_3 , TiO_2 and Cr_2O_3 , and typically represent about 2% of the slag. Steelmaking slags are often described in terms of two important characteristics: the basicity and the state of oxidation of the slag.

Oxides present in slags are described as either network formers, those which form anion complexes in molten slags (acidic), or network modifiers (basic), those which break down anion complexes. The basicity of the slag is the ratio of the concentrations of the basic oxides to those of the acidic oxides. Network formers include such oxides as SiO_7 , P_2O_5 , and Al_2O_3 while CaO, MgO, and MnO are considered basic. In simple slags where lime and silica are the major constituent oxides, basicity is usually defined by the concentration ratio $CaO/RSiO_7$, also known as the V-ratio. However, as the number of constituent oxides increases, the basicity is defined on a molecular basis; converting it to concentrations in weight percent, the ratio can be expressed as:

slag basicity =
$$\frac{%CaO + 1.4 %MqO}{%SiO_2 + 0.84 %P_2O_5}$$
 (2.29)

A large percentage of steel is made using basic slags which are best

suited to yield steel low in silicon, phosphorous and sulphur. In addition, most basic steelmaking slags are nearly saturated with lime and magnesia which significantly reduces refractory consumption. In the BOF practice, the slag composition is controlled primarily by adjusting the lime addition at the start of the blow in accordance with hot metal composition and the required steel specifications.

State of Oxidation

Another important constituent of steelmaking slags is iron oxide. When the oxygen activity of the slag is close to that of the metal, the following reaction may be considered

$$[FeO] \leftrightarrow Fe + [O] \tag{2.30}$$

When the total iron oxide content of the slag is high, the oxygen content of the steel is invariably high. At equilibrium the activity of oxygen in the steel can be determined by:

$$\log \frac{[\$0]}{a_{\text{reo}}} = -\frac{6320}{T} + 2.734 \tag{2.31}$$

A comparison between calculated and measured oxygen content of steel is shown in Fig. 2.27. As can be seen, the slag is not in equilibrium with the metal and, therefore, due consideration should be given to the oxidization of divalent iron to the trivalent state in the slag by the furnace atmosphere. This is represented by:

2
$$FeO_{(slag)} + 1/2 O_{2(s)} \leftrightarrow Fe_2O_3$$
 (2.32)

The equilibrium constant and the effect of temperature of the above reaction (Eq. 2.32) is given by:

$$K = \frac{a_{\text{re203}}}{a_{\text{Fe0}}^2 \cdot (P_{\text{O2}})^{1/2}}$$
 (2.33)

T.

It should be noted that in complex steelmaking slags in equilibrium with liquid iron, the ratio Fe^{3+}/Fe^{2+} is below 0.3, while in steelmaking practice the ratio Fe^{3+}/Fe^{2+} is in the range 0.3 to 0.5. That is, the state of oxidation of iron in steelmaking slags is much higher than that anticipated for slag-metal equilibrium.

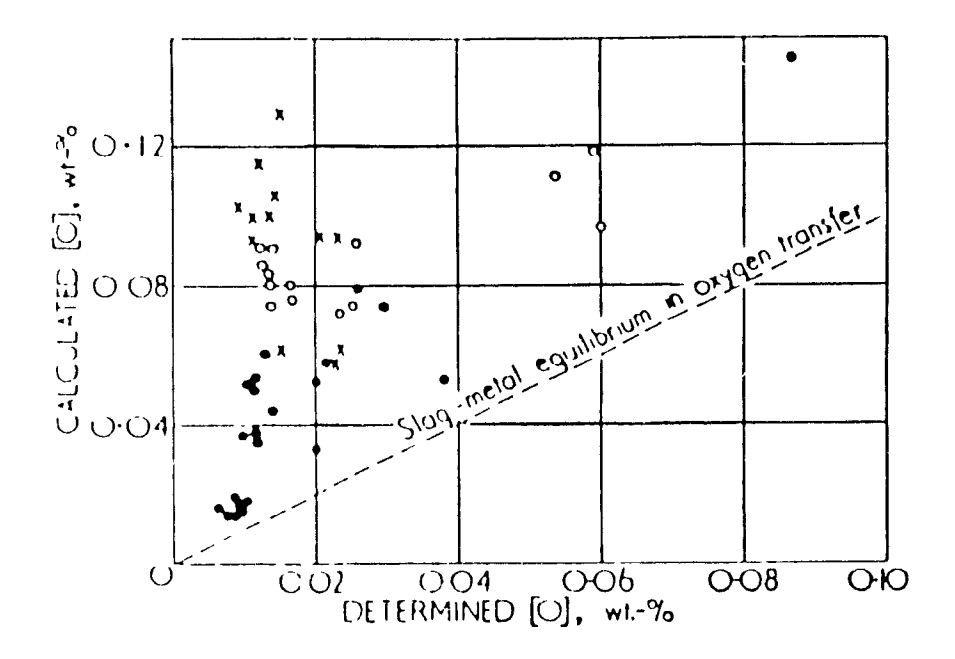


Fig. 2.27 Comparison between calculated and determined oxygen content, different symbols are used for data from different sources^[18].

Carbon-Oxygen Reaction

The carbon-oxygen reaction is the most significant reaction during steelmaking, on a weight basis. This reaction can be represented as:

$$\underline{C} + \underline{O} \leftrightarrow CO_{(a)}$$
 (2.35)

An expression for the temperature dependence of the equilibrium constant, shown below, was developed by Fuwa and Chipman^[19].

$$K = \underline{P_{co}}_{h_c \cdot h_o}$$
 (2.36)

Where the Henrian activities, h_c and h_o in the equation can be approximated by [%C] and [%O], respectively. As was previously stated, the Henrian activity of carbon in iron increases with increasing carbon content. The partial pressure of carbon monoxide is approximately 1 atm for carbon contents below 0.5% and at steelmaking temperatures. As can be seen in Fig. 2.28, where the carbon-oxygen relationship in BOF steelmaking is compared with equilibrium curve for 1 atm CO at $1600\,^{\circ}$ C, most of the data points lie above the C-O equilibrium curve, except at carbon contents below 0.05%C in the BOF furnace. Since the BOF is a dynamic process, it is not surprising to find that the concentrations of the reactants in the bulk metal phase are not in equilibrium with the prevailing CO pressure in the gas bubbles.

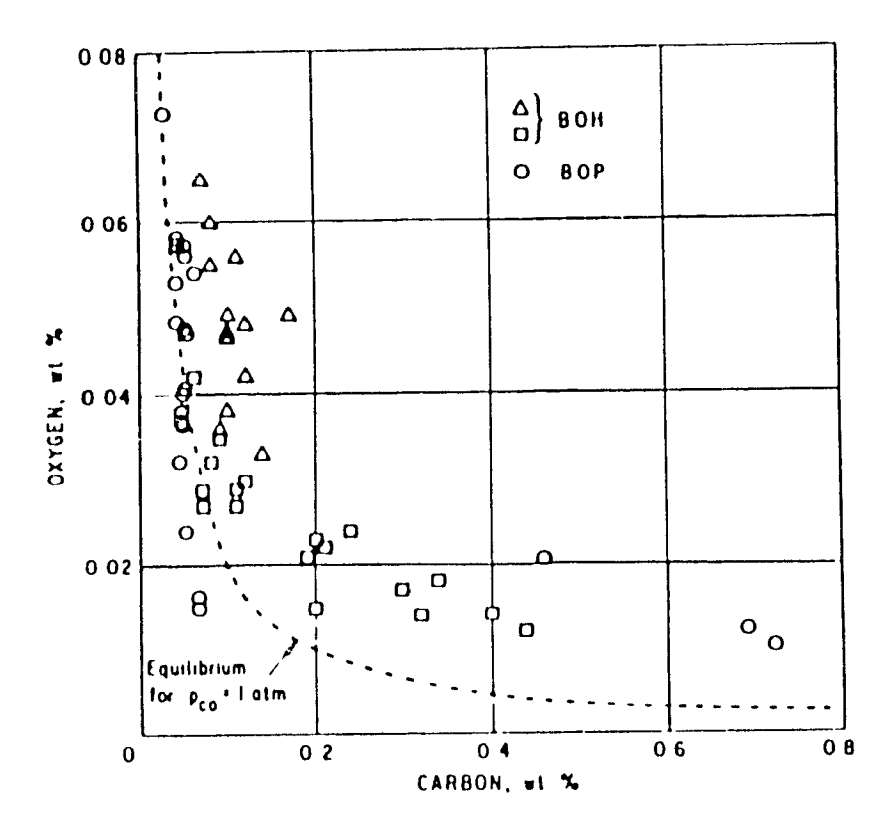


Fig. 2.28 Carbon-oxygen relationship in the BOH and BOF steelmaking processes compared with the equilibrium curve for 1 atm carbon monoxide gas at $1600\,^{\circ}\text{C}^{(4)}$.

Silicon-Oxygen Reaction

The silicon content of the hot metal varies depending on type of steelmaking and ironmaking practices used; typical ranges are 0.5% to 1.5%. The refining reaction, oxidizing dissolved silicon to SiO₂, is exothermic and provides some of the heat necessary to raise the temperature of the bath during oxygen blowing. At silicon contents below about 2% Si, the heat of generation upon oxidation of silicon is 564 kJ/gmol of Si at 1600°C. The silicon and the iron oxide (generated or charged) flux the lime added with the charge and form the slag. Because of the strong affinity for oxygen, the silicon is readily oxidized in the early stages of the blow, as can be seen by the equilibrium constant for this reaction^[20].

$$\underline{\text{Si}} + 2\underline{\text{O}} \leftrightarrow \underline{\text{SiO}}_{2 \text{ (s)}}$$
 (2.38)

0.04[\$Si] - 0.65[\$O] + log[\$Si] + 2 log[\$O] = -4.55 (@ 1600°C) (2.39) where the standard states of <u>Si</u> and <u>O</u> are assumed to be both 1 wt%. For an average oxygen content of 0.04% in the metal the equilibrium silicon in the steel is about 0.002% which is within the range achieved in the BOF process.

Manganese-Oxygen Reaction

The oxidation of manganese can be represented by either

$$\underline{Mn} + \underline{O} \longleftrightarrow MnO \text{ or}$$
 (2.40)

$$\underline{Mn}$$
 + FeO \leftrightarrow Fe + MnO (2.41)

The temperature dependence of the equilibrium constant for reaction (2.41) is given by

$$k = \underline{a_{Mn} \circ a_{Fe0}}$$
 (2.42)

$$log (k) = 8695 - 3.93$$
 (2.43)

where a_{re} = 1 and a_{Mn} = [%Mn] in the iron, a_{reo} is relative to pure liquid iron oxide and MnO is relative to pure solid MnO. The equation (2.42) can be simplified, as shown below, since the molecular weights of MnO and FeO are similar.

$$K = K (\gamma FeO/\gamma MnO) = (%MnO)$$
 (2.44)
 [%Mn] • (%FeO)

It must be noted that the activity coefficients γ_{FeO} and γ_{MnO} increase with increasing ratio of CaO/SiO₂. Therefore, with slags containing CaO and other oxides, the equilibrium ratio K for the reaction may

change with the composition of complex slags. In basic slags nearly saturated with time and magnesia, the value of γ_{MNO} is not much affected by minor changes in the slag composition. If low manganese steel is to be made, eg. Mn < 0.05%, it is necessary to continue blowing to carbon contents down to at least 0.02 %C such that the oxygen activity in the metal can be increased to 800 or 1000 ppm to ensure low residual manganese in the steel and to dilute the %MnO in the slag, primarily by the addition of lime or by employing a two-slag practice.

Phosphorous-Oxygen Reaction

Dephosphorization studies were performed primarily by European investigators because of the high phosphorous hot metal produced by their iron ores. Removal of the phosphorous from iron can only be achieved by oxidation during steelmaking under a basic slag. The oxidation reaction may be represented by a number of reactions, but for simplicity it is represented here by:

$$2\underline{P} + 5\underline{O} \leftrightarrow P_2O_5 (sign)$$
 (2.45)

The equilibrium constant for this reaction is given by:

$$k = \frac{aP2O5}{h_{P}^{2} \cdot h_{O}^{5}}$$
 (2.46)

where the henrian activities of P and O can be represented by their specific weight percentages. The activity of P_2O_5 in the slag is reduced the greatest by lime, hence, bringing about dephosphorization of the metal at reasonable oxygen activities. On the other hand, silicallenders lime less effective as a dephosphorization agent because of the strong interaction between calcium and silicate ions in the slag.

In the BOF, dephosphorization is realized in the early stages of refining when the carbon content of the bath is relatively high. This is facilitated by the formation of a highly oxidizing basic slag in the early stages of the oxygen blow. However, because of the adverse affect of silica on the activity of P_2O_5 in the slag, the silicon content in the charge should be maintained low and/or a two slag practice should be considered. Although low temperature favours dephosphorization, the temperature of the slag must be sufficient to dissolve newly added lime and improve slag fluidity.

Sulphur Reactions

The behaviour of sulphur during oxygen steelmaking is complicated because of the numerous reaction paths that can be taken, however, the most frequently discussed reaction is

$$\underline{S}_{(metal)} + O^{2-}_{(slag)} \leftrightarrow \underline{O}_{(metal)} + S^{2-}_{(slag)}$$
 (2.47)

One of the most critical factors governing desulphurization is the state of oxidation of the bath. The sulphur distribution ratio, (S)/[S], is inversely proportional to the iron oxide content of the slag, or the oxygen content of the metal when approaching equilibrium conditions. The prevailing oxidizing conditions in the BOF do not promote significant removal of sulphur from the metal, thereby explaining the existence of external hot metal desulphurization units which employ reduction techniques such as lime injection.

2.4 Steelmaking Reaction Rates

The success of oxygen steelmaking process is no doubt largely attributed to its refining rate. Compared to the open hearth process, the BOF can refine the hot metal and scrap in a fraction of the time. However, most of the problems which arise in attempts to control the process are associated with the high rate of chemical reactions. Therefore, a thorough understanding of the reaction rates is a prerequisite to control of the BOF process.

The actual refining time in a basic oxygen steelmaking furnace is extremely short in comparison to the entire cycle of a heat. During this refining period, the general pattern of the reactions in the vessel is given in Fig. 2.29. The characteristic feature is that silicon is oxidized preferentially before carbon. The reason for this is essentially thermodynamic, hence, any oxidized iron or carbon will be reduced by dissolved silicon until the silicon content of the metal is very low. Oxygen entering the vessel is partitioned approximately according to Fig. 2.30. In this case the decarburization-rate curve would appear as in Fig. 2.31.

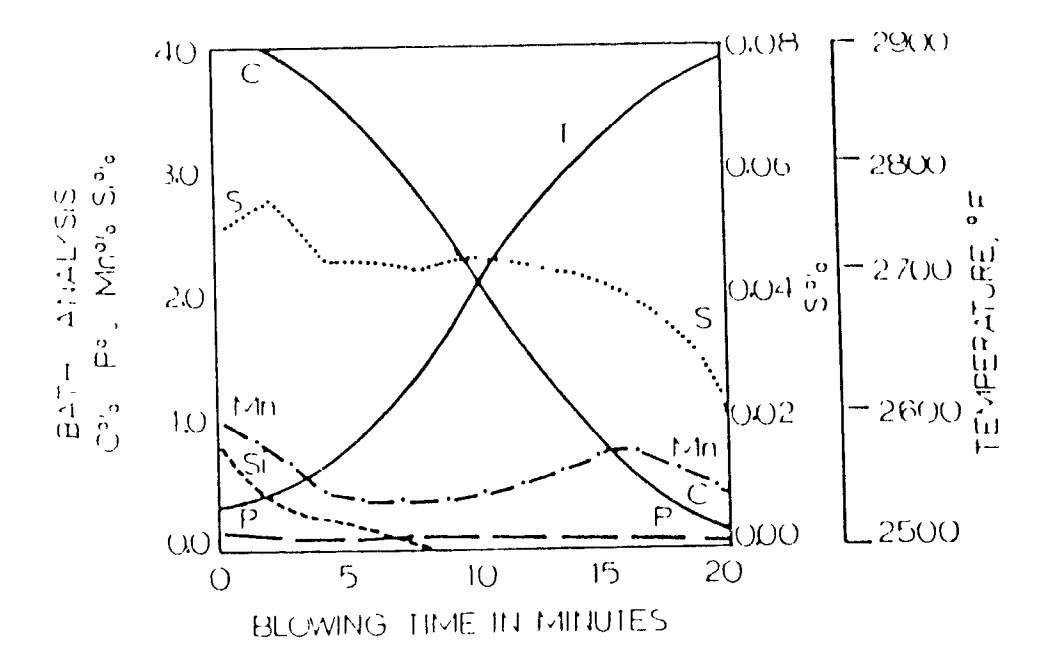


Fig. 2.29 Removal of the major constituents from the metal bath during the BOF process $^{(4)}$.

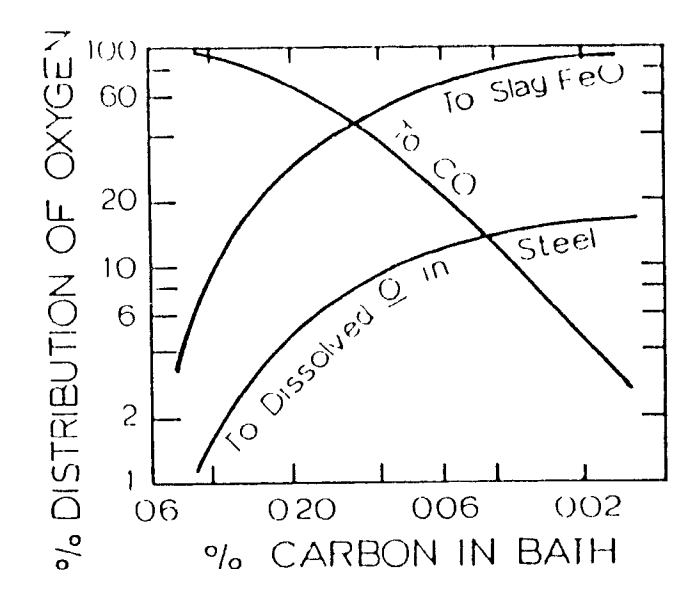


Fig. 2.30 Distribution of oxygen between steel, slag, and decarburization near the end of the blow $^{[4]}$.

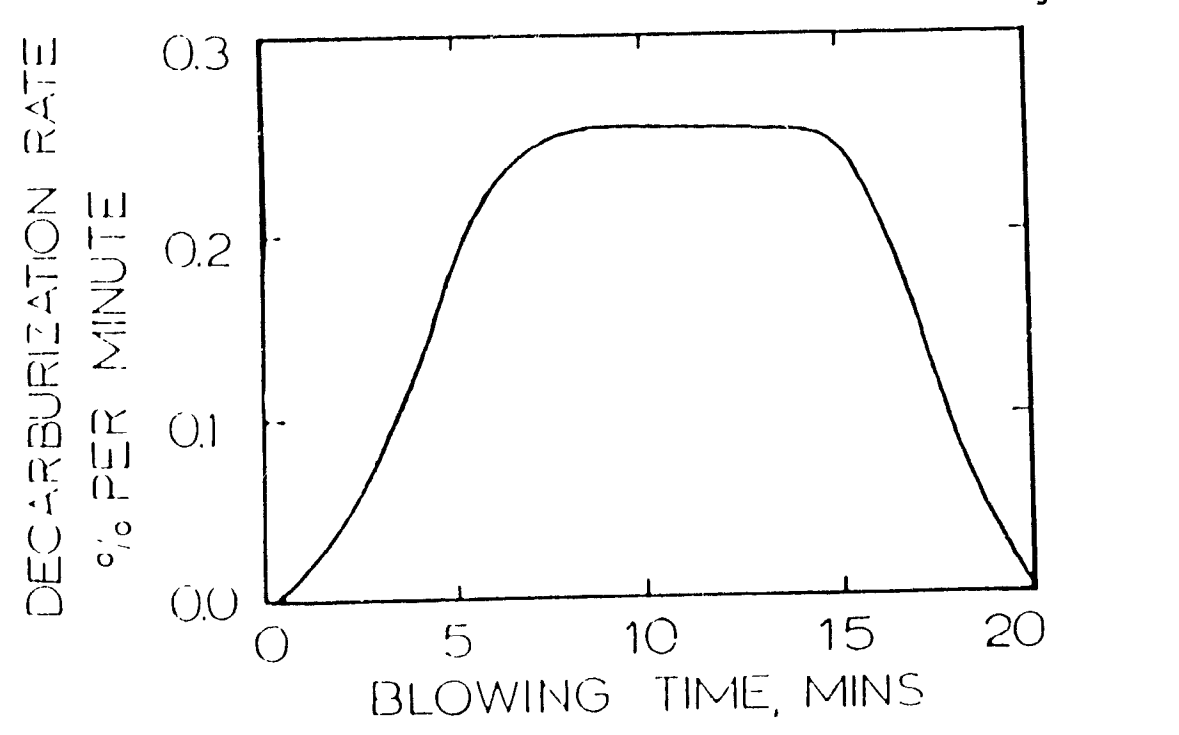


Fig. 2.31 Typical decarburization rate curve for a BOF heat [4].

The partition of oxygen is a complex function of metal and slag compositions and interfacial areas. In the early developments of the BOF process, it quickly became apparent that the slag would foam out of the vessel's mouth. Inspection of the foaming slag revealed entrapped gas bubbles and metal droplets and concluded that a significant portion of the refining reactions occur in the slag. Confirming this conclusion were several experimental studies that indicated as much as 30% of the metallic bath gets emulsified into the slag. As a result, very large surfaces of contact between metal and slag are allowed to exist. For this reason, slag formation and slag/metal emulsion will be discussed first and then the reactions taking place in the emulsion.

The formation of the emulsion is governed by the interfacial tension between the slag and metal and the energy required for the creation of new surfaces. In the situation where equilibrium exists between phases in contact, this parameter depends solely upon composition. However, with rapid mass transfer occurring across the interface, primarily oxygen, it may decrease the interfacial tension appreciably, thereby facilitating the formation of an emulsion. The energy required to form this new surface, regardless of when it is formed comes primarily from mechanical energy sources such as the impingement force of the oxygen jet and the stirring action of the carbon monoxide gas.

The contour of a liquid surface under the impingement force of a jet has been the subject of numerous investigations. Three types of contours, depending on the jet velocity and nozzle height, have been distinguished by $Molloy^{(21)}$ (Fig. 2.32):

- dimpling with a slight surface depression
- splashing with a shallow depression
- penetration with an apparent reduction of outwardly directed splash

Only the last two types of behaviour are encountered during normal steelmaking operations; these types of behaviour form metal droplets. However, as can be seen in Fig. 2.32, jet penetration has a further influence on the surface area offered to contact the gaseous oxygen and to the trajectory of the oxygen loaded droplets. This governs the type of decarburization sice and the overall oxygen partition between the various elements dissolved in the metal at any given time.

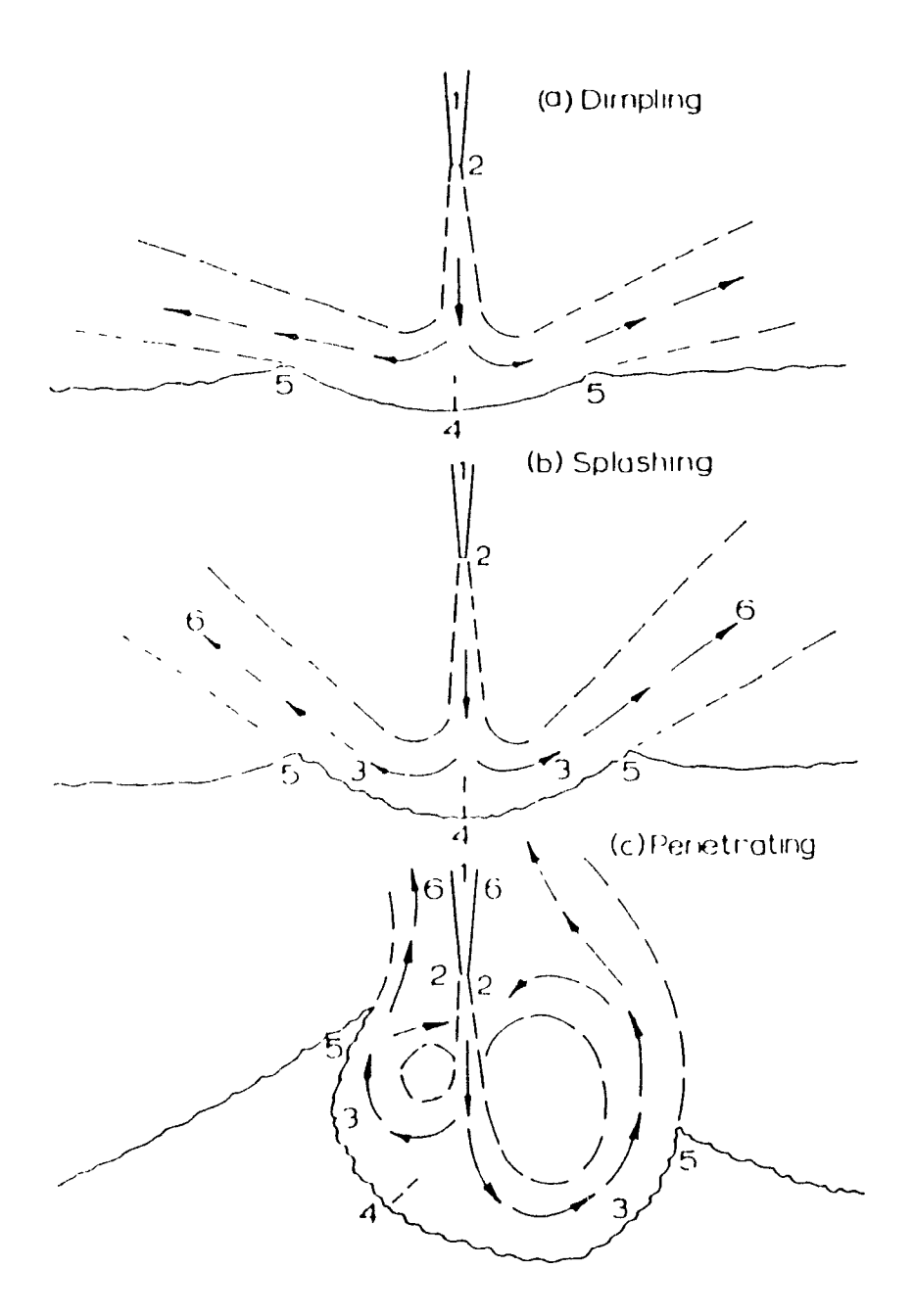


Fig. 2.32 Comparative geometry of the flow modes⁽²¹⁾. Legend: (1) nozzle body; (2) entrainment region of the original jet; (*3) entrainment region of the wall jet across the phase interface; (4) stagnation point of the wall jet; (6) two-phase exit flow.

The earliest direct measurements of the depth of the jet penetration under steelmaking conditions have been performed by Flinn et al [27]. From their work, an empirical relationship was derived from a series of studies made on vessels ranging from 0.05 to 100 tons, as shown below:

$$1_{p} = 1.5 \ \underline{P_{1} \cdot D}_{H} + 1.5$$
 (2.49)

where $l_r = depth of penetration (inches)$

P_d = nozzle pressure (psia)

D = nozzle diameter (inches)

H = nozzle height above quiescent bath (inches)

or

where $l_p = depth of penetration (m)$

P_d = nozzle pressure (atm)
D = nozzle diameter (m)
H = nozzle height above quiescent bath (m)

The empirical relationship has been applied by Rote [23] to the lance operating conditions of five different plants. As reported in the literature, the ratio of jet penetration to bath depth was found to vary between 0.4 to 0.8.

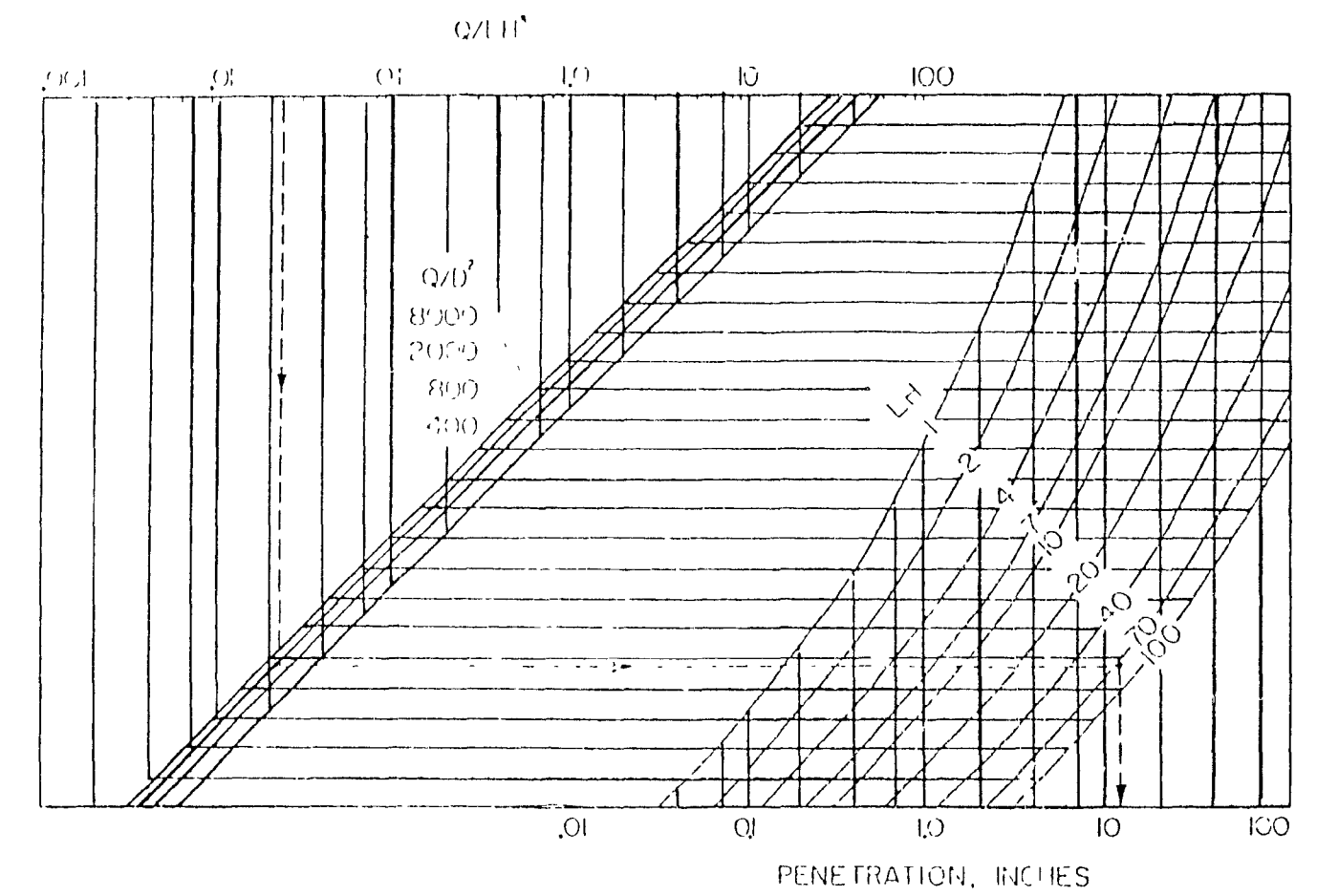


Fig. 2.33 Nomograph for determining jet penetration in molten steel. Q is the blowing rate per nozzle in scfm, LH is the lance height in inches, D is the nozzle diameter in inches^[24].

In another study, Shirma et al^[24] showed that the characteristics of an oxygen jet can be successfully simulated on a water model. Complementing their study were numerous 200 lb BOF simulations, whereby a small quartz window, for filming the cavity, was an integral part of the vessel wall. From this work Shirma et al also developed a nomograph for determining jet penetration in molten steel, shown in Fig. 2.33. These results also agreed well with those of Rote. Therefore, significant penetration is achieved by the oxygen jet during normal steelmaking practices, at least during part of the blow.

Unfortunately, these considerations give no indication of the physical arrangement of the slag and the metal above the level of maximum penetration. Two extremes may be considered; a layer of relatively dense slag pushed towards the walls and a metal bath penetrated as if it were a single phase system, or a thick layer of metal/slag gas emulsion above a metal bath with very little jet penetration in the latter phase. This latter type of behaviour has been observed by several investigators.

When the penetrating jet is blown above two layers of liquids investigators have noted the classi pattern of penetration through the liquid. However, they have also noted very rapid projections of the more dense phase as droplets into the lighter medium results in an emulsion. As a result, jet penetration into the denser phase is reduced. When the emulsion height goes above the nozzle level, the oxygen pump is described as a pump ejector as shown in Fig. 2.34. This affect is easily detected by sound intensity measurements, the emulsion damping the noise of the oxygen jet.

Another source of mechanical energy required to create new surfaces is the action of CO bubbles rising from the bath. This mechanism has been clearly demonstrated in mercury/water systems whereby each CO bubble rising through the interface between the two phases carries along a film of mercury that subsequently peels off and ruptures. Hence, scattering droplets of mercury into the water phase. As a result, the surface area between the two phases increases.

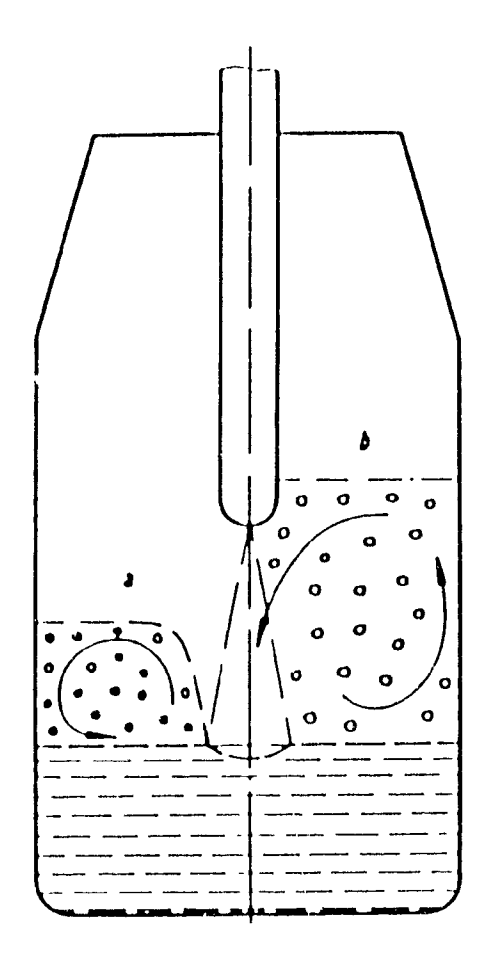


Fig. 2.34 Diagram showing the flow set up in a foaming slag by a gas jet from (a) a lance above the foam and (b) from a lance within the foam [4].

Although the CO bubbles tend to promote emulsification, large CO evolution inside the emulsion is the most stabilizing factor. CO bubbles may tend to counterbalance gravitational forces on metallic droplets by remaining in contact with their metal droplet. Furthermore, the coalescence of two metal droplets is impeded by a gaseous CO film, thus, preventing direct contact. Therefore, anything that inhibits movement of metal droplets or gas bubbles within the emulsion is also a stabilizing factor. Destruction of the emulsion is facilitated by either coalescence and sedimentation or by complete combustion of the metallic droplet.

Temperatures measured in the hot spot, under the oxygen jet are in the range of 2200°C to 2500°C. This ensures complete combustion of oxygen in the vicinity. Early in the development of the BOF process, the hot spot was considered as the only possible place for decarburization, except at low carbon levels. As the process developed, another opinion had gained support; a very large proportion of the carbon combustion occurs in the slag/metal emulsion. For the former opinion to be valid, oxygen has to be transferred, as iron oxide, from the hot spot to the decarburization site. Other, although minor, decarburization sites suggested have been the refractory walls, and along the trajectory of CO bubbles within the metal.

The evolution of the slag during oxygen steelmaking depends on numerous factors such as lance height, oxygen flow rate, flux additions, etc. An example of the composition evolution of BOF slag is represented in Fig. 2.35. An increase in the iron-oxide content during the first part of the blow is followed by a reduction of this oxide in conjunction with an increase in slag height. Towards the end of the blow, a steady increase in iron oxide occurs.

At the beginning of the blow there is almost no liquid slag present. Any oxides that have remained in the vessel from previous heats have frozen by the addition of scrap and relatively cold hot metal. When the slag is solid or very viscous, the slag can be pushed away from the impingement site towards the walls. This permits the jet to impinge directly onto the hot metal.

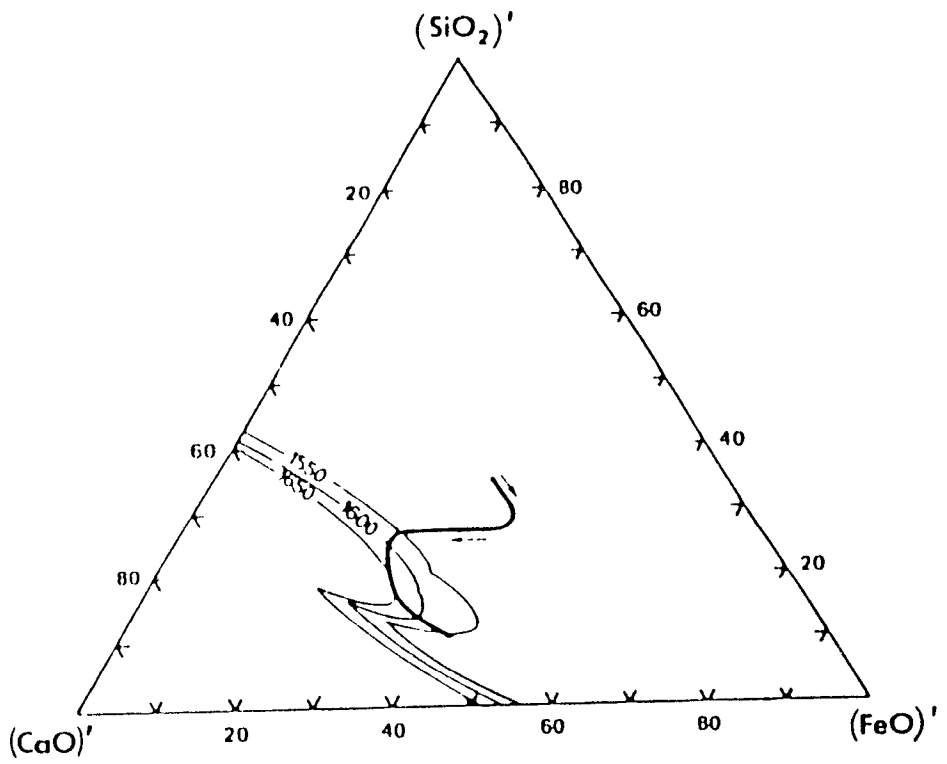


Fig. 2.35 Compositional change of slag in a BOF vessel with variable lance height during the blow^[4].

The start of the main period of the blow is defined as the moment that an emulsion is formed, which requires a fluid slag. The heat and fluidifiers required to form this slag are brought to the slag by the metal droplets emanating from the impact zone. Their reactions in the jet zone have superheated them to high temperatures and left them partially refined and covered with layers of oxides of iron, manganese, and silica. The mass of the slag can then rapidly reach 1550°C and a liquid slag, where lime can be dissolved, is formed. The variation in the start of this emulsion formation is certainly one of the important causes of variability from heat to heat.

As was previously mentioned, the oxygen content is always in excess of that required for equilibrium with p_{co} = 1 atm. Analysis of the metal

droplets ejected from the vessel show an oxygen content much more in excess and a carbon content lower than the bulk metal. Indeed the minor element content of the metal droplet is significantly less than the bulk metal. From this analysis of the droplets, several conclusions can made; (1) metal droplets are more efficiently decarburized than the bulk metal and (2) the droplet size has an influence, the smaller the droplet the more decarburized it is.

During this period, the major site of decarburization can be adjusted somewhat; to occur under the jet a very penetrating jet is used and, at high carbon levels, the jet has an efficiency of almost 100% decarburization. This means that there is little oxygen left for the emulsion. When this practice continues for an extended period, the slag becomes dry; the liquid part of the slag disappears due to the reduction of its iron oxide contents by CO rich gases or by carbon in the metal droplets. The operator of the vessel typically responds to this condition by softening the oxygen jet by either reducing the flow rate or by raising the lance.

On the other hand, very soft oxygen jets tend to oxidize mostly the slag. High iron oxide contents may build up and the Fe³'/Fe²' ratio increases. If excessively soft blowing conditions prevail long enough, the size of the foaming emulsion, and, therefore, the generation of CO bubbles in the slag increases. In the extreme case, the reactions become violent and hazardous. Meyer et al^[25] have established the patterns of decarburization that promote heavy slopping as shown in Fig. 2.36. Curves **a** and **b** correspond to heats in which the rate of

decarburization early in the blow was quite fast, but showed a sudden decreuse in the rate at the arrows. Since the oxygen flow continued uninterrupted, the rate of FeO formation must have increased at this point and continued for several minutes. When the rate of CO evolution began to increase, the result was heavy slopping. Curve c is an average of several heats which did not exhibit slopping nor the decarburization pattern of curves a and b. A slower decarburization rate is not the solution as can be seen in Fig. 2.36. Heat B in the figure exhibits a slower decarburization rate than heat A, identical operating conditions, meaning that FeO built up until the eight minute mark, at which time the rate increased drastically and heavy slopping occurred. The above observations confirm that a balance between hard and soft blowing must be maintained.

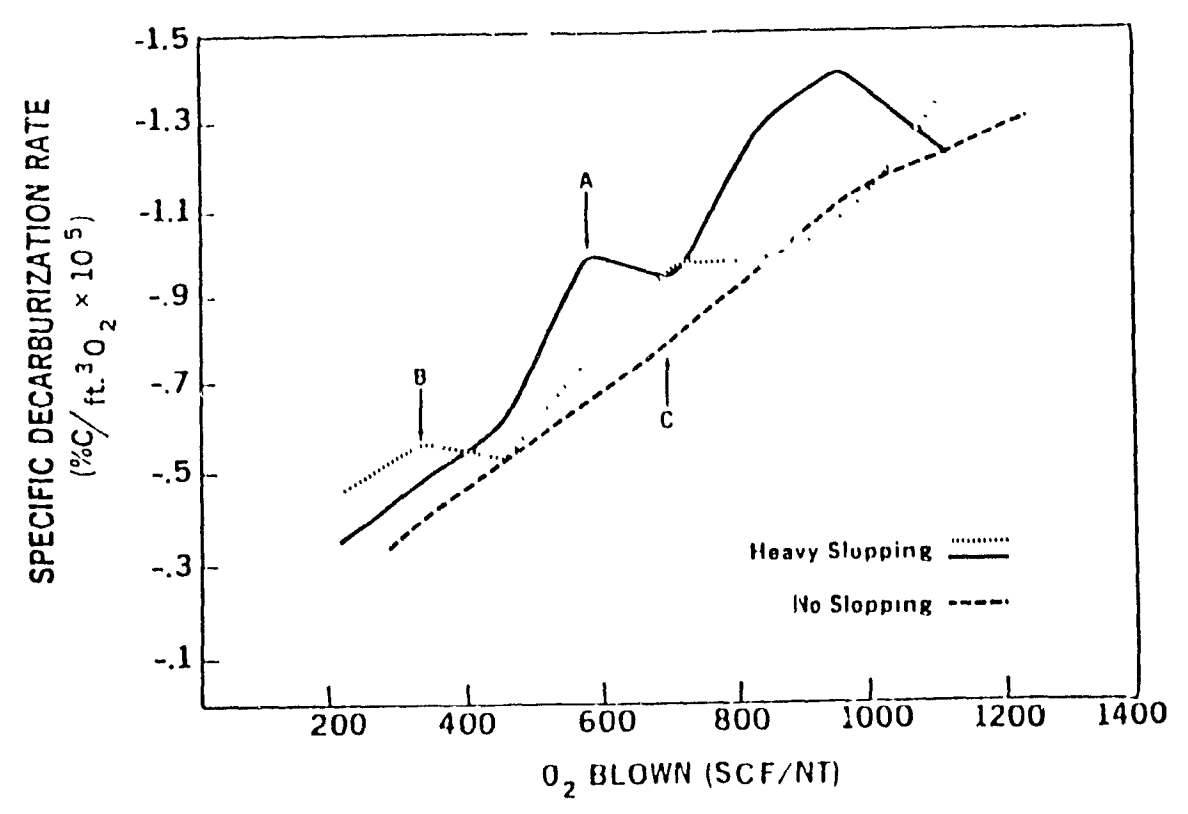


Fig. 2.36 Decarburization rate curves taken during the critical slag formation period^[25].

As long as the concentration of carbon, manganese, or silicon is still significant, the overall rate of the reactions is governed by the rate of oxygen supply from the slag. The chemical reaction step does not limit the rate of the process. Indeed, it has been suggested that at times the rate is limited by the supply of FeO to the slag, an oxygen source.

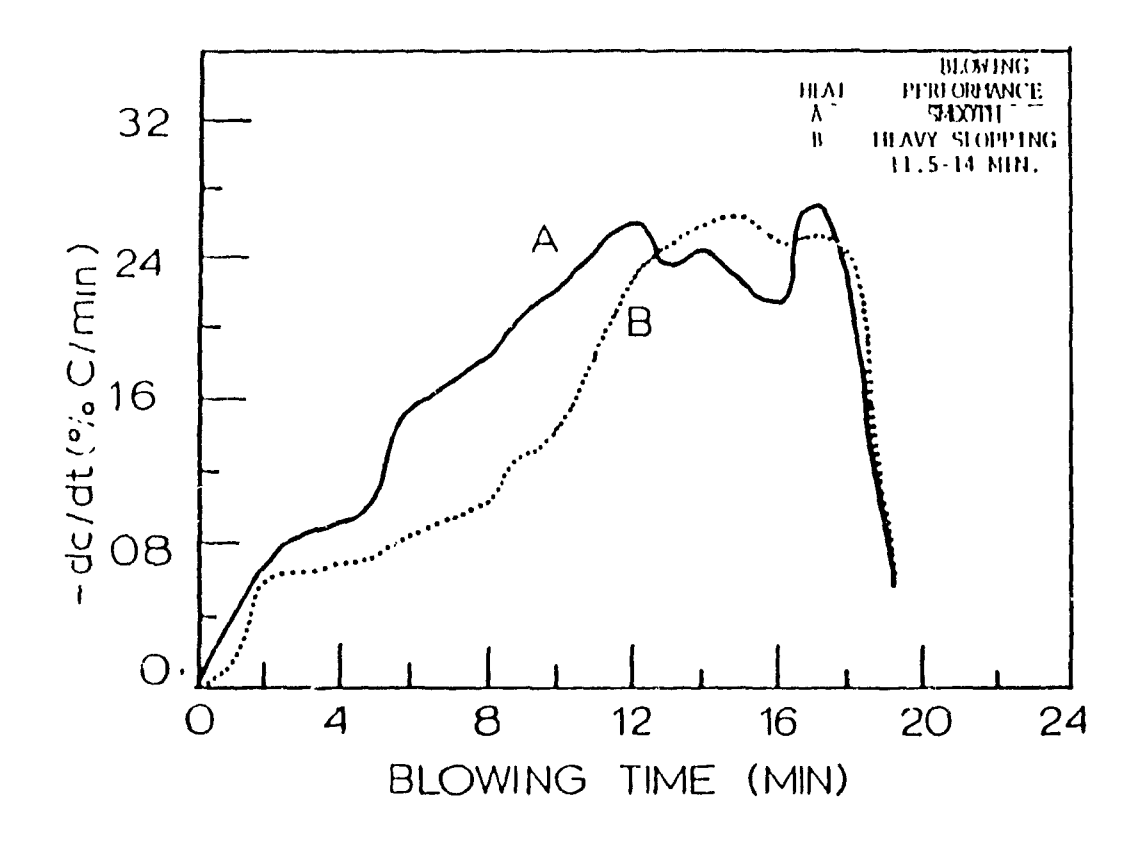


Fig. 2.37 Comparison of decarburization rates for smooth and sloppy heats $^{[25]}$.

1

At the other extreme, as the bath carbon content becomes low (0.02%C), the rate of mass transfer of carbon from within the metal to the reaction interface becomes the rate limiting step. Since this mechanism is slower than the preceding one and the residence time of each droplet in the slag is decreased due to an increase in the fluidity of the slag, the overall process rate decreases as shown in Fig. 2.37. The slag fluidity increase due to a higher iron oxide content.

As a final topic, scrap melting during the BOF process is discussed because of its impact on the chemistry and temperature of the steel. It has been acknowledged that scrap is a major factor responsible for difficulties in end-point temperature control. Indeed it is not uncommon to find unmelted scrap in the vessel at tap.

The mechanism by which scrap enters the molten bath can be broken into four unique stages. In the first stage when the hot metal is poured over the cold scrap a skin of hot metal freezes over the steel. The thickness of the skin of solid hot metal depends largely on the capacity of the scrap to absorb the thermal energy and maintain the temperature of the hot metal below solidus. Once the scrap has been heated to the liquidus temperature of the hot metal, at least at the surface of the scrap, the solidified layer melts away.

The rate at which stages 1 and 2 are completed depends strongly on the

scrap thickness and the heat transfer coefficient. It should be noted that the type, shape and size of the scrap are elusive parameters and, in general, a scrap charge will contain a large variety of these parameters. Therefore, it is sometimes useful to consider the volume to surface ratio of the scrap piece or bulk. Scrap with a low volume to surface ratio will complete stages 1 and 2 faster. The other parameter affecting stages 1 and 2 is the heat transfer coefficient. In general, the greater the bath agitation, the higher the heat transfer coefficient. Therefore, as one might expect, those steelmaking processes having gas injection through the bottom of the vessel have a higher heat transfer coefficient.

Once the hot watal is remelted in stage 2, the thermal energy of the scrap continues to increase until the temperature profile of the scrap is uniform and equal to the bath temperature, which continues to rise. For a major portion of the blow, the carbon content of the bath is higher than that of the scrap. During this time, the surface of the steel scrap is subjected to carburizing conditions which requires mass transfer of carbon from the bulk metal to the scrap surface. This is stage 3 in the overall process; Fig. 2.38 shows the general definition of the terms used to analyze this stage while Fig. 2.39 shows the carburization process. The major parameters governing the rate of this stage are the volume to surface ratio of the scrap and the mass transfer of carbon from the bulk to the scrap, which is improved by greater bath agitation.

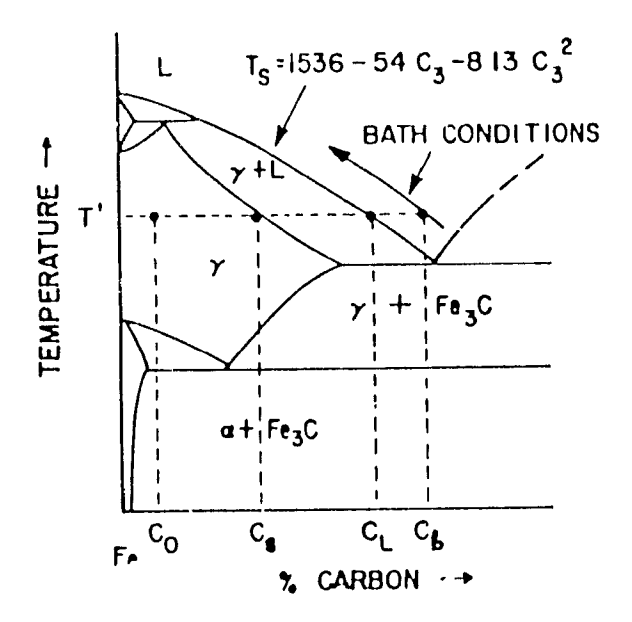


Fig. 2.38 Definition of conditions and terms used in analysis of scrap melting. C_{o} is the scrap carbon content and C_{b} is the bulk carbon content of the bath.

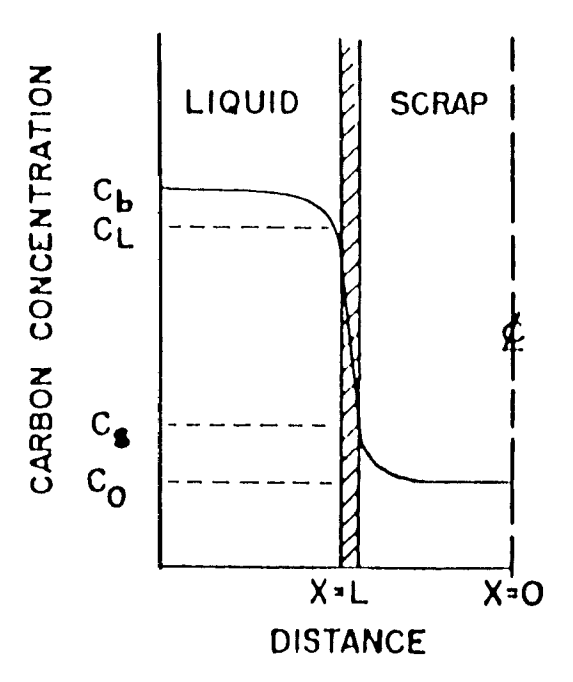


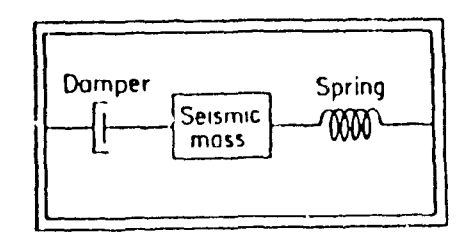
Fig. 2.39 Scrap carburization mechanism during scrap melting in the BOF process.

The duration of this stage is of course dependant on the bath temperature and carbon content of the scrap and the bulk metal. Once the temperature of the bath reaches the melting point of the scrap, any remaining scrap will melt rapidly. This is stage four in the process, and is not necessarily reached.

3. Accelerometer Transducer

3.1 Introduction

An accelerometer, as the name implies, is a transducer that can measure the acceleration of a body. Acceleration is defined as the rate of change of velocity with respect to a reference system. The common sensing element of all accelerometer transducers is the seismic mass (Fig. 3.1). In its simplest form, the seismic mass is restrained by a spring, and its motion is dampened in a spring-mass system. When an acceleration is applied to the transducer case, the mass moves relative to the case (Fig. 3.1-b) When the acceleration is removed the spring returns the mass to its original position (Fig. 3.1-c). The accelerometer transducer can be used to measure vibrations by monitoring the displacement of the seismic mass from its original position with respect to time, ie. oscillation.



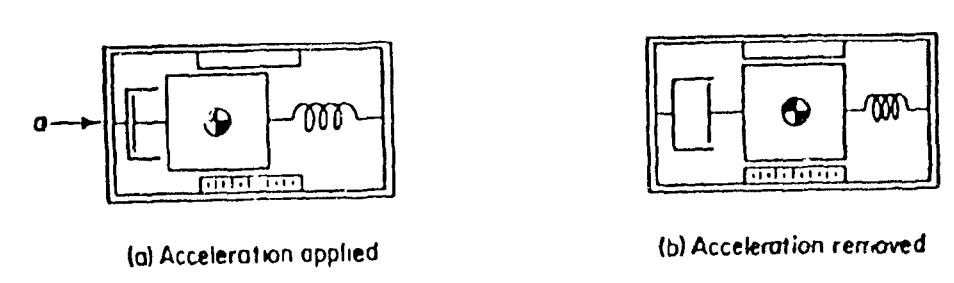


Fig. 3.1 Basic spring-mass system of an acceleration transducer.

The type of accelerometer transducer employed in this study is the piezoelectric acceleration type, which is primarily intended for the measurement of vibratory acceleration and shock. The transducer relies on the piezoelectric effect, which is the phenomena of generating an electric charge when certain crystalline materials are pressed or squeezed.

The basic premise of the accelerometer, in the field of process metallurgy, is the inhement solid-liquid-gas interactions which cause the containment vessel to vibrate during the process. The status of these interactions can be determined by the relative magnitude of the vessel vibrations. Thus, the accelerometer, a vibration sensitive device, can be used as a sensor to monitor the status of these interactions.

The remaining portion of this chapter provides a general description of accelerometer transducers, and a detailed description of piezoelectric accelerometers^[26].

3.2 General Description of Accelerometers

Accelerometer transducers can be categorized by the type of acceleration, linear or angular, which they neasure. The seismic mass in a linear accelerometer is usually of circular (solid or annular) or rectangular shape in cross section. The mass can be linked to the case by flexures made to slide along a bar, or it can be otherwise restrained from motion in any but the sensing axes. The seismic mass of an angular accelerometer, which can be a disc pivoted at its center

and restrained by a spiral spring, responds to angular acceleration with an angular displacement.

The basic types of accelerometer transducer designs are:

- · Capacitive
- Photoelectric
- Potentiometric
- Reluctive
- Strain-gauge
- Servo
- · Vibrating element
- · Piezoelectric

Capacitive

Capacitive acceleration transducers rely on a change in capacitance in response to acceleration. This is achieved by implementing a fixed stator plate and a diaphragm of matching configuration to which a circular seismic mass is attached. The diaphragm acts as a restraining spring as well as the moving rotor, or electrode, of the capacitor. Acceleration acting on the mass causes the diaphragm to deflect and its capacitance to the stator to change proportionally. When the capacitor is connected into an A-C bridge, an A-C voltage of varying amplitude can be produced as the transducer's output. A frequency-modulated output can be generated by using the capacitor in an oscillator tank circuit. Transducers of this type have not been produced commercially to any significant extent. However, the capacitive principle has been applied in certain servo accelerometer designs.

Photoelectric

Photoelectric acceleration transducer designs utilize the motion of the seismic mass as a shutter between a light source and one or two photoelectric sensors (photoelectric sensors measure light intensity).

The output of the photoelectric sensor is proportional to acceleration. This type of transducer is primarily intended for relatively slowly varying acceleration and are not generally available. The more common type of accelerometer transducer for the application of measuring slowly varying acceleration is the potentiometric acceleration transducers.

Potentiometric

In potentiometric transducers a seismic mass is mechanically linked to a wiper arm which moves over the active portion of a resistance element with full-span deflection of the mass. Most potentiometric accelerometers incorporate overload protection to limit the wiper travel when accelerations exceed the transducer's range. Various types of dampening mechanisms are usually applied to minimize vibration-induced noise in the transducer output due to wiper whipping and large changes in instantaneous contact resistance between the wiper and the resistance element. In addition, there is usually some sort of amplification linkage used between the seismic mass and the wiper arm.

Reluctive Transductive

There are two types of reluctive transduction elements that are used in commercial accelerometers, an inductive bridge type and the differential-transformer type. The frequency response of the reluctive type is substantially higher than that of the potentiometric designs. In addition to the higher frequency response, the internal components of the reluctive type can be made from materials usable at fairly high temperatures.

Strain-Gauge

The strain-gauge transducers convert acceleration into a change of resistance due to strain in two or, more commonly, four arms of a Wheatstone Bridge, and they exist in a variety of designs. The circuits are mounted to the spring in a mass spring system and to a separate stress member additional to the spring, or between the seismic mass and a stationary frame.

Servo

Servo accelerometers are widely employed when demands for close accuracy and high-level output warrant their relatively high cost. They typically employ a closed loop servo system such as force balance, torque balance or null balance. The basic components consist of a seismic mass, a sensor which detects the motion of the seismic mass, a servo-nulling amplifier, a restoring coil, and an output resistor. The motion of the seismic mass is transduced into an error signal in the servo system by the motion detecting sensor. The error signal is amplified by the servo-nulling amplifier which causes a feed-back

current to flow through the restoring coil and the output resistor. The restoring coil is mechanically linked with the seismic mass in a mass-coil system. The current from the servo amplifier causes a torque to be produced by the coil which is equal and opposite to the acceleration generated torque acting on the mass-coil pendulum. At this point the servo system is in a force-torque balance condition. The current from the servo-nulling amplifier required to achieve the balance is directly proportional to the applied acceleration. Since the output resistor has a fixed value, the output voltage of the transducer is also proportional to the acceleration.

Vibrating-Element

The vibrating element principle has been applied in an acceleration transducer used for space booster acceleration telemetry where an overall measurement system accuracy within ±0.25% of full scale deflection is required. The high cost of this type is due to the difficulties involved in the design and manufacture. The operating principle is quite simple. A tungsten wire, the vibrating element, is attached at one end to a seismic mass and at the other end to a fixed part of the transducer case. Motion of the seismic mass causes a change in the tension of the wire and hence in its resonant frequency. The wire is in a permanent magnetic field established by a pair of magnets parallel to the wire. A current passed through the wire causes it to vibrate at its resonant frequency. This oscillation is maintained in a feedback circuit whose frequency controlling element is constituted by the wire-magnet assembly. The signal in the circuit is then coupled to an amplifier from which the transducer output is

obtained. The output amplitude is essentially constant in the measuring range. The output frequency, however, changes with acceleration in a parabolic fashion.

3.3 Piezoelectric Acceleration Transducers

The most common acceleration transducers are the piezoelectric type and are designed primarily for the measurement of vibratory acceleration and shock.

The piezoelectric effect was discovered in 1890 by Pierre and Jacques Currie when they observed that electrical charges were produced by a quartz crystal when weights were placed on it. The term is derived from the Greek word piezen, which means to squeeze. Various researchers subsequently showed that about forty types of crystalline materials generate an electrical charge when they are pressed or squeezed so that they undergo minute dimensional change (ie. in length, width or thickness). The Currie brothers also discovered the inverse effect, dimensional change when an electrical charge is applied to the crystal.

3.3.1 Crystal Materials

There are two basic types of crystal materials, natural and synthetic. The latter are invariably ceramic mixtures. Natural piezoelectric crystals, with the exception of tourmaline and quartz, are artificially grown from an aqueous solution of the material under closely controlled conditions. The transduction element is created by slicing a slab from the crystal along a carefully chosen crystallographic axis, then plates of the desired configuration are cut from the slab. Tourmaline, a complex silicate of aluminum and boron, and silica crystals are usually selected from those found in their natural state. However, quartz is the only natural crystal material to have found widespread application in acceleration transducers.

Quartz plates, when stressed in thickness-shear, thickness expansion, or length expansion modes, are characterized by a high and stable frequency. Thus, they can be used over a wide range of temperatures. A major disadvantage, however, is that their sensitivity is quite low.

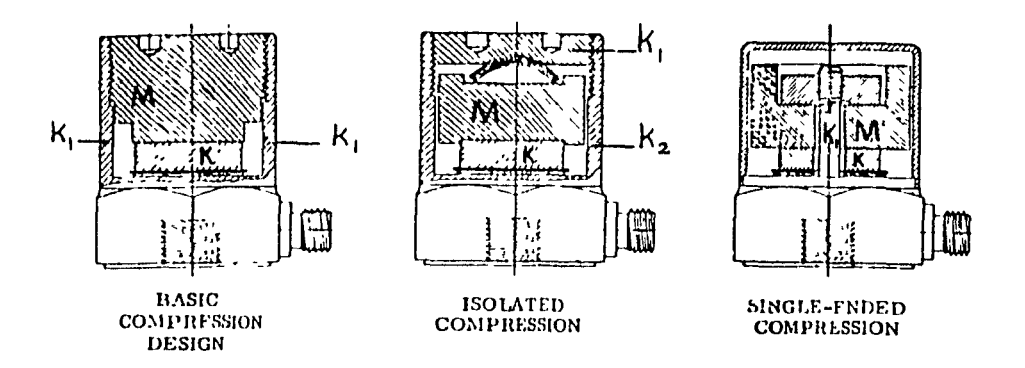
Ceramic crystals are employed more frequently than natural ones. Most piezoelectric ceramics contain various mixtures of such materials as lead zirconate, lead niobate, lead zirconate/barium zirconate. The manufacture of a ceramic element begins with mixing various known proportions of compounds in a ball mill along with a binder. The mixture is then molded into the desired shape in a hydraulic press. The result is a soft bisque which is removed from the mold and is sintered in a high temperature kiln. After sintering the ceramic is cooled to form a hard shaped object, which is subsequently polarized

by exposure to orienting electric fields. The polarizing operation causes the ceramic to exhibit the required piezoelectric qualities. Temperature cycling, aging and cleaning complete the manufacturing process. Electrodes can be metal films made integral with the surface by high-temperature firing.

An important characteristic of piezoelectric ceramic materials is their Currie point, the temperature at which the piezoelectric quality is lost. The Currie point, therefore, determines the upper limit of the operating temperature range of the transducer. The operating temperature is always specified well below the Currie point to provide a margin of safety. Currie points can vary from 30°C to 570°C.

3.3.2 Designs

Piezoelectric accelerometer designs can be typified by those shown in Fig. 3.2. The acceleration sensing axis is perpendicular to the base. Crystals are polarized in such a way as to minimize output due to acceleration along other axes. A portion of the spring action of the spring-mass system is provided by the crystal (k in Fig. 3.2) itself in all designs. In the basic and isolated compression designs, the transducer case also contributes to the elastic component of the system. A curved spring in the isolated-mass compression design adds a third elastic member. Thus, the operation of both transducer types is affected by any forces acting on the case which tend to alter its elastic characteristics.



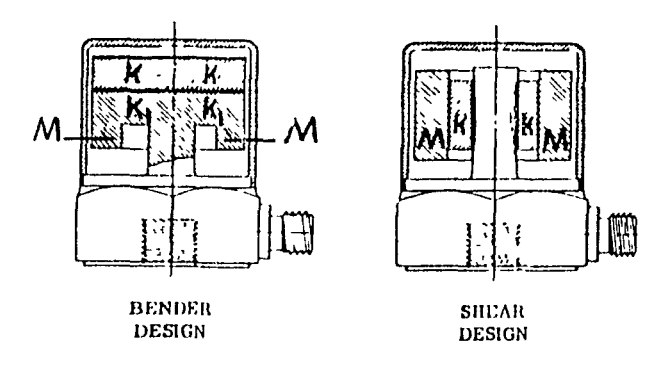


Fig. 3.2 Typical piezoelectric acceleration transducer designs showing; (k) crystal, (m) seismic mass, (k1,k2...) secondary elastic members [26].

Case sensitivity is minimized in the following three designs: single-ended, bender-design, and shear-design. However, strains in the base of the five types can cause undesirable effects on transducer performance to various extents. In the compression designs the mass is preloaded against the crystal so that an output of alternating polarity is produced when compression is alternately increased and relieved due to vibratory acceleration. In the bender design the crystal is bound to a mushroom-chaped mass. In the arrangement shown in Fig. 3.2, the mass also acts as an elastic member. The rim of the assembly deflects upward and downward with respect to its support

center. The shear design implements an annular crystal bonded to a center post on its inside surface and to an annular mass on its outside surface. Deflection of the mass, upwards or downwards, causes shear stresses across the thickness of the crystal.

The case of many piezoelectric accelerometers are electrically connected to one electrode or a set of electrodes. The case is hermetically sealed to prevent the entry of moisture. An internal thread in the base is the typical provision for mounting. In a situation where the case must be electrically insulated from the measured structure an insulated mounting stud can be employed. Cases too small for mounting by means of threads can be cemented to the structure.

3.3.3. Signal Conditioning

The output (charge or voltage) of the piezoelectric transducer is smaller than that which most telemetry or readout systems require, and, more importantly, the output impedance is much higher than usable in virtually all electronic measuring systems. Thus, signal conditioning circuitry is required for piezoelectric accelerometers. To transform this high impedance into one of a much lower value, a cathode-follower, emitter-follower, or amplifier is connected to the transducer with as short a cable as possible as the installation will allow.

Since the cable is on the high impedance side of the amplitude, it requires special attention. The cable should be as free as possible

from triboelectric noise (noise induced by friction between the conducting and insulating portions of the cable). The friction can be reduced by employing a graphite lubricant between the conductor and the insulation. Several transducer designs incorporate signal conditioning within the transducer case.

3.3.4 Sources of Error

Errors can be produced within the transducer by mechanical deformation of the case, by stresses caused by uneven thermal expansion and by spurious electrical signals generated across the crystal electrodes due to charge separation in the crystal in response to a step change in temperature. This last effect is known as the pipoelectric effect, and can be minimized by proper transducer design.

Transverse sensitivity, sensitivity to acceleration in axes other than the sensing axis, can also be minimized by proper design.

The most frequent cause of transducer failure, however, is breakage of the coaxial cable conductor at either connector due to improper handling.

3.3.5 PCB 308B02 Ouartz Accelerometer

The type of piezoelectric accelerometer employed in this study is the PCB 308B02 manufactured by PCB Piezotronics^[27]. The model is primarily designed to measure low to medium frequency (1 to 3000Hz) vibration and shock motion on heavy structures of industrial machines, machine tools, vehicles, suspensions, engines, etc.

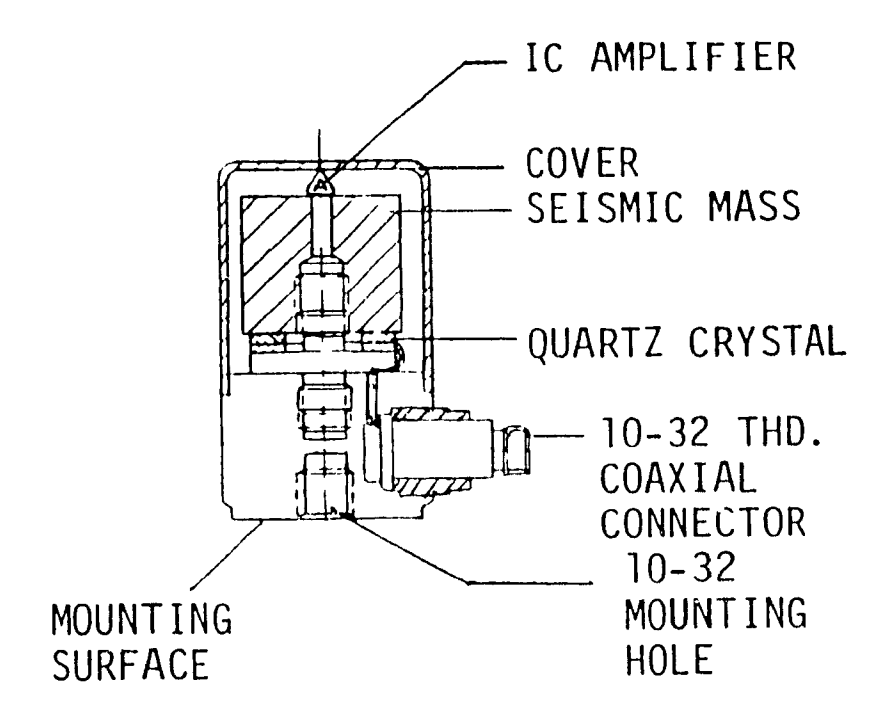


Fig. 3.3 Schematic of the PCB 308B02 accelerometer from PCB Piezotronics [27].

This is a heavy, rugged instrument for prolonged service in industrial and vehicle environments. The structure of the model contains a quartz compression mode element, an integrated circuit gain amplifier and an over-voltage protection circuit. The gain amplifier is self contained so that the system sensitivity is independent of the power supply unit. A schematic of the PCB 308B02 is shown in Fig. 3.3. The power supply unit provides a constant current of 4 mA via a single thin coaxial cable, which reduces noise and attenuation problems.

Installation of this transducer is facilitated by a mounting stud in the base of the unit. Essentially there are three basic techniques of mounting the unit to the structure. Firstly, the mounting stud itself mounting or a stud mounting. Secondly, an adhesive mounting base can be mounted onto the stud. This special base permits the unit to be bonded to the structure by use of epoxy or another suitable adhesive. The third technique of mounting the unit is extremely versatile and simple. This technique employs a magnetic mounting base which can be threaded onto the stud. Of course, its application is limited to magnetic structures.

Special care must be taken with coaxial cables and their connection to the transducer unit. The cable should be clamped or taped to the measured structure approximately 2.5 to 3 inched from the transducer permitting slack on the cable for stress relief. This should be practised because high strains can be transmitted through the free length of cable to the accelerometer.

In addition, RTV rubber boots that cover the accelerometer should be implemented. These boots are particularly useful for protecting the accelerometer from thermal and mechanical damage.

4. Control of the Oxygen Steelmaking Process

4.1 Introduction

į

The development of the BOF and other oxygen steelmaking processes has placed greater emphasis on productivity and control. This need stems from the fact that a typical BOF shop has typically only two to three vessels whereas the open hearth shop has up to 15 furnaces to produce the same annual production. Coupled with the fact that numerous steel plants have shifted their open hearth production to BOF shops, gains in productivity and control of the process readily translate into profits.

In general, the objectives of the BOF process are to produce a given weight, temperature and composition of blown metal which, through the addition of the appropriate alloys in the steel ladle, can produce a product of a specified composition. Typically, the aim weight of steel in the ladle is a standard amount, facilitating the synchronization between steelmaking and casting departments. The temperature and composition of the steel is dictated by the type of steel to be produced and the casting process to be employed.

To achieve the above mentioned objectives, three primary elements must be controlled in the BOF; these are carbon, phosphorous, and sulphur. The carbon content is no doubt the most important and is the primary objective of most control schemes. The importance of the sulphur and phosphorous contents are determined, to a large extent, by the composition of the hot metal. Generally sulphur is considered more important in a low phosphorous hot metal practice and phosphorous is

of primary importance in a high phosphorous practice.

To minimize material consumption, increase yield, and ensure the required ladle composition, blown metal weight must be controlled so that the correct weight of steel is tapped into the ladle. Production of liquid steel in excess of the ladle capacity is tapped into the slag pot from the BOF, significantly decreasing yield. On the other hand, production of liquid steel in an amount significantly less than the standard weight will cause numerous problems downstream at the casting facilities.

End-point temperature is one of the most critical parameters in steelmaking as it significantly affects product quality; there is a narrow range of furnace and ladle temperatures for optimum steel quality. Although the significance of this parameter has diminished with the introduction of ladle furnaces, end-point temperature also greatly affects the service life of the refractory linings and, hence, production costs.

As mentioned above, control schemes vary from plant to plant. An optimum method for a shop depends largely on the product mix, casting process employed, and hot mecal availability. Control schemes are typically based on a charge calculation that is refined by either a predictive-adaptive static model or on a continuous or periodic measurement of process variables, such as carbon, in a dynamic control model or a combination thereof. Regardless of the control strategy, there are several desirable attributes that facilitate good BOF

control[4]:

- Consistent hot metal of accurately known chemistry and weight.
- Scrap of consistent density and with low harmful residual elements such as sulphur, copper and tin.
- Lime, dolomite and other fluxes of consistent chemistry and sizing.

The importance of obtaining these attributes is readily understood when one hears BOF operators say that a simple charge calculation model is sufficient when these attributes are obtained. However, these requirements are seldom fully m.t in practice. This absence has led to the development of numerous control schemes, some of which incorporate direct and non-direct measurement of variables on a periodic and/or continuous basis, that attempt to refine the basic charge model.

In this chapter, static control schemes are reviewed first, followed by a discussion of dynamic end-point control schemes covering both periodic and continuous measurement of variables.

4.2 Static Control

4.2.1 Introduction

The static control model is the starting point in the production of any particular type of steel. Indeed, whether the oxygen steelmaking process is controlled dynamically or pseudo-dynamically the various components which are charged before, or shortly after the start of the blow are determined by the static model. Static control of the BOF process is essentially a charge calculation model. Thus, the static control model is a critical component in any process control scheme.

There are basically three different types of static control models in existence today, these being:

- Predictive
- •Statistical
- •Predictive-Adaptive

The predictive static model is based on the thermochemical and mass balance relationships of the process. On the other hand, the statistical static model is based on a series of correlations between the process inputs and outputs, treating the BOF as a black box. Statistical static models appeared after early predictive models yielded large deviations between predicted and actual results, however, only a small improvement in end-point temperature predictions was obtained^[28]. The limitation of these two types of static control models facilitated the development of a predictive-adaptive static control scheme. In fact, the typical static model is a combination of the predictive and static models and is referred to as predictive-adaptive.

Regardless of the type of static model, the basic objective of the calculations is to determine the amounts of each individual component which must be charged into the vessel in order to produce a desired final steel composition, temperature, and weight. At the present time, a typical charge calculation model is required to perform the following four tasks:

- •Ordering Calculation
- •Blowing Calculation
- •Reblow Calculation
- •Posteriori Calculation

The ordering calculation determines vessel additions such as the weight of hot metal, scrap, burnt lime, and recycled slag. All of these are needed in varying amounts to produce the desired characteristics of the steel. The purpose of this calculation is to "order" the various components and to have them prepared for the charge. In the calculation, the composition and temperatures of the various components, such as hot metal, slag, etc., are often presumed to be represented by the previous analysis of these components.

Unfortunately, it is often the case that the amounts of hot metal and scrap ordered are not the same as that delivered to the vessel. Therefore, the hot metal is normally weighed in the transfer ladle once it has been charged from the torpedo car. In addition, the previous analysis of the hot metal may not represent the composition or temperature of the hot metal that will be charged into the vessel. Thus, a sample of the hot metal is taken for chemical analysis and the temperature is measured. Furthermore, the actual weight and type of scrap charged may differ from that requested. Consequently, another

charge calculation must be performed to account for the new values of weight, composition, and temperature in the various components.

Hence, the objective of the blowing calculation is to provide an adjustment according to the values of the materials actually charged into the vessel. This enables a more representative description of the main components to update the model. In these calculations the weight of scrap and hot metal become constraints within the model, along with the composition and temperature of these materials and the desired steel product. These constraints are then applied to determine the weights of the remaining parameters. The desired slag composition and weight is also a constraint within the model. The main parameters that are determined at this point are the total amount of oxygen required to refine the hot metal, the weight of the ore addition (coolant), and the flux additions.

The blowing calculation assumes that the main parameters of decarburization rate, or efficiency, and the temperature rise that would occur in the upcoming heat, can be characterized by the values of those parameters which occurred in previous heat(s). In addition, the model assumes that the values given for various components are correct. These assumptions are not always valid, resulting in a steel whose composition and/or temperature are not the same as those calculated. This necessitates a reblow calculation, in which the calculation determines the corrective action required to achieve the composition and temperature desired.

As stated, the objective of the reblow calculation is to determine the corrective action required to achieve the desired composition and temperature. The calculations are usually based on an analysis of the steel composition after the main blow and a temperature measurement. The two basic corrective actions that can be performed are addition of coolants and oxygen blowing. The reblow calculation is repeated until the composition and temperature lie within an acceptable range, or when the steel is downgraded. Downgrading of a heat simply implies that the original steel specifications could not be obtained and, therefore, the steel produced is classified as another type of steel, usually of a less desirable steel grade.

Once the blow has been completed, the posteriori calculation is performed. The objective of this calculation is to update certain parameters, such as the rate of temperature rise for the model in the next heat. In doing so, the calculation determines the closing items in the balances for the heat just finished. The basis of this calculation is the final composition and temperature of the steel.

4.2.2 Predictive Models

The thermochemical and mass balance relations describing the BOF process have long been available [29]; with only minor modifications, these relations are the basis of the predictive static model. The earliest publication of a predictive model was by Slatosky [30], although the original aim of the control scheme was to control only temperature by means of adjusting scrap addition. This model, initially implemented on a complex slide rule, was successfully transferred to an analog computer to avoid operator error.

The first control model developed for use with a digital computer was described by Boltz in 1967^[31]. In this application extensive effort was made to provide reliable inputs and complete chemical analysis and The system was designed to control carbon, temperature, sulphur, phosphorous, total oxygen blown and tapping weight. were directly interfaced with the computer, minimizing operator effort. The model went so far as to have bias switches that permitted adjustment for short and long term swings in furnace turndowns. charge model flow sheet, illustrated in Fig. 4.1, is divided into four sections. Section A contains all computations which occur only once per charge calculation, whereas section B contains computations which may be performed several times. Section C contains the possible combinations of known and unknown factors which are used in the simultaneous solution of heat and iron balances. The first iteration is normally based on a specific steel product weight desired and a known weight of scrap in the scrap box. The final computations in this section are the oxygen volume, burnt lime, slag FeO and slag weight.

Section D verifies that the results obtained by the previous sections are within preset tolerances. If they are not, then another iteration is performed until a valid solution is obtained.

FLOW CHART OF CHARGE CALCULATION

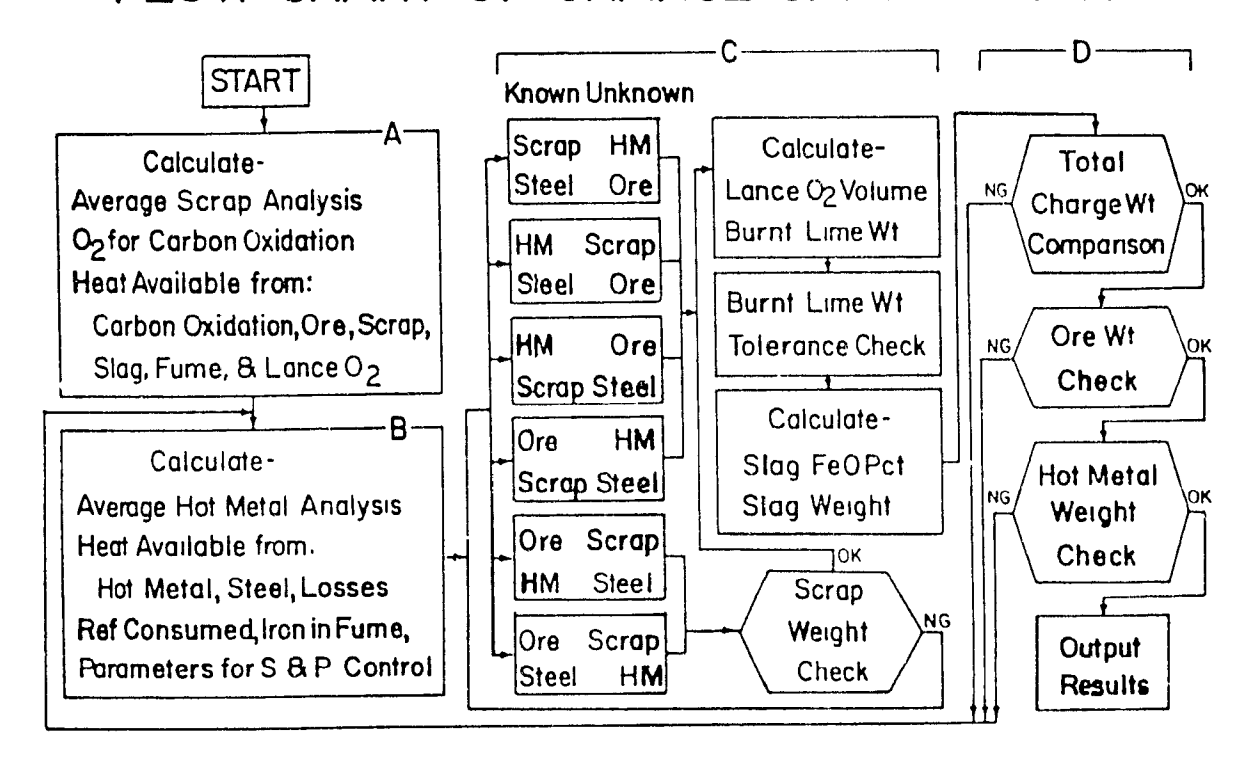


Fig. 4.1 Flowchart for charge calculation (after D.G. Poltz (311)).

The development of statistical models stems directly from the earliest operators that controlled the process. If a heat was turned down too low in temperature, the operators would tend to blow more oxygen or add more hot metal for the next heat. Like the operator, the statistical model reacts according to the inputs and outputs of previous heats. More specifically, the statistical model is based on a series of equations that relate all the output variables with the input variables. The coefficients of these equations are based on a limited number of recent heats. Thus, the model treats the process as though it were a black box.

One such model was developed by Katsura et al⁽³²⁾, after an initial attempt with a predictive model that yielded large deviations between predicted and actual results. Through the development of the statistical model, evolved the assumption that relatively long term changes in the process were affecting the sensitivity of the regression analysis. Therefore, a control equation utilizing the data of only the last heat was developed:

 $T_u = T_p + [f(X_{1u}) - f(X_{1p})] + [f(X_{2u}) - f(X_{2p})] + \dots (4.1)$ where T_u is the estimated turndown temperature of the upcoming heat. T_p is the measured turndown temperature of the previous heat. X_1 , X_2 ... are the mathematical weightings, while analyses, end-point conditions and $f(\lambda_1)$ are some function of the refining variables. This version of the control model had improved the end-point temperature, however, as with the predictive models, the results obtained were not satisfactory.

4.2.4 Predictive-Adaptive Models

The predictive-adaptive model combines both the predictive and statistical models. The basic charge calculation is based on the thermochemical and mass balance relations of the process. Coefficients of some of the variables are modified in a statistical manner to respond to changes in the process. One such model was developed by CRM^[33].

Although the CRM model is similar in some respects to the Boltz model, it has two additional features that are worth noting. First, after the completion of the blow, analyses of the slag, steel and actual quantities charged, are used in a posteriori calculation to determine oxygen efficiencies and differences between calculated and actual slag and temperature conditions. The corrected factors are then used in calculations for the next heat. Changes in the factors that are recommended in this calculation are typically damped by including the recommended changes from several heats.

The second and more important difference is in the calculation of the slag volume and composition using physico-chemical principles. From the phase diagrams of the slag system, correlations have been established between sulphur in the steel, sulphur partition ratio and slag weight. In addition, the lime saturation boundary in the pseudoternary has been defined in terms of the slag iron content for a specific BOF practice and a system of six equations and six unknowns established for the slag describing the interrelationships between the principle steelmaking components CaO, MgO, MnO, SiO₂, Fe_TO, and P₂O₅.

For each slag iron content the amounts of each of the other five components can be computed and for each slag composition the contents of P, O, C, and Mn in the steel product are determined as well as an $(S)_{slag}/S_{Fe}$ ratio. The coefficients used in the above equations are adjusted by posteriori calculations in a statistical manner.

4.2.5 Limitations of Static Models

Performance, or reliability, of a static model is strongly dependant on the accuracy of the inputs into the model. In fact, if the variables could be measured accurately, the static model could describe the process and its end-points. Extensive effort has gone into designing systems with better input analyses, weights and instrumentation. As a result of these efforts, static models have shown some marginal improvements in end-point control.

Several investigators ^[34,35,36] have calculated the amount of deviation in turndown temperature which could be expected based on variations in input variables. One very important point brought forward by Meyer et al⁽¹⁰⁾ is that only a minor deviation between the calculated and actual slag iron oxide can cause a significant difference in the turndown temperature. Although the magnitude of this deviation is greater in theory than in practice, its magnitude is significant.

Furthermore, the fundamental assumption of static control models is that if the heat is blown at the same lance height and oxygen rate, the decarburization rate and, indirectly, the heat generated will be the same as that of the preceding heat. Analysis of off-gas indicates that

this assumption is invalid. The decarburization rate may not remain the same for heats treated under identical conditions. Since this change is not predictable, turndown control of static models invariably deviate from actual values. Hence, the need for dynamic control of the steelmaking vessel.

4.3 Dynamic End-Point Control

4.3.1 Introduction

The basic assumption behind BOF dynamic control is that, although the decarburization rate is not directly related to the bath carbon for all heats, it is directly related to the heat in progress. From this assumption, and from monitoring the decarburization rate, directly or indirectly, it is possible to solve for an instantaneous bath carbon and determine the amount of oxygen required to reach the aim bath carbon.

One of the earliest attempts to dynamically control the BOF was reported by IRSID^[37,38]. The system was based on the principle that if one knew the inputs, particularly the total amount of carbon charged, one had only to analyze the percent carbon in the waste gas and measure the volume of waste gas to determine the quantity of carbon leaving the furnace per unit time and determine the carbon in the bath at any time by integration:

$$C_{t} = C_{i} - \int_{0}^{t} \frac{\partial C}{\partial t} \, \partial t \tag{4.2}$$

In the above equation, C_t and C_i are the carbon content at time t and the initial carbon content, respectively. Errors are compounded in the system through small errors in the waste gas volume, instrumentation, and uncertainty of the charge carbon. The magnitude of the compounded error is significant in light of the relatively small amount of carbon present in the bath at tap, C_t . As a result, this technique has received little attention.

Ensuing work focussed on the exponential decay characteristic exhibited by the decarburization rate curve, Fig. 4.2. One system of particular significance was developed at Jones and Laughin^[39,40]. In this work, coefficients of the exponential decay equation for the heat in progress (determined by off-gas analysis, mass flow equipment and from Eq (4.2)), solve for the instantaneous bath carbon and the amount of oxygen required to reach the aim carbon; the exponential equation may be expressed as:

$$R = R_{p} (1 - e^{(-k(C - Co))})$$
 (4.3)

where:

R = instantaneous decarburization efficiency [kg C / m_{02}^{3}]

R_p = maximum decarburization efficiency encountered during the course of the heat

k = constant for the heat in progress

C = % carbon in the bath corresponding to the decarburization efficiency R

 $C_0 = \text{extrapolated bath carbon content when } R \text{ equals zero.}$

The equation above may be rearranged to:

$$C = \frac{-\ln (1 - R/R_p) + C_o}{k}$$
 (4.4)

There are several mathematical methods for calculating the coefficients of the exponential equation and then determining the bath carbon; the most common technique being non-linear least squares. Once these coefficients have been determined, the remaining oxygen required can be obtained by rearranging and integrating equation (4.3).

$$R = \frac{\partial C}{\partial O} = R_p \left(1 - e^{(-k(C - Co))}\right) \tag{4.5}$$

He.ice, lance oxygen required to obtain the final carbon, $C_{\rm f}$, can be expressed as

$$\Delta O_{c} = \int_{C_{t}}^{C_{f}} [R_{p} (1 - e^{(k(C \cdot Co))})]^{-1} \partial C$$
 (4.6)

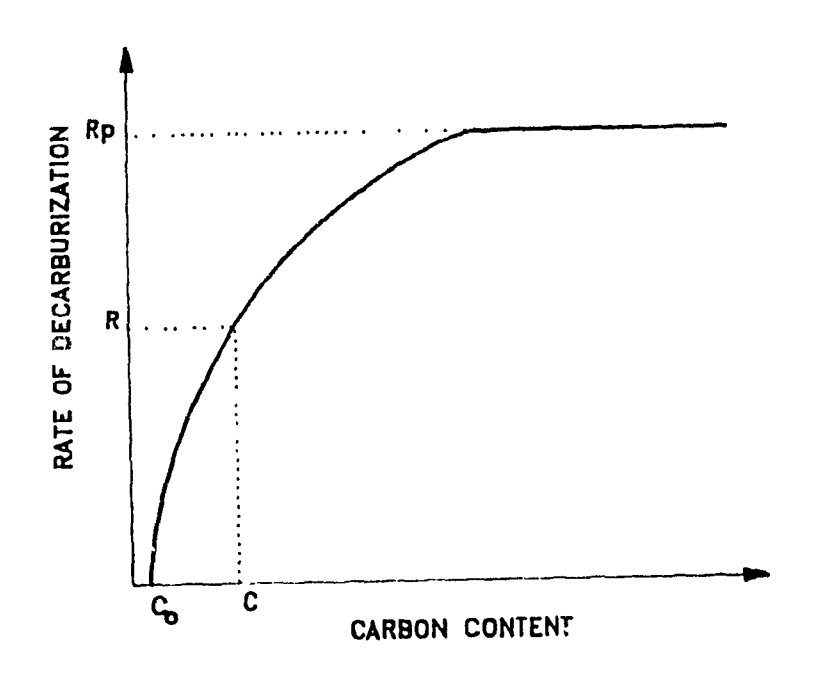


Fig. 4.2 Exponential decay characteristic exhibited by the decarburization rate curve.

The Jones and Laughin system employed a separate model to obtain temperature. Near the end of the blow an expendable bomb thermocouple, weighted to ensure penetration into the metal bath, was used to obtain a temperature measurement. From this and an empirical relationship relating the bomb temperature and the remaining quantity of oxygen to blow, the end temperature was determined.

From the development of these two early attempts to control the BOF, one can see the basic dynamic control philosophies employed today. The first philosophy is to detect characteristic changes in the rate of decarburization and relate a signal, such as the carbon content of the off-gas, to the bath carbon content. The other philosophy is to actually sample the metal bath, as in the case of the expendable bomb thermocouple. The latter philosophy, in its most complete form, has culminated in the sublance technology. In the sublance technology the bath carbon is also sampled. The remainder of this chapter is devoted to the dynamic control of the oxygen steelmaking process.

4.3.2 Periodic Measurement of Variables

The sublance technology was first reported by Kern and Stelts^[41] in 1968 and was in commercial operation in 1967^[42]. The development of the sublance system was spurred by the inadequacies of the static charge model and the waste-gas analysis^[41]. This problem was compounded by the high carbon product mix. Table 4.1 summarizes the end-point control for low, medium and high carbon for BOF's at Bethlehem Steel in the second half of 1967. This data indicated the need for improvement in the control of carbon and temperature, especially for high carbon ranges.

Table 4.1 End-Point Control Performance at Bethlehem's BOFs [41].

Aim Carbon	Waste Gas	Reblow	Static Charge
Range	Analysis	Prediction	Model
Low (%C<0.07)	±0.014	±0.015	±0.030
Medium (0.07 <u><</u> %C <u><</u> 0.2)	±0.040	±0.025	±0.080
High (%C <u><</u> 0.2)	N/A	±0.045	±0.200
Temperature All Ranges	± 50°F	± 31°F	± 85°F

The development of the sublance was facilitated by several empirical relationships that adequately described the decarburization and bath temperature change resulting from a reblow. The decarburization relationship were developed by determining the quantity of reblow oxygen required to remove carbon over narrow ranges. Temperature changes resulting from reblowing was expressed as a linear function of oxygen blown. This capability suggested a control scheme based

on knowing the carbon and the temperature near the end of the blow.

To confirm this control scheme, Kern and Stelts performed a follow-up study whereby they compared the reblow-prediction to the static charge model. As shown in Table 4.1, the accuracy of the reblow-prediction was greater, even more so for medium and high carbon grades. The investigators noted that the improvement in accuracy was in large part due to a relatively short reblow period.

Since carbon determination without turning down the vessel was the main problem (sampling of the bath temperature through dispensable thermocouple bombs was available at this time), Kern and Stelts focussed their attention on the development and testing of devices for carbon determination. The devices relied on the liquidus arrest temperature technique; a sample of steel is allowed to solidify in a liquidus cup and as it solidifies the plateau in the temperature-time trace served to indicate the carbon content of the steel sample. It must be noted that the liquidus cup technique was available at that time, however, the general practice was to stop the blow, turn the vessel down and take a deoxidized spoon sample.

Kern and Stelts experimented with a drop-in, expendable device. The problem encountered with the drop-in technique was the short life span of the transmitting wires since a minimum of 25 seconds was needed to obtain the liquidus arrest temperature. 'n all, seven correct readings were recorded in 22 trials. Further attempts to improve the drop-in device were halted because of the success with a

sublance device.

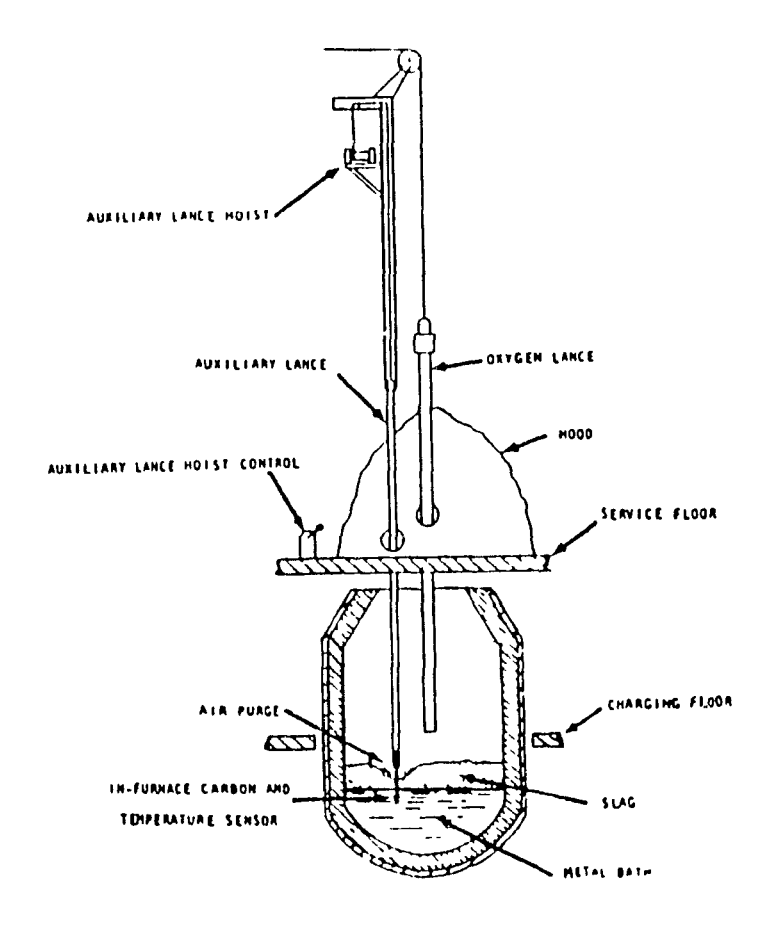


Fig. 4.3 Schematic showing the relative location of the sublance $^{[41]}$.

The sublance system designed by Bethlehem Steel^[43] was water cooled and entered the furnace through a hole in the plate hood approximately 1.68m from the furnace center line (Fig. 4.3). Vertical movement was controlled from a console on the service floor. The initial design of the liquidus carbon sensor proved to be inadequate, most of the devices burned off in the BOF. These problems were eventually overcome; the essential features were (Fig. 4.4) a refractory cup, a thermocouple element to measure the temperature of the solidifying steel sample,

sample inlet ports, a covering to prevent slag entrainment, an aluminum deoxidizer, a thermocouple to measure bath temperature, interconnecting wires and a protective sleeve. The investigators reported a 90% success rate with this sensor lance design.

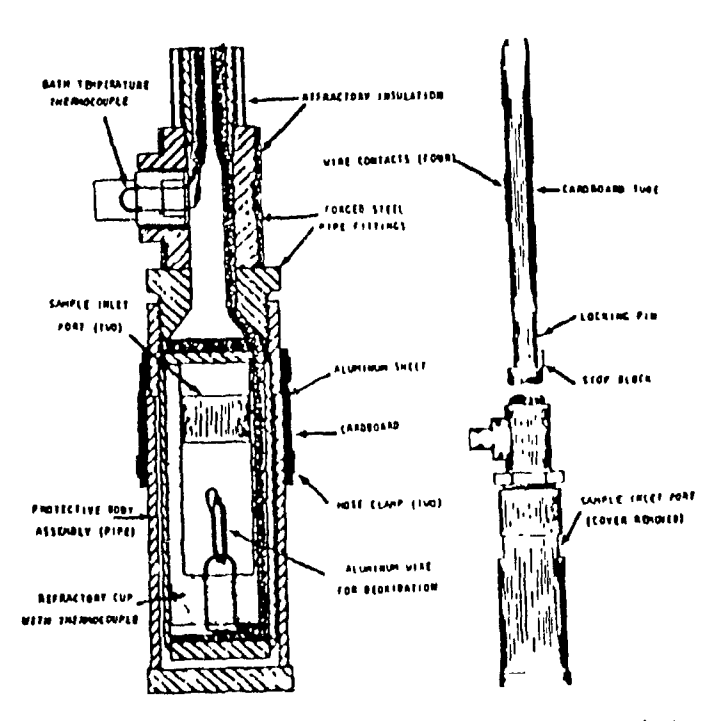


Fig. 4.4 Early design of the sublance probe [41].

The effect of alloy elements in depressing the liquidus curve is well documented^[44]. This effect presented a concern to Kern and Stelts, primarily because the composition of the metal is not known in advance. To overcome this hurdle, the sensor lance was calibrated. Figure 4.5 compares the liquidus temperature to the carbon content obtained from the conventional spoon sample. With this calibration curve, the carbon determined by the liquidus temperature agreed with the actual carbon

within ± 0.04 %C with 95% confidence. Bath temperature measurements with the sublance were within $\pm 14\,^{\circ}$ C with 95% confidence when compared to measurements taken in the conventional manner.

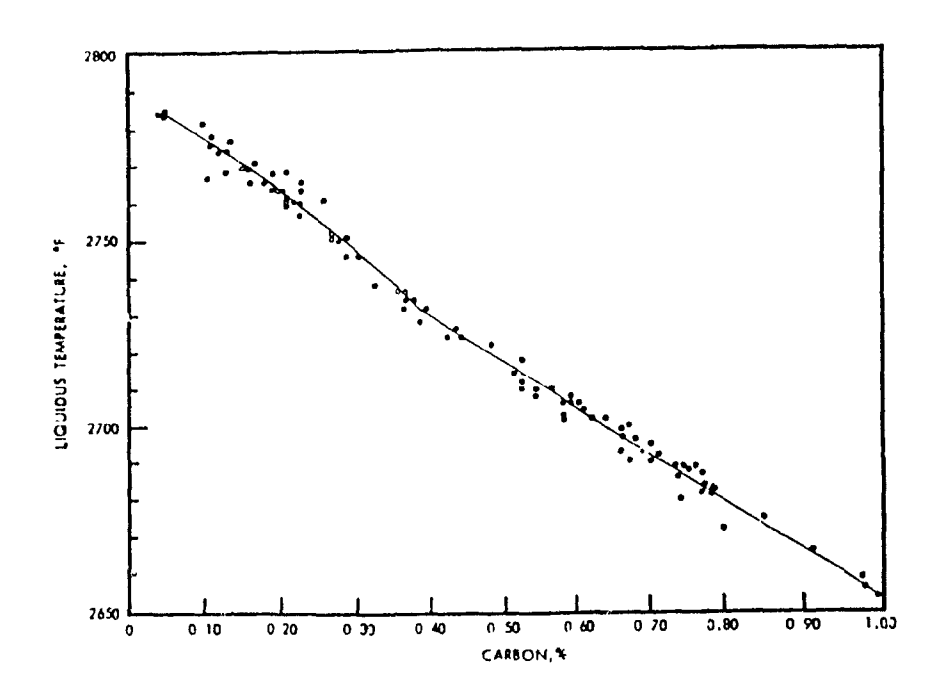


Fig. 4.5 Comparison between liquidus temperature and carbon content $^{(41)}$.

At this stage in the development of the sensor lance, the normal time from oxygen off to oxygen on for a sublance test was less than two minutes. The next step in its development was to integrate it into the process control scheme. Essentially the control procedure developed was identical to the static control model except that the blow was interrupted after 80 to 90 percent of the aim oxygen had been blown. At that time the sublance was lowered into the bath and a carbon and temperature measurement were taken; note that the lance was withdrawn

after a bath temperature measurement was obtained and the liquidus thermal arrest were determined as the lance was withdrawn. The oxygen volume and coolant required to meet the aim carbon and the predicted temperature rise was determined by a series of empirical relationships. The results presented by Kern and Stelts for sublance control indicated that the sublance improved carbon end-point prediction for medium and high carbon steels, Table 4.2, when compared to the static charge model. Although no improvement was seen for low carbon, the application of the sublance was deemed beneficial because sampling time with a sublance was only 20% of the time required for a conventional spoon sample. Temperature end-point control was reported to improve significantly.

Table 4.2 End-Point Control Performance at Bethlehem's BOFs [41].

Aim Carbon Range	Blow Interrupt Prediction	Blow Interrupt Control	Static Charge Model
Low (%C<0.07)	±0.028	±0.031	±0.030
Medium (0.07≤%C≤0.2)	±0.056	±0.059	±0.080
High (%C≥0.2)	±0.78	Insufficient Data	±0.200
Temperature All Ranges	± 50°F	± 35°F	± 85°F

The sublance system has significantly improved since the 1967 trials at Bethlehem Steel. Most importantly is the improvement in

reliability and availability. In fact, several steel producers are claiming >95% availability for in-blow measurements while the oxygen blow is uninterrupted, and an overall availability >97% of the sublance system^[42,45,46,47]. The high availability is due, in large part, to modifications made by numerous vendors and operators of the sublance technology. A noteworthy design improvement is the automatic sublance probe charger designed by Hoogovens^[28]. In addition to the improvements in availability, the accuracy of the sublance system has been improved. Figure 4.6 shows the carbon and temperature error for the Bethlehem and Nippon Steel Corp. sublance systems. The results from the static charge model are included for comparison.

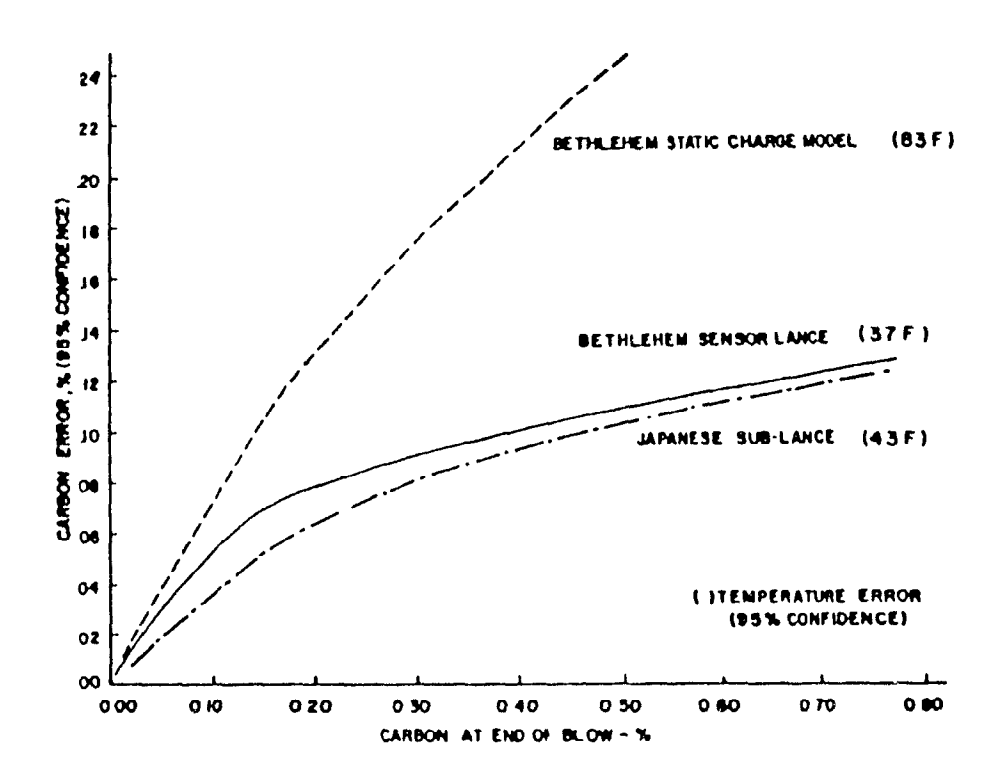


Fig. 4.6 Carbon error as a function of bath $carbon^{(42)}$.

There are two main limitations to the use of sublances for process control, namely the capital costs and engineering difficulties associated with incorporating a sensor lance where the hood was not designed for a third lance (or in the worst case an OBM shop which does not have the overhead space to install one), and process limitations. The main process limitations are erroneous bath carpon and temperature measurements, subsequent errors due to the variation in decarburization rate during the final blowing period, and errors in the temperature attributable to variable rates of temperature rise per increment of lance oxygen.

Erroneous liquidus carbon and temperature measurements have been attributed to slag, oxygen content of the steel, damage due to impact with unmelted scrap, and the manufacturing quality of the probe^[4]. As noted by Kern and Stelts, the end-point control prediction is greatly improved when the bath is sampled with the sublance system closer to the estimated end-point. However, sufficient room must be allowed for the case when the static charge model prediction has gone astray.

Nonetheless, the improvements made to the sublance system have permitted some steelmakers, particularly the Japanese, to obtain substantial gains in productivity and reduce costs. Its implementation world wide is limited primarily by the prohibitive capital costs; a conservative estimate for the installation of the sublance in a three vessel BOF shop is \$15 million (Cdn in 1987). For this reason and the others described above, there has been a move to measurement of the infurnace variables.

4.3.3 Continuous Measurement of Variables

4.3.3.1 Introduction

The development of sensors which continuously monitor the status of the refining process allows, for dynamic control schemes to respond to any deviations from the optimum refining path. Hence, end-point control is improved not only in terms of the end-point, but also from guidance during the entire heat. Invariably, dynamic control systems that employ continuous sensors to guide the refining process respond by modifying the blowing practice, i.e. lance height and oxygen flow rate, or by modifying the slag formation through the addition of fluxes.

The sensors described in this section are most commonly used for blowing/slag formation control and end-point control. However, the characteristics of some of these sensors limit their direct application for end-point control. That is to say, these sensors must be used to control the progress of the heat in order to improve end-point control. The sensors that are described in the following section are:

- •Off-Gas Analysis
- •Fume Temperature
- •Acoustic Analysis
- •Vibrational Analysis

4.3.3.2 Off-Gas Analysis

The earliest application of off-gas analysis was reported by the IRSID organization in $1963^{[37]}$. The technique was based on a dynamic carbon mass balance, as described by Eq. (4.2). As was mentioned earlier, the major drawback to this technique was that the actual carbon content towards the end of the refining process was often less than the total

cumulative errors in the system. For this reason the developers of this control scheme pursued other directions.

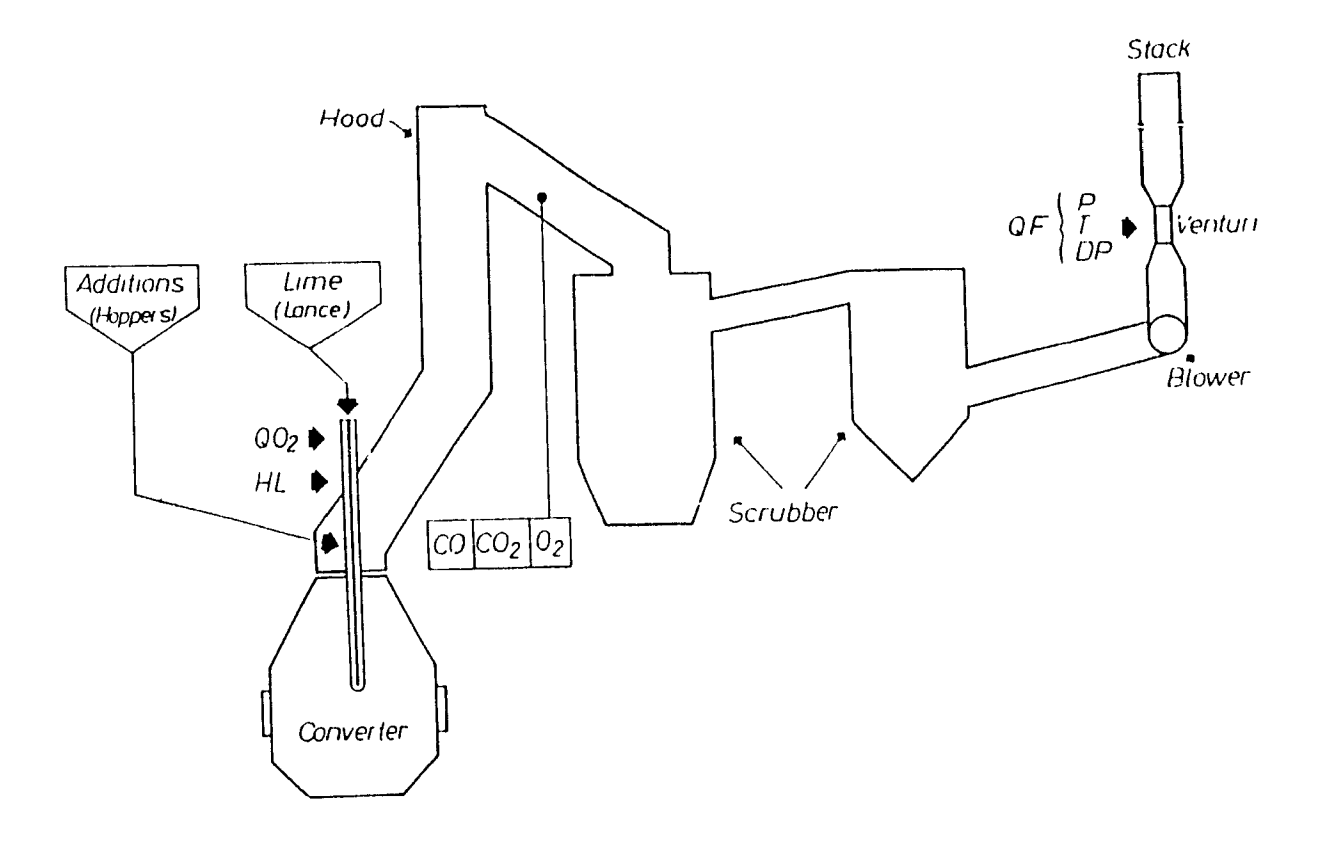


Fig. 4.7 Schematic showing the general arrangement of sensors employed for off-gas analysis at the steel works of Cockerill-Chertal [49].

The major avenue taken to develop an end-point control scheme using off-gas analysis was to characterize the decarburization rate curve. A schematic showing the general arrangement of sensors employed for off-gas analysis at the steel works of Cockerill-Chertal is shown in Fig. 4.7. The flow rate of fumes, QF, is calculated from measurements of differential pressure, DP, absolute pressure, P, and temperature, T, taken at the venturi placed in the stack.

The decarburization rate, $\partial C/\partial t$, is obtained by means of the following relationship:

$$\frac{\partial C}{\partial t} = K \cdot QF \cdot \frac{(CO + CO_2)}{100}$$
 (4.7)

in which: $K = \frac{1}{1.864} [kg C/ Nm^3]$ $QF = Flow rate of fumes [Nm^3/min]$ CO = CO volume in fumes [%] $CO_2 = CO_2 volume in fumes [%]$

A typical decarburization curve determined from off-gas analysis is shown in Fig. 4.8. As the heat progresses, the carbon removal rate increases until it reaches a maximum. Toward the end of the blow, the carbon removal rate decreases and the curve approximates an exponential decay curve. The break point at which the rate of decarburization decreases from its maximum value and after which the curve assumes an exporential decay usually occurs below 0.5% carbon. According to Kern and Stelts, this break-point can vary over a wide range from heat to heat (42). This break point has been the focal point of numerous decarburization models. The most popular decarburization model being the exponential one described earlier in Section 4.3.1.

Kern and Stelts attempted to introduce specifically end-point control, without controlling the refining process during the main part of the blow, at Bethlehem Steel^[42]. They employed the off-gas analysis to detect the break-point carbon and predicted end-point carbon with the exponential model. The results obtained are summarized in Table 4.1. Unfortunately, a significant quantity of steel produced was high

carbon, greater than the break-point carbon, and, therefore, the control scheme utilizing the off-gas was not applicable.

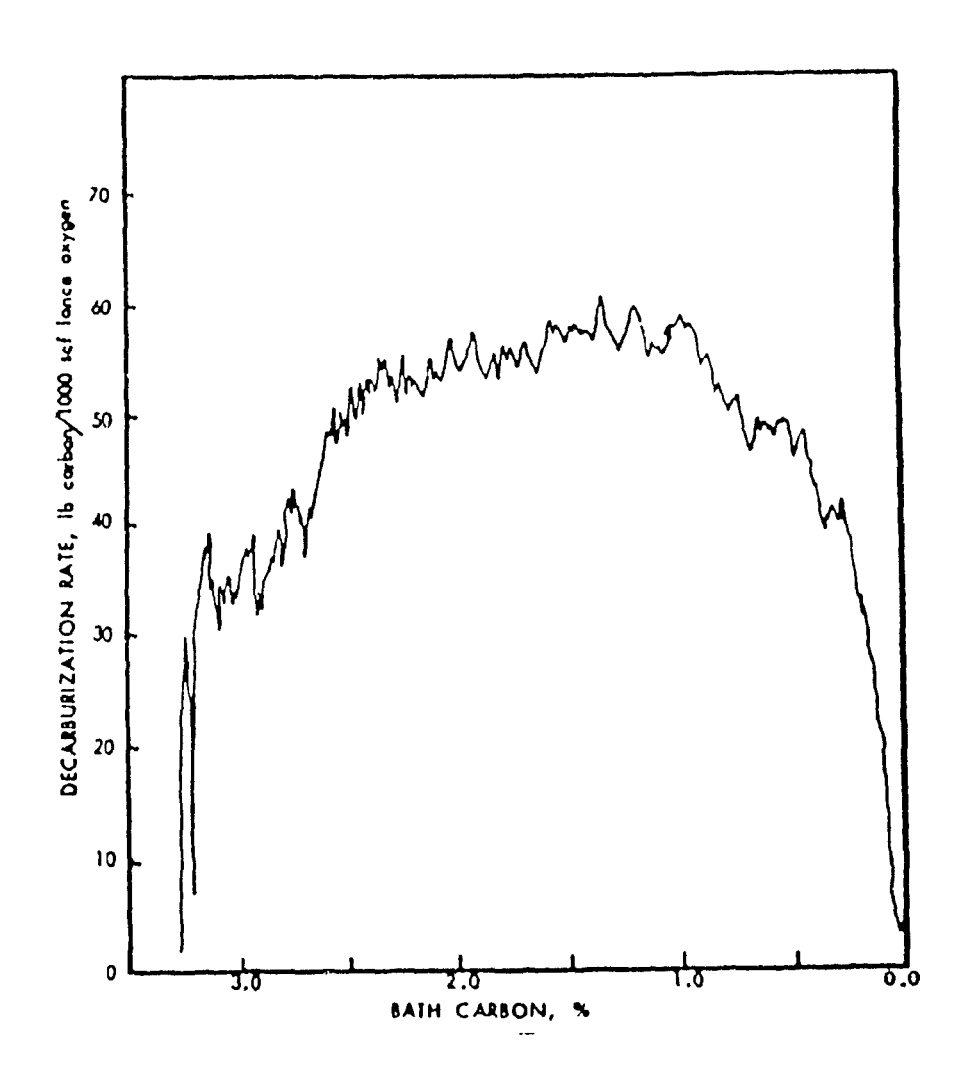


Fig. 4.8 Typical decarburization ${\bf rate}$ curve from waste gas analysis ${}^{[42]}$.

A noteworthy application of the off-gas analysis system to control the refining process, was reported by Anderson et al^[50]. In this application the decarburization rate, determined with the aid of the off-gas analysis system, is used to calculate a continuous oxygen balance in the vessel. From this balance, Anderson was able to show the oxygen partition, and decarburization pattern for various lance practices, as shown in Fig. 4.9. The aim of the control scheme was to control the decarburization rate, which would be critical in the first 40% of the blow, solely via the lance height.

The results of implementing the off-gas analyzer and other process control equipment, such as the sonic meter (to be discussed later), weighing systems for materials, computer and communication systems are summarized in Fig. 4.10. Significant improvements in yield, lance life and vessel lining life have been obtained by this technique.

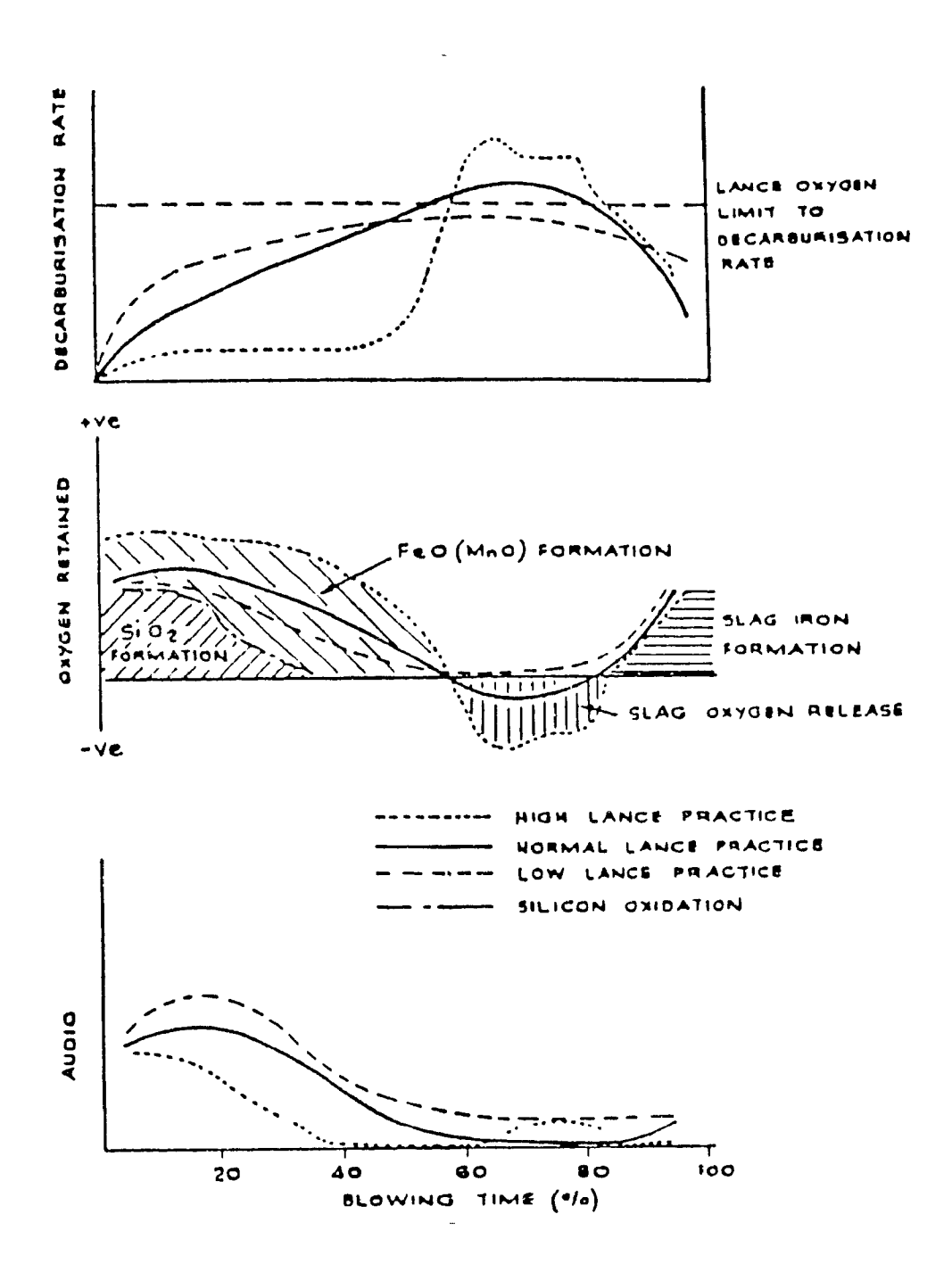


Fig. 4.9 Oxygen distribution principles as determined by off-gas analysis [50].

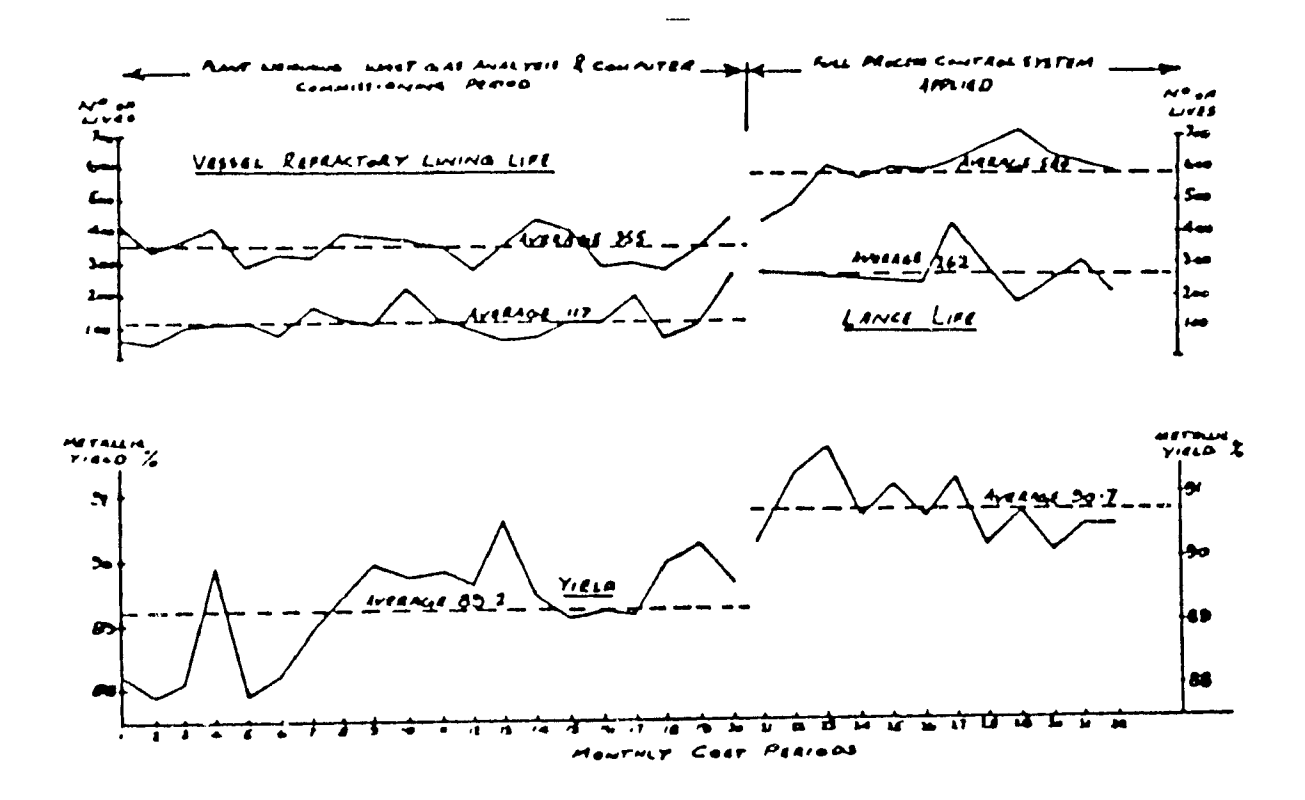


Fig. 4.10 Effect of full process control on liquid steel yield, vessel refractory life, and oxygen lance life^[50].

4.3.3.3 Fume Temperature

The applications of fume temperature measurements as a dynamic control sensor have been documented by numerous investigators [51,52,53]. Different methods are employed for the measurement of the fume temperature, in most cases thermocouples are considered adequate. For the specific application of BOF control, the aim is to obtain a reliable and reproducible measurement. Accuracy of the measurement is of a lesser concern.

The choice of the optimum measuring point is a critical problem. To minimize the time lag, the measurement must be performed as near as possible to the vessel mouth. On the other hand, a good agreement between the temperature and decarburization rate is only obtained if CO combustion is complete. It is also necessary to maintain the thermocouple relatively free of dust.

An excellent correlation between the gas temperature and the decarburization rate calculated from the off-gas analyzer appears in Fig. 4.11 for a 170 ton vessel, note the time lag of 15 seconds between the two measurements. The short response time of the fume temperature signal makes it an ideal dynamic control sensor. The fume temperature is used to control the initial rate of decarburization; the control scheme imposes on the oxygen flow rate a value such that the fume temperature will follow a linear increase of predetermined slope α , shown in Fig. 4.12. The slope has been chosen in order to allow continuous lime dissolution without exaggerated slag oxidation. When the maximum desired decarburization rate has been reached, the

controller maintains a constant value until 85% of the total oxygen has been blown. From that moment the oxygen flow rate remains constant until the end of the blow. The results obtained by the CRM model are shown in Table 4.4.

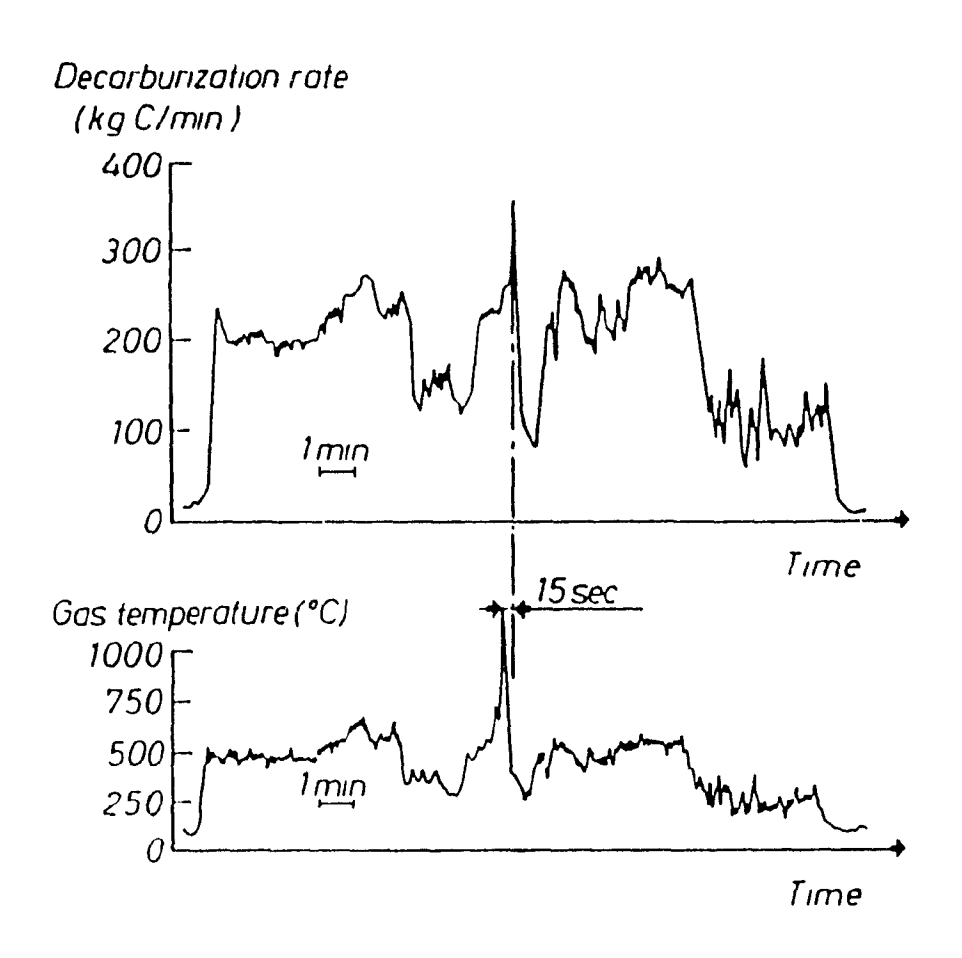


Fig. 4.11 Evolution of the off-gas temperature and of the decarburization rate as determined from off-gas analyzers $^{\{53\}}$.

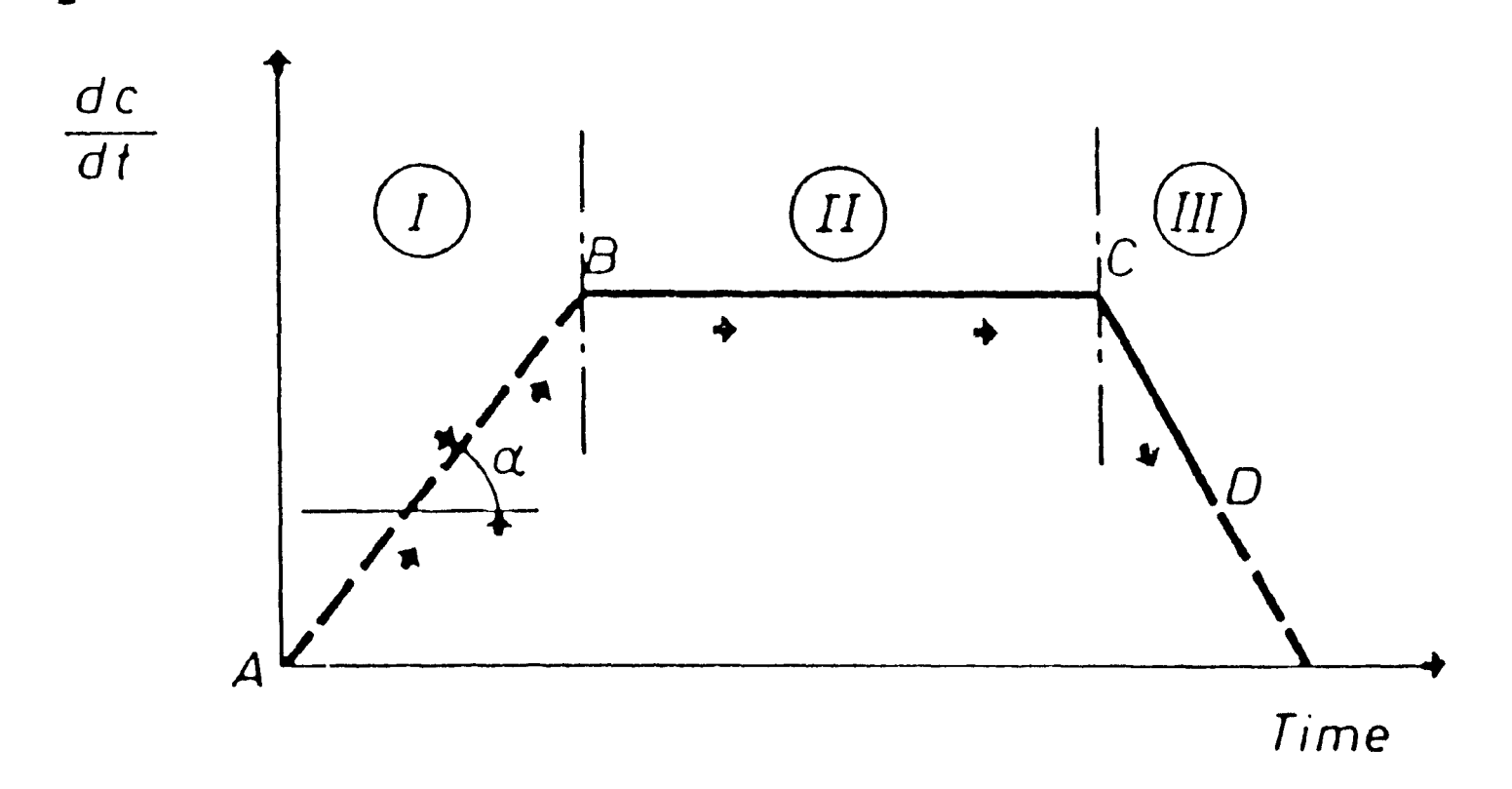


Fig. 4.12 Decarburization model showing the trajectory of the rate of decarburization^[53].

Table 4.3 End-Point Control Results for Static Charge Model and a Dynamic Control Scheme Using Fume Temperature Measurements[53].

Control Scheme	Turndown Temperature	End-Point Carbon 10 ⁻³ &C
Static	± 15.5	± 22.9
Dynamic	± 12.8	± 14.5

Acoustic analysis of the sounds emitted from the BOF is not a novel concept. Early in the development of the BOF process, operators frequently determined the carbo break-point by noting a discernible decrease in the noise leve manating from the vessel. Furthermore, Klarding analyzed the moise originating from within a Bessemer converter in 1950⁽⁵⁴⁾ Although he obtained interesting results, the subject was not pursued. CRM has worked extensively on noise measurement to control the trajectory of the decarburization rate^{(5),50}. This effort has culminated in the patenting and world wide sales of the Sonic Meter. The success of the sonic meter as a BOF control sensor is clearly indicated by its acceptance in numerous steel plants.

The sonic meter consists of three distinct elements: a water cooled probe, a condenser microphone of a cylindrical shape that is fitted into the probe, and an electronic unit for amplification, filtering and recording of the sound intensity in the selected frequency band. The distance between the microphone and the electronics can be as long as 120m, hence, the unit can be located in a clean room. Positioning of the water cooled probe depends on the dust loading in the clearance between the hood and the vessel. Figure 4.13 presents the positions previously tested in different steel shops; position two is preferred because of reduced maintenance and health risks.

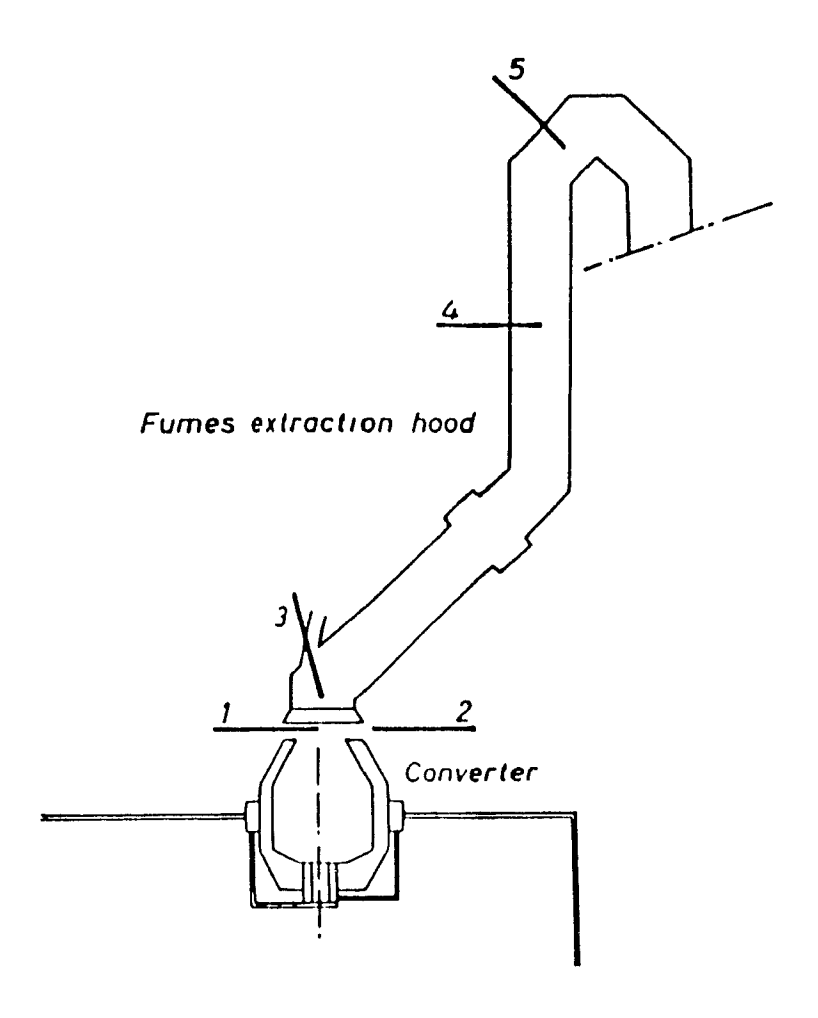


Fig. 4.13 Previous testing locations of the sonic meter $^{[52]}$.

Frequency analysis of the noise was performed to determine the appropriate frequencies to consider. Figures 4.14 and 4.15 show the frequency spectra in a relative amplitude scale during the refining process. Curve a in Fig. 4.14 is representative of the beginning of the blow (no foam present) whereas curve b belongs to a foaming period during the same heat. Nilles and Holper^[53] reported that these spectra show very clearly the foam modulation effect between 100 and 250 Hz. Frequency analysis also permitted the investigators to detect and, later, filter out the effect of other contributions to the spectrum.

For example, consider curve **c** in **Fig.** 4.15, note the peak at $\approx 400 \, \text{Hz}$ that was attributed to an engine. In the low frequency range (<100Hz), Ramelot and Claes^[55] have qualitatively linked the evolution of sound to the rate of decarburization. The relationship can be expressed as:

Sound Intensity =
$$A \cdot QCO + B \cdot QCO_2$$
 (4.8)

where A and B are constants and QCO and QCO₂ are the CO and CO₂ evolution rates, respectively. The first term represents a source of sound linked to the rate of CO evolution. While the second term represents the combustion of CO gas in the vessel. In normal practice, the investigators claim that the latter term is relatively weak.

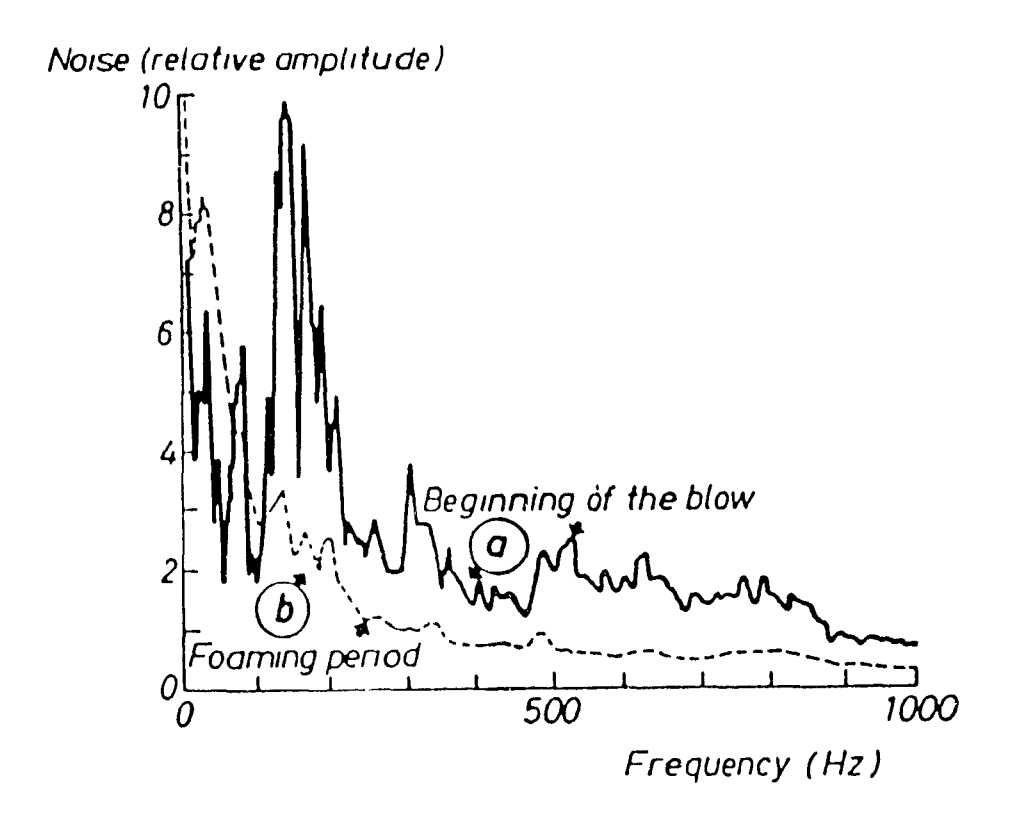


Fig. 4.14 Noise spectra at two different moments during the blow [55].

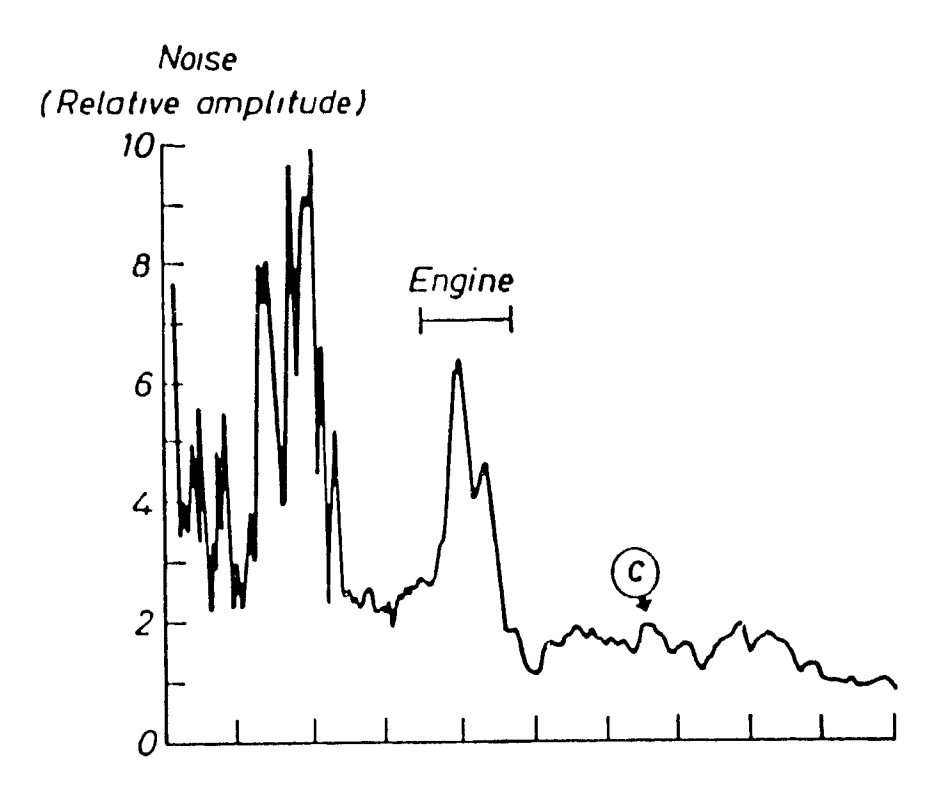


Fig. 4.15 Appearance of background noises in the spectra during the $blow^{\{55\}}$.

Additions made during the blow (in particular iron ore and lime) generally create a significant modification in the intensity of the sound. The magnitude of the modification is directly related to the effect of the addition on the decarburization rate. In a similar manner, changes in the blowing practice, such as lance height and oxygen flow rate, greatly modify the sound emissions during the blow. A typical sound intensity-time trace for a 150-tonne OBM steelmaking vessel at Forges de Thy-Marcinelle et Monceau^[56] is shown in Fig. 4.16.

4

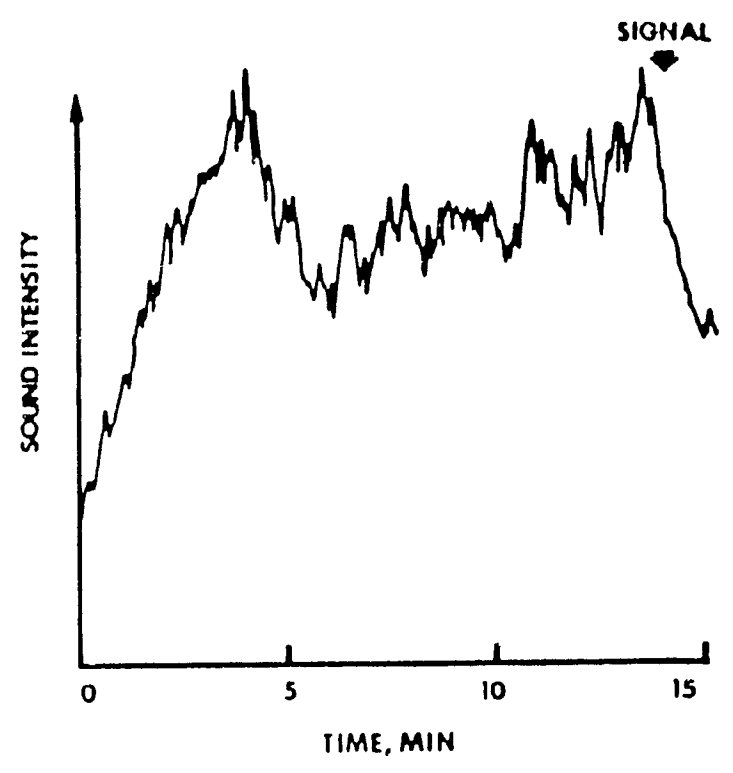


Fig. 4.16 Sound intensity-time trace during a typical blow [56].

4.3.3.5 Vibrational Analysis

One of the earliest reports on vibrational analysis of a steelmaking vessel was presented by Bardnheuer and Oberhäuser⁽⁵⁷¹⁾. The vibration analysis was also done in conjunction with acoustic analysis on a 40 tonne LD-AC vessel. The vibration sensor was a piezoelectric accelerometer that had a maximum operating temperature of 400°C, however, actual operating temperatures rarely exceeded 260°C. The accelerometer was attached onto the trunnion ring as shown in Fig. 4.17, both horizontal and vertical vibrations were tested. The results indicated that the horizontal component of the vibration was not of interest. Hence, their vibration analysis concentrated on the vertical component. The vibrational frequency band that was found to be of interest ranged from 1080-1100 Hz. Figures 4.18 and 4.19 show the

relative intensity of the frequencies 1080Hz and 1100Hz, respectively. In addition to the vibration intensity, lance height is also shown. As can be seen there is a qualitative correlation between the vibration intensity and the lance height, albeit weak. For unknown reasons, the investigators did not continue to develop either the vibrational or acoustical analysis.

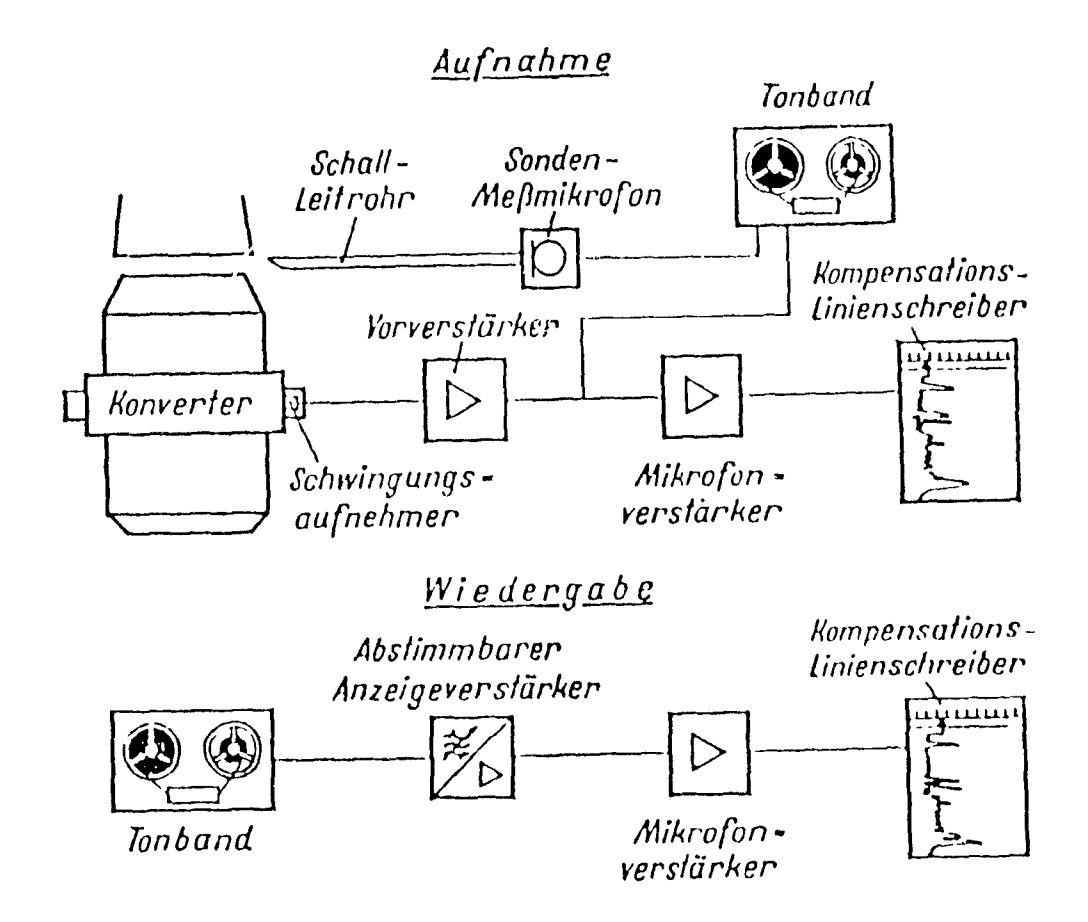


Fig. 4.17 Schematic showing the vibration analysis system attached to a BOF vessel $^{[57]}$.

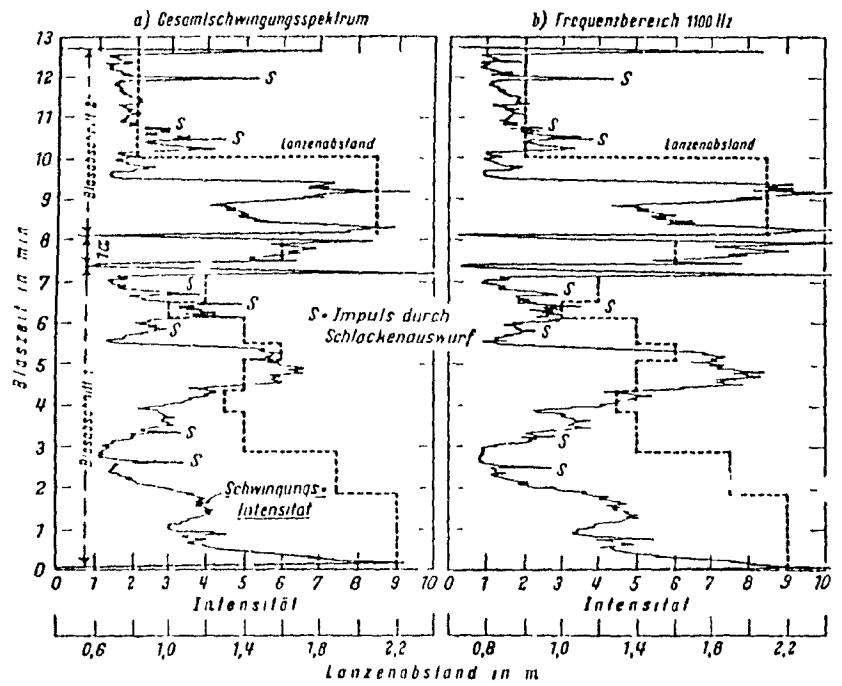


Fig. 4.18 Vertical vibrations of a 40 tonne BOF, showing both the overall vibration intensity and the intensity of the 1100 Hz frequency^[57].

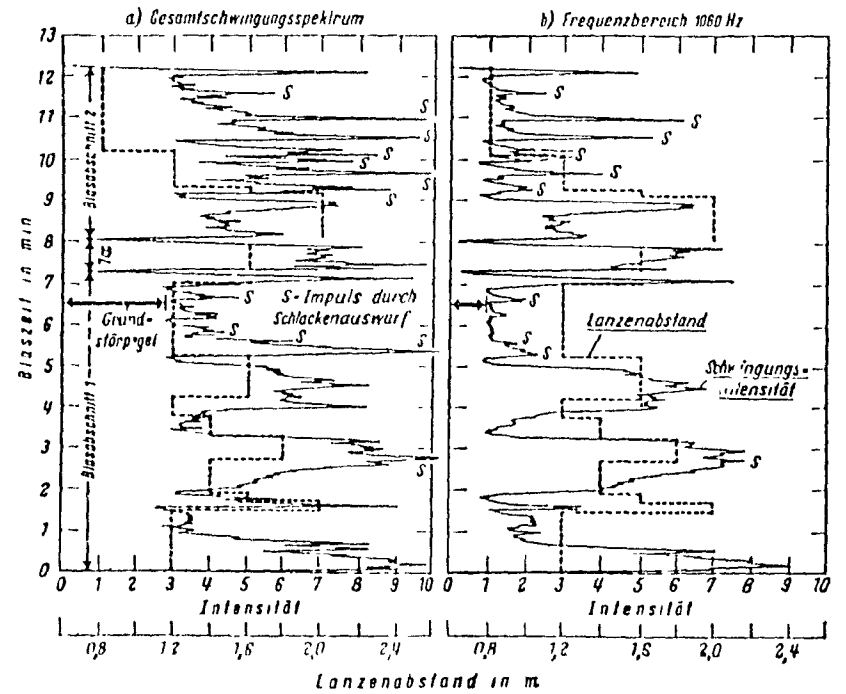


Fig. 4.19 Vertical vibrations of a 40 tonne BOF, showing both the overall vibration intensity and the intensity of the 1080 Hz frequency^[57].

Grenfell et al⁽⁵⁸⁾ reported on the application of continuous vessel weighing in 1977. Although this application was not, at first, directly related to vibrational analysis, the results obtained during their investigation are worthwhile reporting here. Grenfell reported that BSC had attempted continuous vessel weighing as early as 1970 at BSC's Llanwern plant.

In response to the success at Llanwern, FSC had decided to install continuous vessel weighing at Ravenscraig during the installation a new No. 3 BOF shop. As a result of the experience gained at Llanwern, only four weighing transducers were required per pedestal. Aside from rome initial problems associated with the driving mechanisms, BSC obtained a good standard of static weighbridge accuracy. This, Grenfell noted, was not to be considered as a replacement for similar weighing systems used at the hot metal and scrap preparation stations, but as a double check. The double check serves two purposes; the first purpose is to correct the inputs in the static charge model and, secondly, to avoid posteriori adjustments that are based on incorrect charge inputs.

The vessel weighing equipment generated three dynamic traces during a BOF blow; an in-blow weigh change trace, a rate of weight change trace and an activity trace (Fig. 4.20). The activity trace was described by Grenfell as a measure of the vessel vibration and the kinetic energy dissipated by the CO gas as it passes through the slag layer. The general shape of the activity trace closely follows that of the rate of decarburization. Through experience, the BSC operators

were able to characterize the heat in progress and, if required, take appropriate action.

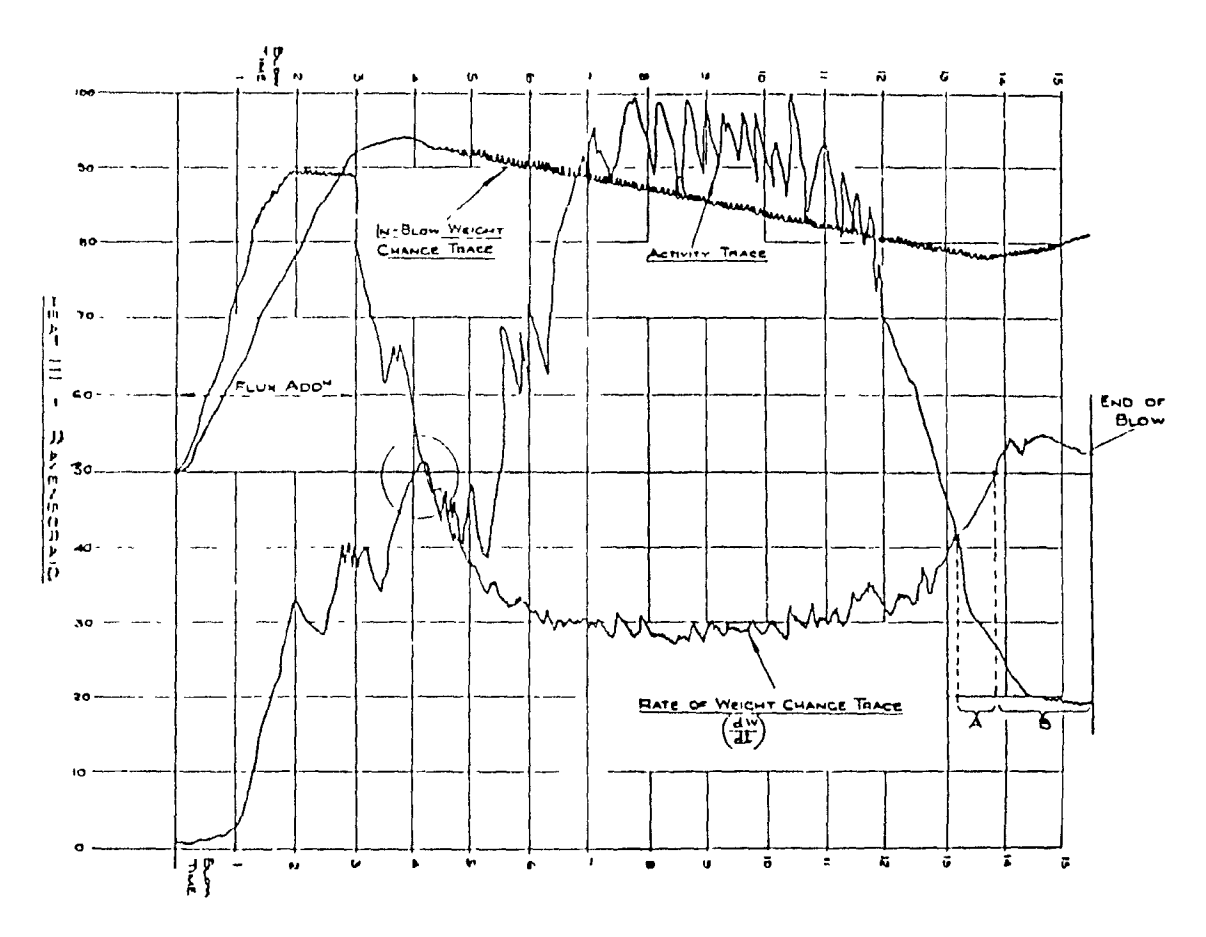


Fig. 4.20 Dynamic traces generated by the continuous weighing system $^{(58)}$.

In addition to blowing control, the activity trace was used to provide an indication of the end-point carbon. The technique was based on the fact that the vessel vibrations were directly related to the quantity of CO gas evolved. Furthermore, Grenfell states that the vibrations have been characterized as low frequency and exist within a narrow range. The BSC carbon end-point control scheme correlated the

i L

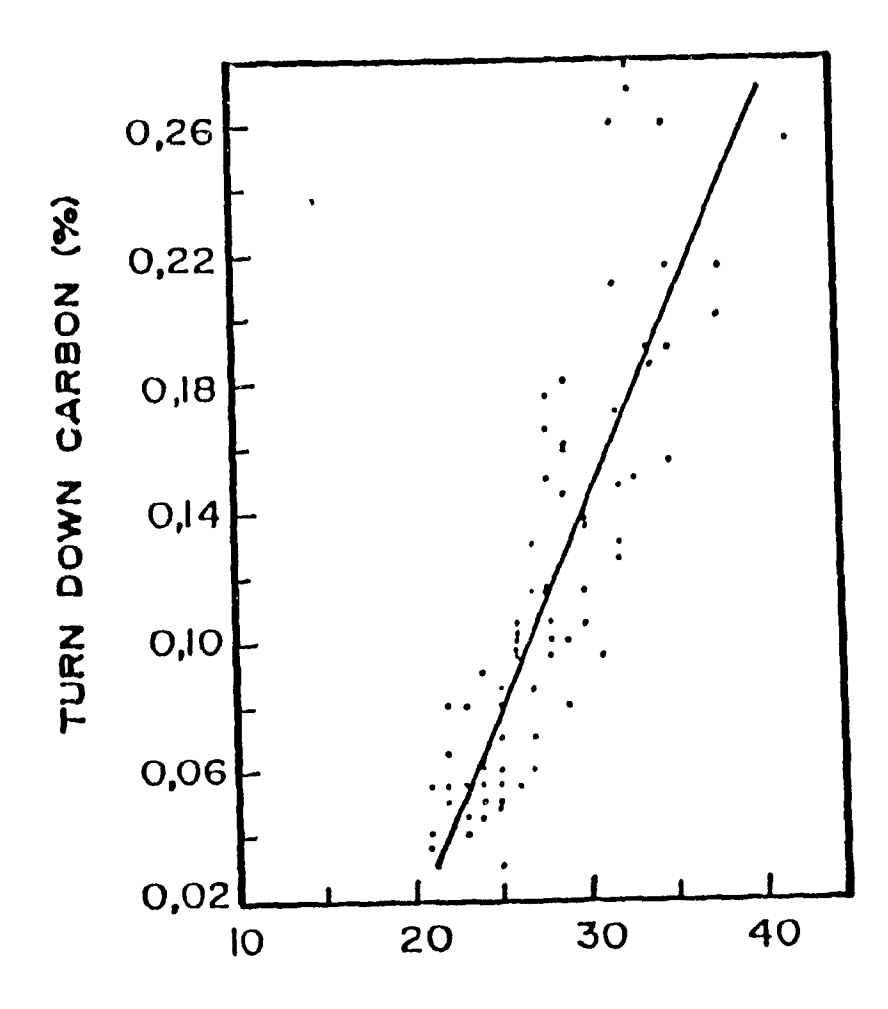


Fig. 4.21 Relationship between turndown carbon and turndown activity $^{[58]}$.

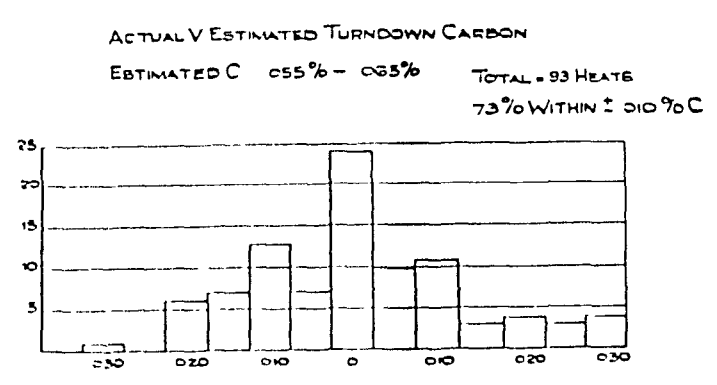


Fig. 4.22 Histograms showing predictive turndown carbon performance of vessel weighing equipment^[58].

CRM has investigated the application of accelerometers to monitor vessel vibrations during OBM and BOF steelmaking^[59,60]. Although their investigations were not exhaustive, several interesting outcomes were presented. First, an excellent correlation was claimed between the vibration intensity of the vessel and the intensity of the noise emitted from the process. This may explain why the vibrational analysis did not receive as much attention. However, in the more recent reference of Jacobs et al^[60], it was suggested that its application may be more appropriate with steelmaking operations that have an extremely quiet process. In this case, Jacobs et al report that the application of the accelerometer to monitor the vibrations of

the oxygen lance is more appropriate.

This application of the accelerometer was pioneered by Kawasaki Steel^[61,62]. The principle of lance vibration is based on the transfer of kinetic energy from the slag to the lance due to foaming. It was found that the foaming slag height can be estimated from the magnitude of the vibration. Figure 4.23 shows the schematics of the lance vibration monitor. The lance, suspended with wires, could be displaced by the metal/slag emulsion that moved around in the vessel. Since the natural frequency of the lance itself is low, a piezoelectric accelerometer was selected. Since the direction of the vibration is not constant during the blow, two accelerometers were arranged at right angles to each other and the composite acceleration was calculated.

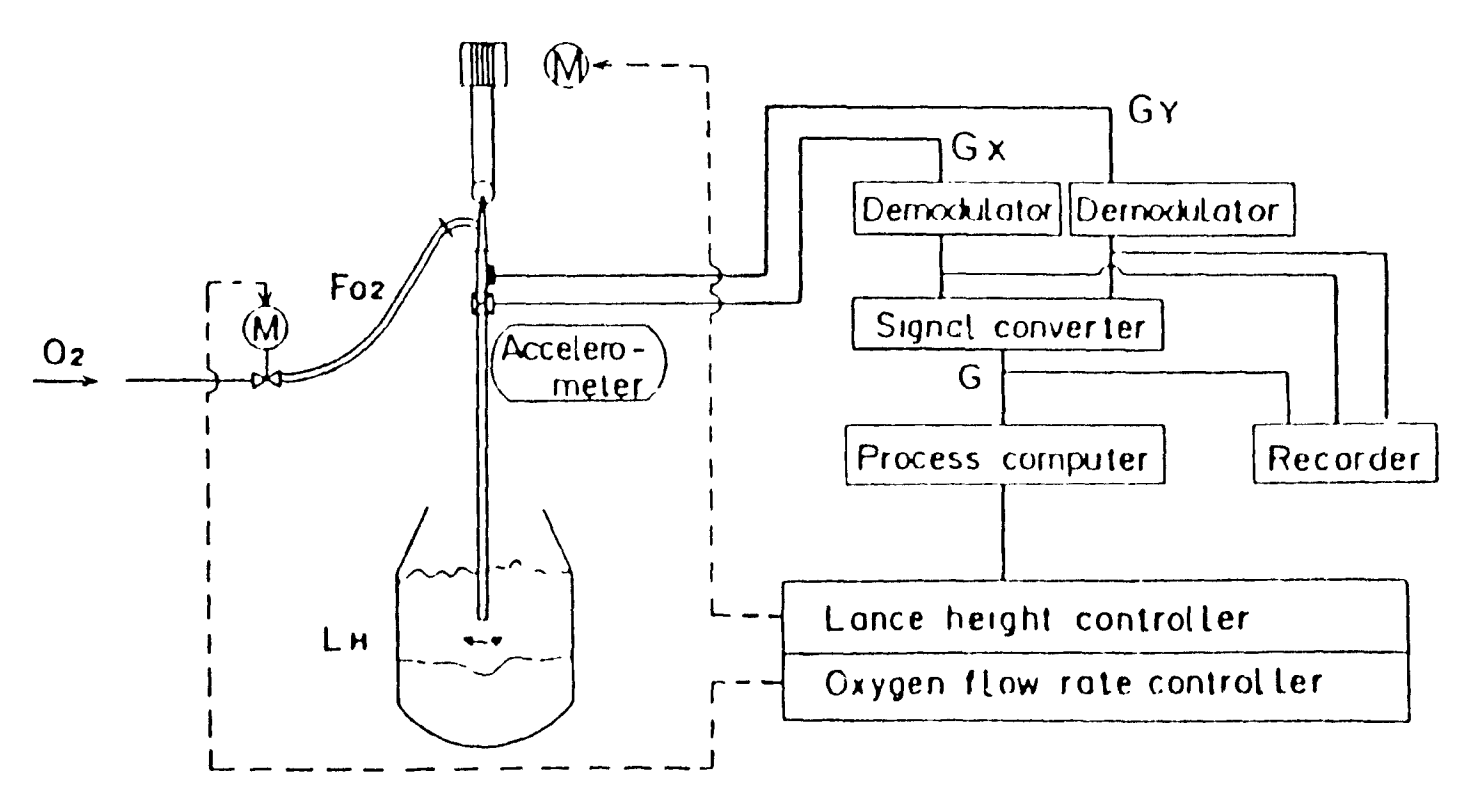


Fig. 4.23 Schematic showing the application of two accelerometers for slag formation control on a 250 tonne BOF^[61].

Frequency analysis determined that the peak value is observed near the natural frequency of the lance, at 0.39Hz, and that the spectral intensity at any frequency increases with increasing foaming slag height, Fig. 4.24. Iida et al^[62] were able to correlate the intensity of the vibrations to the oxygen flow rate and lance height Fig. 4.25(a). The relationship can be expressed as:

$$G = a F_0$$
 $(S_h - L_h) + b$ (4.9)

where: G = acceleration of lance vibration [cm/s²]

 $C_{op} = \text{oxygen flow rate } [\text{Nm}^3/\text{min}]$

 S_h = foamy slag height [m]

L_h = lance height over the bath [m]

a&b = constants.

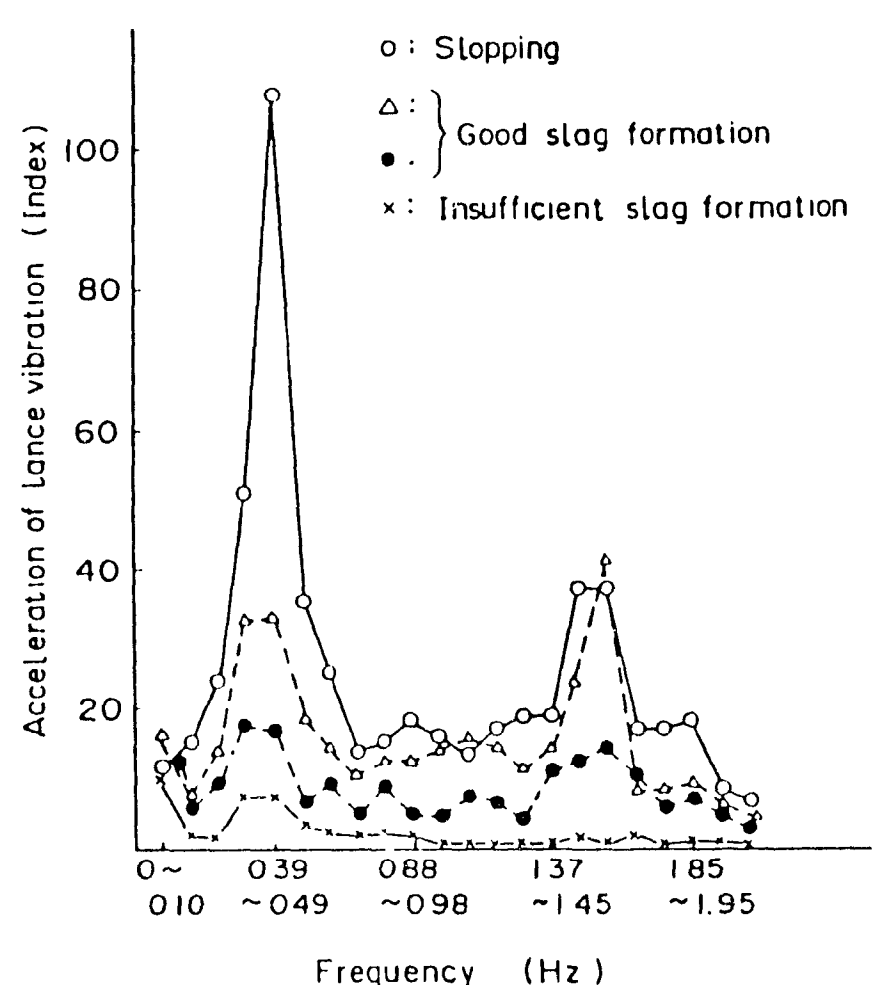


Fig. 4.24 Frequency spectrum of the composite lance vibration[62].

The validity of Eq(4.9) was verified on a $^1/_{10}$ water model of a 250 tonne vessel. Air was injected through a lance, with four holes, onto water containing foaming and viscosity agents. The results of the water model agreed closely with Eq(4.8), as can be seen in Fig. 4.25(b). To calculate the slag height in the actual vessel, Iida et al transformed Eq(4.9) and added an additional term, B_h , to account for changes in the vessel bottom:

$$S_h = \frac{G - b}{a \cdot F_{02}} + L_h + B_h$$
 (4.10)

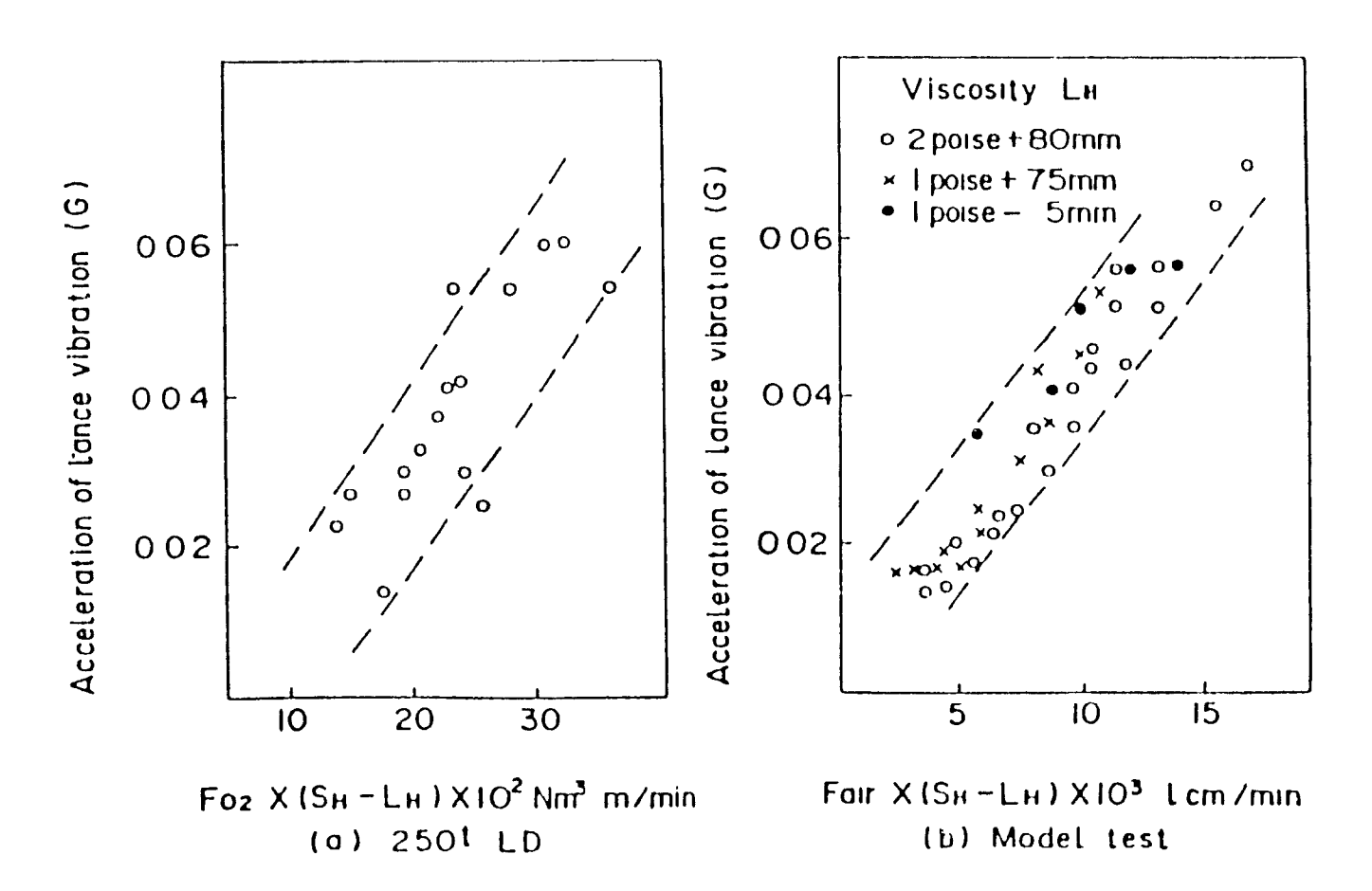


Fig. 4.25 Relation between acceleration of lance vibration and foaming slag height $^{[62]}$.

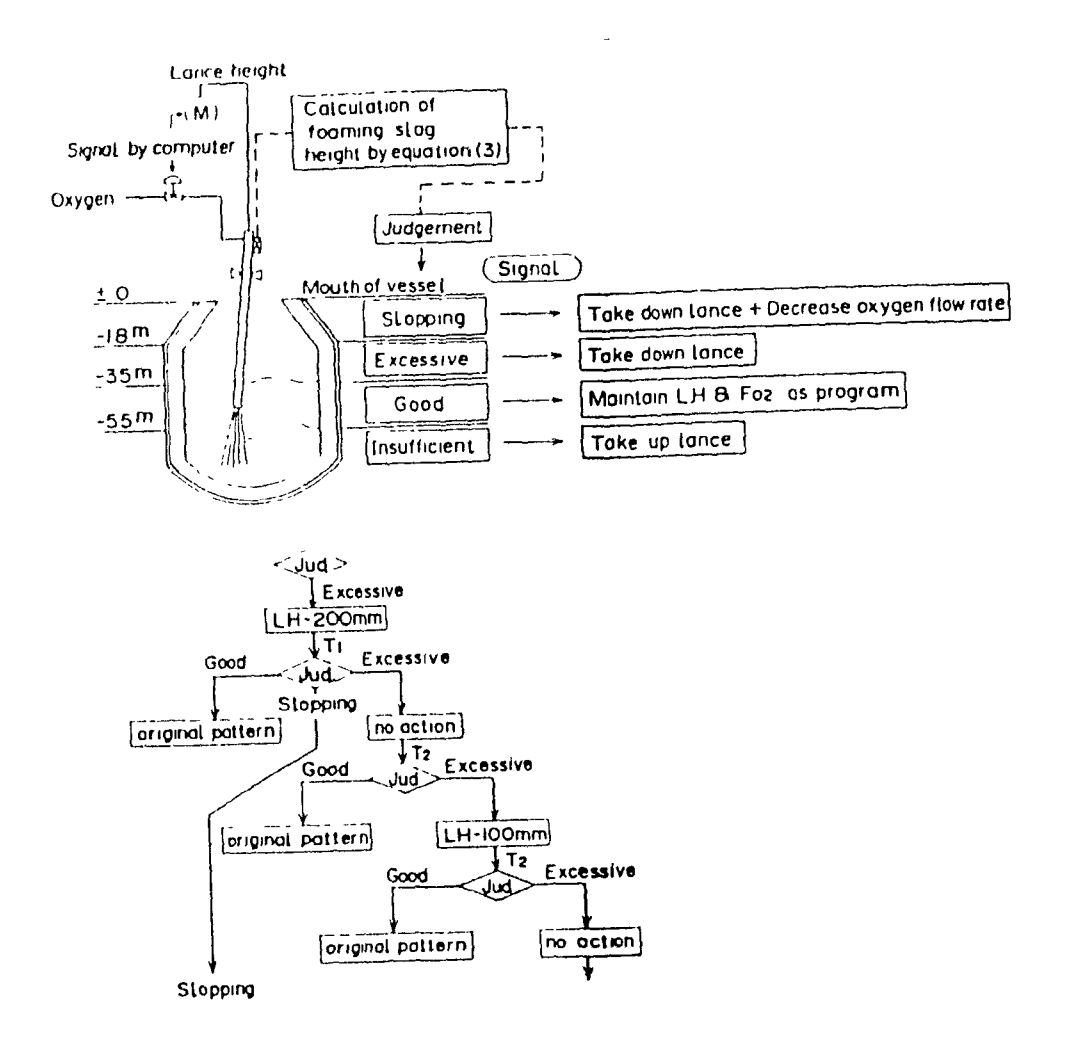


Fig. 4.26 Concept of the slag formation control scheme [62].

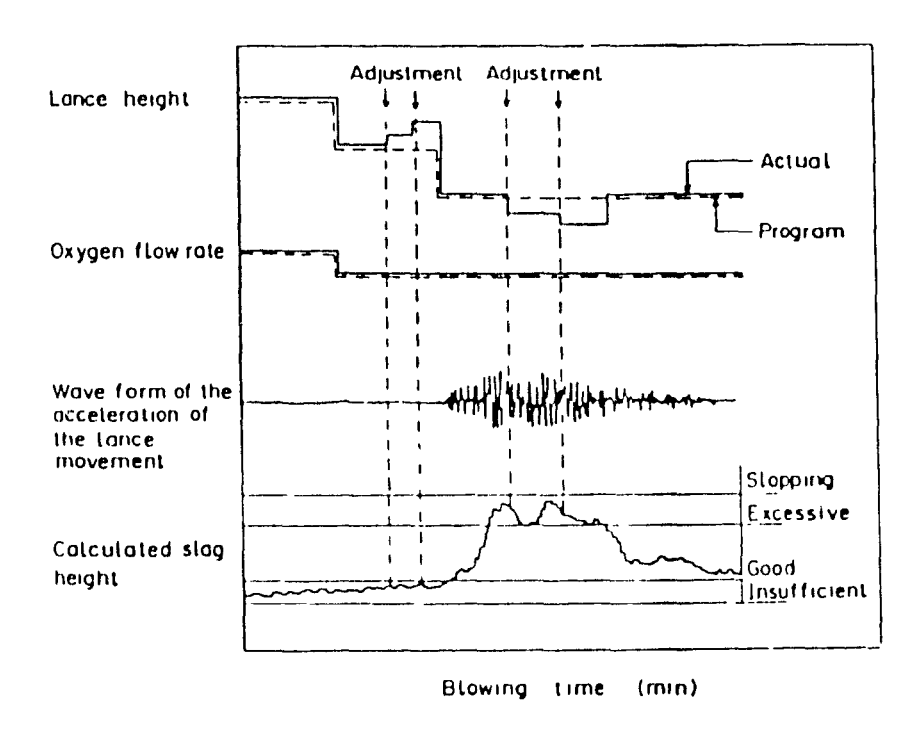


Fig. 4.27 Example of automatic blowing control^[67].

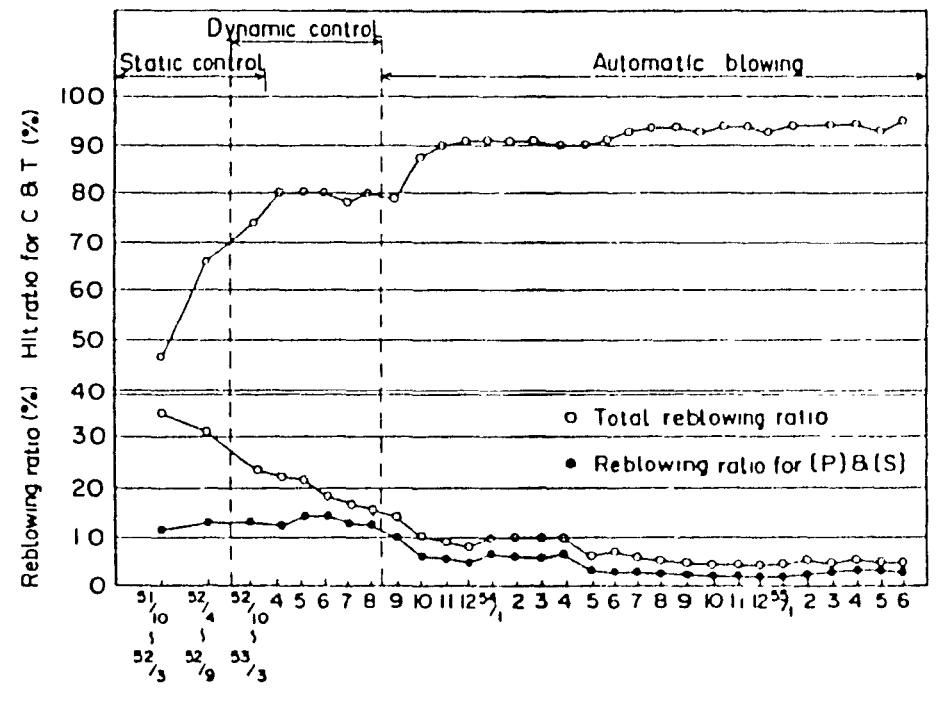


Fig. 4.28 Improvement of blowing results at Kawasaki's Mizushima No.2 $\mathrm{BOF}^{\{62\}}$.

Kawasaki Steel also applied the accelerometer to measure furnace vibrations⁽⁶³⁾. Although Ohnishi et al⁽⁶³⁾ did not directly describe the application with any great detail, they did present some remarkable results using the accelerometer to control slag formation. Specifically, Ohnishi et al described a blow-end phosphorous control and estimation technique that employed primarily the accelerometer. They were able to correlate a specific characteristic of the furnace vibration during blowing to the blow-end phosphorous content in the K-BOP.

The furnace vibrations encountered during the blow were measured in the axial direct on of the trunnions, as shown in Fig. 4.29. The specific characteristic of the vibration signal, denoted as Δt , was defined as the difference between the time at the end of the blow and the time at which the vibration signal falls below a specific value, denoted as d_{mm} , in the later half of the blow. A good correlation was obtained between Δt and the blow-end phosphorous, as shown in Fig. 4.30. In addition to blow-end phosphorous, Ohnishi et al also reported an excellent correlation between Δt and the total iron in the slag, (T.Fe), which itself was correlated to the oxygen content in the steel at blow-end (Fig. 4.31).

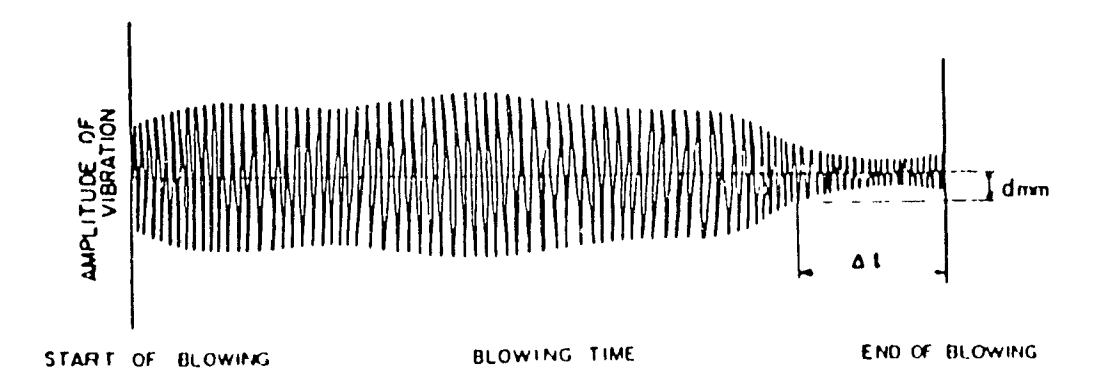
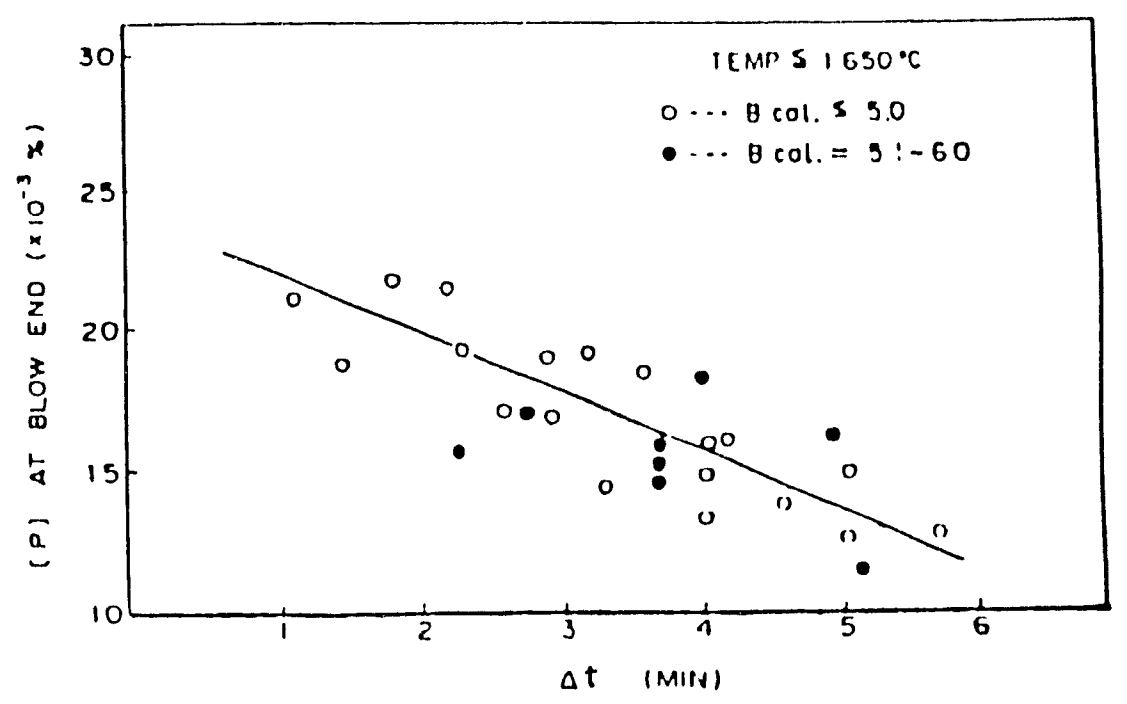


Fig. 4.29 Change of the vibrations of a K-BOP furnace during the refining period $^{[63]}$.



 $\Delta^{\mbox{\it l}}$. Blowing time in which the amplitude of vibration falls under d mm

Fig. 4.30 Relation between Λ^{+} and [P] at blow-end^[63].

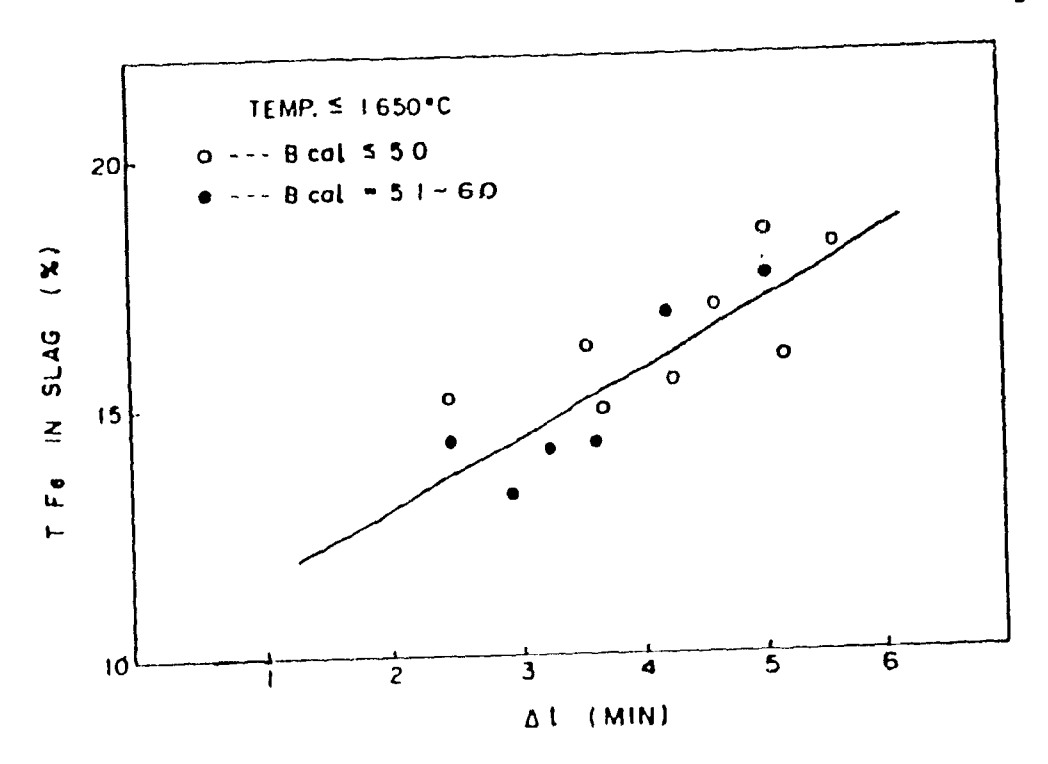


Fig. 4.31 Relation between Δt and (T.Fe) in slag^[63].

Given the degree to which Ohnishi et al was able to correlate blow-end phosphorous, (T.Fe) and, indirectly, the oxygen content of the steel at end-point, the author of this thesis proposes that Ohnishi was able to directly correlate Δt to the end-point carbon, at least for low carbon steels. The reason being that at low carbon contents the steel approaches the C-O equilibrium curve.

5. Application of the Accelerometer in Metallurgy

5.1 Introduction

The accelerometer has seen limited use in metallurgical industries. The major application to date has been in predictive and trouble shooting maintenance on plant machinery and, more specifically, has become an indispensable tool for the maintenance of rotating equipment such as motors, pumps, fans, and cable windings. Its application is based on the presumption that a system functioning properly will vibrate differently than one experiencing such problems as alignment, bearing wear, et cetera.

The application of the accelerometer is further advanced as a preventative and trouble-shooting maintenance tool by the analysis of its signal. The analysis of the signal is often considered as the fingerprint of the problem. Plant maintenance personnel match the fingerprint of the troubled machine with a series of prints that exemplify a particular problem.

The implications of such a maintenance tool are enormous when one compares the relative cost of replacing a critical fan, and subsequently stopping production, and changing its bearings or performing a major alignment during a scheduled production stop. For example, if a steelmaking plant produced 150 tons/hour at an average sale price of \$575./ton, the loss of revenue would be \$86,250./hour. The relative cost of preventative maintenance and/or trouble shooting would be the accelerometer and ancillary equipment (say \$25,000. capital cost) depreciated over its life, plus the salary of the

maintenance personnel (say \$25./hour).

The accelerometer signal is often scanned and analyzed for a reproducible anomally that indirectly describes the state of the process. This is quite different from other sensors where an exact magnitude is desired, such as temperature. In this chapter several applications of the accelerometer in the steel industry are presented to the reader to provide insight into the usefulness of the accelerometer. The format of the descriptions is presented below. First, purely mechanical applications are presented followed by several applications which involve the mixing of solid-liquid-gas phases in metallurgical vessels. The specific application of the accelerometer as a BOF end point control sensor is not described in this chapter, but is included in the chapter devoted to BOF process control (Chapter 4). Finally, to conclude this chapter an application of the accelerometer in continuous casting is described. This application is both mechanical and metallurgical in nature, providing a natural conclusion to this chapter.

- Mechanical Applications preventative maintenance down coilers
- Multi-Phase Mixing Applications rimming steels ladle stirring wire feeding slag detection

5.2 Mechanical Applications

5.2.1 Predictive Maintenance Programmes

Maintenance of an integrated steel plant can cost approximately 10 to 15% of the total net sales. The cost, or budget, for plant maintenance can easily approach one billion for repairs and maintenance on existing facilities. Maintenance practices in the steel industry can be classified into three categories: breakdown, preventative maintenance, and predictive maintenance.

Breakdown maintenance, in general, is the need to perform repairs on damaged equipment, it can be considered as event-based. In its worst case, the damaged equipment has failed catastrophically and the production line must shut down. In these circumstances, the true cost is not just the repair, but also the cost associated with the loss of business. As a result it is considered the least desirable of the three maintenance categories.

Preventative maintenance is line-based; inspections or repairs are performed or adjustments and parts are changed on a regular basis. In some cases machines are even dismantled and inspected at an appropriate time. In other cases, parts are changed after a specific period of time, regardless of their condition. The objective of preventative maintenance is to avoid the occurrence of a breakdown. The main disadvantage is that equipment can be dismantled unnecessarily when there is nothing wrong, or worse, fail soon after as a result of poor workmanship during reassembly. In addition, parts can be replaced long before their serviceable life ends, thus unnecessarily increasing

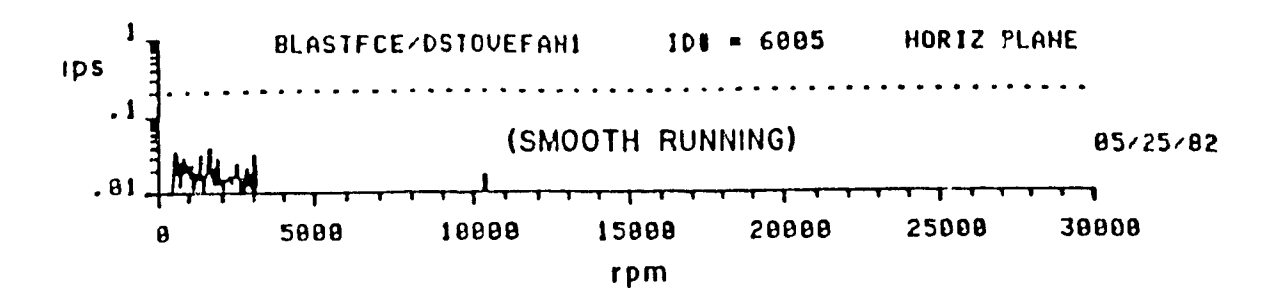
operating costs.

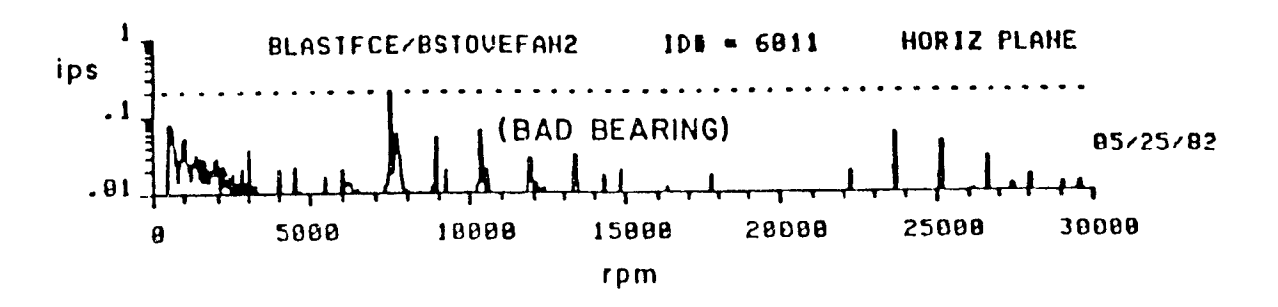
Predictive maintenance is condition based. Parts are replaced or repaired only when their condition indicates the need. Through various techniques the condition of an item of equipment is monitored and, as its condition deteriorates, plans are made to rectify the situation, i.e. replacement, adjustment, etc.. Predictive maintenance offers the same advantages as preventative maintenance but without the need for unnecessary replacements or overhauls.

Several techniques are available to monitor the condition of a piece of equipment. For example, magnaflux testing of a crane hook can detect the presence of small cracks; an analysis of the lubricating oil in a large gear box can detect gear wear. However, for the numerous rotating machinery in the steel plant, such as pumps, fans, generators, and motors, nothing provides more insight into the condition of the machine than vibration signature analysis. By measuring the vibration of the machine and its various components and comparing them to previous measurements, deteriorating trends can be noted and repairs made before the vibrations reach catastrophic levels.

A typical predictive maintenance strategy is a mix of two extremes. On one hand, the program is based on manual data collection and analysis that requires portable equipment. On the other hand, the program calls for automatic data collection, with dedicated sensors mounted on each critical machine and permanently linked to the central system for analysis. Bethlehem Steel developed a dynamic predictive maintenance

system that was based on the measurement of the machine's condition under load, by unskilled operators, and on an automated analysis system^[64]. Under normal conditions, the results of the analysis were made available the following day.





5.1 Comparison of vibration signatures for identical fans, one running smoothly and one with a bad bearing^[64]

The vibration signature is essentially a Fourier transformation showing the vibrational amplitude and the frequencies at which the vibrations occur. The comparison of the current signature with previous signatures completes the analysis. Depending on the type of machine the analysis can detect such problems as imbalance, bad bearings, misalignment etc.. An example is presented in Fig. 5.1.

5.2.2 Accelerometer Application in a Down Coiler

Quality of the coiled product of the hot strip mill is strongly influenced by the effectiveness of the wrapper rolls in forming the coil at the initial stage of winding. Conventional wrapper rolls, energized by an air cylinder, do not press the strip onto the mandrel for a considerable portion of the initial winding period; impact loads occurring when the stepped portion of the coil passes under the wrapper rolls causing the wrapper rolls to bounce, Fig. 5.2. As a result of the bouncing, several strip defects, such as slippage, telescoping and nicking marks, are generated because of the rapid acceleration and deceleration of the mandrel.

A new coiler, designed by Nippon Tteel Corp. and Ishikawajima-Harima Heavy Industries Co., was developed to minimize the bouncing of the wrapper rolls [65]. Each wrapper roll is controlled by an electro-hydraulic servo-system that activates a hydraulic cylinder, by applying appropriate pressure to the strip and by changing its position in response to control commands. Accelerometers are an integral component of the system.

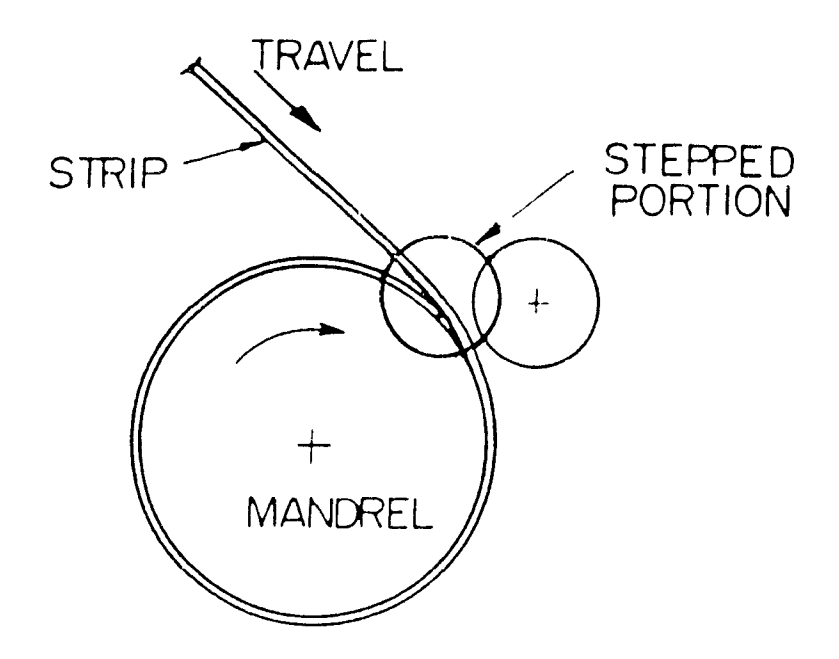


Fig. 5.2 Strip overlying the leading edge makes a stepped portion in coil surface^[65].

Two accelerometers are employed, one is located on the neck of the bottom pinch roll, the other at the No. 4 wrapper roll section. Figure 5.3 schematically presents the wrapper roll control system. The first accelerometer is used to detect the entry of the strips into the pinch roll. As shown in Fig. 5.4, the accelerometer signal increases dramatically as the strip enters between the two pinch rolls. A pulse generator, attached to the bottom pinch roll, is used to predict the entry of the strip into the wrapper. The second accelerometer is used to detect the position of the head end of the strip with respect to the number four wrapper roll. After that, tracking of the head end is facilitated by a pulse generator attached to the mandrel of the down coiler.

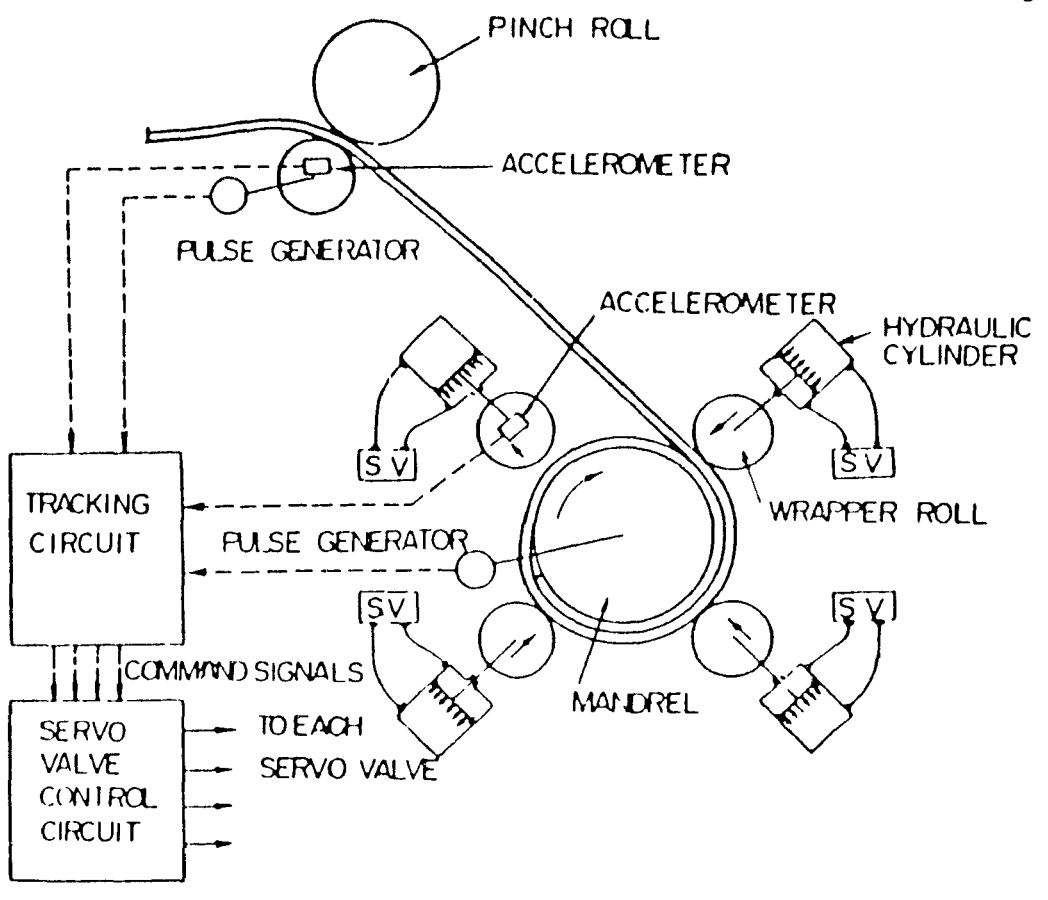


Fig. 5.3 Wrapper roll control system^[65].

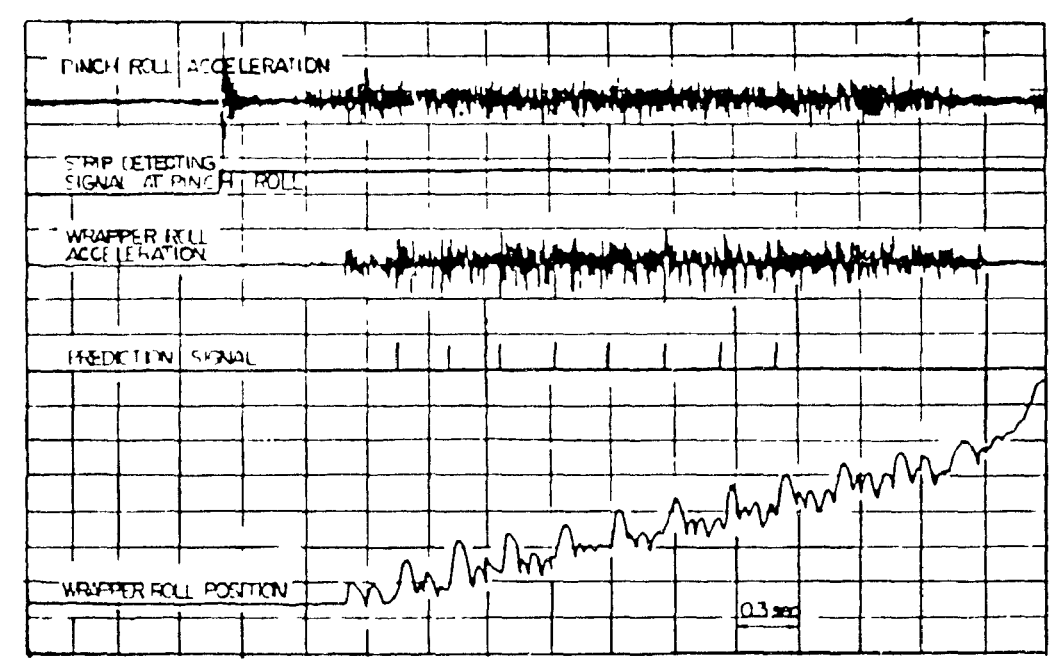


Fig. 5.4 Signal-time traces for the sensors of the tracking circuit $^{(65)}$.

When the number of pulses corresponds to the angle between the No. 4 and the No. 1 wrapper. The electro-hydraulic servo system retracts the wrapper roll away from the mandrel whenever the stepped portion passes between the wrapper roll and the mandrel. The control action minimizes damage to the wrapper rolls, its mechanical system and to the strip itself. A prediction pulse is also made for each of the four wrapper rolls. An example of the wrapper roll control is shown in Fig. 5.5. This control technique is applied to all wrapper rolls in the down coilers.

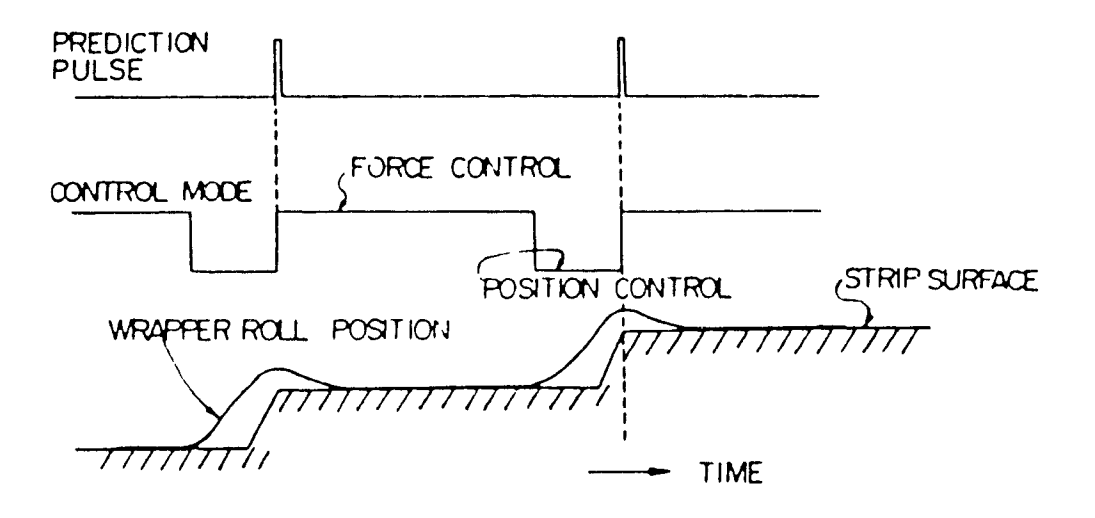


Fig. 5.5 Wrapper roll withdraws in position control mode, then presses strip onto the mandrel in force control $mode^{(65)}$.

5.3 Multi-Phase Mixing Applications

5.3.1 Introduction

Ì

The application of the accelerometer in multi-phase mixing studies is facilitated by the inherent solid-liquid-gas interactions which cause the metallurgical vessel (ie. furnace, ladle, ingct) to vibrate during the process. Thus, by monitoring the vessel vibrations with an accelerometer, the status of these interactions can be related to the process.

In 1974, Destate et al reported the earliest application of an accelerometer as a mixing sensor^[66]. Their application focussed on rimming steels and the intensity of the rimming action in an ingot mold during solidification. In a later application, the accelerometer was used to determine, empirically, the mixing power of ladle stirring gases. The application was generalized by Mucciardi et al^[67,68] as the mixing power of inert gas injection. The same research group employed the accelerometer during the wire feeding of volatile reagents into hot metal. The performance of the wire feeding process was evaluated, in part, by the accelerometer signal. The accelerometer was also applied as a slag carryover detector by the British Steel Corporation in 1983.

5.3.2 Rimming Steels

During the solidification of steel, the solubility of gases dissolved in the steel decreases and the excess gases are expelled from the metal. Of specific interest is the chemical equilibrium between carbon and oxygen. As the temperature of the steel decreases, these two elements react to form carbon monoxide while the system attempts to

attain a new equilibrium. The evolution of CO gas during solidification in an ingot mold is commonly called rimming and is observed as a boiling action.

With the appropriate rimming action, the steel cast in the ingot mold is virtually free of voids or blow holes. This steel, once rolled, has an excellent surface and ductility quality and is referred to as a rimmed steel. Rimmed steel is usually tapped from the furnace with only a small quantity of deoxidizers in the ladle, virtually no additions are made to the furnace prior to tapping. The aim is to have a sufficient oxygen level dissolved in the steel and a teeming temperature to give the desired rimming action. Typically, the rimming action of the first ingot is observed visually by an operator, who makes adjustments when necessary. Modifications may be in the form of adding deoxidizers or gas evolving materials to latter ingots.

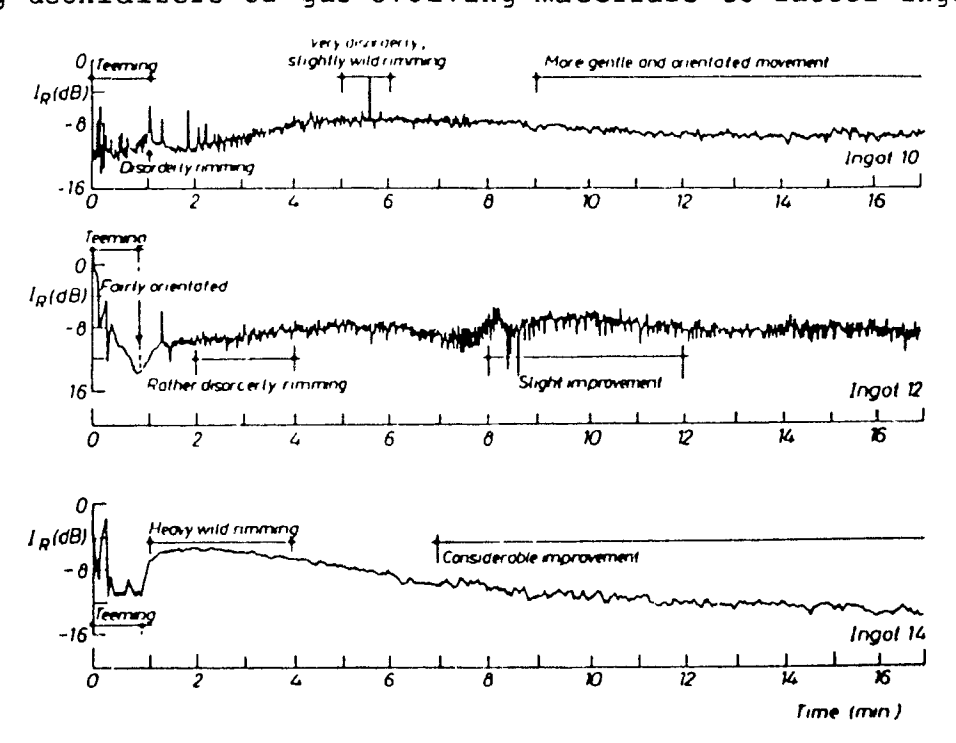


Fig. 5.6 Measurement of the rimming action of rimmed steel using an accelerometer [66].

Destate studied the acoustic and vibrational phenomena associated with gas evolution from rimming steels in 1974 with the aim of improving the adjustments made by the operators. Furthermore, the study was able to associate specific characteristics of acoustic and vibrational signals to the intensity of the rimming action and indirectly to the quality of the rimmed steel. An example of the accelerometer attached to an ingot mold is shown in Fig. 5.6.

5.3.3 Ladle Metallurgy

Ladle metallurgy is a secondary step in the steelmaking process. purpose is to produce high quality steel that satisfies stringent requirements relating to the surface, the internal quality and the mechanical properties. To achieve high quality steels, ladle metallurgy is used to control temperature, chemistry and cleanness of the steel. To a large extent, the effectiveness of a ladle metallurgy unit to perform these tasks depends on how well it can homogenise the steel and remove solid oxide inclusions from the steel. Typically, an inert gas is either injected into a melt via a porous plug or a Regardless of the technique that is used, the submerged lance. injected gas impacts a "mixing power" into the melt. This pow r input is taken to comprise both the potential and kinetic energies of the gas that are transferred to the liquid steel upon injection. studies are often employed to determine the optimum conditions of the stirring practice, such as inert gas flow rate and ladle geometry.

It is a well established fact that mixing time is a function of mixing power inputs $^{[69,70]}$. Several obtrusive techniques have been developed to

measure the mixing times directly, typically employing a dye tracer. These techniques, however, are limited in their applications and are most commonly used in conjunction with water model studies. Thus, the development of a non-obtrusive sensor, capable of measuring the mixing power, can provide a technique of deducing mixing times in hot metal systems.

, E

Mucciardi et al^[67,68] performed two extensive studies to determine the feasibility of correlating the mixing power input with the relative magnitude of the vibrations of the vessel as measured by an accelerometer mounted on the exterior of the vessel. The two trials were conducted in separate systems, one in water, the other in molten lead.

Mixing trials using water consisted of an elliptical water tank, 2201 working volume, and a centrally located, inert, submerged lance, as shown in Fig. 5.7. The accelerometer was attached directly underneath the center of the plexiglass tank. Trial conditions evaluated various lance immersion depths (0.25, 0.5, and 0.75 of the lance depth), inert gas flowrates (4.6 - 30 l/min. NTP) with a constant nozzle diameter of 50mm. Owing to the simplicity of the system studied, mixing times during inert gas injection were measured directly via tracer dispersion curves.

Mixing time, as defined in this study, is the time required to achieve a dye concentration change equal to 90% of the total concentration change after injecting the dye. The tracer dye, green food colouring,

was injected into the gas stream and concentration was readily measured from a photocell. The application of the photocell is explained further in reference⁽⁶⁸⁾. At the same time the tracer dye was being monitored, accelerometer readings were sampled at a nyquist rate of 12 Hz for a duration of two minutes.

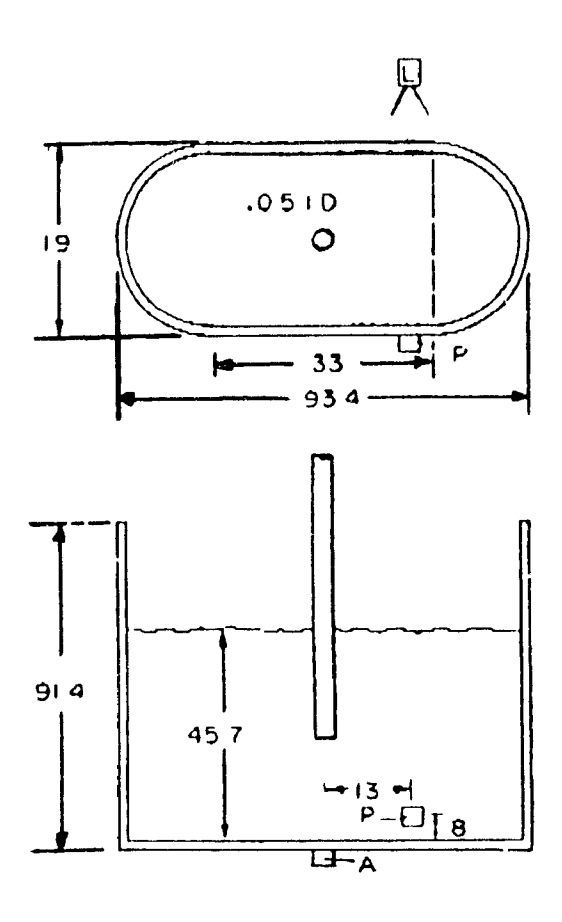


Fig. 5.7 Experimental configuration for water system. All dimensions are in cm. (A: accelerometer, P: photocell, and L: light source) [68].

1

The water model study found that the mixing power input had a discernible effect on the vibration intensity, defined in the study as the average slope of the integrated accelerometer signal. A distinct correlation between the accelerometer signal and the power input was found to prevail, a summary of the results is presented in Fig. 5.8.

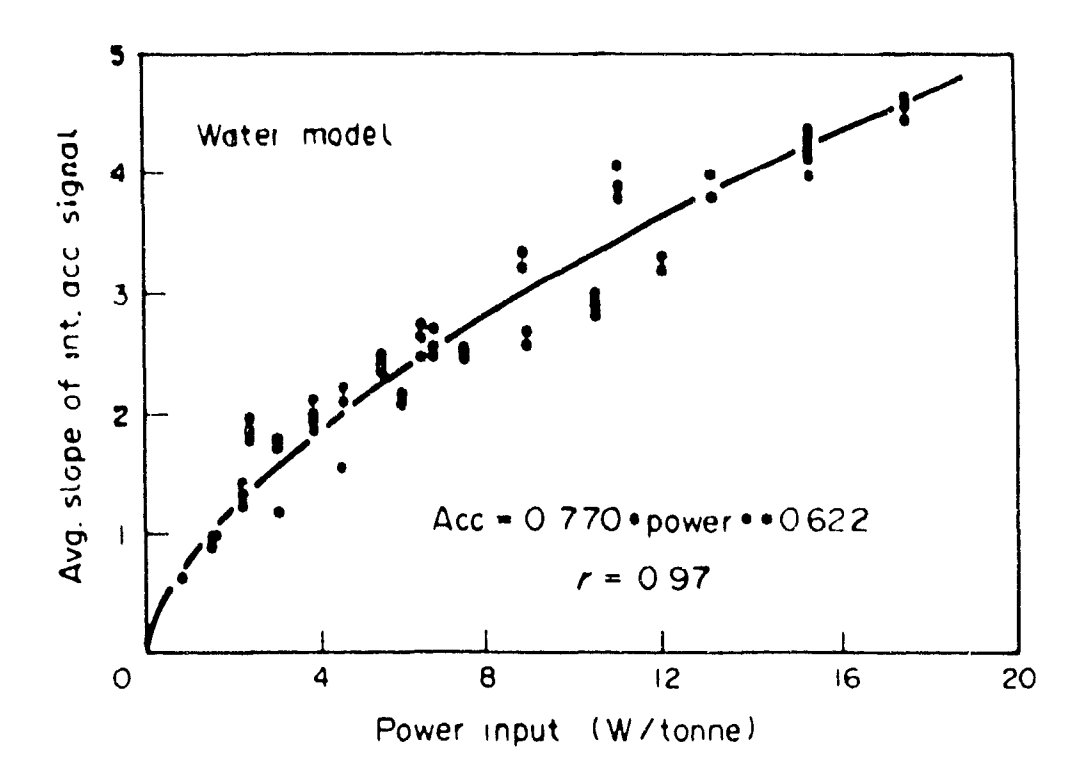


Fig. 5.8 Correlation of the transformed accelerometer signal as a function of the computed mixing power input for the water model study [68].

(mV)

In the second study, a molten metal system was used. The purpose of this study was to determine the degree of correlation between vibration intensity and a number of physical parameters. The effect of varying gas flow rates, lance depth, and nozzle diameter was studied. The liquid metal system consisted of a molten lead bath contained in an alumina crucible which was set in an induction furnace. Nitrogen gas stirring was achieved by injection through a submerged steel pipe. The accelerometer was mounted on one of the legs supporting the furnace. In a similar fashion to the water model system, accelerometer readings were sampled at a rate of 12 Hz for a period of two minutes.

The study revealed that the accelerometer was responsive to changes in flow rate, lance depth, nozzle diameter and even bath temperature. An example of the effect of flow rate on the vibration intensity is shown in Fig. 5.9. Thus, the investigators concluded that the sensor was responding to the net power input. As was the case in the water model system the investigators were able to summarize their results in a correlation (Fig. 5.10):

$$\dot{\varepsilon} = a Acc^b$$
 (5.1)

where $\dot{\varepsilon}$ =mixing power input (W/tonnes)

Acc =slope of the integrated accelerometer signal

a =a variable that is a function of the system
 configuration and accelerometer sensitivity

b =constant that is not dependant on the system configuration or accelerometer position.



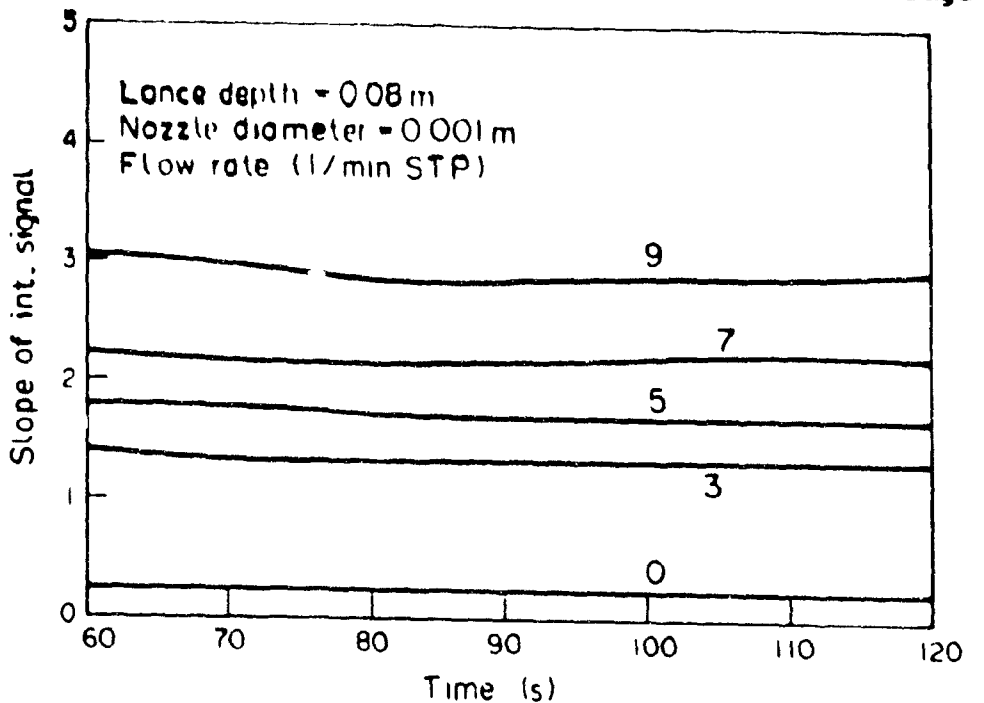


Fig. 5.9 Slopes of the integrated accelerometer signal at various flow rates in molten lead system^[67].

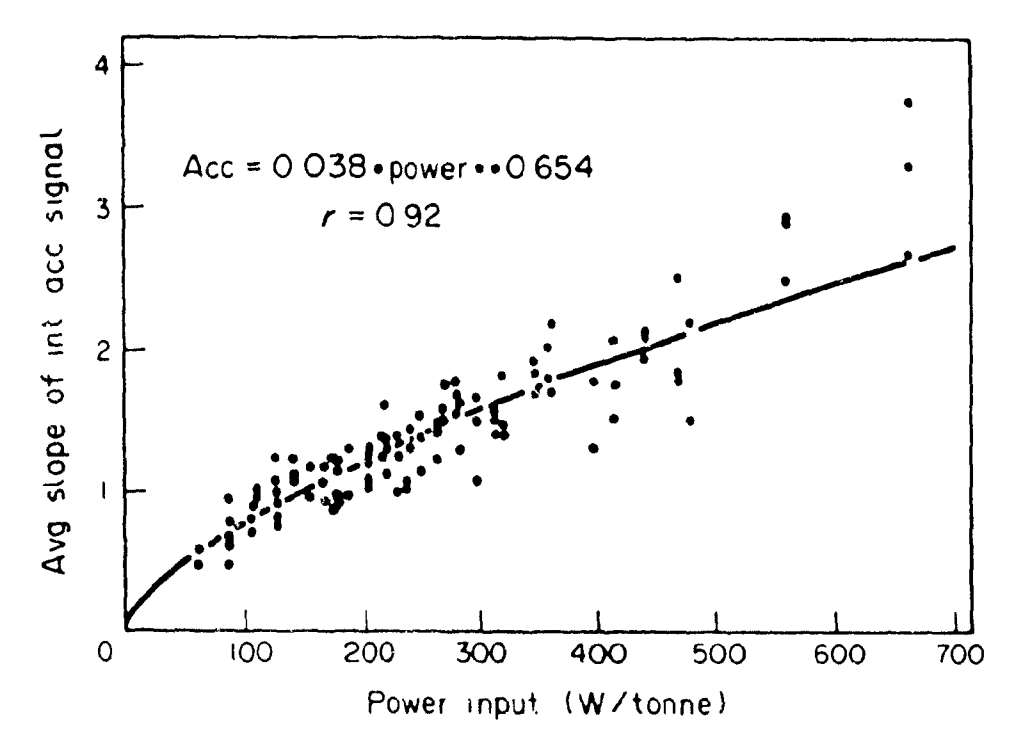


Fig. 5.10 Correlation between the transformed accelerometer signal and the computed mixing power input for the molten lead system^[67].

The investigators noted that the quantity "a" in Eq. (5.1) is a function of the system configuration, including such parameters as vessel shape, lance location and accelerometer position. For example the constant "a" was found to be 1.52 in the water model while in the lead system "a" was found to be 149. Although the exact relationship between the constant "a" and the parameters describing the system configuration was not mathematically quantified, the quantity "a" is constant for a specific system configuration. Hence, the application of the accelerometer as a mixing sensor requires that each configuration be first calibrated to determine the quantity "a".

Mixing time, as previously stated, is a function of the net power input as shown below. The magnitudes of the constants k and n are subject to debate.

$$\tau = \mathbf{k} \cdot \dot{\mathbf{\epsilon}}^{\mathrm{n}} \tag{5.2}$$

where τ = mixing time (s)

 $\dot{\epsilon}$ = mixing power input (W)

k & n = are constants

In one study by Asal et al⁽²¹⁾, the magnitude of n was reported to vary between 0.23 and 0.45. To confirm their results, Mucciardi et al computed the magnitudes of k and n for the water model study. The mixing times were then correlated with the vibrational intensity of the vessel. A summary of their results is shown in Fig. 5.11.

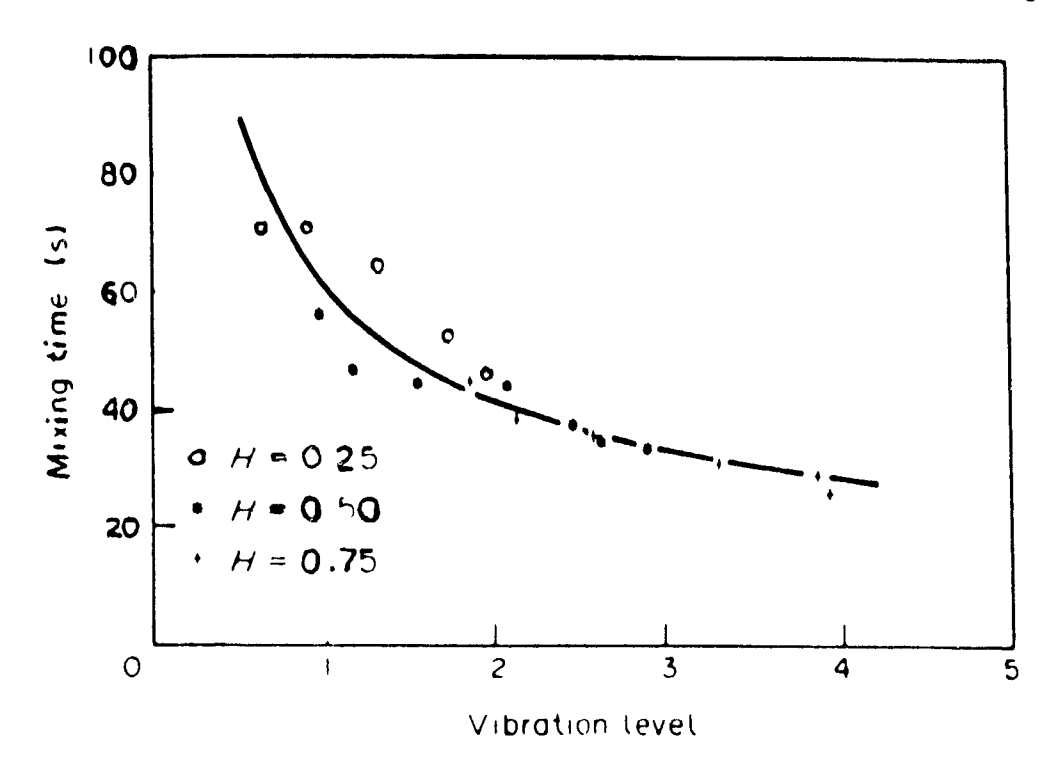


Fig. 5.11 Correlation between mixing time and the vibrational intensity of the water model where:

Mixing Time = $61.1 \text{ Acc}^{-0.562}$ and r= $0.94^{(67)}$.

In summary, the water model study indicated that:

and the

$$\tau = 61.1 \text{ Acc}^{-0.56} \tag{5.3}$$

Equations (5.3) and (5.2) can be reduced to Equation (4) where n has a value of 0.35, as shown below:

$$\tau = 70.8 \,\dot{\varepsilon}^{0.35} \tag{5.4}$$

The close agreement of the exponent, n, with those of other investigators strongly suggests that the accelerometer can be employed to determine mixing times.

5.3.4 Addition of Volatile Reagents in Ladle Metallurgy

Ladle metallurgy ations, as mentioned above, are used to achieve superior steel qualities. Chemistry control of the steel processed at the ladle station is vital to achieve the required mechanical properties and cleanness of the steel. In addition to the final product, the chemistry "windows" to ensure the castability of the liquid steel at the continuous casting facilities are small and often difficult to obtain. To assist steel producers, several additive systems have been developed. Aside from bulk additions, the two major additive systems are submerged lance injection (ie. CAB, Scandinavian Lancers and Pelamag) and wire feeding (ie. Vallourec/Affival^[72] and Pfizer^[73]). The latter processes rely on the feeding of steel sheathed reagents into molten steel, some of which are extremely volatile at steelmaking temperatures and, hence, pose a number of safety and environmental hazards.

Although considerable effort has been expended on the development of these processes, virtually no effort has been directed to the control of systems that ensure safe and reliable use of these volatile reagents. In an attempt to develop a magnesium wire feeding system, Mucciardi et al⁽⁶⁷⁾ discovered that the accelerometer can measure the relative degree of violence of a reagent during the process. Furthermore, they concluded that the characteristic of a safe, reliable wire feeding operation was the steady state release of its volatile constituents, which was easily detected by the vibration sensitive device.

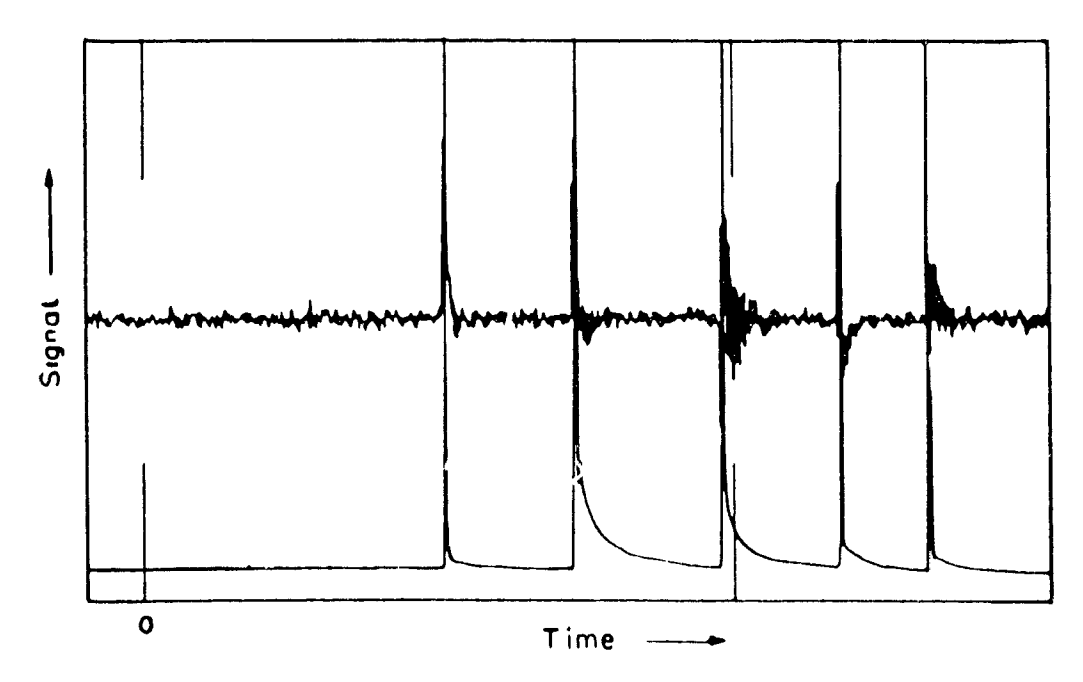


Fig. 5.12 Erratic release of magnesium vapour during a magnesium wire feeding operation. 671.

To illustrate the use of the accelerometer, Mucciardi presented the results of two experiments. In the first experiment, a sheathed magnesium wire, 3.2mm in diameter, was fed into hot metal at 1400°C. The sheathed wire was fed vertically into 25 kg melts at velocities ranging from 0.5 to 3.0 cm/s. The results of the first experiment are presented in Fig. 5.12. The trace emanating from the bottom left hand corner of the graph was produced by a photocell that measured the light illuminating from the mest surface. The accelerometer signal emanates from the middle of the graph on the left hand side. The units from both sensors were intentionally omitted since they are specific to one test. It is clear that large bursts of light coincided with explosions of magnesium below the melt surface, this characteristic is revealed by the accelerometer as brief, yet intense vibrations. Mucciardi deemed this characteristic to be non-productive, and unsafe.

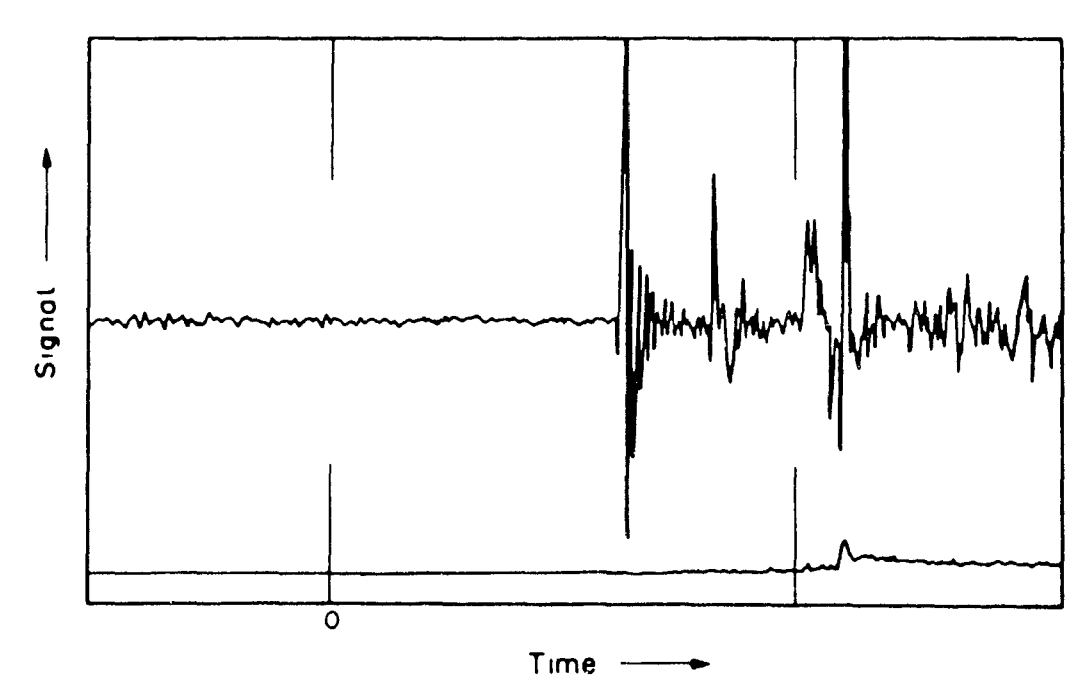


Fig. 5.13 Predictable release of Mg vapour during a magnesium wire feeding operation [67].

In contrast, consider the results of a modified Mg wire shown in Fig. 5.13. Mucciardi concluded that the Mg was released at a relatively constant rate beneath the melt surface. Furthermore, they concluded that Mg vapour had the opportunity to dissolve or react prior to resurfacing. This characteristic was revealed by the absence of photocell activity.

A similar series of experiments were conducted by the researchers using a calcium wire. The results obtained were in agreement with the magnesium wire feeding trials. These experiments led to the development of a novel volatile reagent wire feeding process. Throughout the development process, the accelerometer was used as a means of viewing liquid gas interactions in molten metal.

5.3.5 Slag Detection

The production of low-cost, high-quality steels demands the elimination of slag carryover from one metallurgical vessel to another. The tundish, an intermediate metallurgical vessel between the ladle and the mold, is limited in the quantity of slag it can handle. Operating practices aimed at minimizing the slag carryover call for the removal of a protective ceramic shroud from the steel stream and visual detection of the onset of slag carryover. As a consequence, the steel is exposed to an oxidizing atmosphere and the cleanness of the steel is jeopardized. To avoid this, several techniques have been developed to detect the onset of slag carryover with a ceramic shroud in situ. A schematic of the ceramic shroud practice is shown in Fig. 5.14 to compliment the discussion which follows.

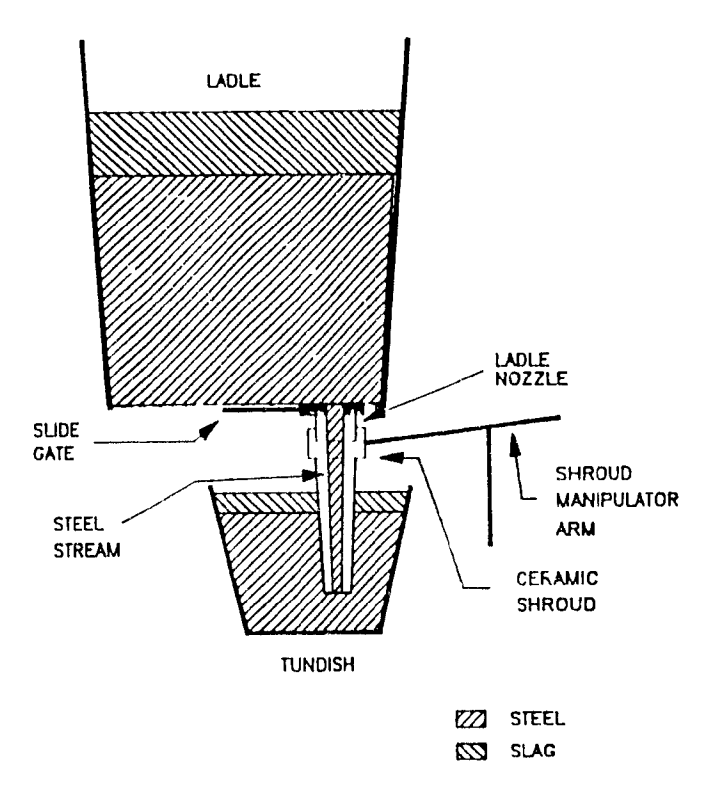


Fig. 5.14 Application of the ceramic shroud during ladle teeming at the continuous casting machine; casting machine is not shown for clarity.

One technique, developed by British Steel Corp. [74], employed an accelerometer to detect the onset of slag carryover. The accelerometer in this application monitors the flow of liquid through the ceramic shroud. Since the physical properties, namely density and viscosity, of steel and slag are significantly different, a marked change in the amplitude of the vibrations can be detected when the liquid in the tube changes from steel to slag, as can be seen in Fig 5.15. The system is comprised of an accelerometer mounted on the shroud manipulator arm and an electronics unit which amplifies and filters the accelerometer signal. An alarm is triggered when the rate of change in the signal amplitude exceeds a predetermined value. The system has been developed on a single strand slab casting machine and has been 100% successful during a 30 heat trial campaign.

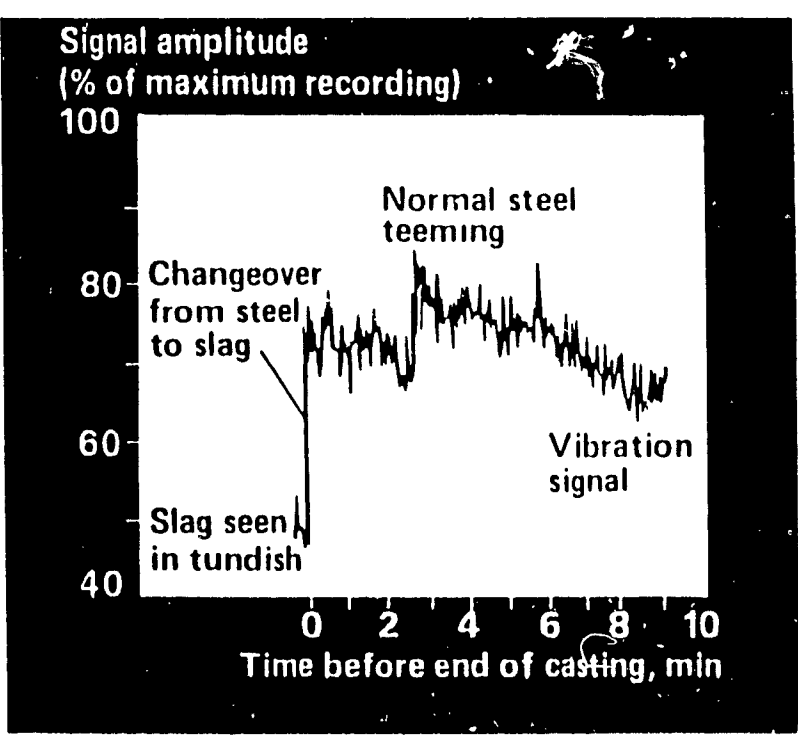


Fig. 5.15 Typical accelerometer signal as a slag detector. The signal shows a decrease in vibration in the ladle-to-tundish shroud due to the changeover from steel to slag at the end of a cast^[74].

5.4 Continuous Casting

Lubrication in the mold diring continuous casting of steel is a critical component of the process. The effectiveness of the lubricating material, typically rapeseed oil or mold powder, is a key parameter in determining not only the quality, but also the productivity of the casting machine. Casting powders, also known as mold powders, are used in conjunction with submerged tundish-to-mold shrouds for the production of slabs and blooms. The mold powder is manually or mechanically placed on top of the steel surface in a semi-continuous fashion. The powder, aside from other crucial characteristics, must be able to melt and form a lubricating film between the solidifying steel skin and the mold walls.

On the other hand, oil lubrication is typically used on billet casters. The oil is dispensed continuously from ports located at the top of the mold and is allowed to flow down the mold wall to the steel surface where it provides a lubricating film between the steel and the mold. Although the mechanisms for oil and powder lubrication are beyond the scope of this thesis, let it be simply stated that the effectiveness of the lubrication medium determines, to a large extent, the magnitude of the mechanical interaction between the mold and the solidifying steel shell.

Centre de Recherches Metallurgiques (CRM) has developed and received a patent for an instrumentation package to measure the mechanical interaction, namely friction, between the steel strand and the mold^[75,76]. The instrumentation, called the M.L. Tektor, employs an

accelerometer to measure the instantaneous movements of the mold. Through an electronics package, the signal is processed to represent the frictional forces, or inversely to the lubrication process.

The M.L. Tektor has been used as a production tool by numerous slab and bloom casters, its limited application on billet casters may be the result of its prohibitive price tag. For normal casting conditions, it has been used to determine the optimum casting speed for a particular mold powder. Likewise, two mold powders can be evaluated. Experience with the M.L. Tektor has led to the characterization of several responses of the signal. For example, the detection of a rapid increase in the signal to a higher yet non-detrimental level indicates an incorrect, or a non-conforming batch of mold powder (Fig. 5.16). Another example of detecting abnormal casting conditions with the accelerometer is shown in Fig. 5.17. In this example the mold powder that "hardens" as '. result of absorption of other oxides and exposure to an oxidizing atmosphere must be slagged from the mold. As a result, the mold powder viscosity invariably increases and, as a result, the friction between the mold and the strand also increases. deslagging, the original properties of the mold powder return and the friction level is reduced.

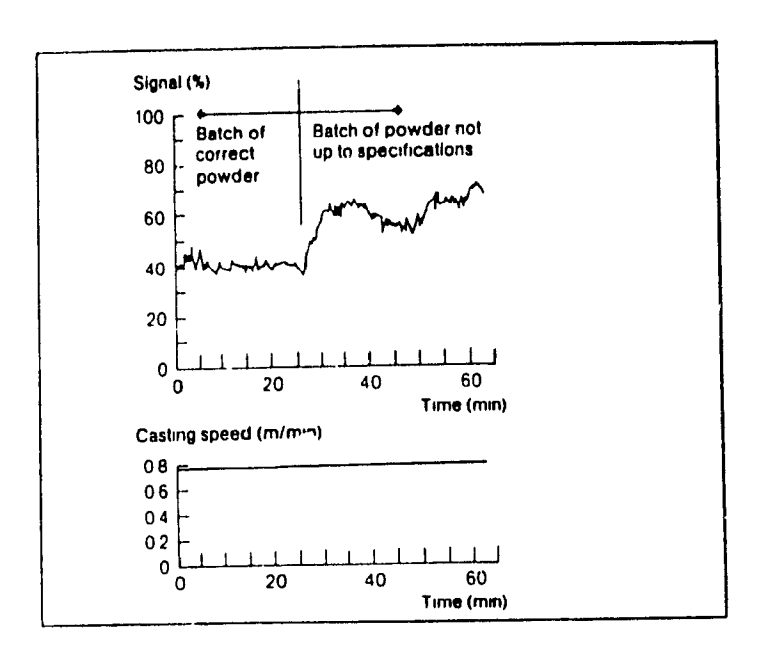


Fig. 5.16 Example of an increasing accelerometer signal as a result of non-conforming batch of mold powder $^{[76]}$.

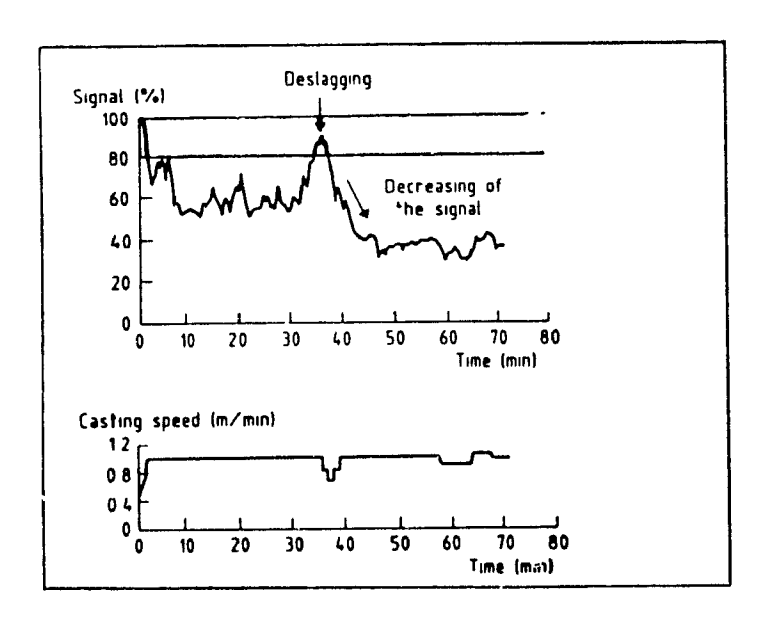


Fig. 5.17 Example of an increasing accelerometer signal as a result of deterioration in the mold powder qualities^[76].

T

A3 a final note to this discussion, it is appropriate to return our attention to mechanical applications of the accelerometer. CRM have also developed and patented a similar instrumentation package that is directed to the oscillating tables of continuous casting machines [75,76]. Specifically, it consists of a set of six sensors that are installed at various locations (Fig. 5.18) and employed to monitor the oscillation mechanisms. In a similar nature to predictive maintenance programs, the information is used to evaluate the alignment of the oscillating table, worn bearings, et cetera. As an example consider Fig. 5.19, when defective bearings were detected on the main transmission bearing of a long lever type oscillator system.

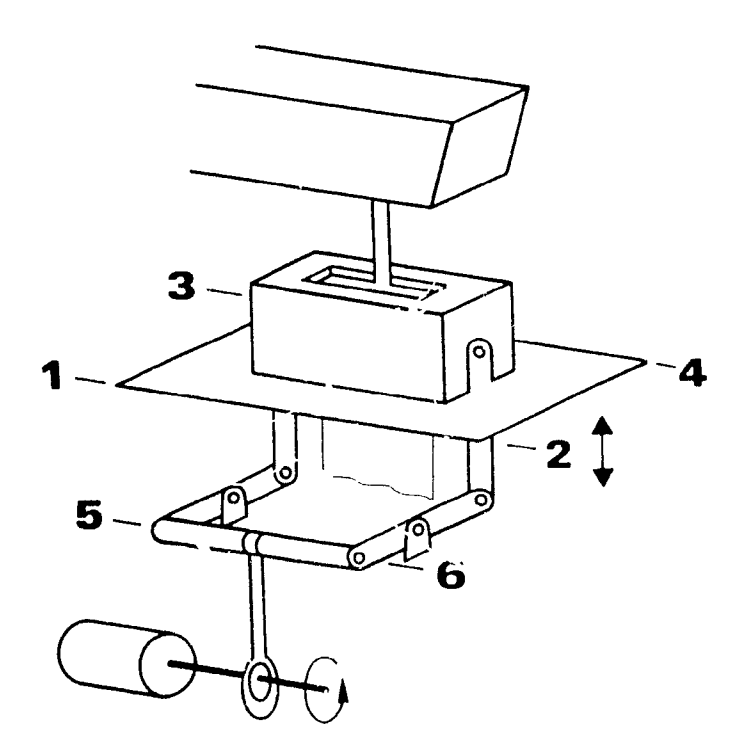


Fig. 5.18 Schematic of a slab casting machine showing the locations of accelerometers used by the M.O. Tektor $^{[76]}$.

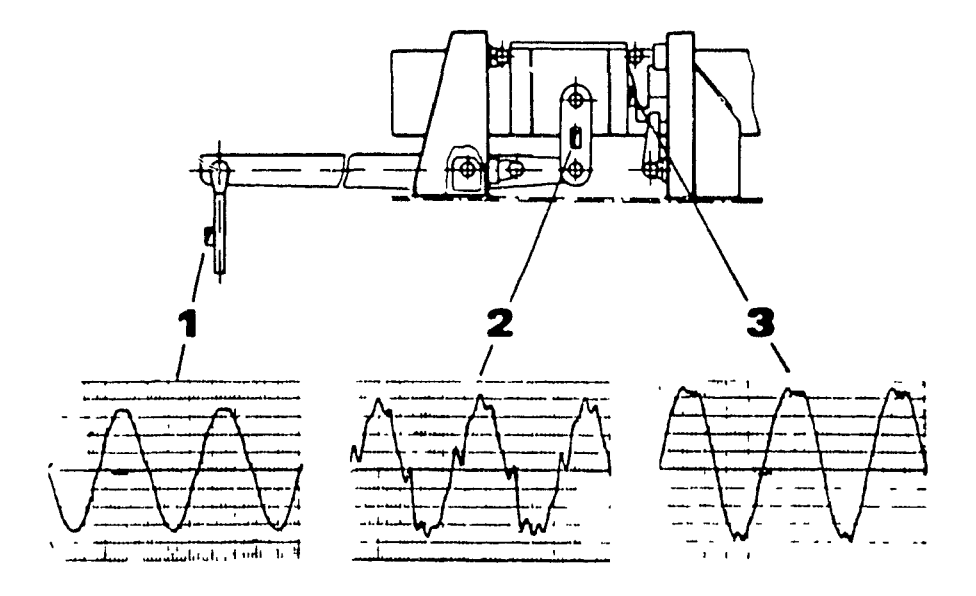


Fig. 5.19 Detection of wear at the main transmission bearing by the accelerometer^[76].

In concluding this chapter, the application of the accelerometer in the steel industry remains, for the most part, mechanical in nature. Furthermore, almost all of the applications are based on the relative response of the signal and are often used to detect the occurrence of anomaly on the basis of deviation from normal operating levels. This remains true for the current work employment of the accelerometer as an end point detector during BOF steelmaking depends on its success to detect an anomaly during the process.

6. Experimental

6.1 Introduction

A description of the laboratory scale BOF vessel is presented in the first portion of this chapter. The data acquisition and control systems that were used in the low and high frequency simulations are detailed in subsequent sections.

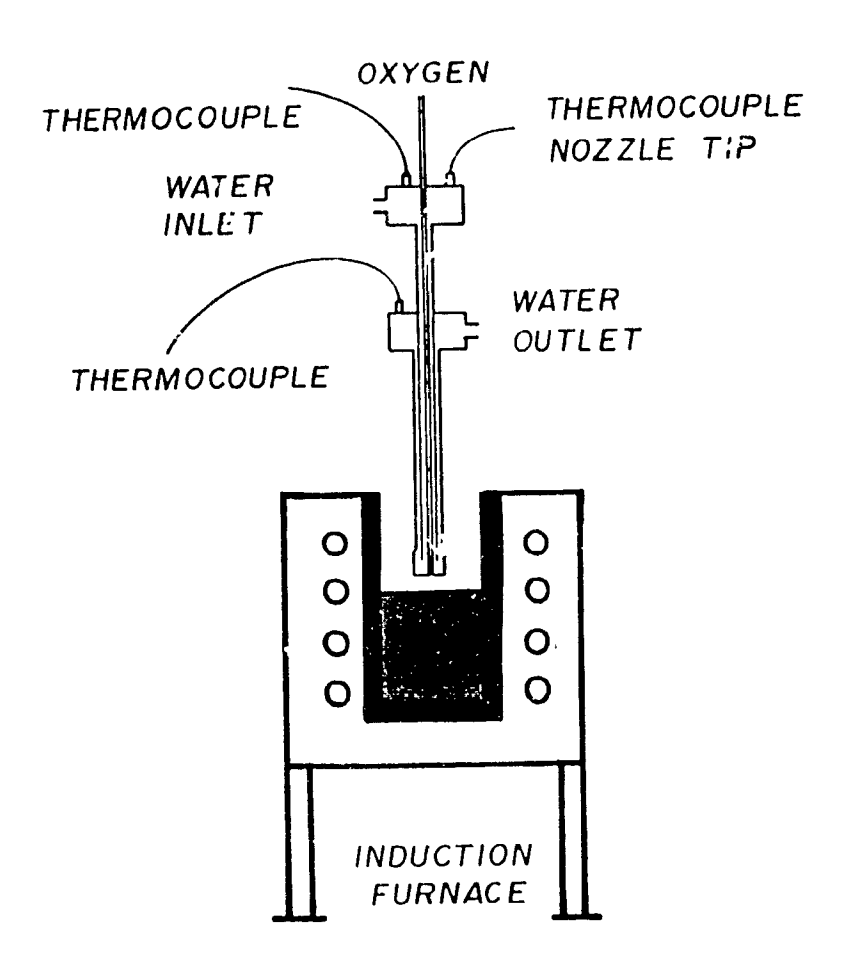


Fig. 6.1 Schemacic of the laboratory vessel.

6.2 Laboratory Scale BOF Vessel

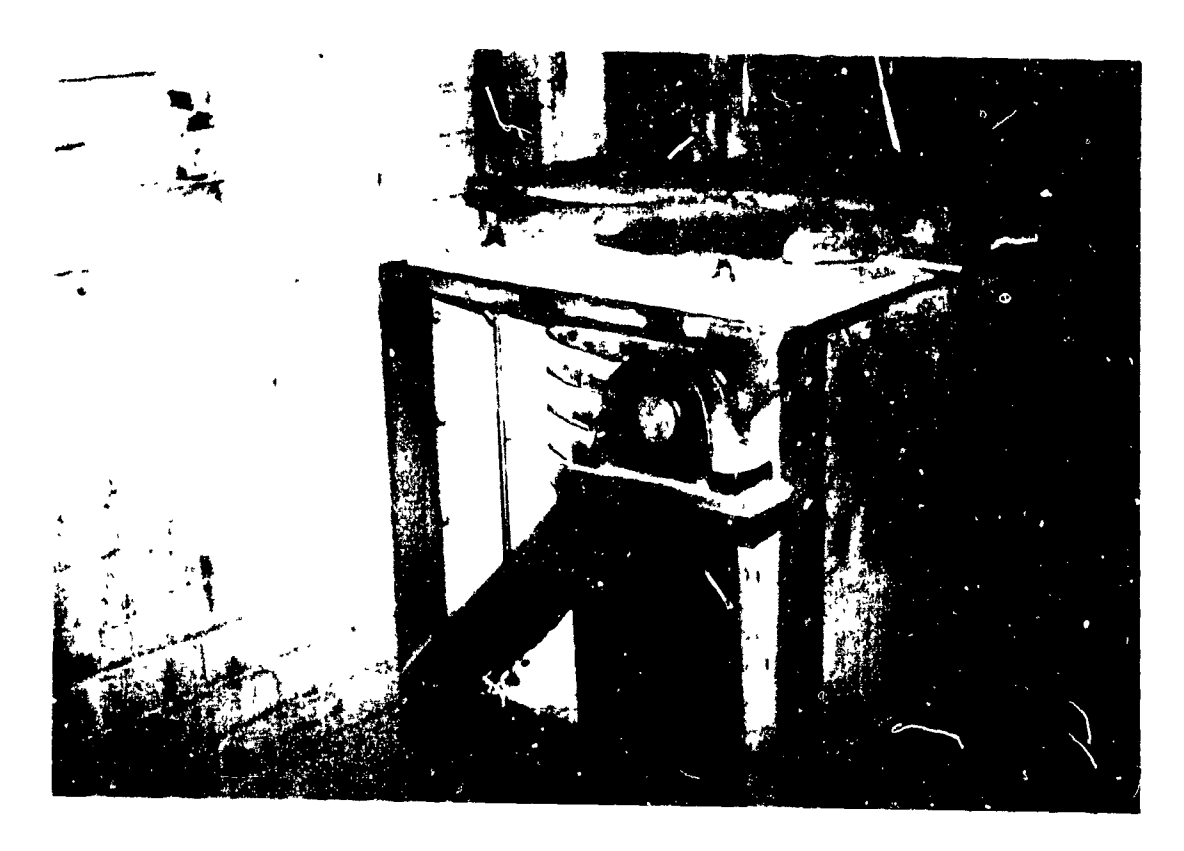
6.2.1 General

The laboratory-scale BOF vessel consisted of an induction furnace used to melt approximately 15 to 23 kg of pig iron (= 4% C) in an alumina crucible. A water-cooled, copper, oxygen lance situated 2.0 to 3.5 cm above the melt supplied oxygen at rates of 0.8 to 1.9 N l/s. The oxygen lance was of straight-bore design, the diameter being 1.5 mm. The accelerometer was positioned at several locations on the structure of the induction furnace. The laboratory vessel can be seen in Fig. 6.1.

The induction furnace employed in the study was a Tocco Melt Master induction furnace. The furnace operated at 3000 Hz and had a maximum power input of 150 KVA at 400 Volts. The internal diameter of the coil was 38 cm and had 10 turns in a 30 cm length. During the course of the study the power supply of the induction furnace was replaced by another unit with similar characteristics. Photographs of the induction furnace and its old control panel are shown in Fig. 6.2.

6.2.2 Oxygen Lance

The oxygen lance represents a critical component in the BOF process. For this reason, considerable effort has been expended to develop a reliable oxygen lance for the BOF simulations. Previous work had determined that a consumable, non-cooled steel lance was not acceptable^[1]. As one might expect, the lance was consumed at a



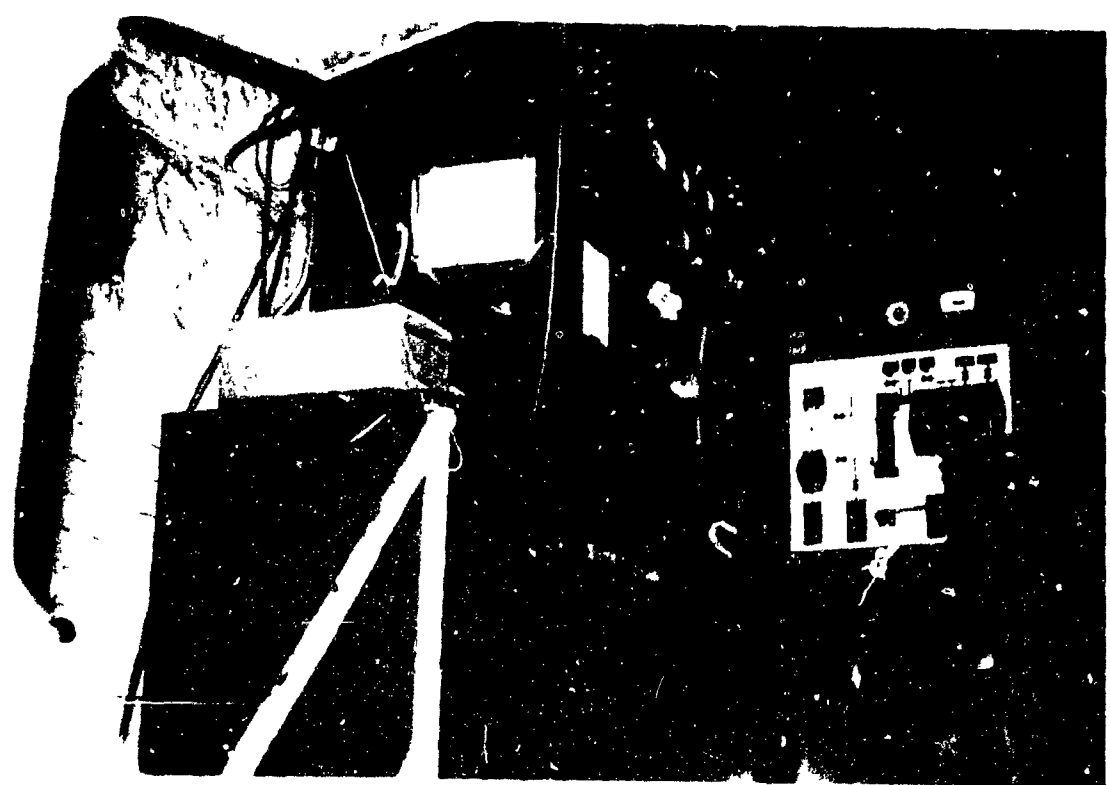


Fig 6.2 Photographs of the (Above) induction furnace and its (Below) control panel

substantial rate and made it impossible to maintain a constant lance height and oxygen impingement force on the bath.

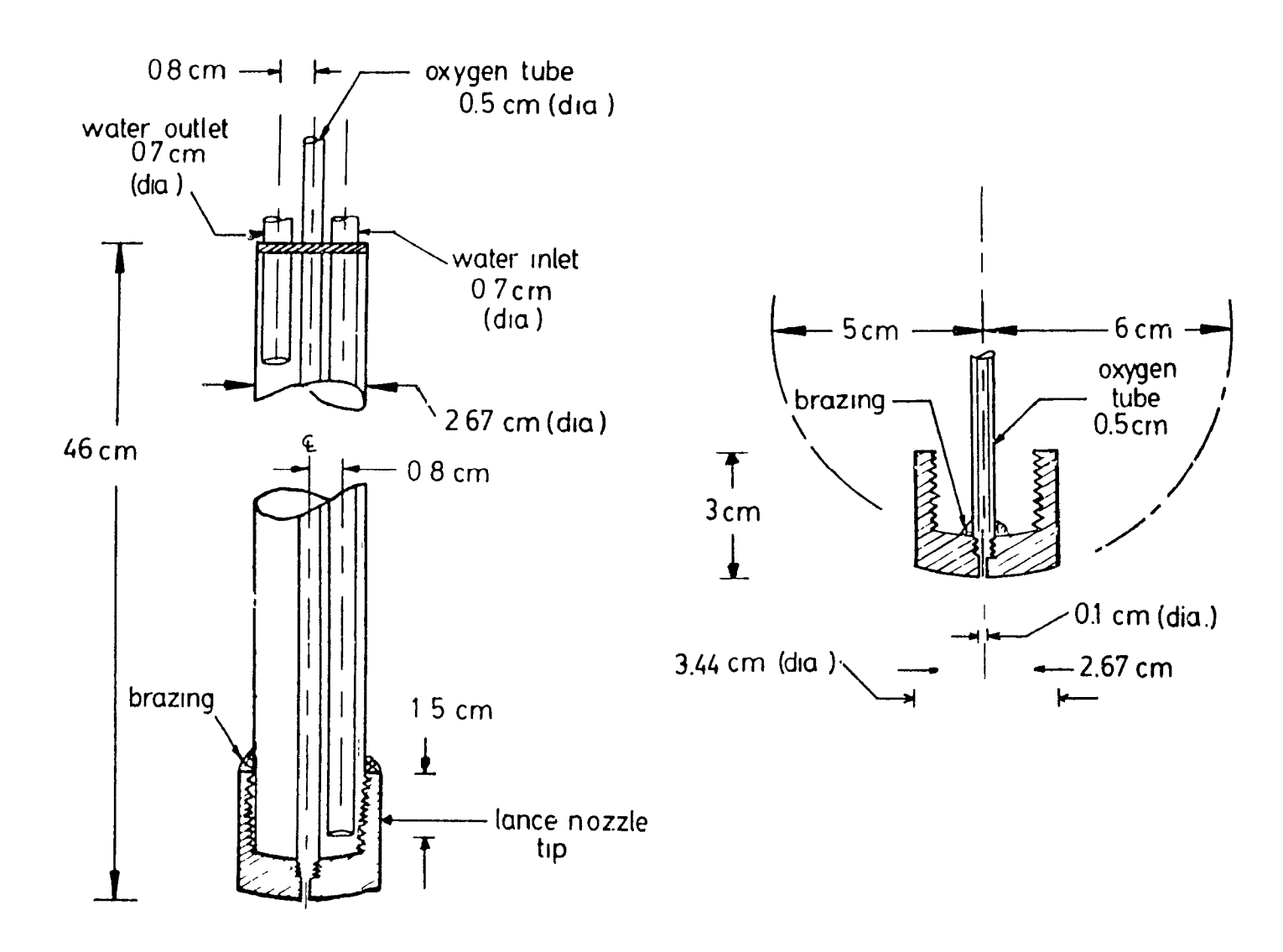


Fig. 6.3 Initial design of a water-cooled, oxygen lance.

From this experience, it was decided that a non-consumable lance was required to maintain blowing characteristics. From previous work, an initial water-cooled lance was designed to overcome this problem. As can be seen in Fig. 6.3, the design did not follow the design of conventional BOF oxygen lances.

Although the operation of this lance was successful for a limited number of simulations, the brazing that sealed the oxygen conduit to the nozzle orifice frequently failed. The main reason for failure was concluded to be the non-concentric design of the conduits, and the limited quantity of cooling water that could be supplied through the relatively small copper tubes. Therefore, it was decided to design and build an oxygen lance which resembled a BOF oxygen lance but avoided the rather complex fabrication of the nozzle.

The second water-cooled oxygen lance, shown in Fig. 6.4, was fabricated from three concentric copper pipes; (1) a 6.35 mm (1/4 in) copper tube that delivered oxygen to the nozzle tip, (2) a 19.05 mm (3/4) in copper pipe supplying water to the nozzle tip and (3) a 25.40 mm (1 in) copper pipe forming the outer shell of the lance and serving as the return conduit for the cooling water. Water conduits were terminated by implementing annular surge tanks. The terminating conduit is threaded to the surge tank while the next inner pipe passing through the surge tank is sealed only at the exit of the surge tank. The latter pipe forms the outer shell of the lance once it passes the surge tank.

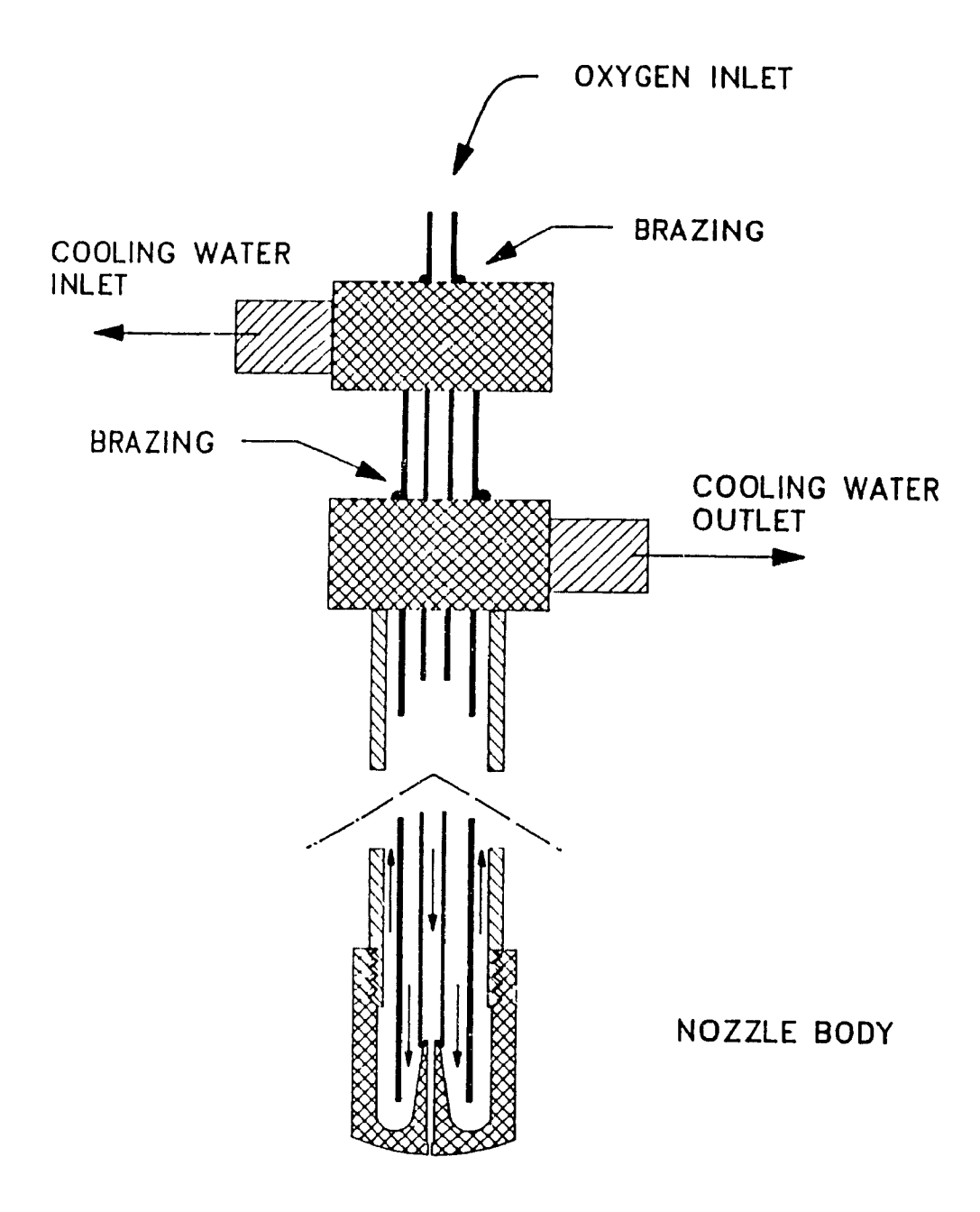


Fig. 6.4 Oxygen lance schematic showing final design.

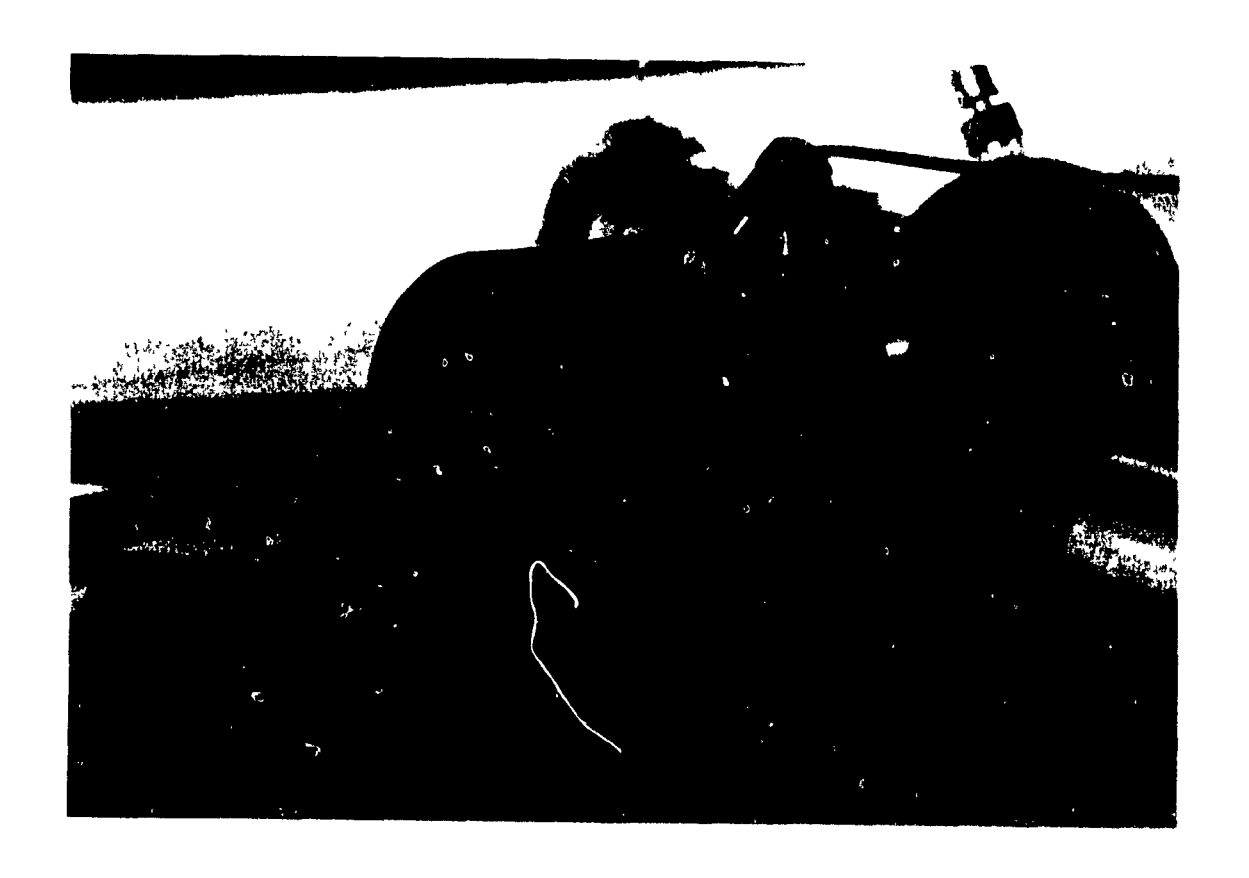


Fig. 6.5 Photograph of the inlet and outlet surge tanks of the water-cooled oxygen lance.

The outer pipe, 25.4 mm (1 in) ϕ , is threaded to the nozzle while the water supply pipe, 19.05 mm (3/4 in) ϕ , is not secured to the nozzle; its haight above the cold face of the nozzle is fixed by the location of the brazing at the top of the outlet surge tank with respect to length of the inlet pipe. The oxygen pipe is pressed onto the nozzle stem and is soldered to ensure a water tight fit. The nozzle itself is machined from a solid copper bar, 41.28 mm (1.625 in) ϕ . The hot face of the nozzle is curved to reduce the thickness of the copper at the outer edges. In addition, the cold face is curved providing

additional surface for heat transfer. A curved surface also reduces the risk of stagnant fluid flow and, consequently, nucleate boiling on the cold face. At the center portion of the nozzle, the copper stem, is cooled primarily by the cooling water and the oxygen gas.

į

The total length of the nozzle was 50.8 mm (2.0 in), from nozzle tip to the threads. The height of the stem is 30.23 mm (1.19 in). The inner bore of the stem is 3.175 mm (0.125 in) in diameter and continues until just before the nozzle tip. Approximately 3.175 mm (0.125 in) from the nozzle tip, the final bore, measuring 1.5 mm (0.0591 in) in diameter starts. This final bore constitutes the nozzle's orifice.

The water and oxygen connections in the vicinity of the lance employed stainless flexible hoses and double shut-off, quick connect/disconnect couplings at both ends. The flexible hoses were long enough to permit the use of ordinary hoses a safe distance away from the vessel. The cooling water inlet was connected to an ordinary sink tap and its exit was placed into the bottom of the sink. The oxygen hoses were connected in, series, to a solenoid valve and a commercial oxygen supply tank, complete with pressure regulator.

The oxygen lance was held in position by means of an annular clamp suspended above the induction furnace. The height of the nozzle above the melt was adjusted prior to a simulation by sliding the lance body through the annular clamp. Once in the correct position above the melt, the clamp was tightened.

The average flow rate through the nozzle was determined experimentally by releasing a specific volume of gas over a known period of time. The average flow rate was then determined. The flow rate was found to be a function of the back pressure of the oxygen tank. Parameters of the oxygen lance are discussed further in Chapter 7.

6.3 Sensors and Relays

In the BOF simulations the data acquisition/control programs monitored three basic transducers; (1) thermocouples, (2) accelerometer, and (3) photocell. The control aspect of the program was to simply open an oxygen valve at the start of the experiment. This section describes the sensors and the relays employed during the simulations, with the exception of the accelerometer which was discussed in Chapter 3.

Oxygen control consisted of a solenoid valve, an Aranco solid state relay, and a mercury form C relay on the HP 3497A Digital/Analog Control (DAC) unit, a schematic drawing is presented in Fig. 6.6. A small power supply unit, 6 VDC - 500 mA, is connected to the solid state relay and the mercury form C relay in the DAC unit. This wiring configuration was chosen because it isolates the high voltage from the DAC unit. When the mercury form C relay is activated it closes the small power supply circuit, which activates the solid state relay switch. Once activated, the Aranco relay closes the solenoid valve

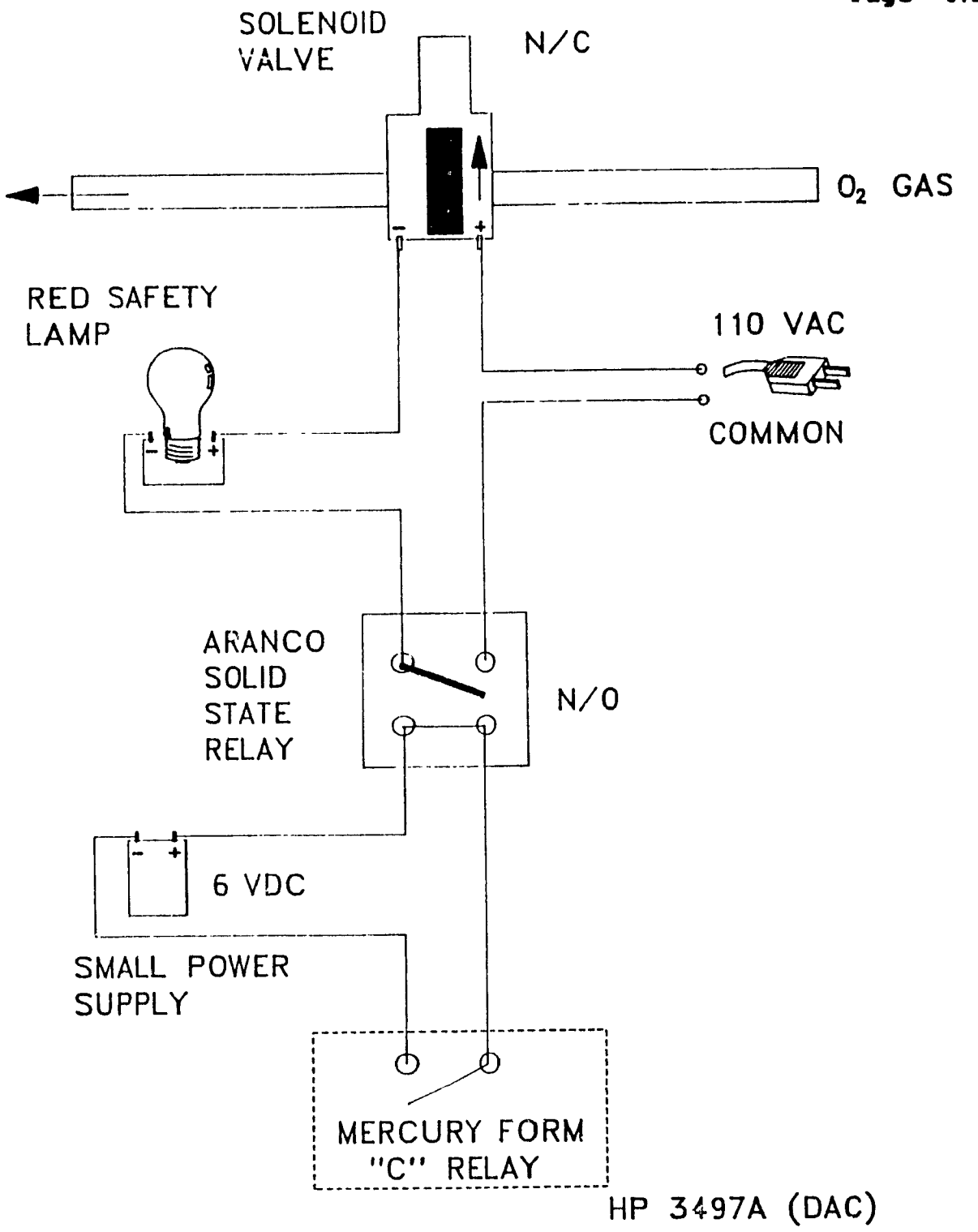


Fig. 6.6 Oxygen control circuit.

circuit, hence, turning on a red lamp (for safety purposes) and the solenoid valve. The solenoid valve is in the open position when the power is on, allowing the oxygen flow to start. At the end of the experiment the mercury form C relay is opened. This deactivates the solid state relay switch and subsequently turns off the solenoid valve and the lamp.

Ì

The thermocouple is used for temperature measurements and is one of the most common sensors in industry and science. Thermocouples are economical and rugged, they also have reasonably good long-term stability. As a result of their small size, they respond quickly and are useful where a fast response in thermal gradients is important. They function over temperature ranges from cryogenics to jet engine exhausts and have reasonable linearity and accuracy.

The thermocouple relies on the fact that the number of free electrons in a piece of metal depends both on temperature and composition. Hence, when two dissimilar metal are in isothermal contact they will exhibit a potential difference (thermal EMF) that is a repeatable function of temperature. This is known as the SEEBeCK effect.

In the BOF simulations, the thermocouples monitored the temperature of the cooling water at the inlet surge tank, the nozzle tip and the outlet surge tank. The thermocouples, chromel-alumel, were cut to the appropriate length and the two wire leads were fused together. For the thermocouple at the nozzle tip, a small hole was drilled through the 19.05 mm (3/4 in) copper pipe at the bottom. The thermocouple was held

in place simply by hooking it in the small hole. The exact locations of the other thermocouples in their respective surge tanks was not a concern. The other end of each thermocouple was passed through an Oring coupling. The thermocouples and the Orings can be seen in Fig. 6.5. The two factors of linearization and compensation were accounted for by using a linear regression, over the operating range of the thermocouples, and maintaining a fixed temperature at the reference junction.

The photocell was employed to monitor the pyrotechnics of the simulations. The photocell was mounted well above the bath and to the side to avoid direct contact with the CO combustion flames. The photocell provides a voltage signal that is proportional to the intensity of the light.

6.4 Data Acquisition and Control

6.4.1 Introduction

The BOF simulations were conducted under two types of data acquisition and control programs, (1) low frequency and (2) high frequency. The programs differed only in the methods used to acquire data and control the oxygen. The low frequency experiments were focused on obtaining a relationship between the amplitude or the accelerometer and the steelmaking process itself. On the other hand, the high frequency experiments attempted to discern the presence of specific vibrational frequencies that can be related to the process.

In this section the two types of programs are described and, where appropriate, the modifications to the experimental procedure are noted.

6.4.2 Low Frequency

The low frequency data acquisition and control program controlled the oxygen flow and monitored the accelerometer and thermocouples; the photocell was not employed in these experiments. The accelerometer circuit was modified by applying a reference voltage across the differential signal from the accelerometer's signal conditioning circuit. By applying a known voltage the effects of noise were greatly reduced. In addition to the voltage, a resistor, 10 k Ω , was used to "short" the signal to a voltage compatible with the thermocouples.

The microprocessor environment consisted of an IBM PC (PC) compatible and HP 3497A Data Acquisition/Control (unit). The PC employed the 8086 processor operating at 4.77 MHz and the Tecmar PC-Mate IEEE-488 interface card; other aspects of the PC are described in Fig. 6.7. The HP 3497A DAC unit employed the digital voltmeter (DVM) and the mercury form C relay actuator options. In addition, the DAC unit was equipped with the IEEE-488 interface, also known as the general purpose interface bus (GPIB). All data acquisitions and control actions were performed by the DAC unit under the request of the PC. The communications between the two units was facilitated by the GPIB interface card in the PC.

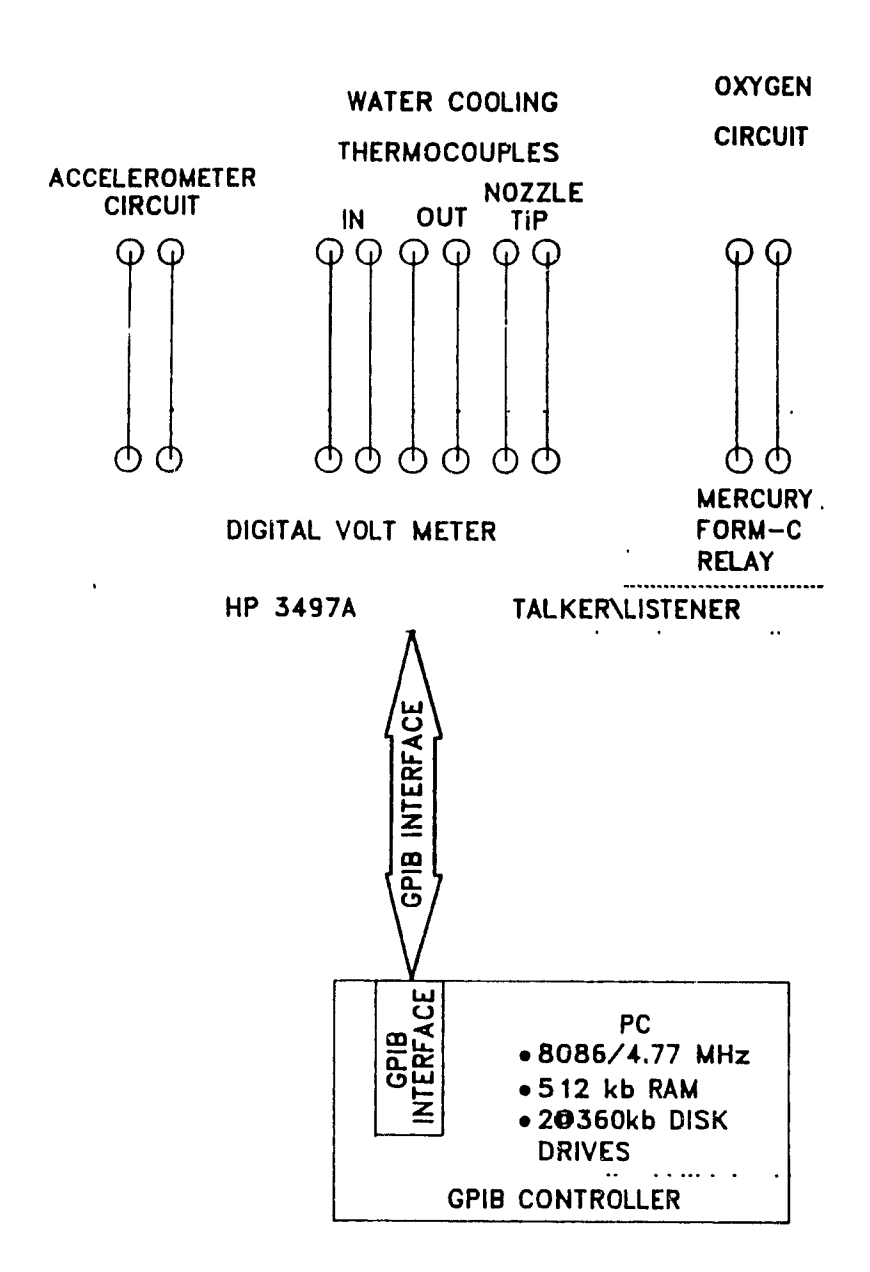


Fig. 6.7 Microprocessor environment during low frequency experiments.

The GPIB communications bus was developed by Hewelt Packard (HP) and is primarily used in the scientific and laboratory fields. It consists of 24 wires (8 of which are grounded) which allow data to be exchanged in a one byte serial, 8 bits parallel format amongst a maximum of 15 devices at speeds of 1Mb/s with full handshaking. One of the 15 devices is assigned as the active bus controller and is responsible for the coordination of the data transfers. The controller can assign itself and other devices as either "talkers" or "listeners", with the restriction that only one device can talk at a time.

The general concept of the bus typically has a computer as the controller and various laboratory instrum its connected to the GPIB. The data transfer rate and control of the data transfers is performed by a three-wire handshake. The handshake technique permits slow and high speed devices on the bus to communicate with each other at the speed of the slowest device. All devices must handshake when general GPIB commands are being sent, but only listeners handshake with the talker for data transmission. This allows for high speed transmission between faster devices, even though there may be slower devices on the bus.

Controller commands consist of bytes whose meanings are divided into four general categories according to the values of bits 5 and 6 of the data lines. When bits 5 and 6 of a GPIB command are zero, the remaining five low-order bits specify various bus commands. The remaining three groups are reserved for device addressing. Device addresses are typically specified by DIP switches located on the

devices.

The Tecmar IEEE-488 interface card provides the PC with complete access to the GPIB. The interface card implements the Intel GPIB chip set comprising of a 8291a GPIB talker/listener, a 8292 GPIB controller and two 8293 bus receivers. The board allows the host to act as either a bus controller or as an addressed talker/listener. The interface card can either be I/O or memory mapped to the internal bus of the PC. The application program, written in advanced basic, incorporated support software supplied by Tecmar (with minor modifications) that provided the control of the GP 3. The program begins by presenting a check list of the sensors and relays accommodated during the experiment. The next stage of the program requests some of the pertinent information required for the experiment such as the reference junction temperature, the duration of the blow, file names et cetera.

The third stage of the program initializes the program itself, the Tecmar interface card, the GPIB, and the HP 3497A DAC unit. Once the initialization has been completed and the control and data acquisition sequence has received a signal from the user, it enters a one minute delay loop. During this delay the oxygen is off, however, the program requests the DAC unit to acquire and send data for the accelerometer and thermocouples every second. The signals from the sensors are displayed to the user on the screen. The acquisition of the data during this delay loop serves as a record of the background noise and initial conditions.

At the end of the one minute delay, the computer requests the DAC unit to close the normally-open mercury form C relay actuator. This causes the solenoid valve to open and a red safety lamp to be illuminated, marking the start of the steelmaking process. The data acquisition sequence is modified to provide for five readings of the accelerometer and one reading of the thermocouples per second. The data acquisition continues in cyclical manner. Once per second the screen is updated. When the looping has terminated the processor requests that the DAC unit to open the relay switch for the oxygen, hence closing the oxygen valve and ending the experiment.

In a final stage the computer requests additional information and then writes the information obtained during the simulation into the specified files. The data is subsequently used in other programs for analysis.

6.4.3 High Frequency

Two independent microprocessors were employed to perform the high frequency data acquisition and control of the BOF simulation experiments. One processor, HP85A, controlled the oxygen and monitored each of the following signals: (1) photocell directed at the mouth of the BOF vessel, (2) the cooling water thermocouple at the exic of the oxygen lance, and (3) the cooling water at the nozzle tip of tip of the oxygen lance at a frequency of ≈ 1 Hz. The inlet temperature was determined to be relatively constant throughout the duration of a simulation and, for this reason, was not monitored.

A second processor was devoted entirely to the data acquisition and storage of the accelerometer signal on the floppy diskettes at a typical rate of 1500 Hz for the entire blow. The components of the data acquisition consisted of a PC, an analog/digital Input/Output (I/O) system board, the accelerometer and conditioning circuitry and, naturally, software to integrate these components. The accelerometer signal conditioning circuit employed low-pass filter that attenuated electrical noise whose frequencies were above 2000 Hz. The accelerometer circuit is shown in Fig. 6.8. The data acquisition system offers an inexpensive, yet versatile technique of sampling the accelerometer signal at high speeds continuously, the only limit being the speed and capacity of the storage medium and the number of these devices available. For the configuration presented in Fig. 6.9 the maximum sampling rate for continuous monitoring is 3 kHz.

The continuous sampling of the signal at high rates is made possible by several features of the Analog/Digital (A/D) I/O board. Specifically, these features are an on board microprocessor to facilitate the I/O functions, a programmable clock providing repetitive A/D data conversions at a user defined frequency, and asynchronous Direct Memory Access (DMA) transfer of the A/D conversions between the board and the computer. Asynchronous requests transfer data while the CPU continues to process the program code. The data acquisition I/O board was a DT-2805 from Data Translation.

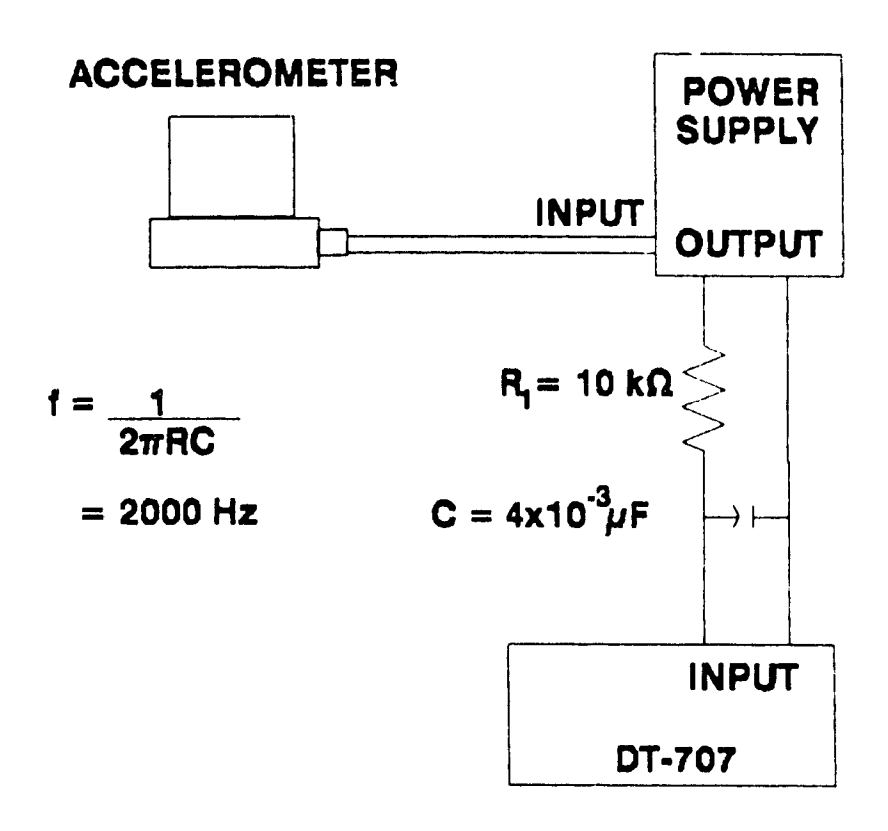


Fig. 6.8 Accelerometer circuit used in the high frequency experiments.

The software essentially performs four main tasks; the first task is to request information concerning the operation of the I/O board, the storage of data, and the duration of the simulation. The second task prepares the I/O board with the required parameters and awaits for a signal to commence the analog to digital conversions of the accelerometer signal. The third task is to control a circular data buffer which receives data from the I/O board and sends data to the floppy disk drives for storage.

Once the A/D conversions begin under continuous DMA control the first A/D conversion data is transferred from the board to the beginning of the buffer. At this point the DMA controller automatically increments its pointer to the next place in the buffer. This is repeated until the end of the buffer at which time the pointers are initialized to the beginning of the buffer, hence, the term circular buffer. As was mentioned above, the data transfer is asynchronous, permitting the program to continue while the transfers are occurring.

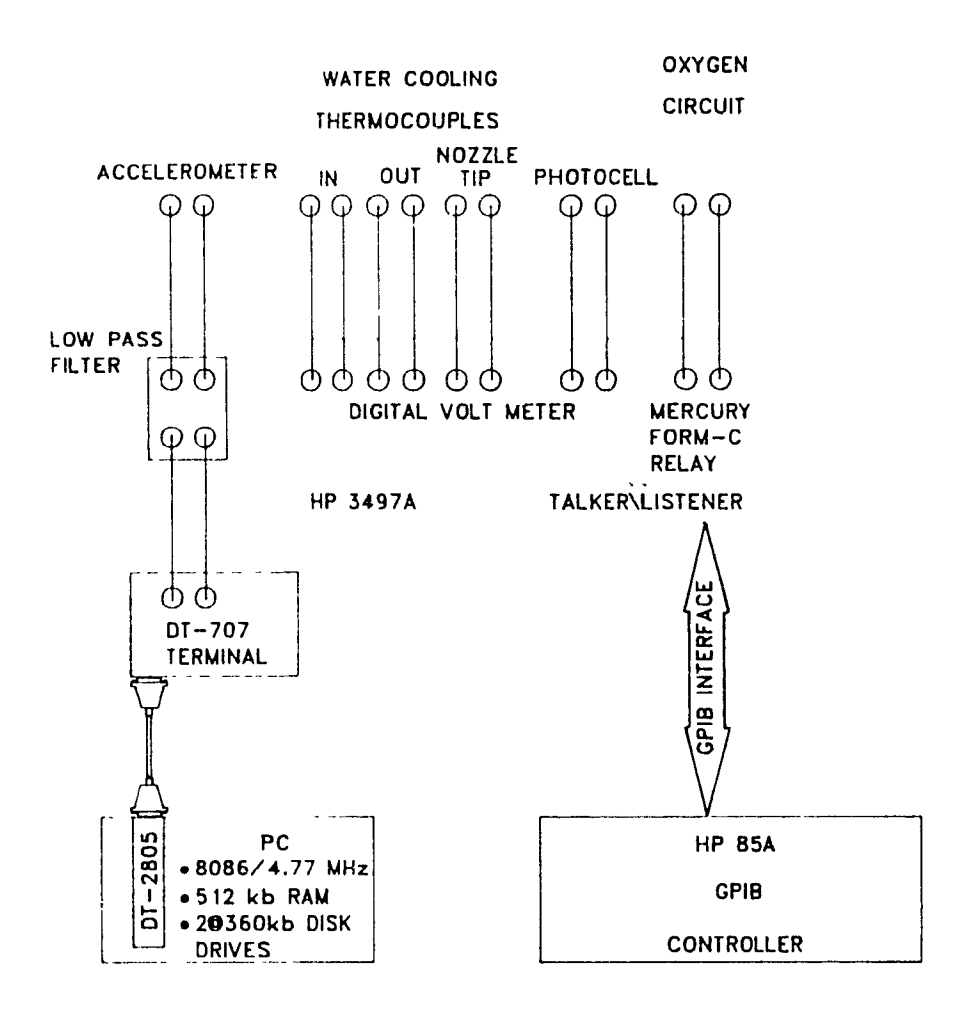


Fig. 6.9 Microprocessor environment during low frequency experiments.

The program enters a wait state after initiating the A/D conversions until the first half of the of the buffer is filled. Following the wait state, the program then simply writes the first half of the buffer in an unformatted form to the disk drives while the DMA transfers continue in the second half of the buffer. Once the first half of the buffer is written to a diskette the program enters another wait state. The second wait state is terminated once the second half of the buffer is filled with A/D conversions. The program then writes the second half of the buffer to the disk drive while the first half of the buffer is being over-written with new A/D conversion values.

The scheme is simply repeated until the end of the blow. An obvious limit to the scheme is the ratio between the time required to write one half of the buffer to a diskette and the time required to fill one half of the buffer, which, for successful operation, must be less than unity. Variables affecting this ratio are the disk access time, frequency of the A/D conversions and the length of the buffer. The final task is to stop the DMA transfer requests. The accelerometer data is subsequently analyzed at a later point in time.

6.5 Experimental Procedure

The first stage of the experimental procedure, regardless of the type of data acquisition and control program, consisted of preparing the charge for melting, mounting the water-cooled, oxygen lance well above the induction furnace and connecting the service lines, oxygen and water, for the lance. At this time the cooling water line was opened

to provide a specific flow rate, typically 125 ml/s, and the melting sequence initiated. The duration of the melting and superheating period ranged from 1.5 to 2.5 hours, depending on the weight of the charge. During this time, the wiring for the sensors and relays was completed and verified.

Once the liquid bath reached the desired temperature, the accelerometer was mounted onto the furnace, as shown in Fig. 6.10. In addition, the bath was sampled and the oxygen lance was brought into the desired position above the liquid surface. These items were the final mechanical aspects of the procedure prior to the start of the blow. This minimized temperature affects on the accelerometer output signal and reduced the risk of having the lance nozzle blocked. The final task required was to initialize the computer programs and, after a brief delay, the oxygen flow was activated.

The oxygen flow marked the true start of the BOF simulation. After the blow was completed, the oxygen lance was raised and the bath was sampled and a temperature taken. Typically, the bath had to be deoxidized by adding aluminum rod in order to obtain an adequate sample. The samples were subsequently analyzed by a LECO CS-240.

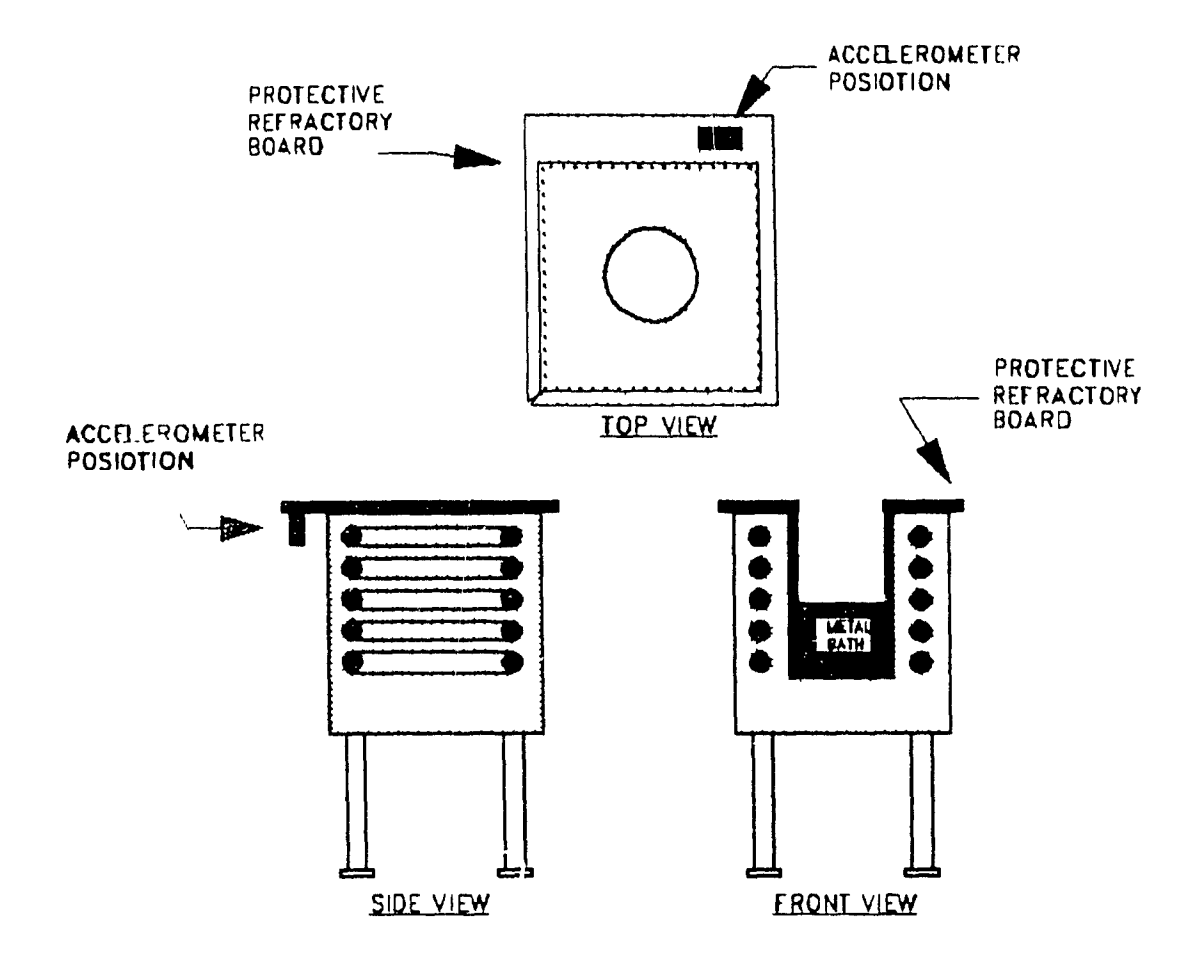


Fig. 6.10 Positioning of the accelerometer on the induction furnace structure.

,

Chapter 7

7. Results and Discussion

7.1 Introduction

To determine the feasibility of the accelerometer as an end-point control sensor, two series of laboratory scale BOF simulations were performed. The first series of simulations were focused on obtaining a relationship between the amplitude of the accelerometer and the steelmaking process itself. Since one can think of vibrations as a variation in acceleration and, therefore, in the accelerometer signal, the first series of simulations monitored the accelerometer signal at a low frequency. On the other hand, the second series of simulations attempted to discern the presence of specific vibrational frequencies that can be related to the process. For this reason, the accelerometer signal was monitored at higher frequencies.

As a final aspect of the research work, the feasibility of the accelerometer for various product mixes, essentially the carbon endpoints of the steel, was determined. This involved terminating several high frequency BOF simulations prematurely in an attempt to elucidate the maximum carbon content of the steel when the accelerometer can detect the final change in the equation describing the rate of decarburization, the carbon content reference point.

In this chapter, a general overview of the operating parameters of the simulations is presented, followed by the results of the low and high frequency simulations in subsequent sections. Concluding this chapter is a discussion on the carbon content reference point.

7.2 General

More than twenty-five BOF simulations were conducted during the course of this research work. The performance of the water cooled oxygen lance proved to be excellent; the nozzle tip was replaced only once due to erosion of the orifice at the tip. In addition, the refractory system, a disposable alumina crucible, containing the liquid metal provided a safe environment in which to conduct this type of work. An example of the steelmaking vessel, after a simulation, is shown in Fig. 7.1; note the absence of any metal penetration.

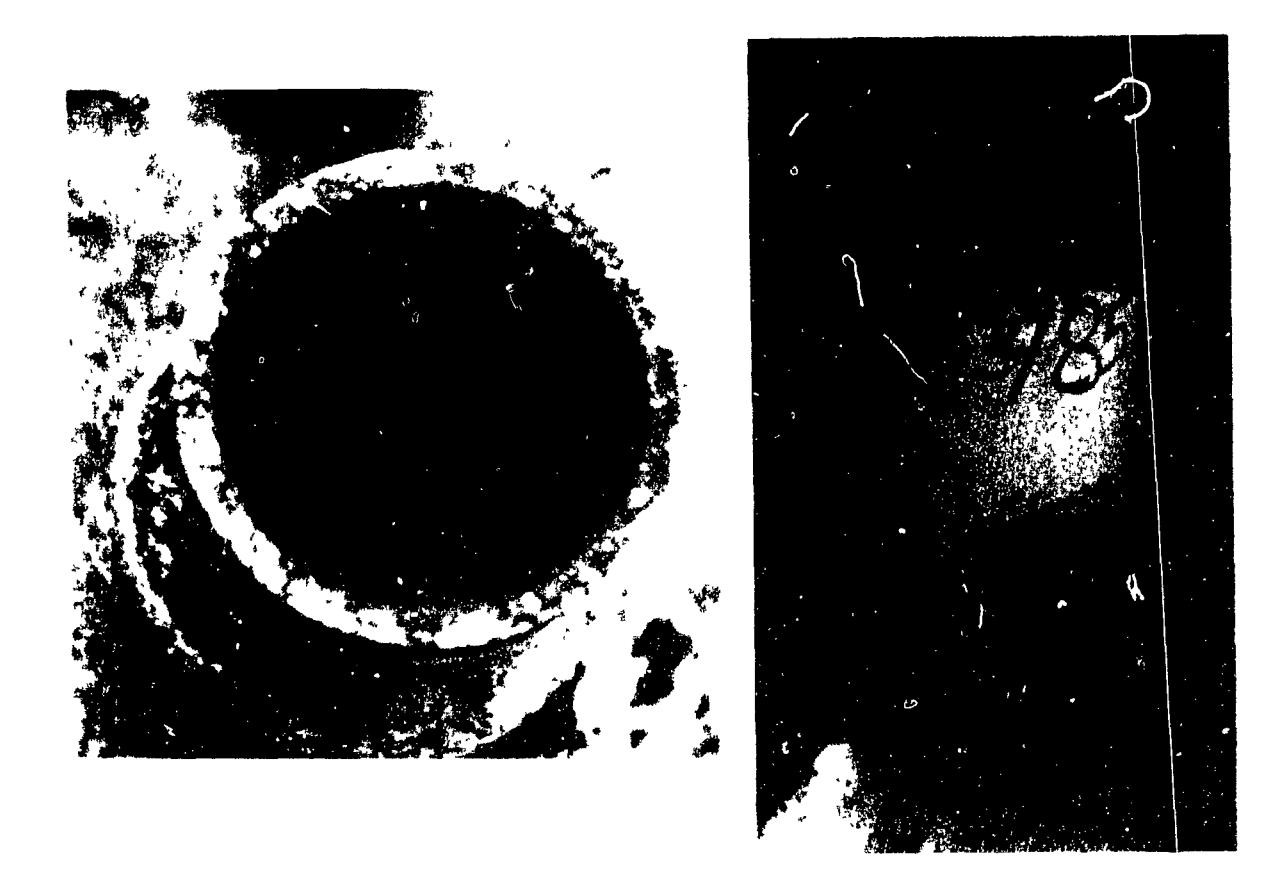


Fig. 7.1 Condition of the steelmaking vessel, an alumina crucible, after a BOF simulation.

Although not all simulations were successful in producing steel as a result of experimental difficulties, the majority of the simulations produced steels with a carbon range of 2.1 to 0.01 % (wt). A summary of the BOF simulations is presented in Table 7.1. The simulations are coded as A1-A4, B1-B10 and C1-C6 representing those simulations performed under low frequency (A) and high frequency (B&C); reconstruction of the furnace following the B series of simulations distinguishes the two series. As can be seen, initial hot metal weight varied from 12.7 to 23.2 kg while the carbon content of the hot metal varied from 3.4 to 4.25 % (wt). The hot metal, referred to as Sorel Metal, was supplied by Quebec Iron and Titanium. parameters of the cooling water were preset for all simulations; a cooling water flow rate of 100 g/s was typically employed. The height of the lance above the melt was determined prior to the start of the oxygen flow and varied between tests from 20 to 35 mm.

As a result of the low volume-to-surface-area ratio of the laboratory scale BOF, additional energy was occasionally derived from the induction furnace. The power setting on the furnace control panels varied from 0 to 12 kVA. The need for additional energy sources complicated the application of a slag phase to absorb liquid oxides. However, previous work proved that the absence of a slag phase did not hinder the simulation. This maybe due to the relatively low quantity of other elements in Sorel Metal.

Table 7.2. Summary of BOF Simulations.

Test	Test Date	Hot	Free	Lance	Height	กับmace	Initial	Final	Change		Pressure		Blown	Blowing	Average	Oxygen
Code		Metal	Board	Depth	Λαο ν•	Power	Carbon	Carbon	ln	initial	Final	Change in	Oxygen	Tlme	Oxygen	Decarburtzation
		Welght			Mert				Carbon	Oxygen	Oxygen	Oxygen	Volume		Flow Rate	Efficiency
		(kg)	(mm)	(mm)	(mm)	(KVA)	(%)	(%)	(%)	(atm)	(atm)	(atm)	([**])	(s)	(N*Vs)	(%)
A/1	Jun-11-1985	13.6	195	162	33	12	4 05	0 01	4 04	152 4	120 4	32 0	1355	1200	1 13	37 9
A/2	Jun-12-1985	13.6	187	167	20	10	4 04	0 01	4 03	1150	905	245	1038	980	1 08	49 4
A/3	Jun-13-1985	1 J.B	200	177	23	12	4.14	0 01	4 13	8 68	68.0	218	923	900	1.03	57 0
A/4	Jun-17-1985	132	200	165	35	12	4 25	0.03	4 22	66 0	44 2	218	923	840	1 10	563
B/1	Aug-20-1985	13.4	185	150	35	10	4 20	0 04	4 18	98 7	755	23 1	981	780	1 28	53 1
B/2	Aug-21-1985	13.6	195	160	35	10	4 01	0 02	3 99	75 5	55 1	20.4	865	810	1 07	58.7
8/3	Aug-21-1685	136	190	155	35	10	4 17	0 01	4 18	55 1	340	21 1	894	900	0 99	59.2
8/4	Aug-27-1985	12.7	200	170	30	10	4 13	0 03	4.10	39 5	204	191	808	720	1 12	60.3
8/5	Aug-27-1985	15.9	175	140	35	10	4.13	2.09	2.04	#N/A	#N/A	#N/A	#N/A	634	#N/A	#N/A
B./6	Sep-06-1985	184	155	120	35	10	4 C5	0 60	3 45	25 9	00	25 8	1096	720	152	543
B/7	Sep-20-1985	141	180	145	35	0	3 40	0 01	3 39	148.3	125.9	22.5	952	810	1 17	46.8
8/8	Sep-25-1985	:43	190	155	35	10	4 14	60.0	4.12	125.2	100.7	245	1038	600	1.15	53 0
B/9	Sep-26-1985	136	195	160	35	10	3 97	0.05	3.95	101.7	69.7	32 0	1355	750	1 81	37 1
B/10	Oct-01-1985	134	200	165] 35	10	3 99	0 01	3 98	54.1	323	218	923	720	1 28	54.0
C/1	Jan-29-1987	141	190	165	25	#N/A	4 00	1 01	2 99	136 1	115.7	20 4	865	720	1.20	45 4
C/2	Jan-30-1987	22 7	220	195	25	#N/A	4 00	1 94	2 06	1157	953	20 4	865	960	0 80	50 5
C.3	Feb-02-1987	23.2	220	195	25	#N/A	4 00	0.44	3 56	87 1	612	25.9	1096	900	1 22	703
C/4	Feb-04-1987	22 2	230	205	25	#N/A	4 00	0 05	3 95	61 2	37 4	238	1009	1298	0.78	81 4
C/5	Feb-05-1987	218	235	210	25	#NA	4 00	0 40	3.60	144 6	115.7	28 9	1226	1050	1 17	598
Слв	Feb-06-1987	23 2	230	205	25	#N/A	4 00	0 04	3 96	1150	87 B	27 2	1154	1080	1 07	743
				! 						1	1					

Table 7.2 Oxygen Jet Penetration During BOF Simulations.

		·			
Test	Test Date	Average	Average Jet	Bath	Average Jet
Code		Impulse	Penetration	Depth	Penetration
		Force	Depth		Ratio
		(N)	(mm)	(mm)	(Unity)
A/1	Jun-11-1985	0.60	40.6	125	0.32
A/2	Jun-12-1985	0.56	46.6	133	0.35
A/3	Jun-13-1985	0.52	43.5	120	0.36
A/4	Jun-17-1985	0.58	38.8	120	0.32
B/1	Aug-20-1985	0.69	42.3	135	0.31
B/2	Aug-21-1985	0.56	38.1	125	0.30
B/3	Aug-21-1985	0.50	36.2	130	0.28
B/4	Aug-27-1985	0.59	42.0	120	0.35
B/5	Aug-27-1985	#N/A	#N/A	145	#N/A
B/6	Sep-06-1985	88.0	47.5	165	0.29
B/7	Sep-20-1985	0 63	40.5	140	0.29
B/8	Sep-25-1985	0.62	40.1	130	0.31
8/9	Sep-26-1985	1.09	52.4	125	0.42
B/10	Oct-01-1985	0.71	42.8	120	0.36
C/1	Jan-29-1987	0.65	46.6	130	0.36
C/2	Jan-30-1987	0.44	39.2	100	0.39
C/3	Feb-02-1987	0.66	47.0	100	0.47
C/4	Feb-04-1987	0 35	35.5	90	98.0
C/5	Feb-05-1987	0.63	45.9	85	0.54
C/6	Feb-06-1987	0 56	43.5	90	0.48

In general, the blowing time was predetermined and ranged from 12 to 20 minutes. The average oxygen flow rate ranged from 0.8 to 1.5 N 1/s and the oxygen decarburization efficiency ranged from 37 to 81%. Although metallic yield was not considered as an essential aspect of the simulations, it was verified on occasion and found to be $\approx 95\%$. In calculating the decarburization rate, a metallic yield of 100% was assumed.

As was mentioned in Chapter 2, $Shirma^{(24)}$ developed a nomograph for

determining jet penetration depth in molten steel. Furthermore, they indicated that the nozzle bore design, straight-bore or convergingdiverging, did not affect the jet penetration depth. For this reason, the nomograph was used to verify the jet penetration depth obtained during the steelmaking simulations. However, as can be seen in Fig. 2.33, the resolution of the nomograph is poor. To overcome this limitation, a relationship developed by Cheslak [77] that agreed with the work of Shirma was used to calculate the jet penetration. relationship, shown below, is a function of the impulse force, the density of the liquid steel and the height of the lance above the melt.

$$a = \frac{2(k_2)^2 M}{\pi y (h+a)^2}$$
 (7.1)

where

11

a = jet penetration depth (m)

 k_2 = constant (6.4) M = impulse force (kg m sec⁻²)

 γ_1 = specific weight of steel (kg m⁻² sec⁻²)

h = lance height above the melt (m)

The results of these calculations, shown in Table 7.2, indicates that the penetration depth of the oxygen jet ranged from 35.4 mm (1.396in) to 52.4 mm (2.064 in). This corresponds to a ratio range of 0.28 to .54 between the jet penetration depth and the bath depth. These values are in agreement with those observed by Rote[23] on industrial BOF vessels.

7.3 Low Frequency

The low frequency simulations, described in Chapter 6, were the first simulations performed. The accelerometer signal was measured at low frequency with the objective of obtaining an amplitude-time relationsh p that follows the ideal rate of decarburization. addition to the accelerometer signal, thermocouples monitoring the cooling water were also monitored. The results of these experiments are summarized in Tables 7.1-7.2 and are coded as A/1 through A/4.

The accelerometer signal and water cooling temperatures at t.e nozzle tip and outlet of the oxygen lance are shown in Figures 7.2 through to 7.13 for each simulation. As was mentioned above, an analysis of the accelerometer signal was performed for each simulation. The analysis involved calculating the variance of small packets of data over the entire simulation, as shown below.

$$\sigma_{c} = \frac{\sum_{i=tn}^{i=n(t+1)-1} X_{i} - \frac{1}{n} \sum_{i=tn}^{i=n(t+1)-1} X_{i}}{n-1}$$
 (7.2)

where σ_i = variance of the accelerometer signal over a specific time

n = the number of accelerometer values in a specific time span X_i = individual accelerometer values from a specific time span t = the start pointer, with respect to time, in the overall accelerometer data set

The time pointer, t , was incremented to match the rate of the acceleroemter acquisition at one second intervals. In addition, the size of the time span, determined by n, was set at 4 seconds or 20 data points. Hence, the analysis was performed in a procedure that is similar to the moving average analysis.

The variance-time relation, for each simulation, is shown in Figures 7.14 to 7.17. Note that the units of the variance axis are intentionally omitted because the specific accelerometer variance values were specific to one simulation.

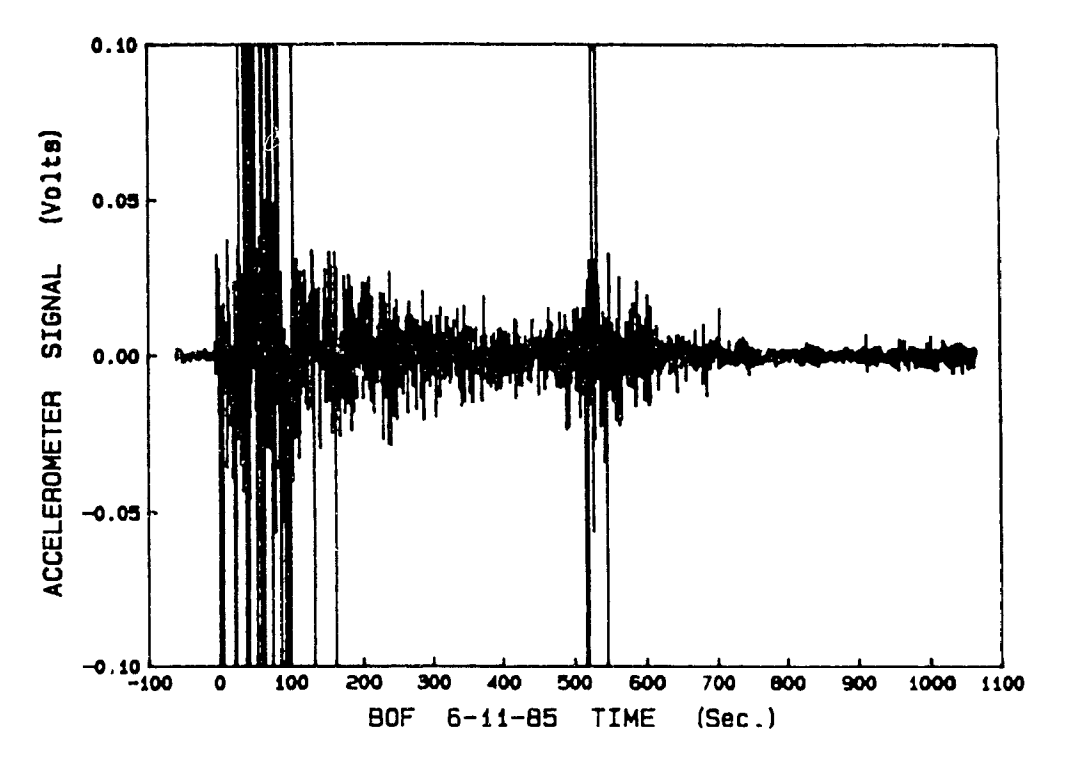


Fig. 7.2 Accelerometer signal during BOF simulation A/1.

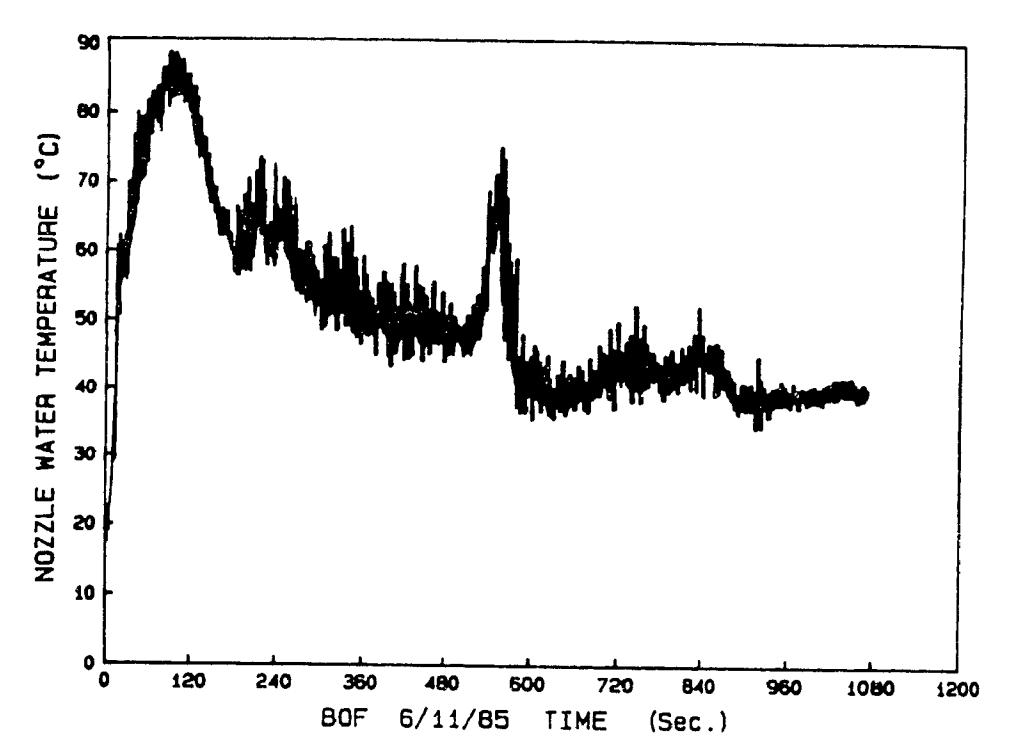


Fig. 7.3 Temperature of the cooling water at the nozzle tip during BOF simulation A/1.

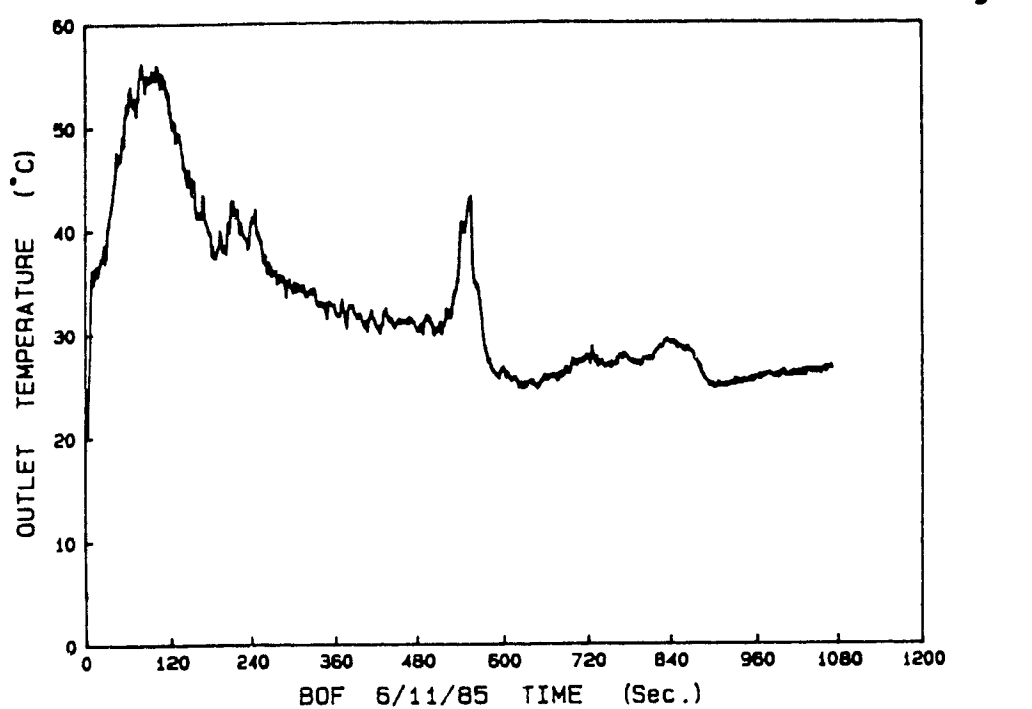


Fig. 7.4 Temperature of the cooling water at the exit surge tank during BOF simulation A/1.

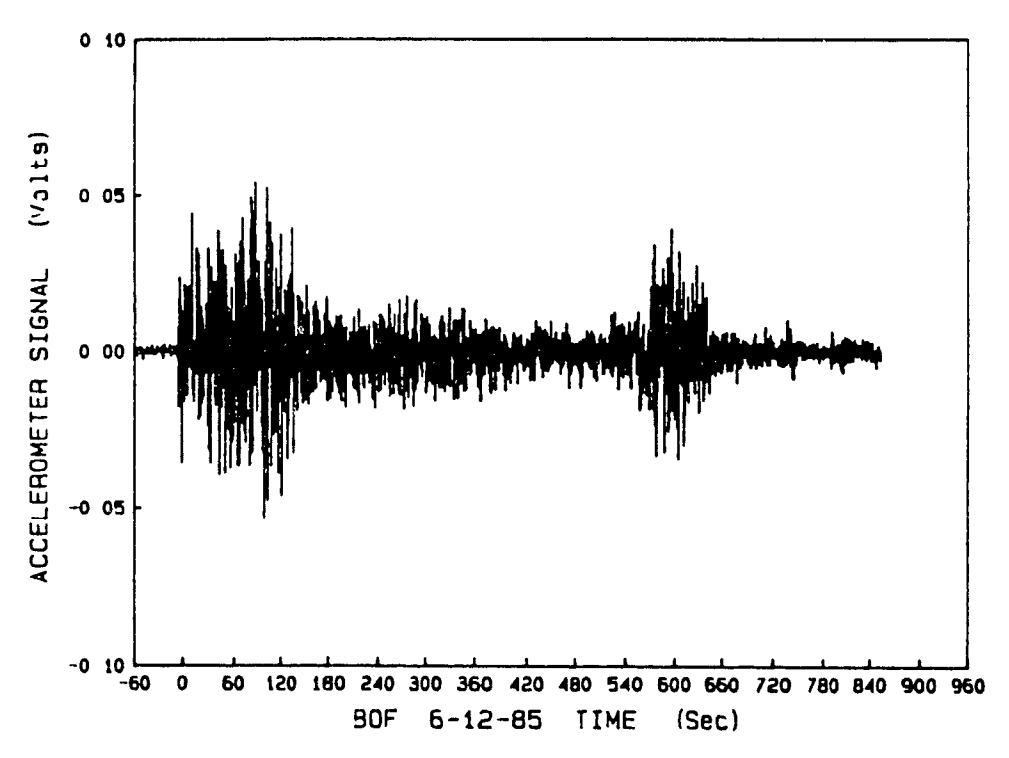


Fig. 7.5 Accelerometer signal during BOF simulation A/2.

Fig. 7.6 Temperature of the cooling water at the nozzle tip during BOF simulation A/2.

(Sec)

6-12-85 TIME

90F

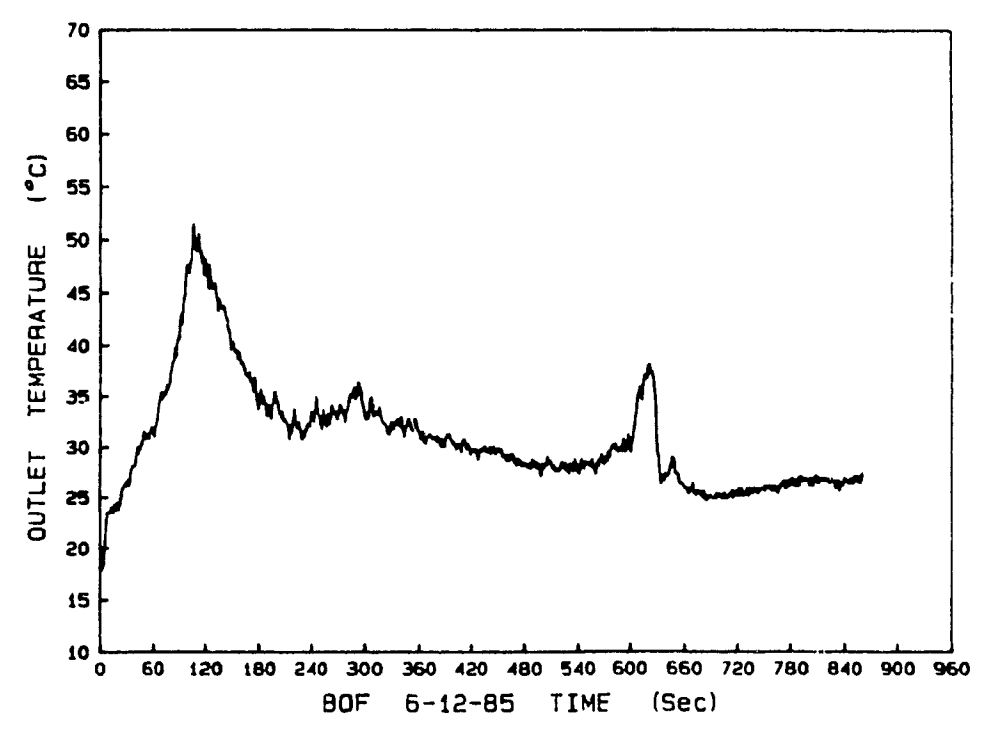


Fig. 7.7 Temperature of the cooling water at the exit surge tank during BOF simulation A/2.

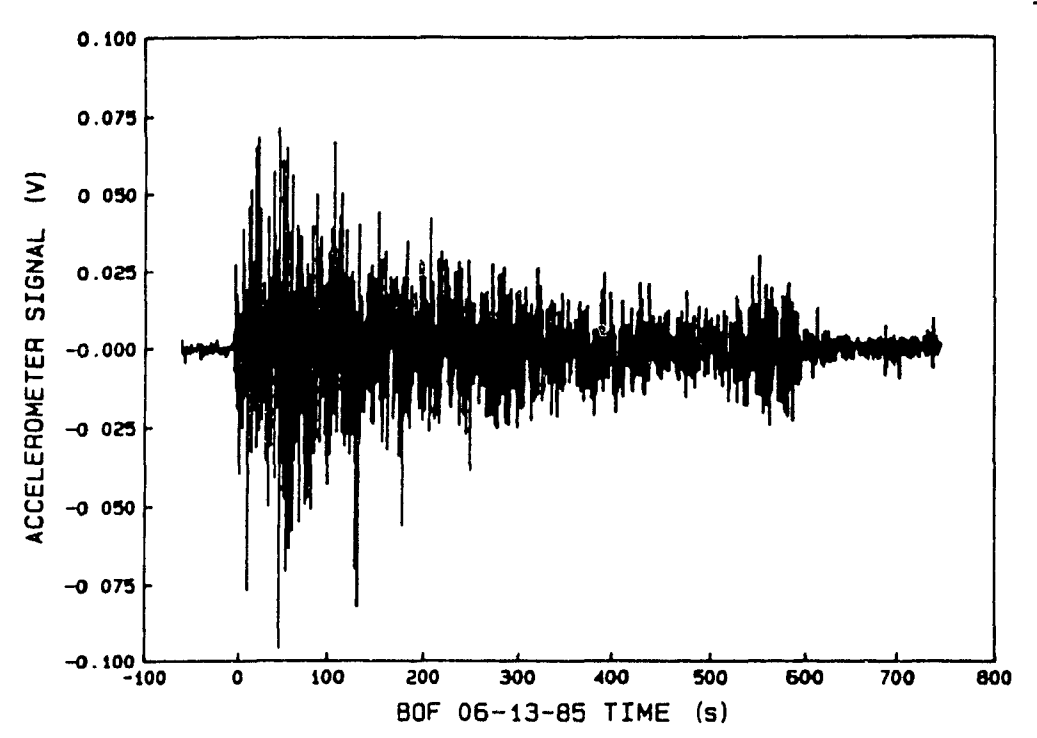


Fig. 7.8 Accelerometer signal during BOF simulation A/3.

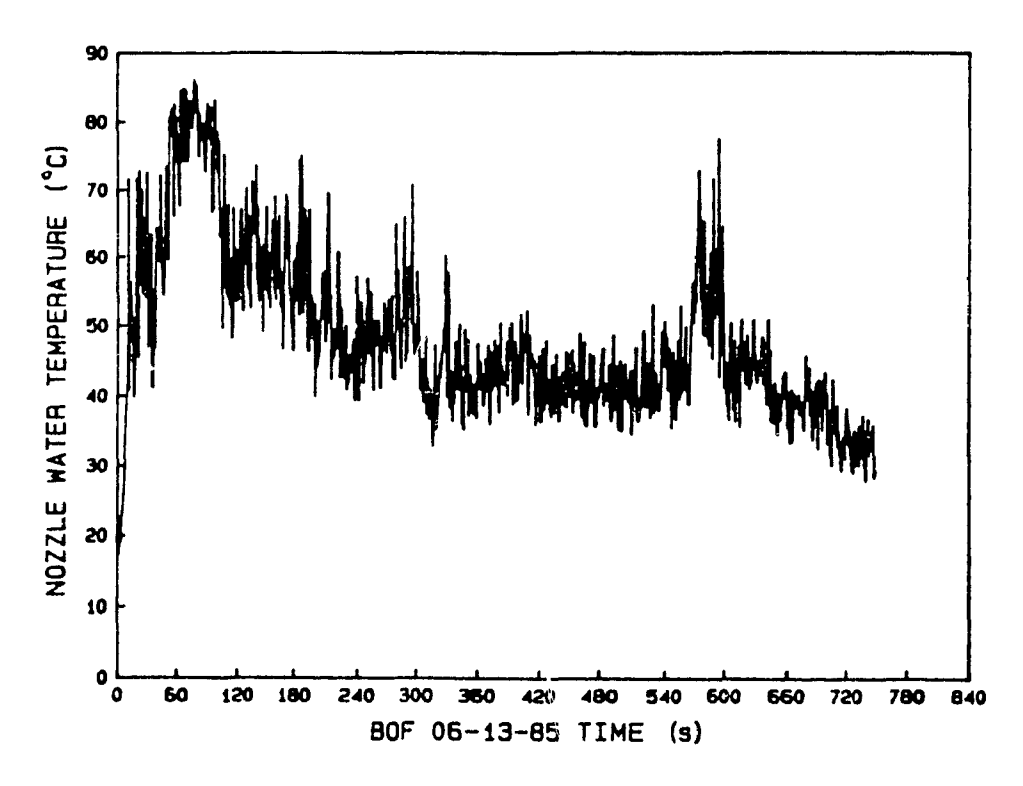


Fig. 7.9 Temperature of the cooling water at the nozzle tip during BOF simulation A/3.

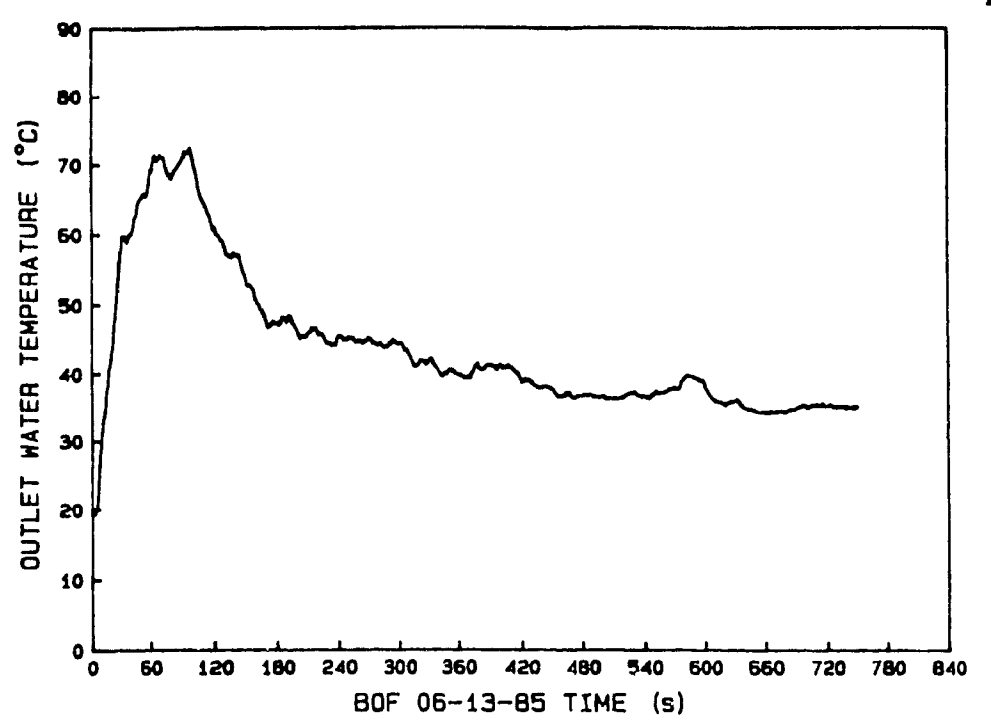


Fig. 7.10 Temperature of the cooling water at the exit surge tank during BOF simulation A/3.

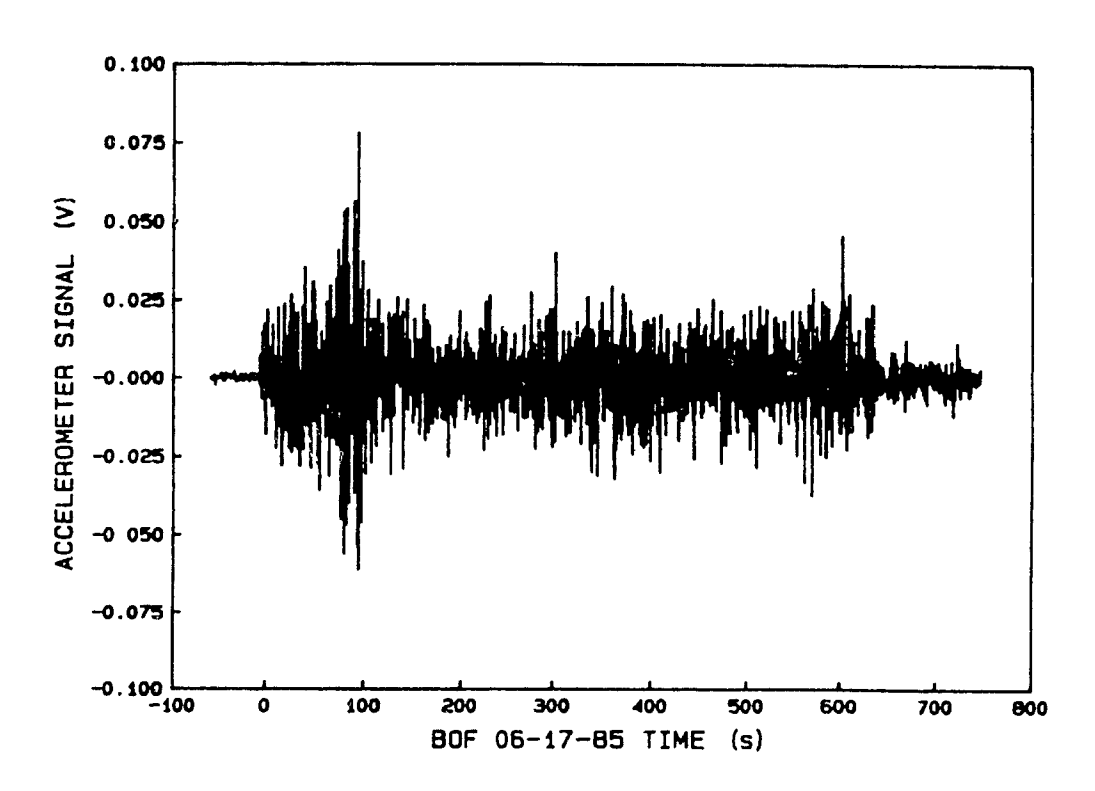


Fig. 7.11 Accelerometer signal during BOF simulation A/4.

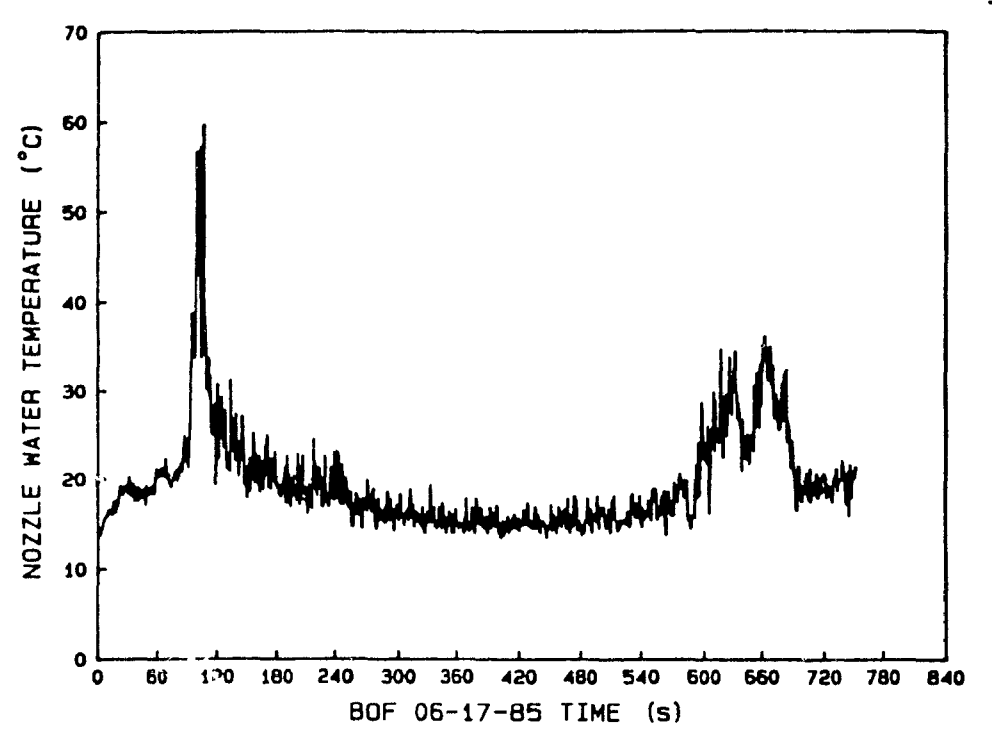


Fig. 7.12 Temperature of the cooling water at the nozzle tip during BOF simulation A/4.

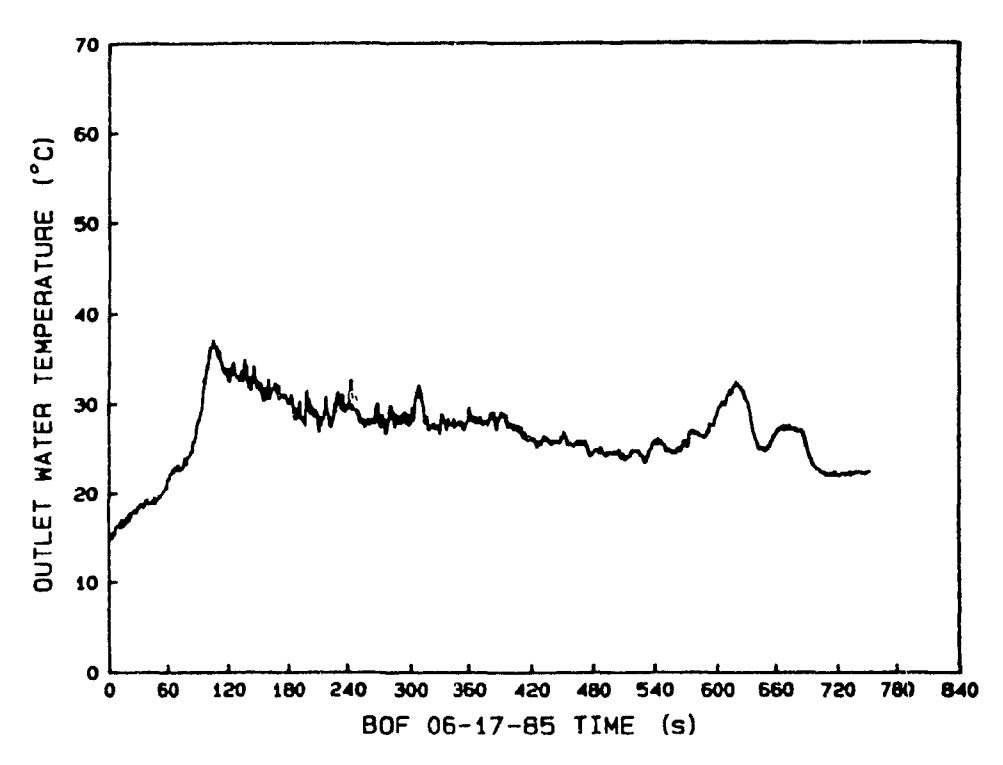


Fig. 7.13 Temperature of the cooling water at the exit surge tank during BOF simulation A/4.

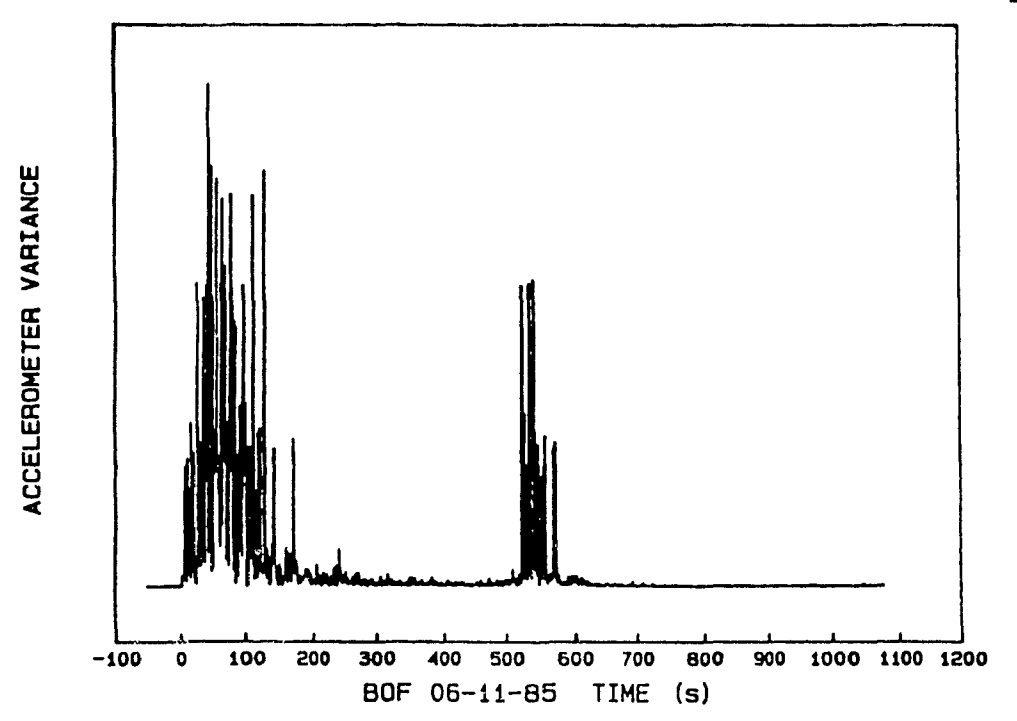


Fig. 7.14 Variation of the accelerometer signal during BOF simulation A/1.

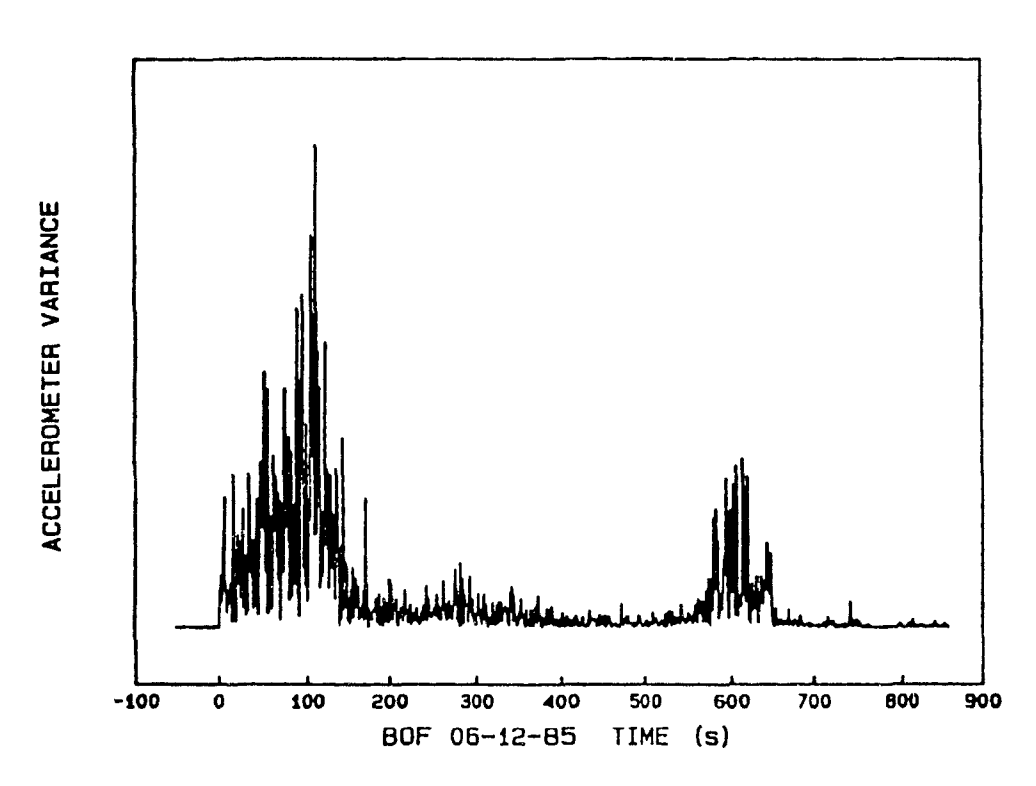


Fig. 7.15 Variation of the accelerometer signal during BOF simulation A/2.

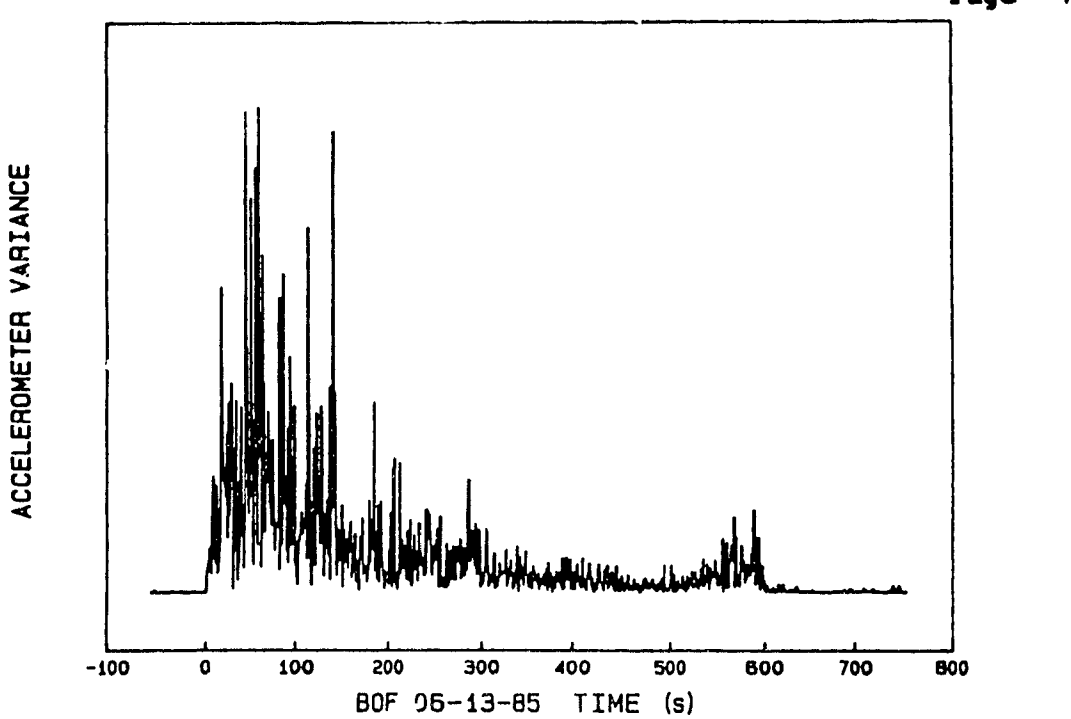


Fig. 7.16 Variation of the accelerometer signal during BOF simulation A/3.

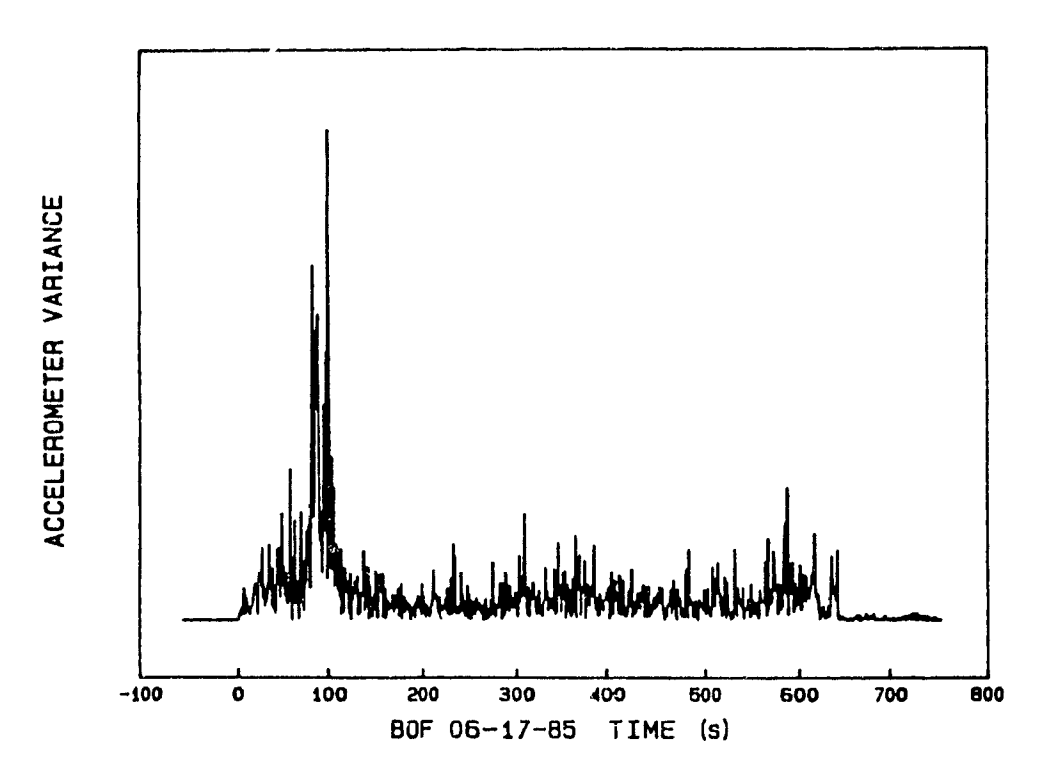


Fig. 7.17 Variation of the accelerometer signal during BOF simulation A/4.

The typical accelerometer variance curve can be described as having three regions. The first region exhibits a characteristic increase in variance, which can be explained by the fact that the rate of decarburization is also increasing. The second region, the middle portion, has the characteristic of a significant, but consistent, variation corresponding to a constant rate of decarburization. The third region has the characteristic of a sharp decrease in the variation of the signal, as the rate of decarburization begins a rapid decay as the level of carbon falls below a critical value towards the end of the blow and the vibrations of the furnace decrease dramatically.

As can seen by comparing the accelerometer variance-time curves to the ideal rate of decarburization shown in Fig. 2.31, these characteristics follow the ideal rate of decarburization. The most important change in decarburization that the accelerometer can detect is the final change in the rate of decarburization because it provides a carbon reference point near the end of the simulation. One can see this anticipated decrease in the variation of the accelerometer signal in Figures 7.14 through to 7.17.

One major deviation from the ideal decarburization curve was found in several variance-time curves and was exhibited as a relatively large increase in the variance just before the final decay in the accelerometer signal, as can be seen in Fig 7.14 and 7.15. However, this increase was not exhibited in simulations A/3 and A/4. This peak has been attributed to an over-oxidized, foaming slag that occurs just

before the final decay point and supplies additional oxygen to the decarburization reaction and subsequently increases the volume of CO_{gas} produced. As a result, the steelmaking vessel vibrates more intensely, increasing the variance of the accelerometer signal.

As can be seen by reviewing these results, the temperature of the cooling water also follows the ideal decarburization path, but not with the same degree of reliability. Because the cooling water flow rate is constant during a particular simulation, the cooling water temperature is proportional to the thermal energy removed by the lance. The thermal energy is transferred to the lance by three menchanisms:

(1) conduction, (2) convection and (3) radiation. As the amount of energy released from the steelmaking process changes, so does the energy transferred to the lance. Moreover, the amount of energy released is largely determined by the decarburnaztion rate, thus, explaining the relationship between the cooling water and the process.

The differences between the outlet and nozzle tip temperatures can be explained by the following two statements:

- (1) Becuase the surge tank thermocouple provides an overall average temperature of the water whereas the thermocouple at the nozzle tip provides an indication of the temperature of the cold water rushing across the cold face of the nozzle tip, the two cooling water temperatures can be quite different.
- (2) Due to the erratic nature of metal/slag splashing, the proximity of the nozzle tip to the bath, and the high rates of heat transfer associated with conduction, the variation in the temperature at the nozzle tip is invariably higher than at the outlet surge tank.

The advantage of the accelerometer over the thermocouples as a dynamic

1

control sensor is its reliability. Consider the results of simulation A/3, Fig. 7.8-7.10 and Fig. 7.16, where the final decay in the decarburization rate cannot be clearly distinguished in the thermocouple signals, however, it is readily seen in the accelerometer signal and, even more clearly, in the variance-time curve at approximately 600 seconds. Moreover, this explains the reluctance of steel producers to pursue the cooling water temperatures as a means to achieve dynamic control of the steelmaking process.

The accelerometer is also sensitive to the operating parameters of the simulation. The weight and carbon content of the metal, for a given oxygen flow rate and lance height, affect the time required to reach the critical carbon content. The oxygen flow rate and lance height can produce similar results.

An additional effect of the oxygen flow rate and lance height parameters is the increase or decrease in the variations of the accelerometer readings after occurrence of the decay. The magnitude of the impact of the oxygen jet on the melt can be a source of this post-decay variability of the accelerometer signal. This situation is evident in Figure 7.15 where the relatively high variation after detection of the decay was a result of the lance height parameter being reduced.

7.4 High Frequency

1

General operating results of the high frequency simulations are summarized in Tables 7.1-7.2 and are coded as B/1-B/10 and C/1-C/6. The "C" series of simulations were performed after the furnace was reconstructed in a new area, hence, explaining the difference in the test dates. Furthermore, the thermocouples for the water cooling and the photocell signals were not retained for future reference in the "C" series.

Operationally, the high frequency simulations were plagued with two notable problems. The most significant was related to the data acquisition program resulting in the loss of the accelerometer data for simulations B/1-B/5. The cause of the data loss was identified as an unforeseen interaction between the data acquisition modules and the system status register of the central processing unit (CPU) that was affecting the data storage module. The second operating problem was damaged accelerometer cables that occurred during simulations B/7, B/8 and B/10 as a result of liquid metal splashes. This problem was overcome by shielding the accelerometer cable within a fibreglass sheath. For reasons described above, only simulations B/6 and B/9 are presented from the "B" series of simulations.

In order to provide a continuation between the low and high frequency simulations, the high frequency simulations are first presented in a similar format. However, as a result of the enormous quantity of data points generated during each simulation, a running average of the accelerometer signal is presented in lieu of the raw data, the running

average is shown below.

$$\overline{X}_t - \frac{1}{n} \sum_{i=tn}^{i=n(t+1)-1} X_i$$
 (7.3)

where X_t = mean of the accelerometer signal over a specific time span n = the number of accelerometer values in a specific time span X_i = individual accelerometer values from a specific time span t = the start pointer, with respect to time, in the overall accelerometer data set

Initially, the time pointer, t, was incremented by one half second and the specific time span was kept at the equivalent of one second, as in the typical running average procedure. However, to simplify the analysis, including the Fourier Fast Transform, it was decided to increment the time pointer by one second and maintain the specific time span, n, at the equivalent of one second. This modification was also employed in calculating the variance-time curves (Eq. 7.2) and did not effect the results.

The mean and variance of the accelerometer signal followed by the cooling water temperatures and the photocell intensity are shown in Fig. 7.18 to 7.27 for simulations B/6 and B/9, while the mean and variance of the accelerometer signal for simulations C/1 through C/6 are shown in Fig. 7.28-7.39. As can be seen the similarities between the low and high frequency simulations is excellent.

The most notable exception, however, is the mean accelerometer signal which is almost always flat. This is the result of the low-pass filter, described in Chapter 6, which essentially shorts the high and low sides of the signal. Although, when the "B" and "C" series are

compared, one can easily detect the drift in the accelerometer mean, especially in simulations C/2 and C/4. The other major exception is the absence of a significant decrease in the accelerometer variance level towards the end of the oxygen blowing period for simulations B/6, C/1, C/2, and C/3. This aspect will be expanded upon further after the results of the frequency analysis are presented.

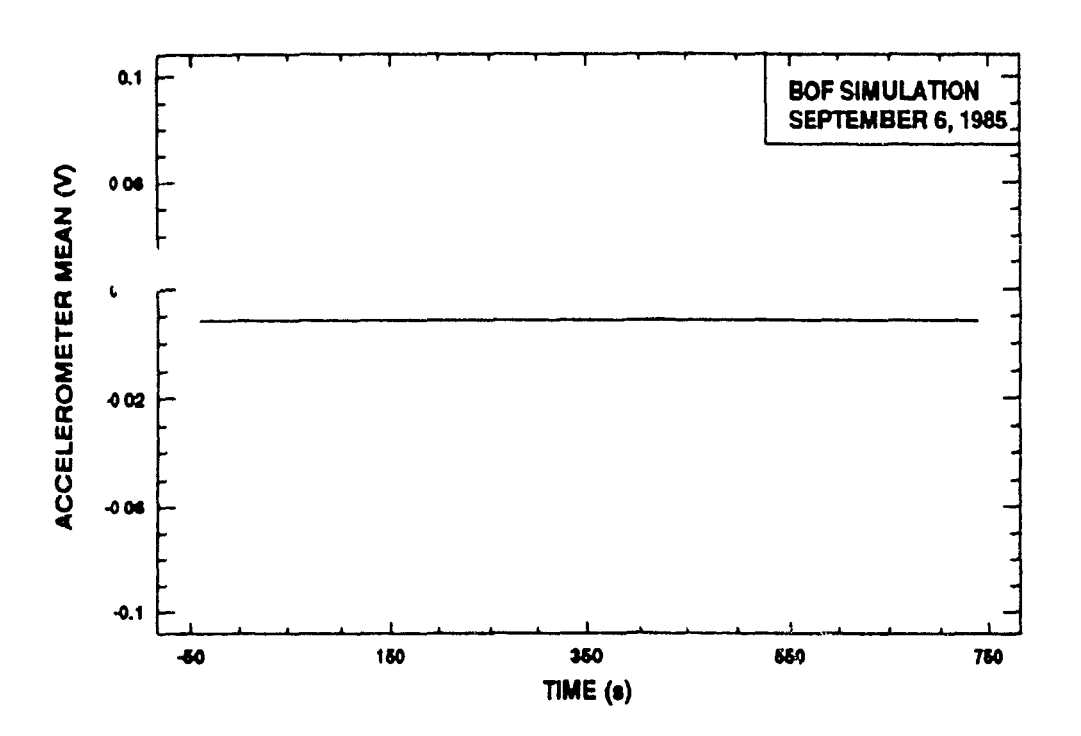


Fig. 7.18 The mean of the accelerometer signal during BOF simulation B/6.

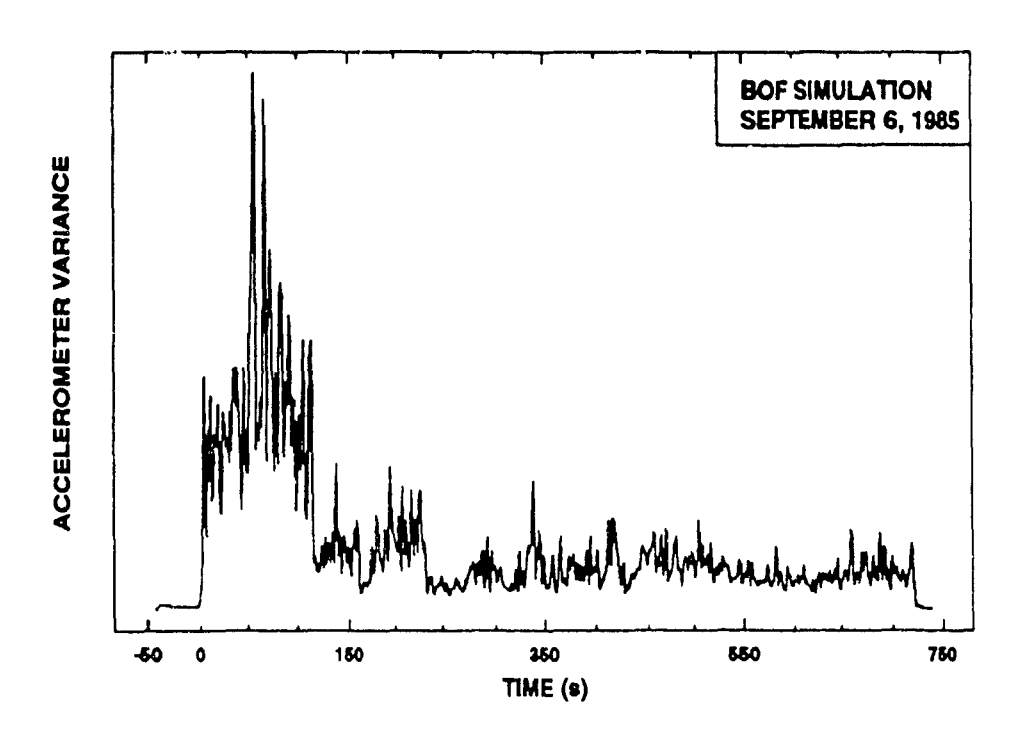


Fig. 7.19 Variation of the accelerometer signal during BOF simulation B/6.

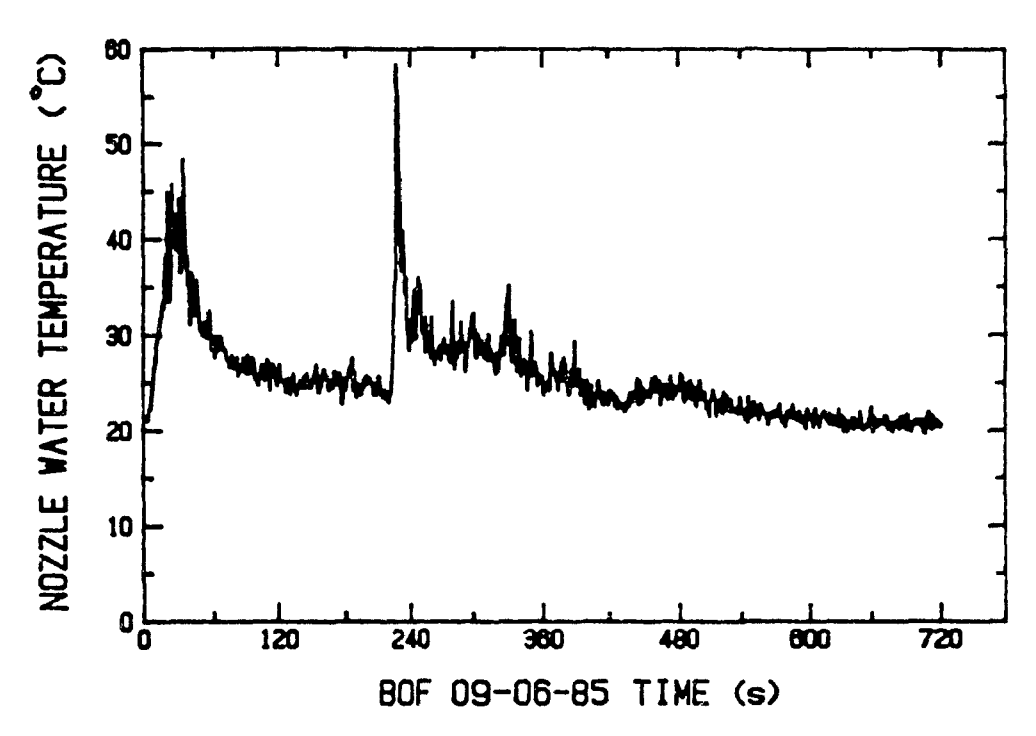


Fig. 7.20 Temperature of the cooling water at the nozzle tip during BOF simulation B/6.

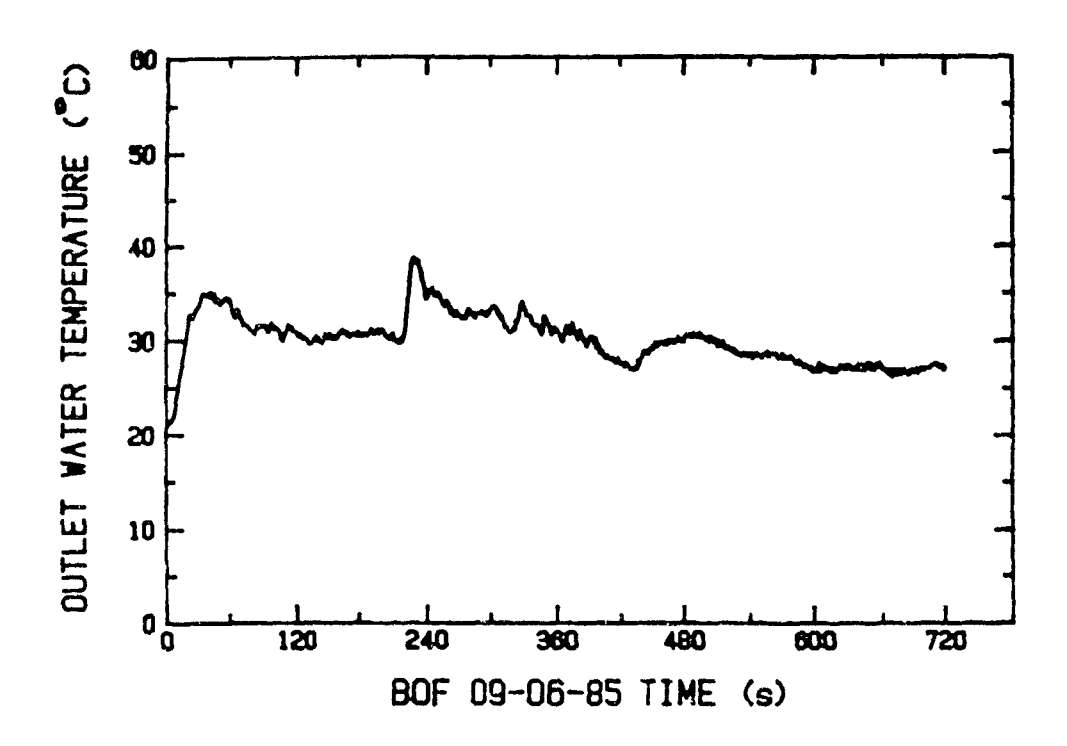


Fig. 7.21 Temperature of the cooling water at the exit surge tank during BOF simulation B/6.

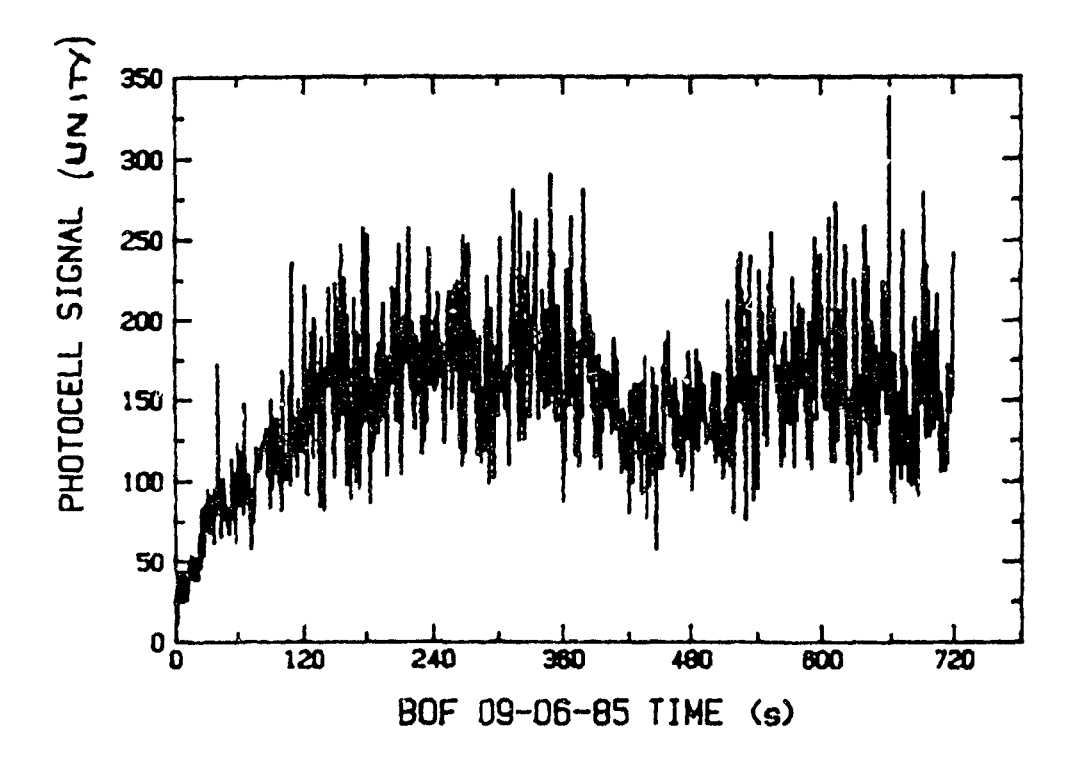


Fig. 7.22 Intensity of the photocell signal during BOF simulation B/6.

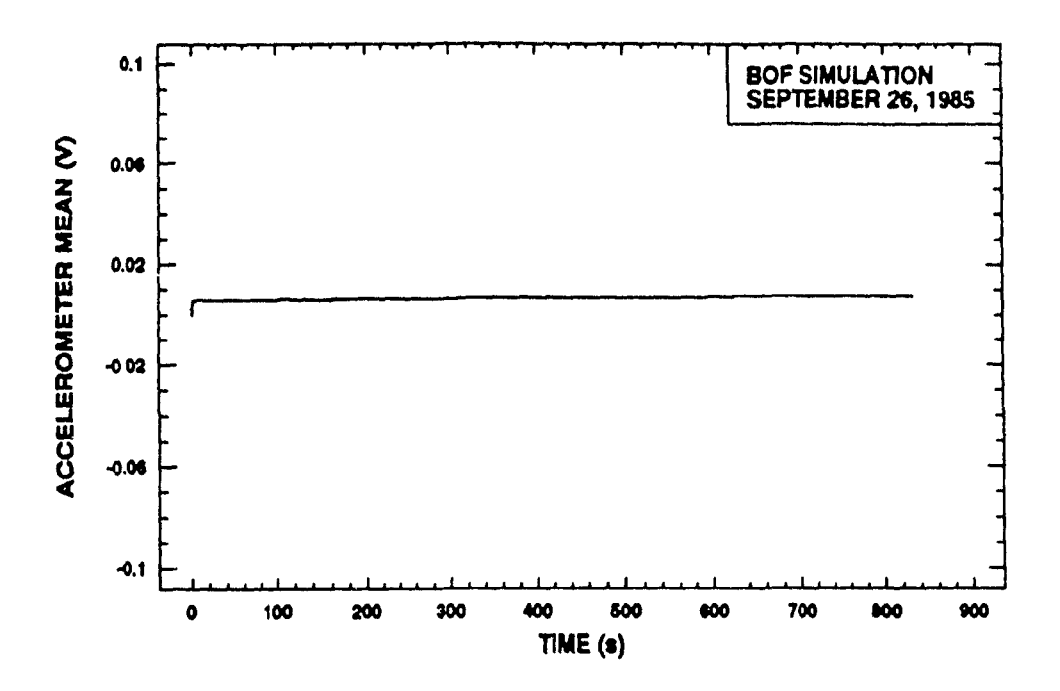


Fig. 7.23 The mean of the accelerometer signal during BOF simulation B/9.

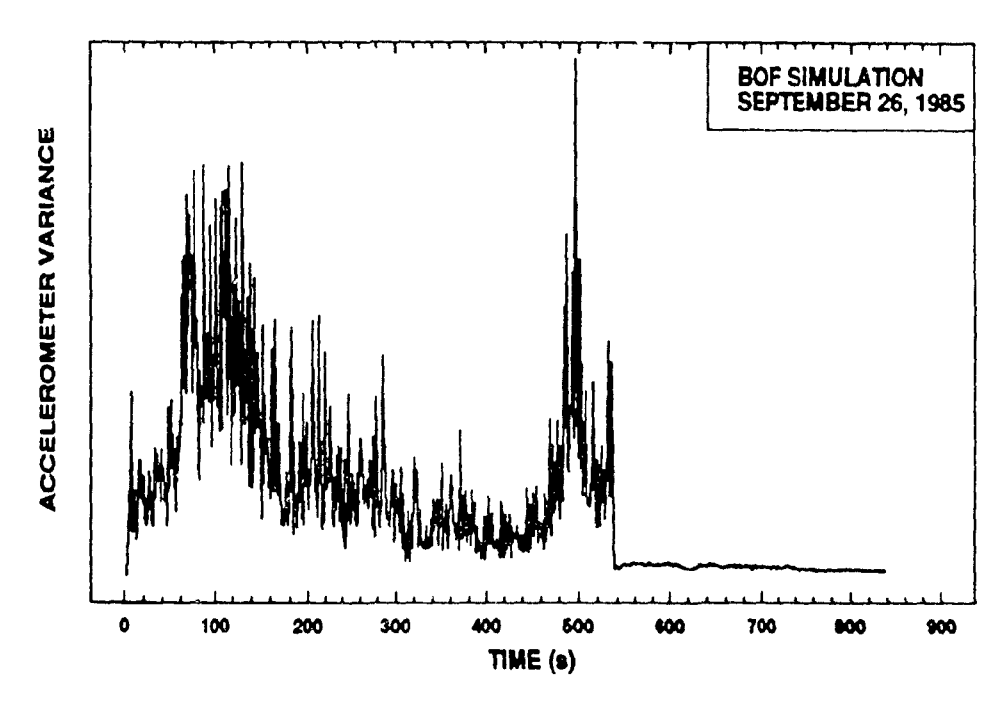


Fig. 7.24 Variation of the accelerometer signal during BOF simulation B/9.

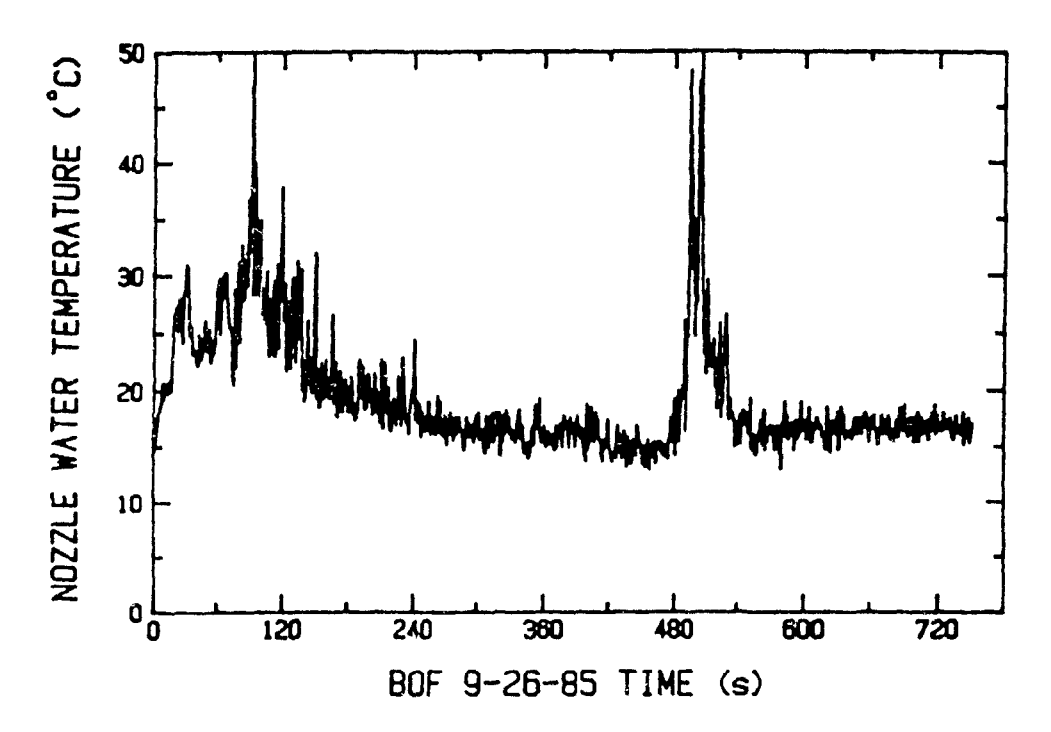


Fig. 7.25 Temperature of the cooling water at the nozzle tip during BOF simulation B/9.

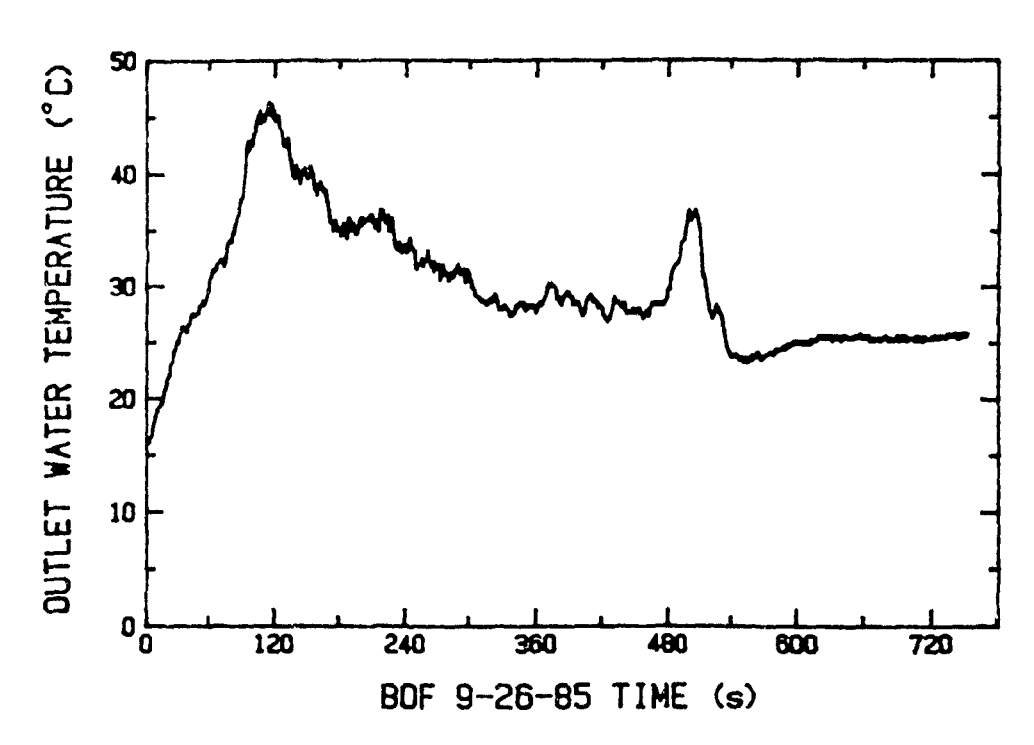


Fig. 7.26 Temperature of the cooling water at the exit surge tank during BOF simulation B/9.

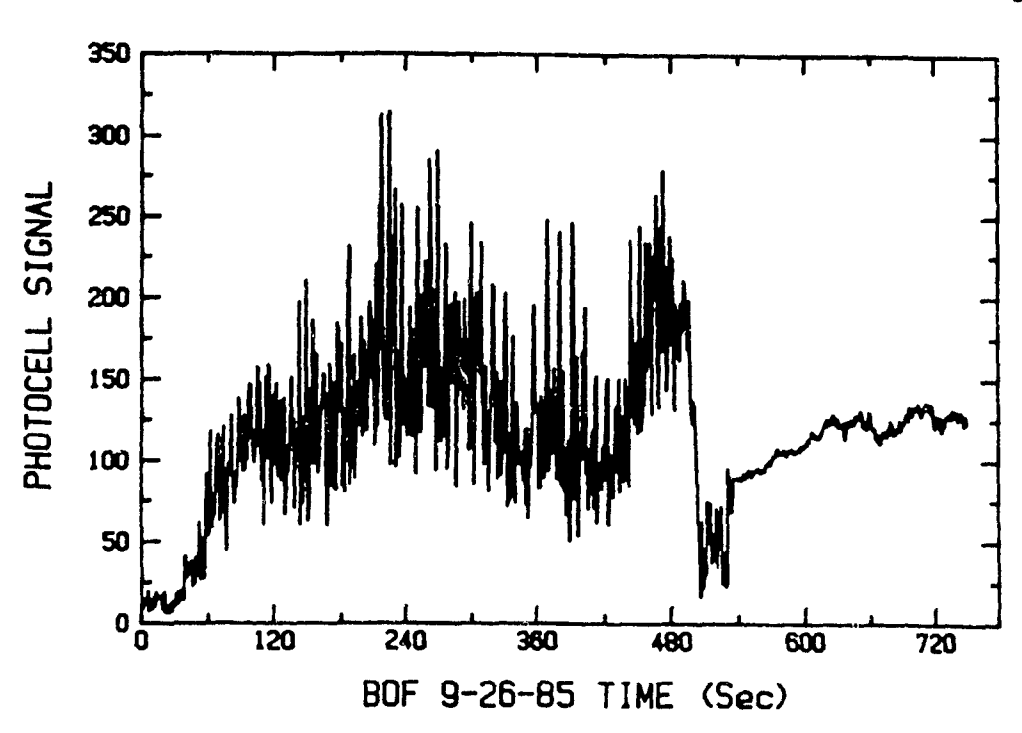


Fig. 7.27 Intensity of the photocell signal during BOF simulation B/9.

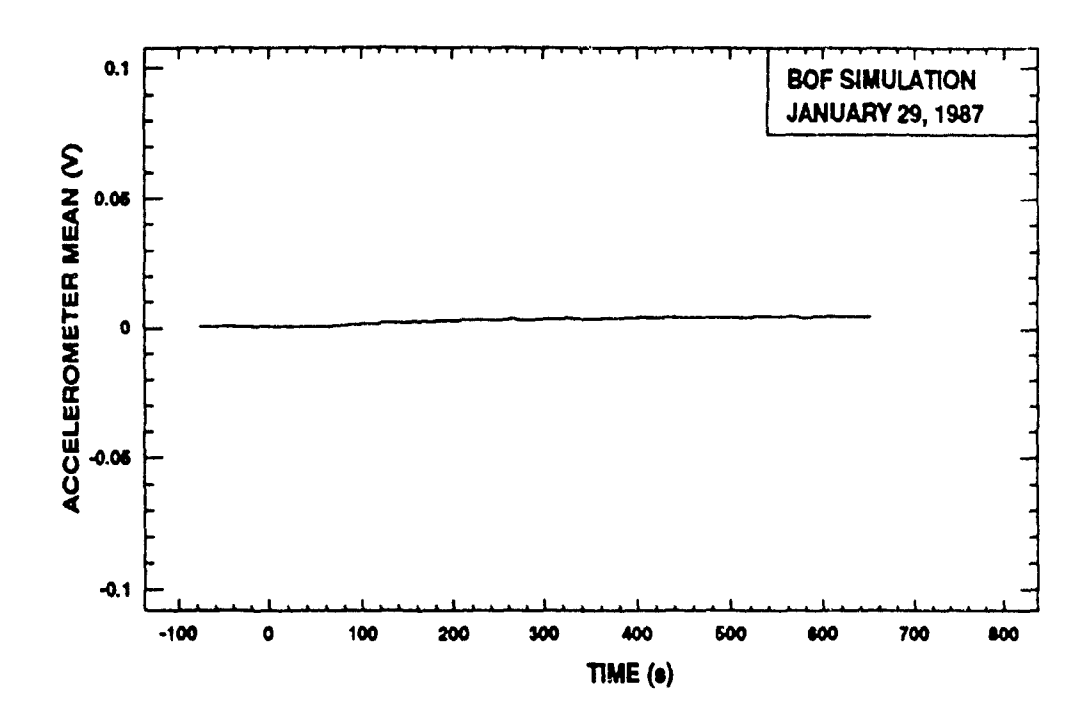


Fig. 7.28 The mean of the accelerometer signal during BOF simulation $\mathrm{C}/\mathrm{1}$.

Fig. 7.29 Variation of the accelerometer signal during BOF simulation C/1.

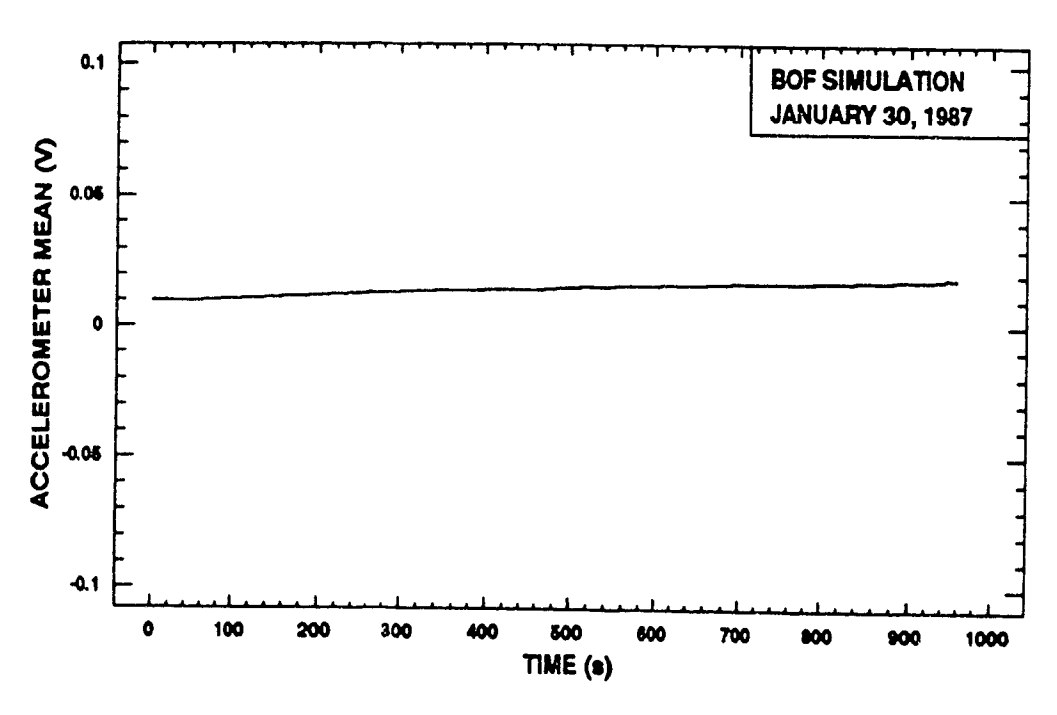


Fig. 7.30 The mean of the accelerometer signal during BOF simulation C/2.

Ž

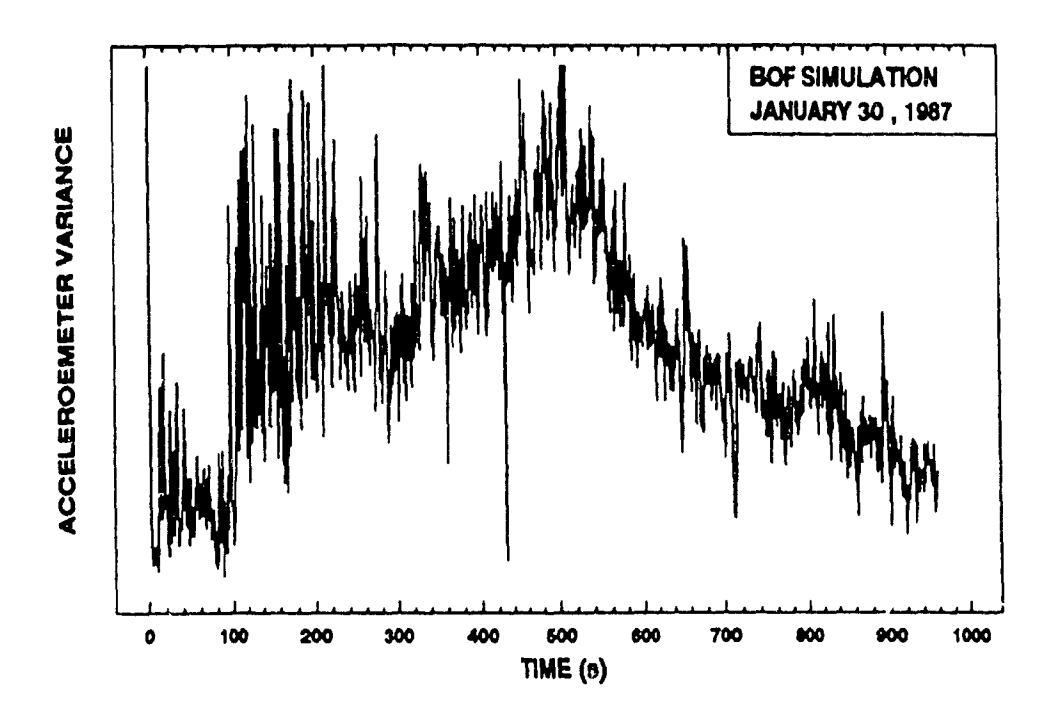


Fig. 7.31 Variation of the accelerometer signal during BOF simulation C/2.

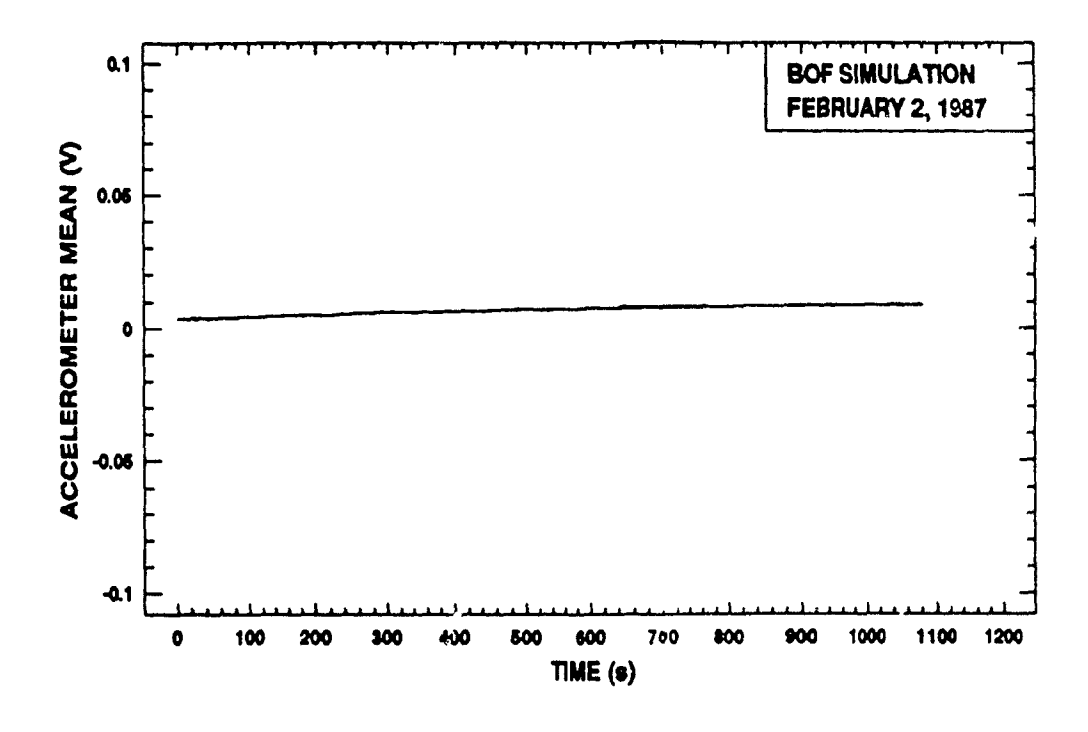


Fig. 7.32 The mean of the accelerometer signal during BOF simulation C/3.

1

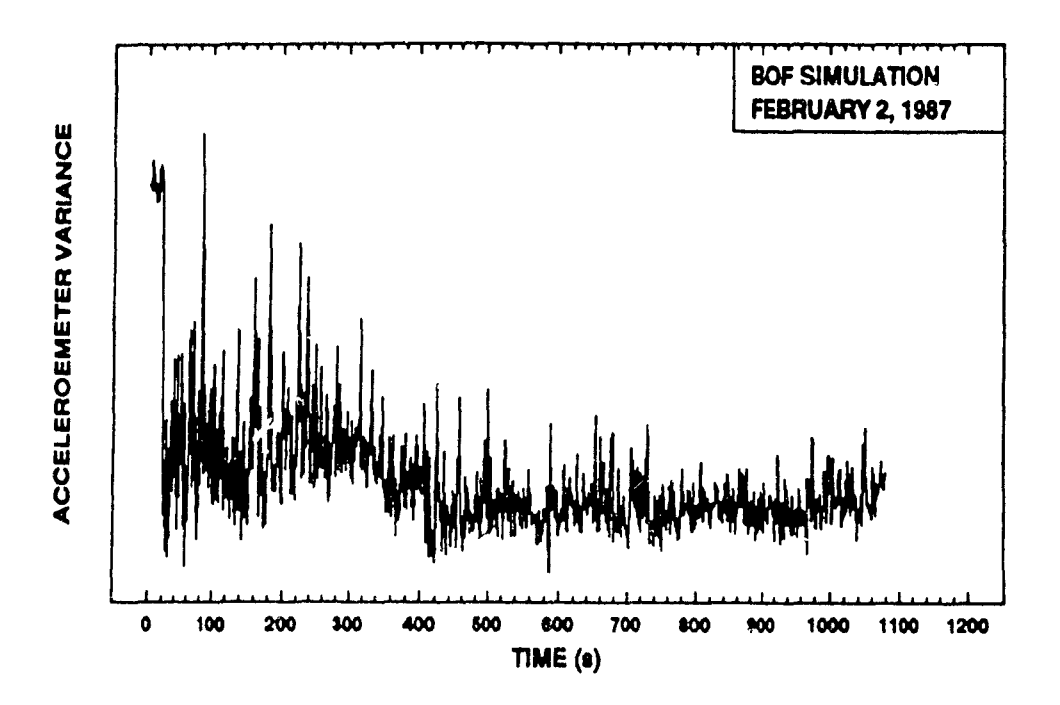


Fig. 7.33 Variation of the accelerometer signal during BOF simulation C/3.

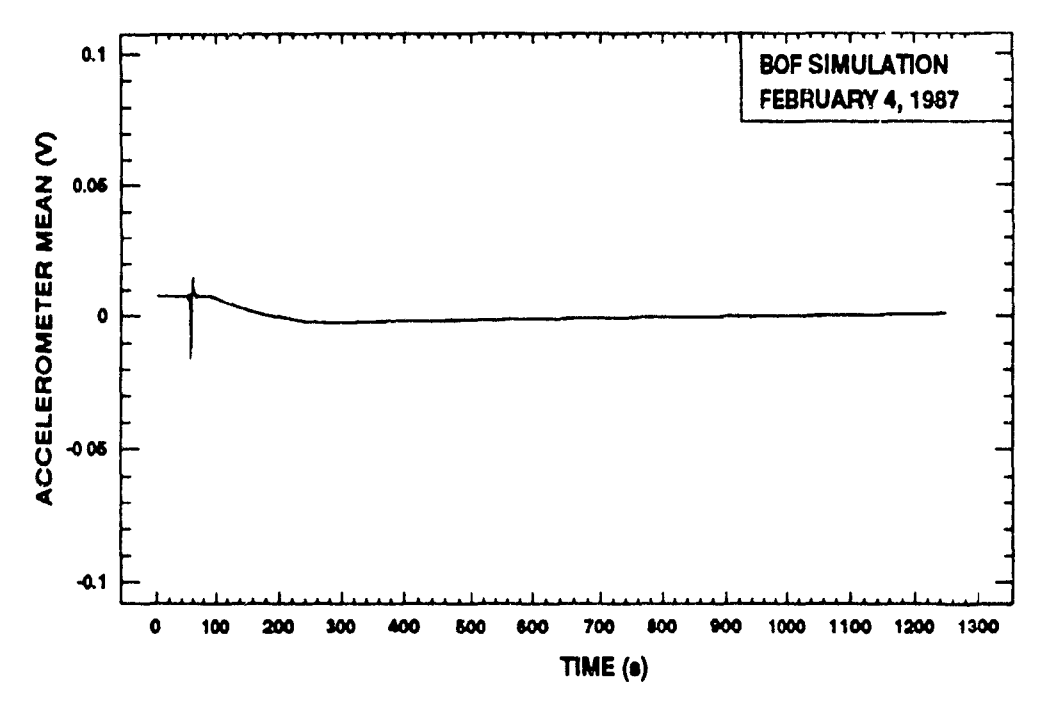


Fig. 7.34 The mean of the accelerometer signal during BOF simulation C/4.

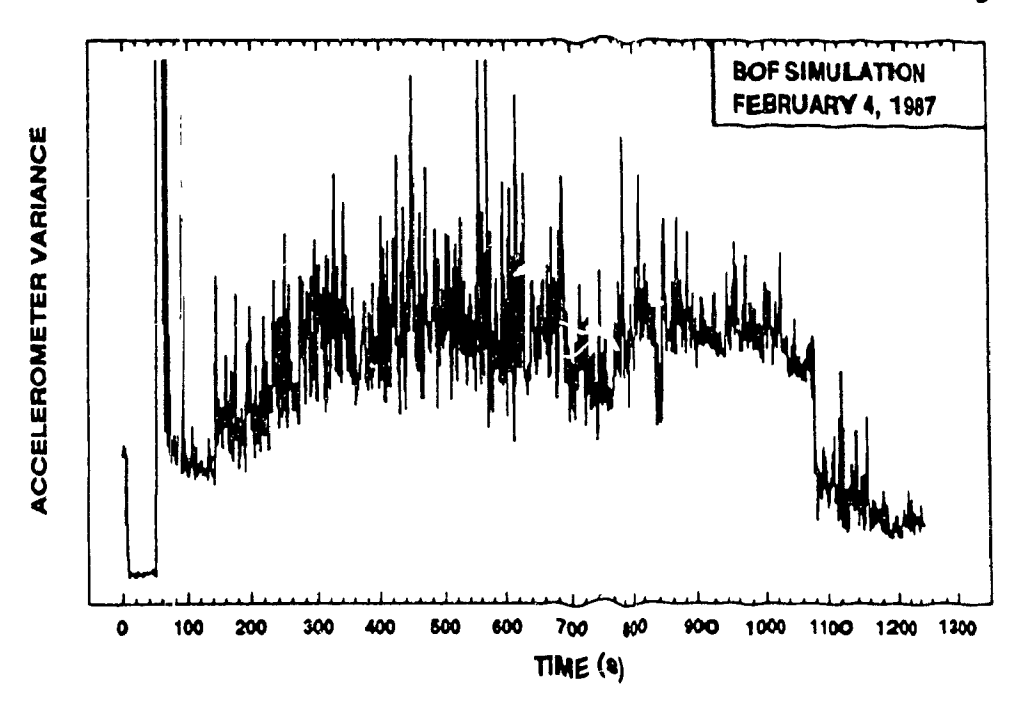


Fig. 7.35 Variation of the accelerometer signal during BOF simulation C/4.

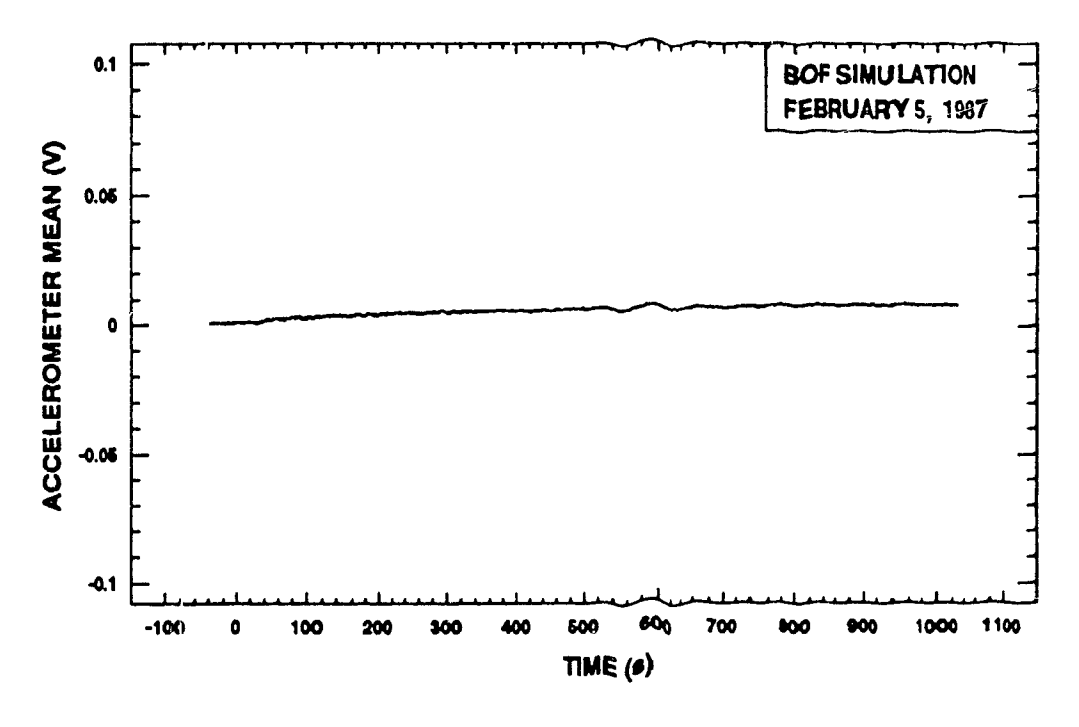


Fig. 7.36 The mean of the accelerometer signal during BOF simulation C/5.

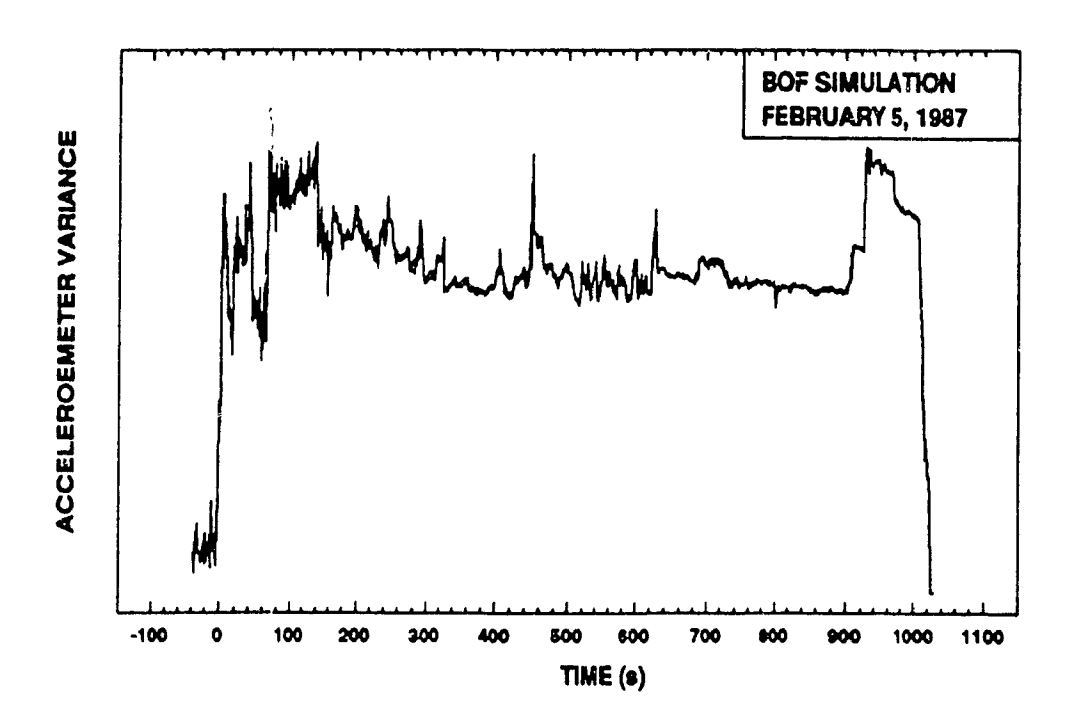


Fig. 7.37 Variation of the accelerometer signal during BOF simulation C/5.

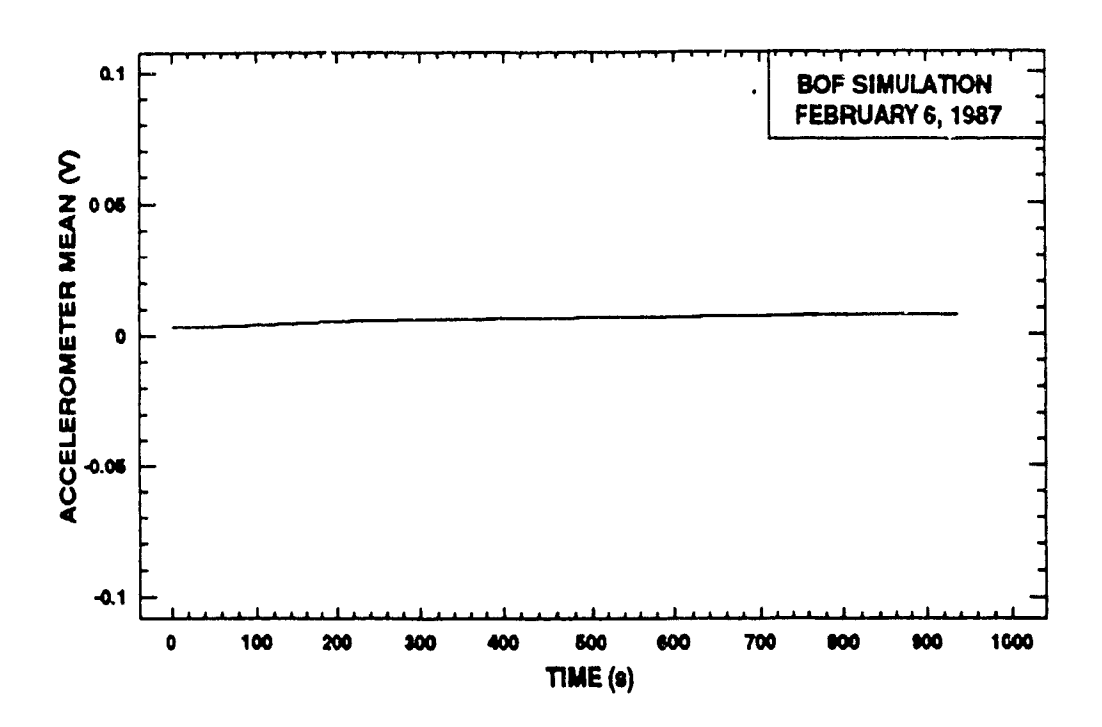


Fig. 7.38 The mean of the accelerometer signal during BOF simulation C/6.

Fig. 7.39 Variation of the accelerometer signal during BOF simulation C/6.

7.4.1 Fourier Analysis Technique

Since vibrations can be considered as being either completely random or periodic, Fourier frequency analysis was performed on the accelerometer signal for those simulations conducted under the high frequency configuration. This involved transforming the signal from the time domain to the frequency domain. Thus attempting to discern the presence of specific vibrational frequencies that can be related to the steelmaking process. Owing to the complexity of the transformation, Fourier analysis is explained below prior to describing the results of the simulations.

The transformation into the frequency domain is greatly facilitated by the discrete Fast Fourier Transform (FFT) algorithm. The transform is essentially a means of interpolating a sum of trigonometric functions through "n" data points. The functions that appear in the Fourier expressions are imaginary exponentials, but by Euler's formula these exponentials are really just the sum of two trigonometric functions in disguise, as shown below.

$$\exp^{(ix)} - \cos(x) + i \sin(x) \tag{7.4}$$

Consider that $F = (f_o, f_1, \ldots, f_{n-1})$ is a data array that is obtained by sampling the accelerometer signal at a fixed rate. The Fourier expansion of the array F is the linear combination of the imaginary exponentials as shown below.

$$f_{k} = \frac{1}{n} \sum_{m=0}^{n-1} f_{m} \exp^{\frac{(2\pi i)}{n} mk}$$
 (7.5)

The f^*_m coefficients are uniquely determined by the requirement that Eq.(7.5) be satisfied for all values of k. Because the exponential functions are pair-wise orthogonal, the f^*_m 's can be determined by using the inner product solution. In fact, it can be shown that the f^*_m 's are given by

Sep.

$$f_{m} = \sum_{k=0}^{n-1} f_{k} \exp^{\frac{(-2\pi i)}{n}mk}$$
 (7.6)

The array $f^*=(f^*_0, \ldots, f^*_{n-1})$ is called the discrete Fourier transform of F. Its elements are determined according to Eq. (7.6). The inverse Fourier transform is the operation by which F is recovered from the coefficient array F^* and is computed according to Eq. (7.5). Since the information can be passed back and forth between F and F^* , it must be the case that the information content of the Fourier coefficients is the same as that of the original data. The following paragraphs address the way in which the frequency concentrations are determined.

To begin, consider a single term from Eq. (7.4) and, using Eq. (7.5), the m^{th} term can be written as

$$f_{m} \exp^{\frac{(2\pi i)}{n}mk} - f_{m} \left[\cos\left(\frac{(2\pi)}{n}mk\right) + i\sin\left(\frac{(2\pi)}{n}mk\right)\right] \tag{7.7}$$

If k is considered as an independent variable, then each of the trigonometric functions has a frequency of m/n in units of cycle per

point. It would thus, appear that the m^{th} term in Eq. 7.5 can be interpreted as the component of the data array of frequency m/n. This is not quite correct because there will be a second term of the same frequency, namely $(n-m)^{th}$ term. To see that this is indeed the case, observe that the $(n-m)^{th}$ term is given by

$$f_{n-m} \exp^{(\frac{(2\pi i)}{n}(n-m)k)} - f_{-m} \exp^{(\frac{2\pi i}{n}-mk)}$$

$$-f_{n-m} \left[\cos(\frac{(2\pi)}{n}mk) - i\sin(\frac{(2\pi)}{n}mk)\right]$$
(7.8)

Now, if the mth and (n-m)th terms are summed together, the result is

$$[f_m + f_{n-m}] \cos(\frac{(2\pi)}{n}mk) + i [f_m - f_{n-m}] \sin(\frac{(2\pi)}{n}mk)$$
 (7.9)

This sum comprises the compete m/n frequency component of F. It contains the contributions from both the mth and $(n-m)^{th}$ elements of F^{*}. However, it is often easier to associate the $(n-m)^{th}$ term with the negative crequency -m/n, and rewrite f_{n-m} as f_{-m} . In that case Eq. (7.9) becomes

$$[f_{\underline{m}} + f_{-\underline{m}}] \cos(\frac{(2\pi)}{n}mk) + i [f_{\underline{m}} - f_{-\underline{m}}] \sin(\frac{(2\pi)}{n}mk)$$
 (7.10)

Notice that two exceptional terms, m=0 and m=n/2 in Eq. (7.5) can be written in simplified forms as follows

$$f_0 = f_0 \exp^{(\frac{(2\pi)}{n}0k)} \tag{7.11}$$

and

1

$$f_{\frac{n}{2}}^{\cdot}(-1)^{k} - f_{\frac{n}{2}}^{\cdot} \exp\left(\frac{(2\pi)}{n} \frac{n}{2}k\right)$$
 (7.12)

Combining these two equations with Eq. (7.10) and (7.5), the Fourier expansion of F can be written in the form

$$f_{k} = \sum_{m=1}^{n/2-1} [f_{m} + f_{-m}] \cos(\frac{(2\pi)}{n} mk) + i [f_{m} - f_{-m}] \sin(\frac{(2\pi)}{n} mk) + f_{0} + f_{\frac{n}{2}} (-1)^{k}$$
(7.13)

One significant property of a Fourier expansion is that if the data is purely real, such as the accelerometer signal, then the spectrum $|F^*|^2$ is symmetric. Thus, only the real portion of the expansion is significant. As a final remark, consider combining Eq. 7.10 and Eq. 7.5, the result represents the mean of the data packet.

7.4.2 Results of Frequency Analysis

Frequency analysis for this research work involved two distinct steps. In the first step, the major frequencies contributing to the accelerometer signal were determined. While in the second step, the behaviour of these frequencies over time was ascertained, thus, elucidating any vibrational frequencies that were related to the steelmaking process. The major frequencies in the first step were determined by dividing the raw data into consecutive packets representing one second of the BOF simulation. Then the FFT was performed on each packet and the major frequencies were recorded.

From this information, the major frequencies for the entire simulation were banded into united groups of frequencies, or band widths. In general, the number of band widths was limited to a maximum of eight. In the second step, the relative contribution of each major frequency band width was determined for every packet of data. Thus, the relative contribution of each major frequency band was determined as a function of oxygen plowing time. To explain this process further, the first step for simulations B/9 and C/3 are presented below.

The power spectrum, essentially the amplitude of each frequency raised to the power of two, provides a graphical forum that clearly identifies the major frequencies contributing to the accelerometer signal at one particular instant of time. For the simulation B/9, three power spectrums are presented in Fig. 7.40-7.42, representing the alternating component (AC) of the accelerometer signal at 65s, 240s and 700s, respectively. Note that the direct component (DC), or the mean, has

been removed from all power spectrums; the DC component is typically represented by frequency 0 Hz. As can be seen in the spectrums, the major frequencies can be grouped into united band widths, such as 46-50 Hz and 65-70 Hz. In fact these two band widths are the major contributors to the AC component of the signal during this simulation.

For the simulation C/3, eight power spectrums are presented in Fig. 7.43-7.48, representing the AC component at 100s, 200s, 400s, 600s, 800s, and 1000s, respectively. As can be seen, there is very little difference between each spectrum. The major frequency band widths selected for further analysis were 10-15Hz, 49-57Hz, 290-295Hz, 303-311Hz, 356-370Hz and 403-414Hz. The most obvious difference between the power spectrums generated for the two simulations is the maximum frequency that is resolved; 750Hz versus 500Hz for simulations B/9 and C/3, respectively.

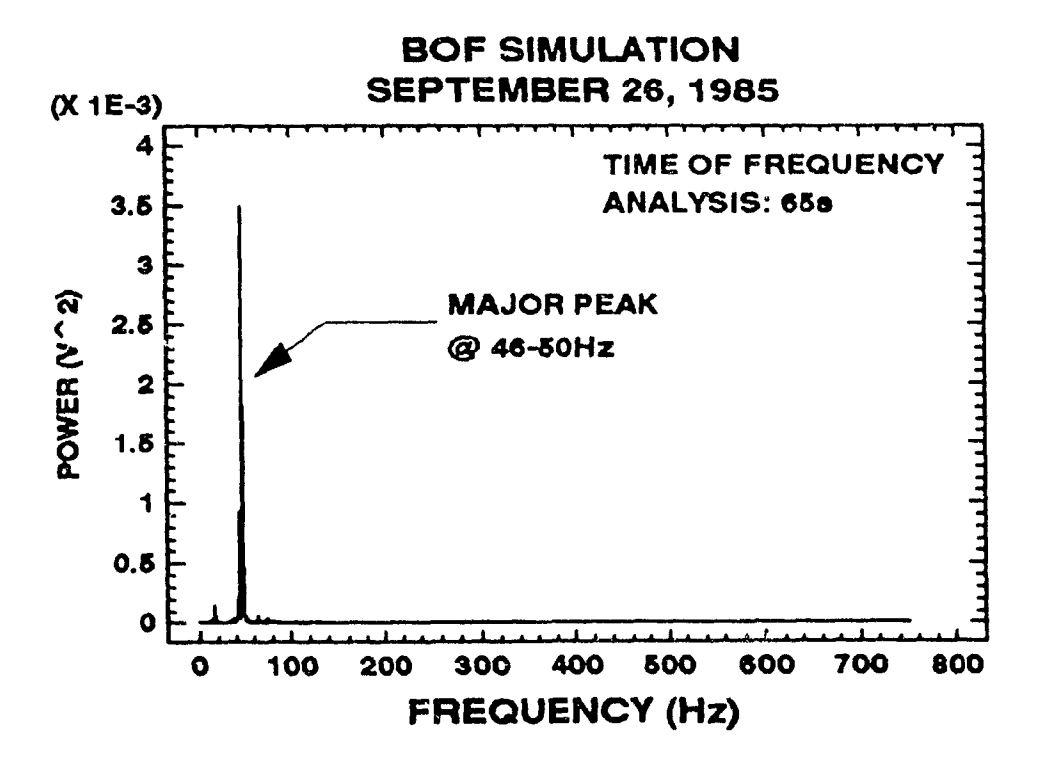


Fig. 7.40 The power spectrum of the accelerometer signal at 65 seconds into simulation B/9.

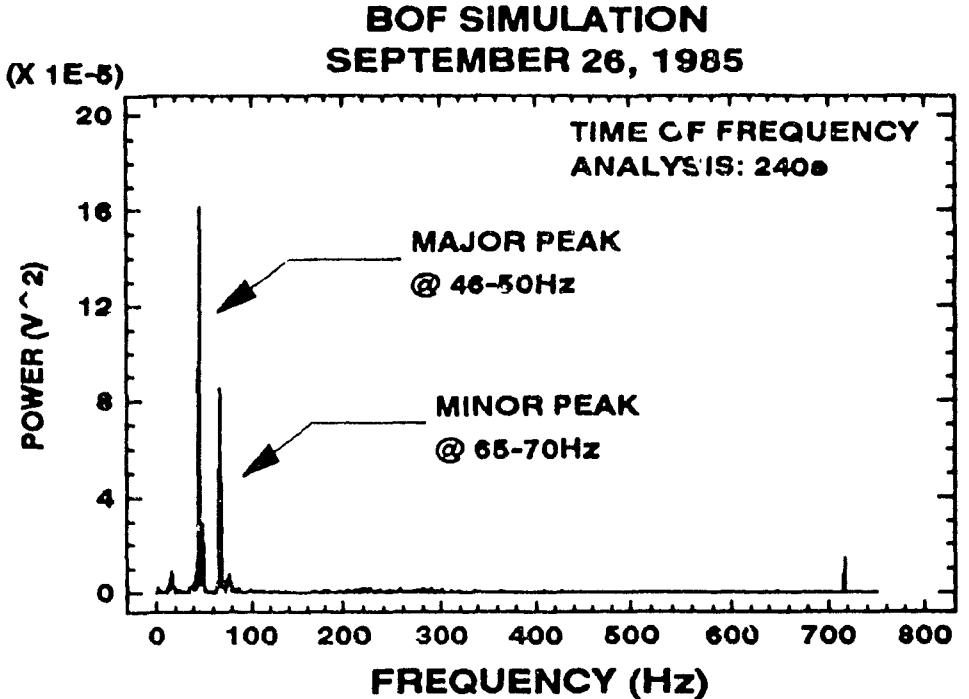


Fig. 7.41 The power spectrum of the accelerometer signal at 240 seconds into simulation B/9.

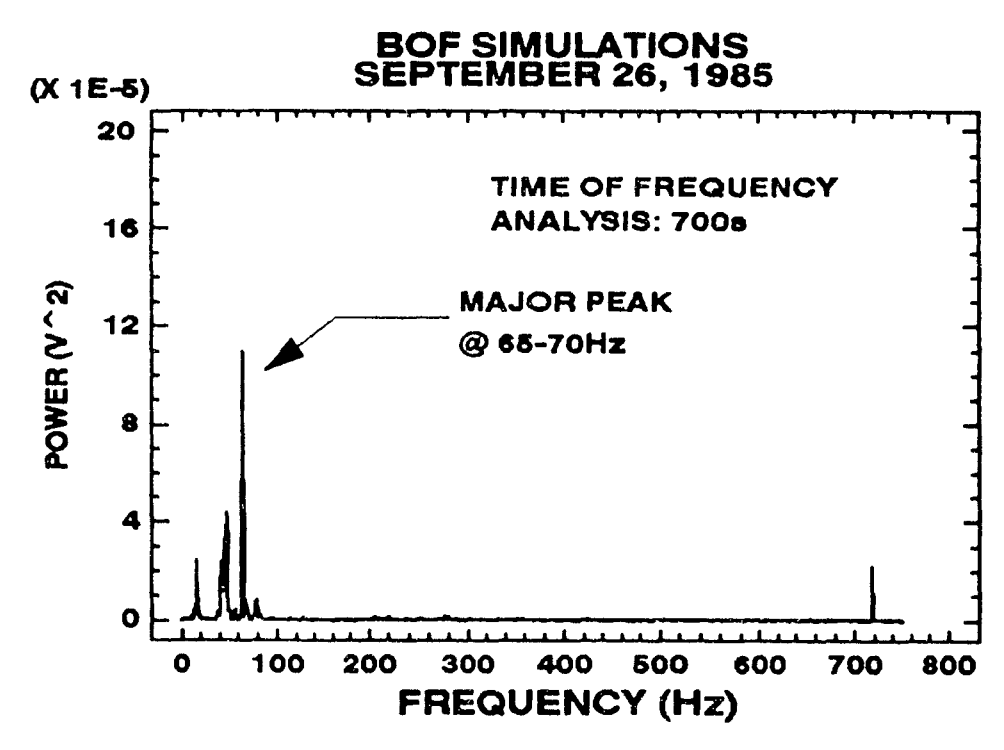


Fig. 7.42 The power spectrum of the accelerometer signal at 700 seconds into simulation B/9.

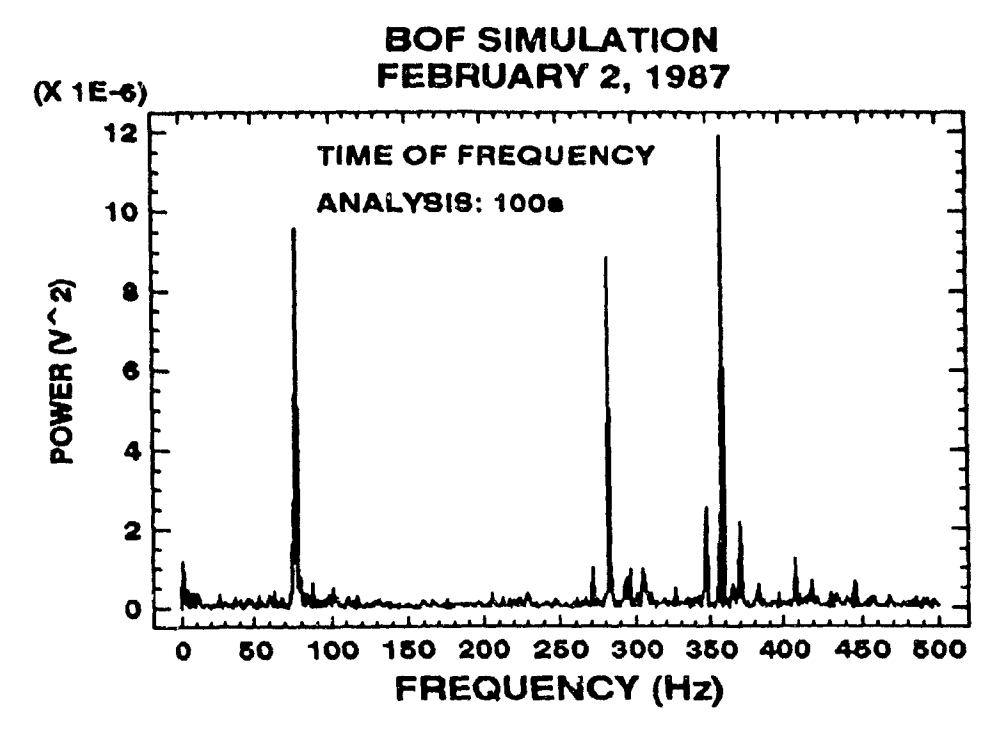


Fig. 7.43 The power spectrum of the accelerometer signal at 100 seconds into simulation $\ensuremath{\text{C}/3}$

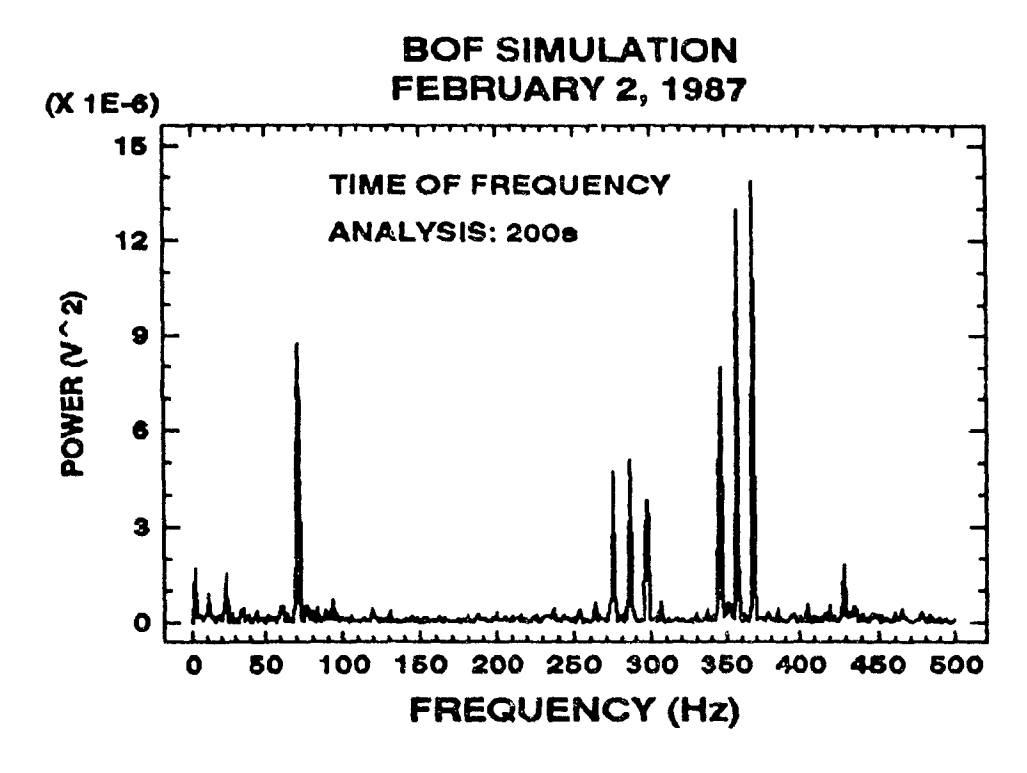


Fig. 7.44 The power spectrum of the accelerometer signal at 200 seconds into simulation C/3.

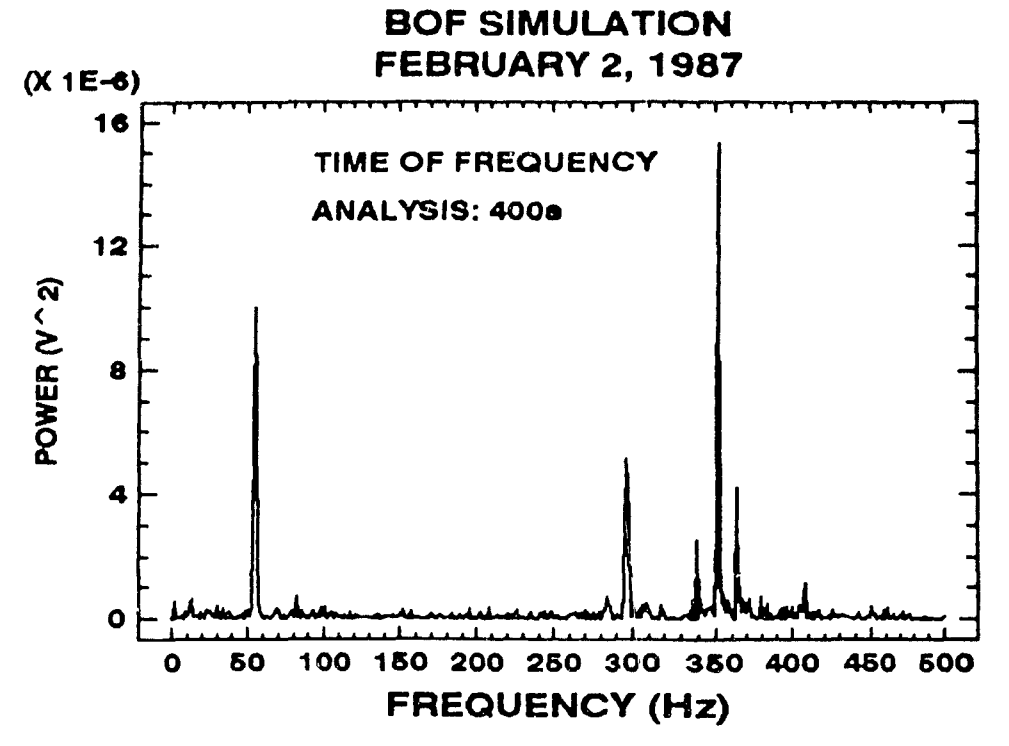


Fig. 7.45 The power spectrum of the accelerometer signal at 400 seconds into simulation C/3.

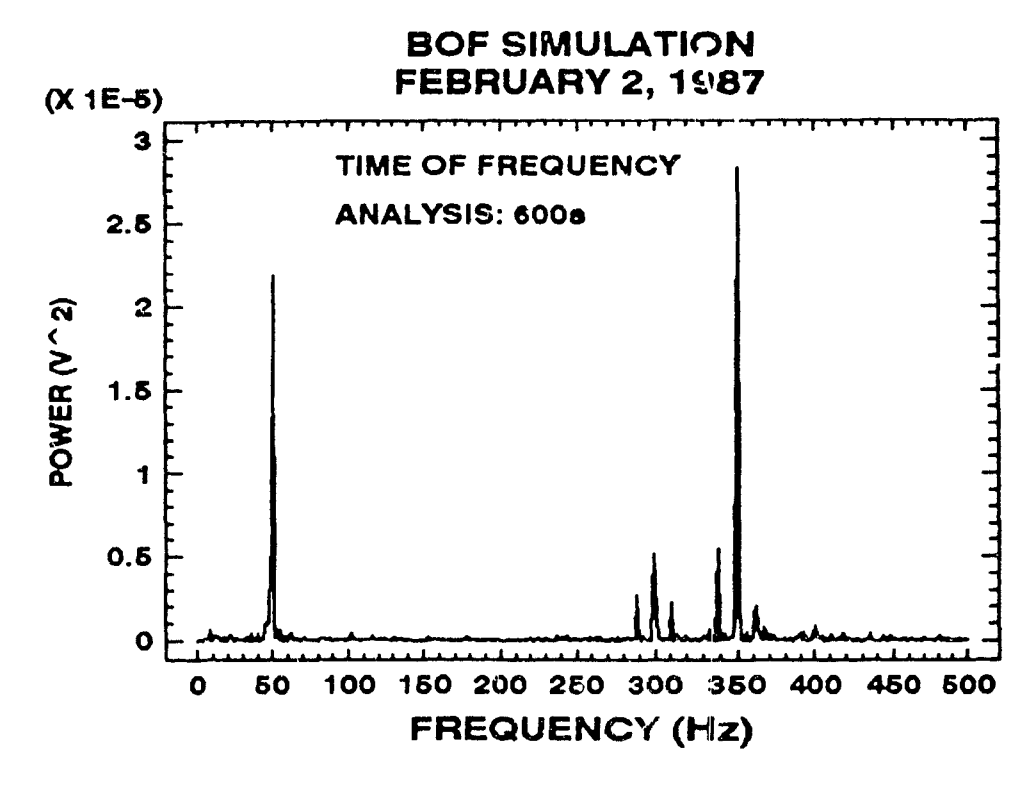


Fig. 7.46 The power spectrum of the accelerometer signal at 600 seconds into simulation C/3.

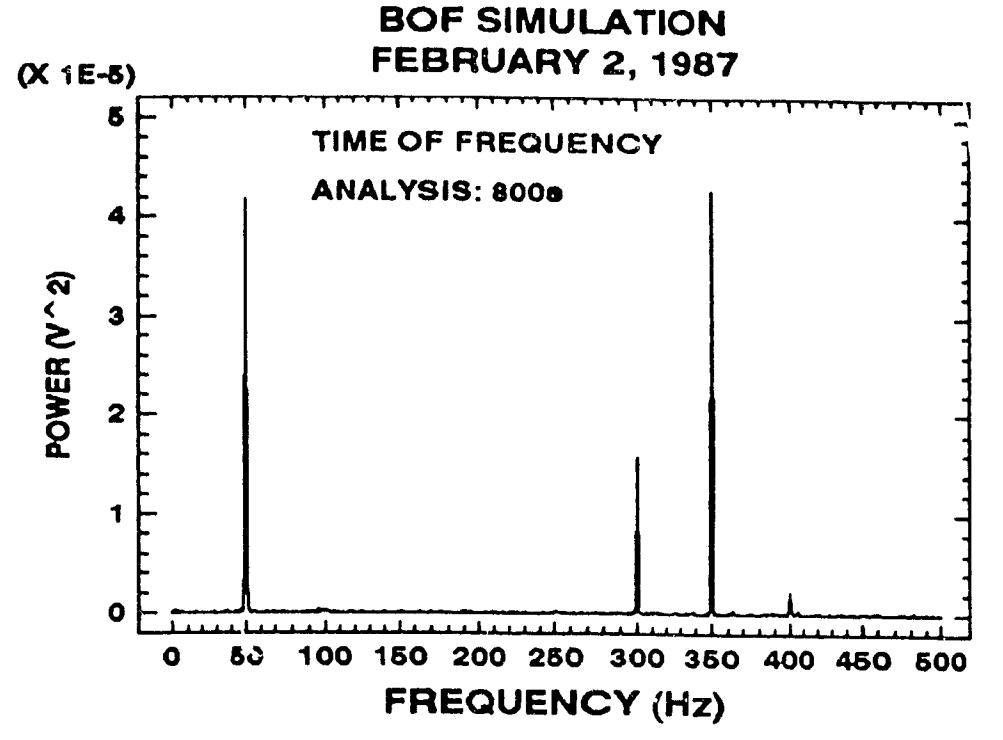


Fig. 7.47 The power spectrum of the accelerometer signal at 800 seconds into simulation C/3.

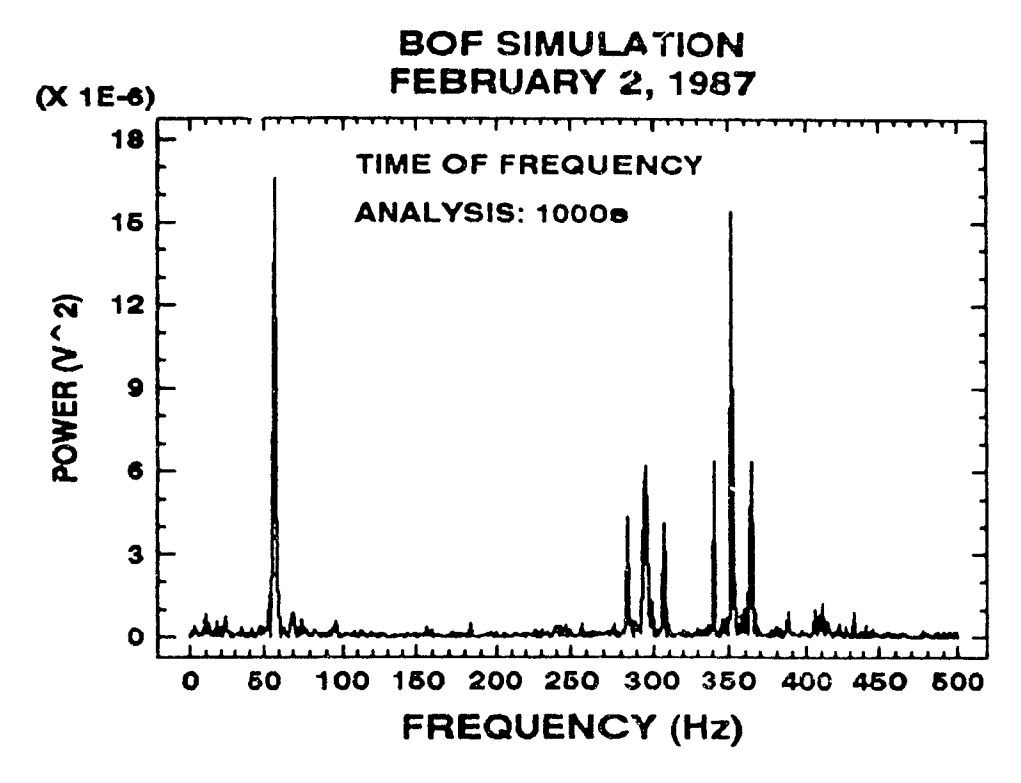


Fig. 7.48 The power spectrum of the accelerometer signal at 1000 seconds into simulation C/3.

The sampling rate determines the highest frequency that can be resolved, typically this is one half of the sampling rate. As was mentioned earlier, only the real portion of the spectrum is of interest. Sampling frequencies for the high frequency simulations are tabulated in Table 7.3.

Table 7.3 Sampling Frequency of the Accelerometer During High Frequency Simulations.

Tost Code	Test Date	Sampling Frequency (Hz)
B/1	August 20, 1985	1500
B/2	August 21, 1985	1500
B/3	August 21, 1985	1500
B/4	August 27, 1985	1500
B/5	August 27, 1985	1500
B/6	September 8, 1985	1500
B/7	September 20, 1985	1500
B/8	September 25, 1985	1500
B/9	September 20, 1985	1500
B/10	October 1, 1985	1500
C/1	January 29, 1985	500
C/2	January 30, 1987	1000
C\3	February 2, 1987	1000
C/4	February 4, 1987	1000
C/5	February 5, 1937	1000
C/8	February 6, 1987	1000

Another major difference between these two simulations was that simulation C/3 had a higher concentration of high frequency vibrations in the spectrum. This characteristic was repeated in every simulation conducted after a major reconstruction of the furnace, resulting in a change in the vibration signature of the furnace. The bolting of the

furnace body to the reinforced cement floor was perhaps the major factor in the change. Although this aspect did not serve to reduce the validity of the results, it did increase the complexity of the power spectrum. To continue with the analysis technique, suffice it to say that the selection of the major frequencies was not straight forward in the C simulations.

With the major frequency band widths selected, the second step in the analysis is performed. In this step, the sum of the power related to a specific band width is divided by the total AC power for each data packet, thus, the AC power is normalized. The results of the second step for simulations B/9 and C/3 are presented Fig. 7.49-7.51. Note that the units of the normalized power are unity. The normalized power-time curves for the remaining high frequency simulations can be found in Appendix A.

As can be seen by reviewing these figures, the normalized power-time curves rarely follow their respective variance-time curves for the entire simulation. Furthermore, the absence of change in the accelerometer's mean, or DC component, from one data packet to another indicates that the accelerometer variance originates in the AC component of the signal. This leaves two possibilities to account for the changes in the signal's variance. One possibility is that the overall power of all frequencies is reduced equally. Another possibility that these two facts suggests is that the role of the major frequencies must decrease or increase at the same time that the changes in the variance are detected.

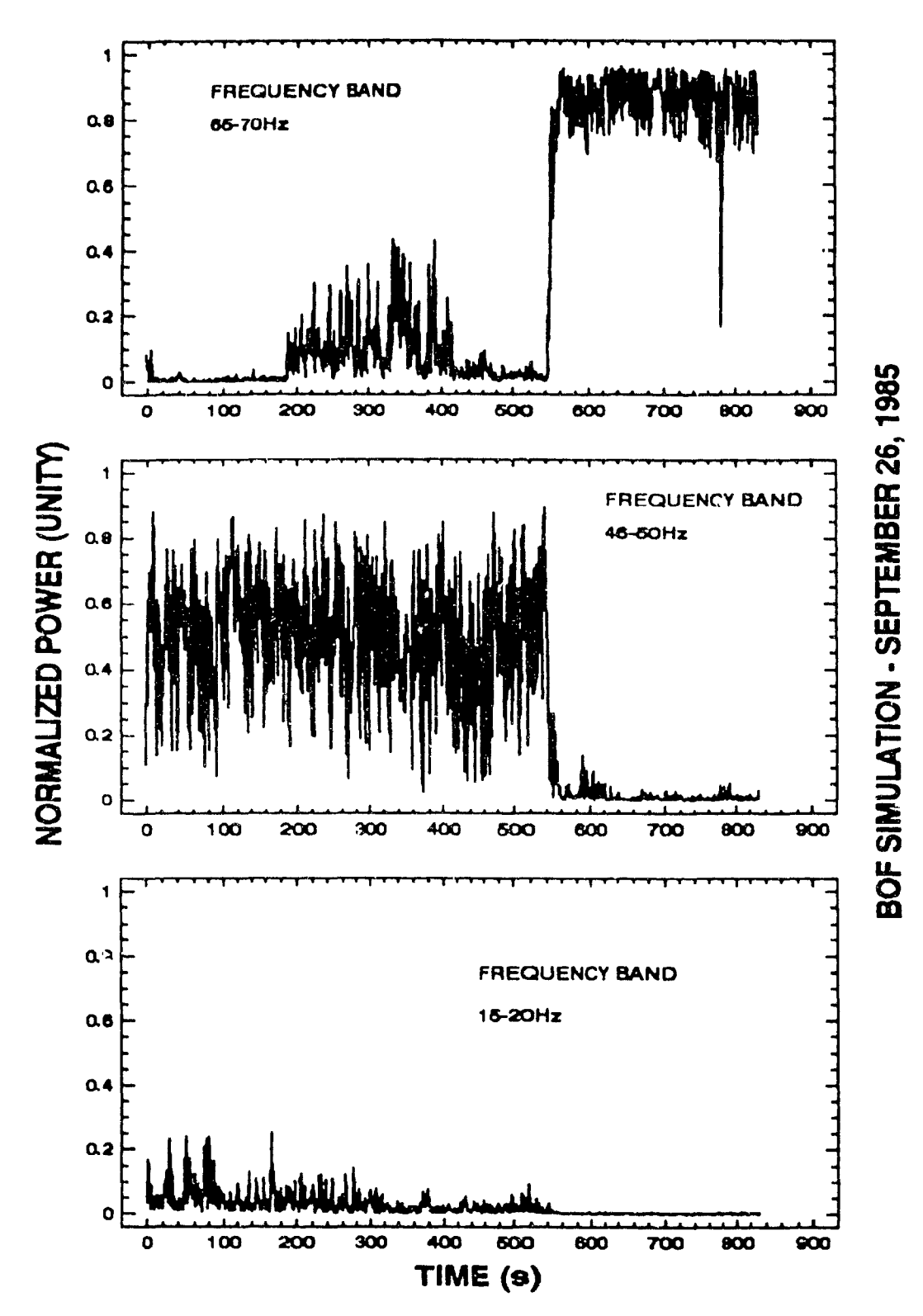


Fig 7.49 Relative contribution of three frequency band widths during simulation B/9.

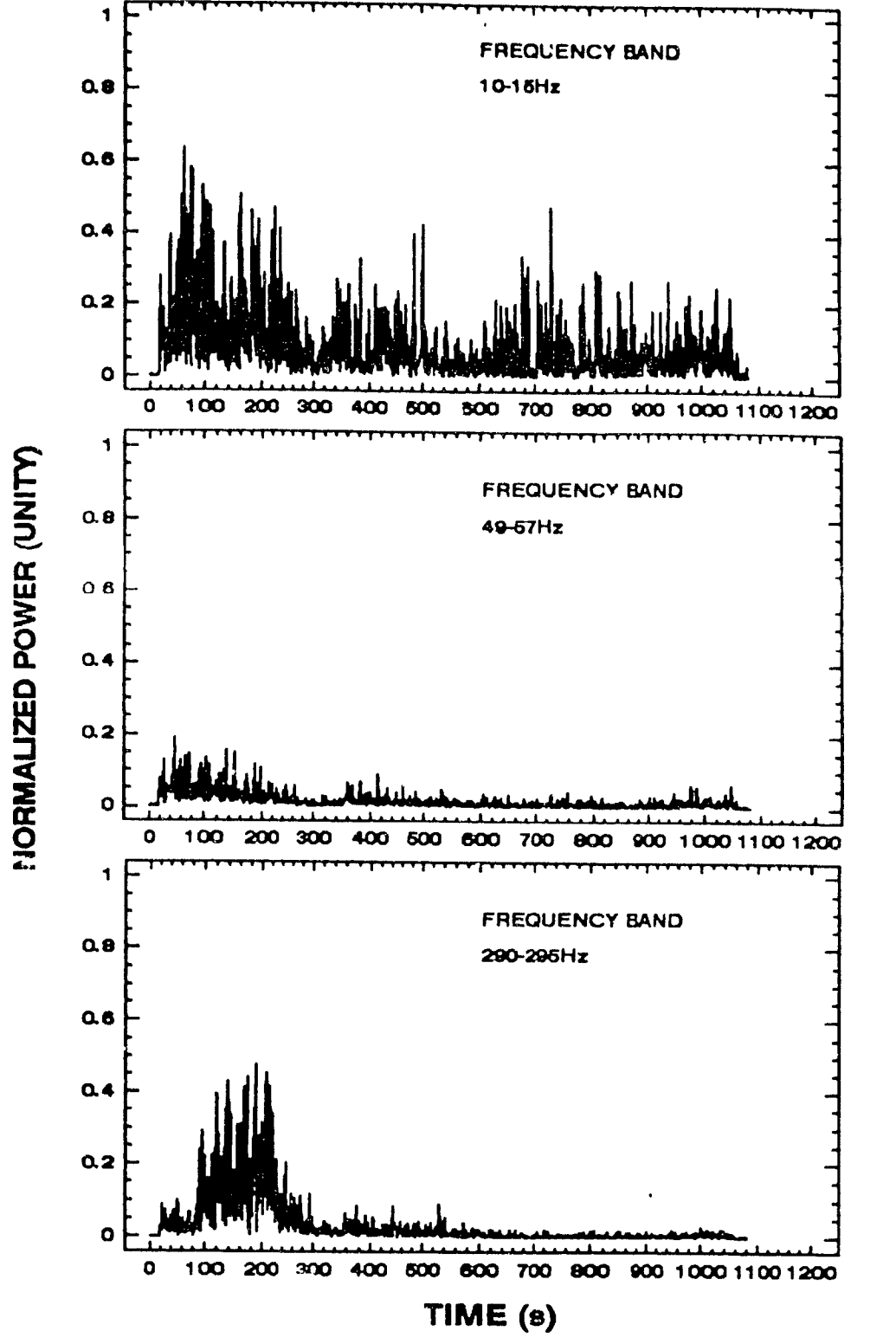


Fig. 7.50 Relative contribution of three frequency band widths during simulation C/3.

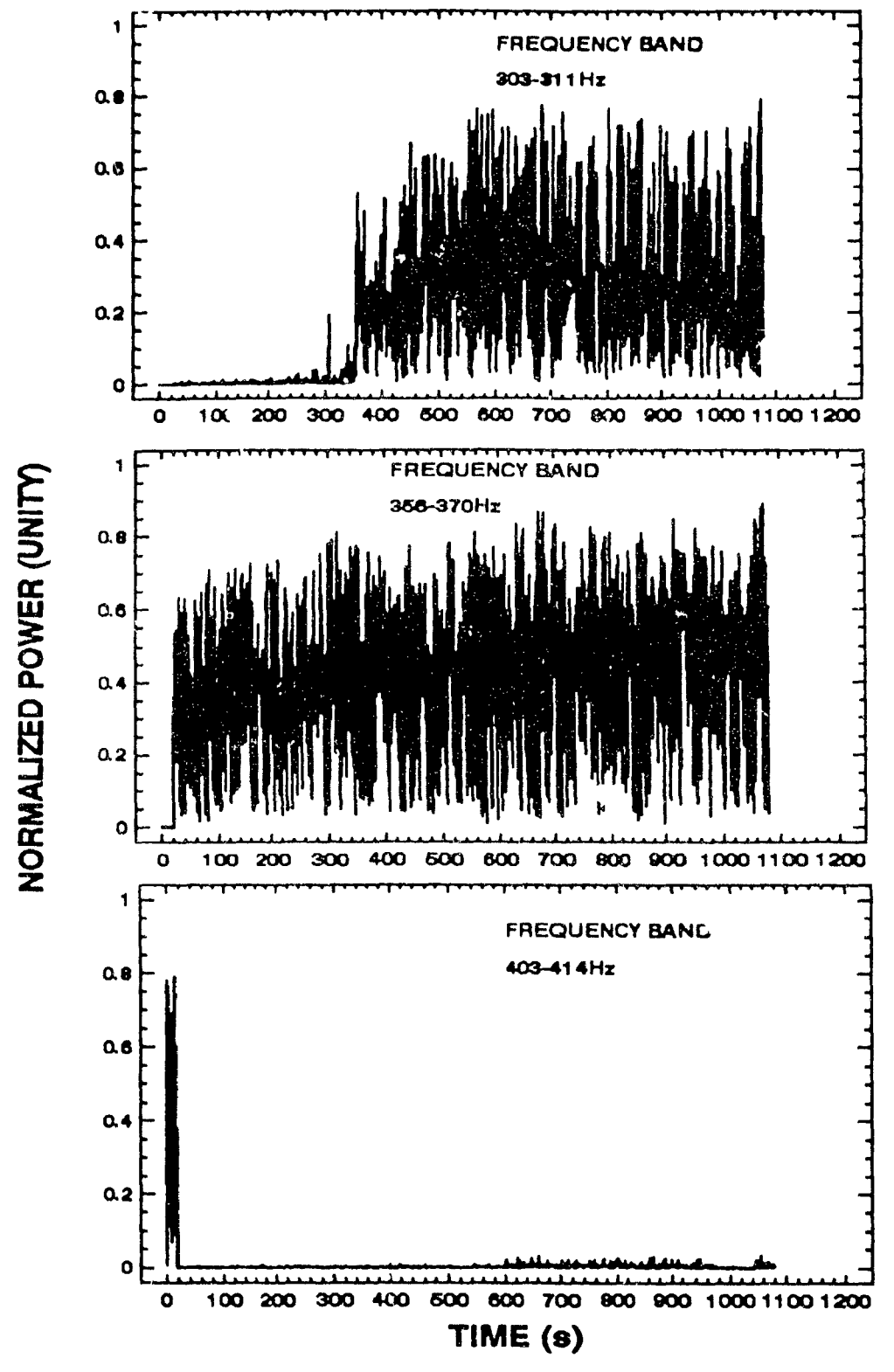


Fig. 7.51 Relative contribution of three frequency band widths during simulation C/3.

An excellent example of the latter is found in Fig.49, where the major frequencies 15-20Hz, 46-50Hz, and 65-70Hz are shown as a function of time during simulation B/9. Although the frequency band 15-20Hz is only of marginal interest during the initial portion of the blow, the frequency band 46-50Hz is significant for the major portion of the blow. In stark contrast, the frequency band 65-70Hz became predominant in the final portion of the blow. Interestingly, the time at which the relative contributions of the frequency bands changed dramatically corresponds well with the final decay of the variance-time curve in Fig. 7.24. However, this pattern was not repeated in every test.

İ

In simulation C/3, the low frequency bands played a less dominant role in the accelerometer signals' AC component, as can be seen in Fig. 7.50 and 7.51. Interestingly, a high frequency band, 403-414Hz, was predominant only at the beginning of the test, lasting only 20 seconds. Records state that the start of the oxygen blow was delayed by approximately 25 seconds, thus, indicating that this frequency may be related to the background noise that was predominant before the start of the simulation. This pattern was also found in simulation B/6, although the frequency band was lower as can be seen in Fig. 7.52. This ability to diffect "background noises" can be used to attribute changes in the signal with noises occurring in the shop which can then be filtered out of the accelerometer signal.

BOF SIMULATION - SEPTEMBER 6, 1985

Fig. 7.52 Relative contribution of three frequency band widths during simulation B/6.

Another interesting aspect of simulation C/3 is that the frequency band 356-370Hz remained predominant throughout the entire blow, while the frequency band 10-15Hz made only a moderate contribution to the signal. However, the frequency band 303-311Hz was becoming more predominant towards the end of the blow, but never became a major contributor to the signal. In reviewing the variance-time curve for simulation C/3, one can see that the final decay in the variance never occurred, hence, explaining the difference in the patterns between these two simulations presented above and also indicating the significance of the carbon reference point.

7.5 Carbon Reference Point

The results presented above clearly indicate that the accelerometer can follow the decarburization path both in terms of the variance-time curve and the normalized power-time curve. More importantly, it can also detect the carbon reference point at which the decarburization rate begins to decay at the end of the oxygen blow. The carbon content value of this reference point determines whether the accelerometer is applicable to a specific steel shop or product mix produced; the product mix specifies the end-point carbon to a large degree. If the end-point carbon for a specific product is above the carbon reference point, then, clearly, the accelerometer is not applicable. In some circumstances, a steel shop will produce only one type of product and, therefore, imposing a limitation on the application of the accelerometer. Thus, it is important to determine the carbon reference point that the accelerometer is capable of detecting.

As was mentioned earlier, several BOF simulations were interupted and the bath sampled to elucidate the carbon reference point. Figure 7.37 shows the accelerometer variance-time curve for a BOF simulation stopped just after the decay point; the carbon level in the bath was 0.40% C. This indicates that the carbon reference point was equal to or greater than 0.40% C because of oxidation occurring after the oxygen blow was stopped and before the bath was deoxidized and sampled.

*

One interesting study on the carbon reference point was performed at the Technical Research Institute at the Yawata works of the Nippon Steel Corporation by Ichinoe et al [78]. In this study, several relationships were developed that described the carbon reference point as a function of the oxygen blowing rate and coefficients of the rate of decarburization for the middle and final portion of the ideal decarburization path; the coefficients were described as a function of the oxygen blowing rata. These relationships are summarized in Fig 7.53 where the carbon reference point is plotted as a function of the oxygen blowing rate. As can be seen, it appears that the carbon reference point is greater than 0.52 %C and that it increases as the oxygen blowing rate increases. This latter characteristic was not revealed during the current research work, however, it is believed that this characteristic may be due to the oxygen blowing conditions. Morever, the present author suggests that a varying carbon reference point may be due to an over-oxidized, foaming slag that increases the decarburization rate just before the decay, a common occurrence for higher oxygen flow rates.

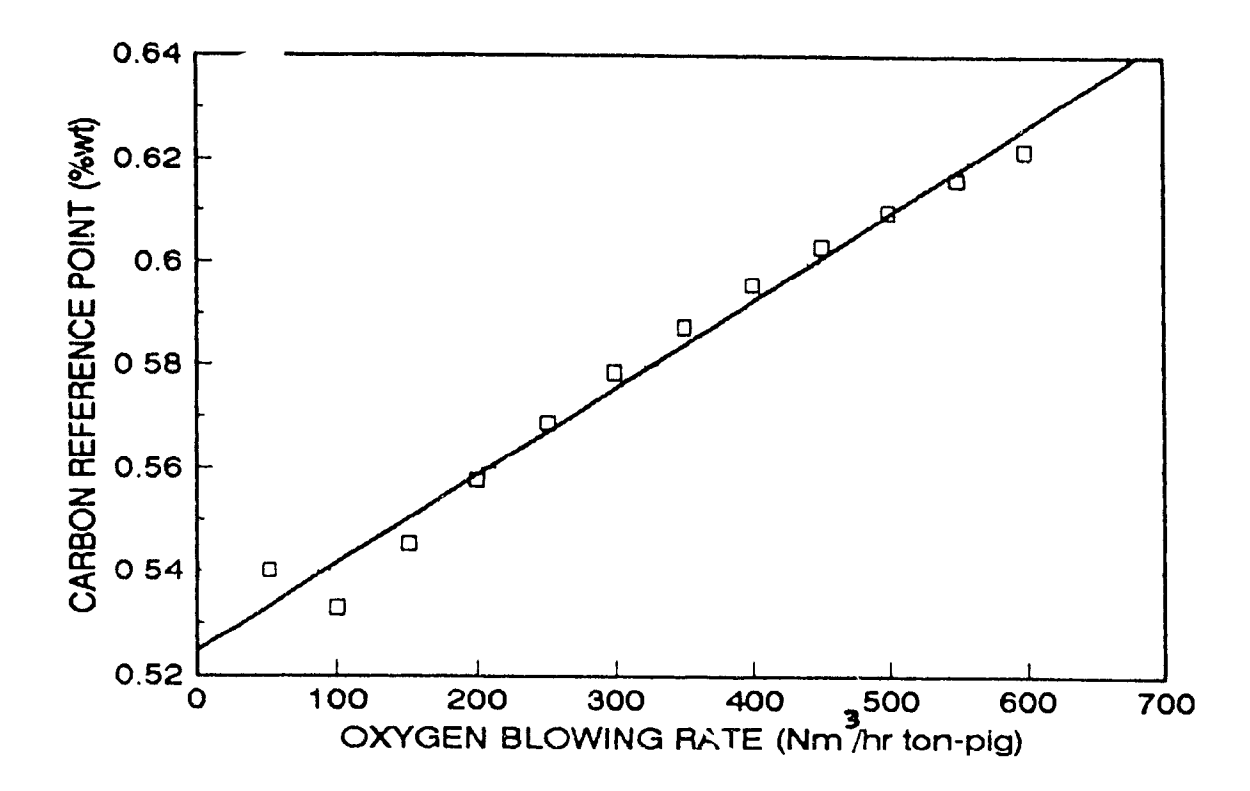


Fig. 7.53 Relationship showing the carbon reference point as a function of the oxygen blowing rate (After Ichinoe. 281).

Other BOF simulations performed in this study indicated that 0.40 to 0.44 %C appears to be the range over which one can clearly distinguish the decay in the accelerometer signal. Consider simulations B/6 (Fig. 7.19), C/1 (Fig. 7.29), C/2 (Fig. 7.31) and, in particular, C/3 (Fig. 7.33) where their respective variance—time curves did not exhibit the final decay. The lowest carbon content measured without detection of the final decay was 0.44 %C in simulation C/3. This range for the carbon reference point is slightly higher than the value reported by Kerns and Stelts⁽⁴¹⁾ for off-gas analysis; indicating that the accelerometer may have a better response time to changes in the steelmaking process. Furthermore, the difference between the carbon

reference points for the two type of sensors suggests that a time delay exists between the change in the decarburization rate and the detection of the carbon reference point. Of course, an end-point control sensor that reduces this time delay is preferential.

i

Further development of the accelerometer as an end-point control sensor requires systematic development in a steelmaking shop to determine the value of this carbon reference point with greater statistical significance. Detection of the carbon reference point can be made by a combination of the variance and frequency analysis techniques whereby frequency filtering would permit only those frequencies that described the steelmaking process to be present in the final version of the accelerometer signal. This final version of the signal would then be analyzed by the variance technique. Thus, by combining the frequency and variance analysis, shop noise would be virtually eliminated from the accelerometer signal used in an end-point control scheme.

With the carbon reference point well established, correlation between turndown carbon and blowing time after detection of the reference point, (Δt) , can be determined from historical data for various blowing conditions. This type of end-point control scheme for an accelerometer was first suggested by Ohnishi^[63] for the control of end-point phosphorous and, as was mentioned by the author of this thesis in Chapter 4, indirectly for end-point carbon as well.

Chapter 8

8. Summary and Conclusions

In an attempt to determine the feasibility of the accelerometer as a carbon end-point control sensor for BOF steelmaking, two series of BOF simulations were conducted at McGill University. To perform these simulations, previous work by the author of this thesis clearly indicated the need for a non-consumable oxygen lance to maintain a constant jet penetration force on the metal bath. To overcome this prerequisite, a water cooled, copper oxygen lance was designed and fabricated. In addition, two experimental configurations were developed for the laboratory scale simulations.

In the first experimental configuration, the accelerometer signal was monitored at low frequencies in an attempt to obtain a relationship between the amplitude of the accelerometer and the steelmaking process itself. In the second experimental configuration the accelerometer was sampled at high frequencies to discern the presence of specific vibrational frequencies that can be related to the process.

The results of the two series of simulations clearly indicate that the accelerometer is able to follow the rate of decarburization during the blow. From these results, several simulations in the second series were terminated prematurely in an attempt to determine the carbon reference point, the point at which the decarburization rate begins a rapid decay in the final portion of the oxygen blow. The carbon content of the bath at the time when the accelerometer can clearly

detect this change determines whether the accelerometer can be applied as a carbon end-point control sensor or not.

From the present research work, the following conclusions can be drawn:

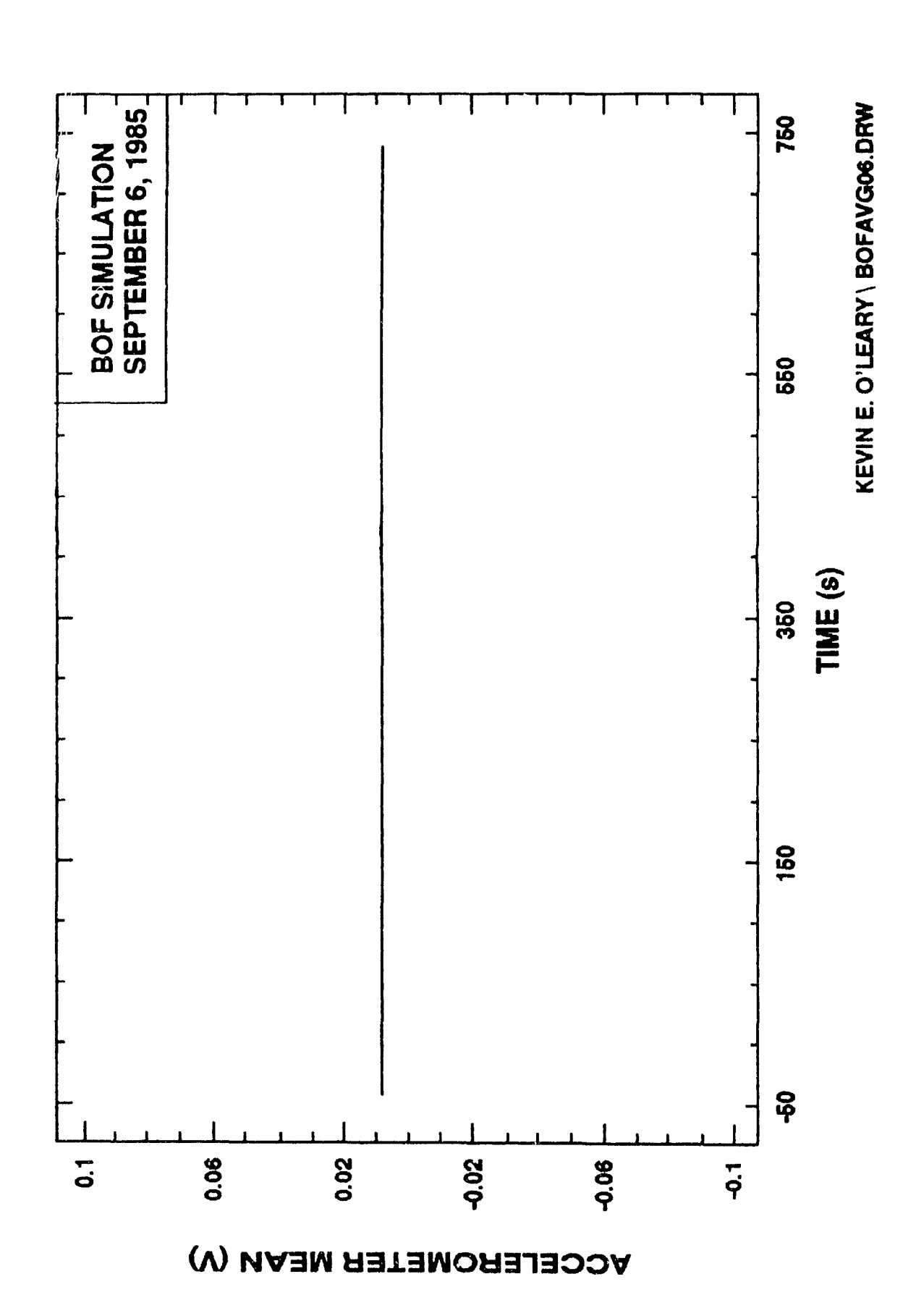
- 1.) The alumina crucible as the steelmaking vessel provided a safe environment in which the BOF simulations can be conducted.
- 2.) The design of the water cooled, copper oxygen lance proved to be excellent. A counter current water cooling design greatly improved the heat transfer at the nozzle tip and reduced the erosion rate of the nozzle tip. Furthermore, the design of the lance permitted oxygen jet penetration depths into the bath that are comparable to industrial BOFs.
- 3.) Investigations have shown that the accelerometer produces a reliable signal that can be applied to a simple end-point control scheme for oxygen steelmaking. Such a scheme would involve the detection of a characteristic decline in the variation of the transducer's signal; this decline represents the critical carbon content reference point, at which value the rate equation describing the bath changes. The carbon reference point has been determined to be $0.40 \le 5C \le 0.44$ at which the accelerometer can clearly detect the decay in the decarburization rate. The time to the end of a particular blow would be determined from a correlation of the time elapsed from the critical carbon content reference point (i.e. time to turndown) and the turndown carbon content.
- 4.) The increase in the decarburization rate ist before the final decay in the variance of the accelerometer signal can be attributed to an over-oxidized, foaming slag that provides additional oxygen to the decarburization reaction and increase the volume of CO_{jus} produced. As a result, the intensity of the vibrations measured by the accelerometer increased.
- 5.) The accelerometer transducer appears to be more responsive to changes in the steelmaking process and, in particular, can detect the final decay in the rate of decarburization earlier than systems that rely on off-gas analysis.
- 6.) The accelerometer variance-time curves provide an excellent forum to interpret and present the results from both the low and high frequency simulations. The typical accelerometer variance-time curve closely resembles the ideal rate of decarburization.

- 7.) Background noises can be clearly identified by Fourier analysis of the accelerometer signal. This information, in turn, can be used to develop filters to eliminate the affect of roise on the accelerometer signal. This is a significant advantage in an industrial shop where numerous sources of noise exist.
- 8.) The vibrational characteristics of the furnace changed drastically after being reconstructed. Furthermore, as a result of the change, the power spectrum became more complex and predominant frequencies were considerably higher.

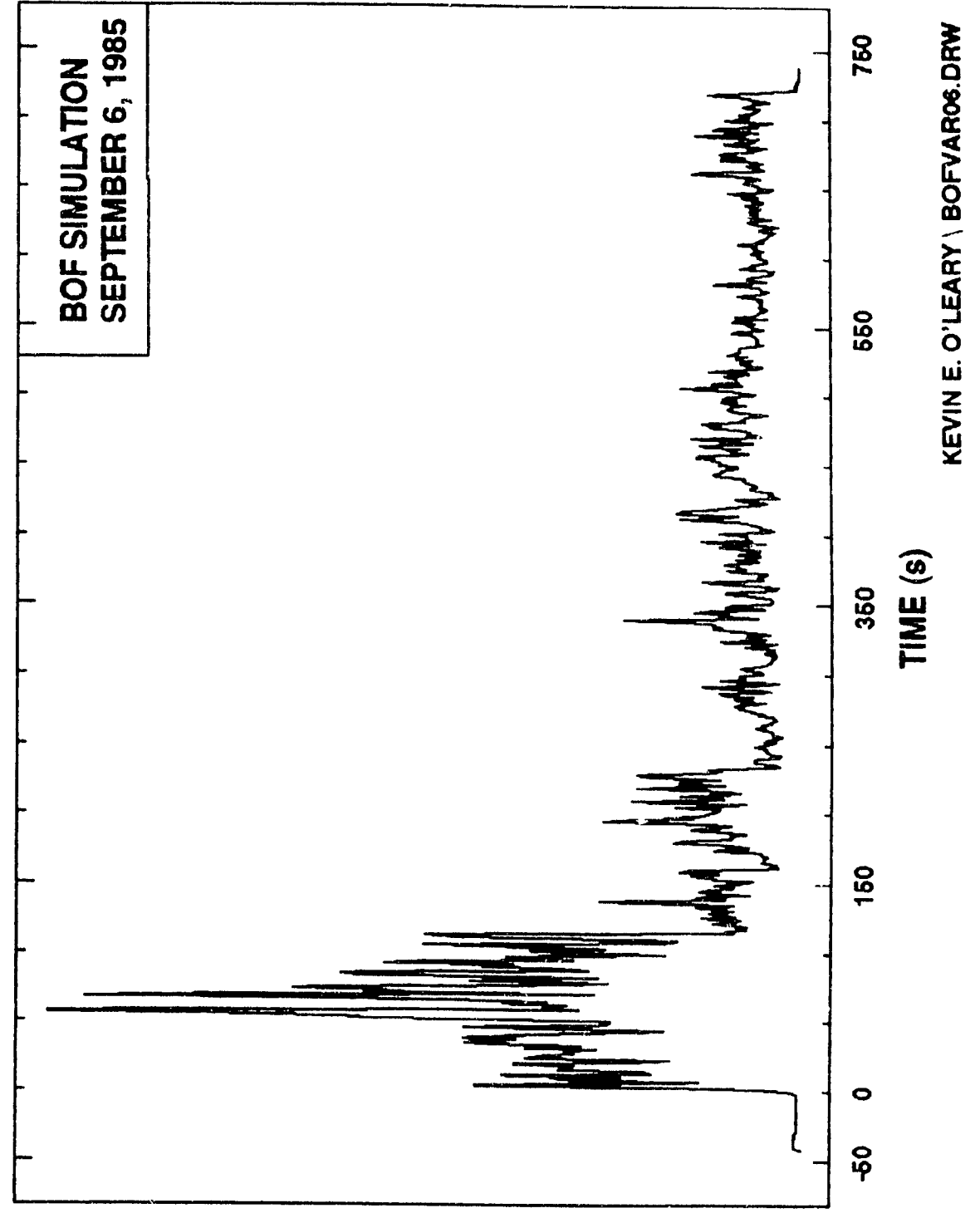
APPENDIX A

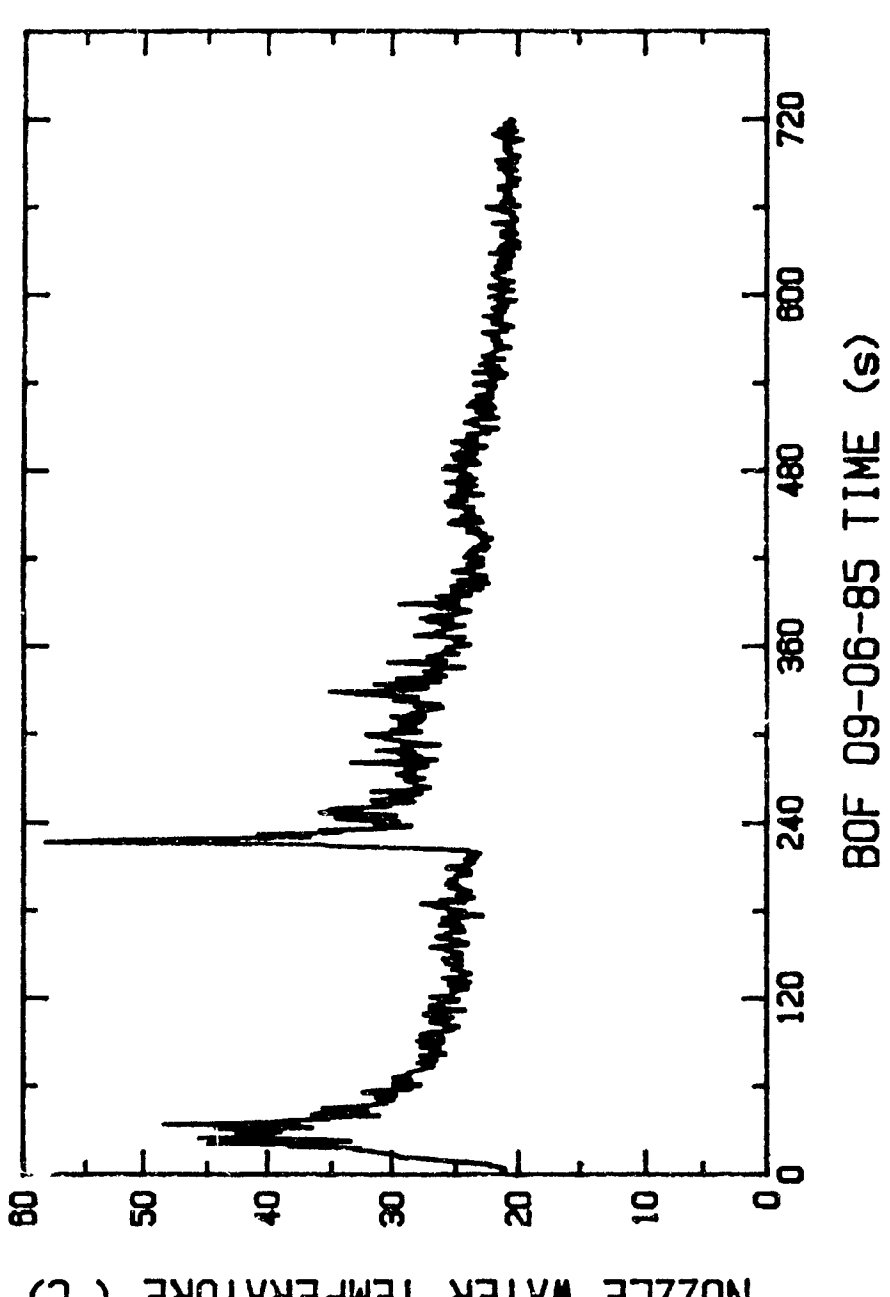
Analysis of High Frequency Simulations

Test Code: B/6		Test Date: September 6, 1985		
Operating Parameters	·:			
Hot Metal Weight:	18.4 kg	Final Carbon:	0.60 ·wt	
Free Board:	155 mm	Change in Carpon:	<u> 3 45 wt</u>	
Lance Depth:	120 mm	Blown Oxygen Volume:	1096 N•1	
Height Above Melt:	35 mm	Blowing Time:	720 s	
Furnace Power:	10 kVA	Oxygen Flow Rate:	1.52 N•1/5	
Acculerometer Signal	. Analysis:			
Sampling Frequency:		1500 Hz		
Decay in $\partial C/\partial O$ Observed:		Not Observed		
Time of Observation:		N/A		
Major Frequency Bands Analyzed:		39-43Hz, 47-51Hz, 67-72Hz, 163- 167Hz, 172-176Hz, and 343- 347Hz.		

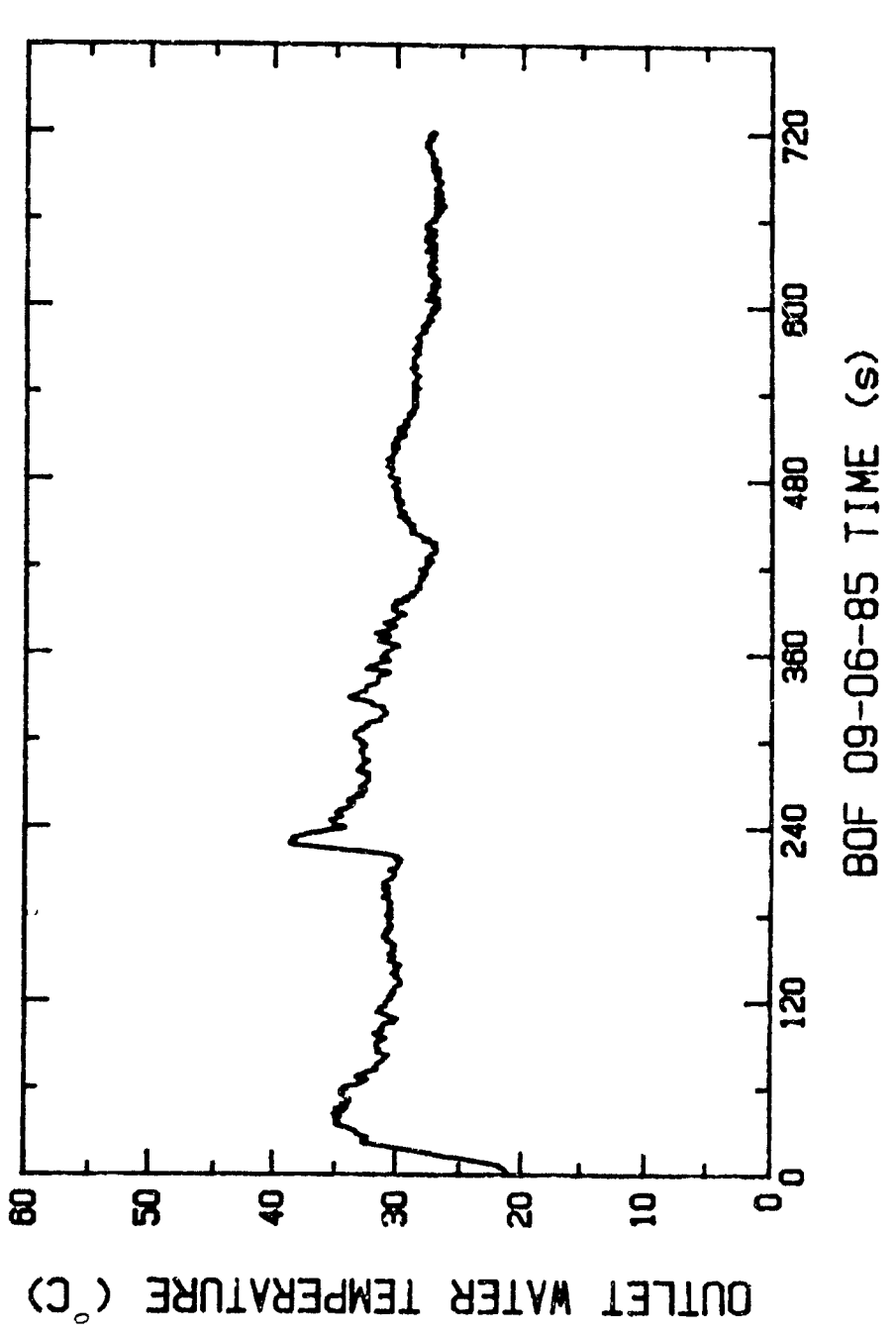


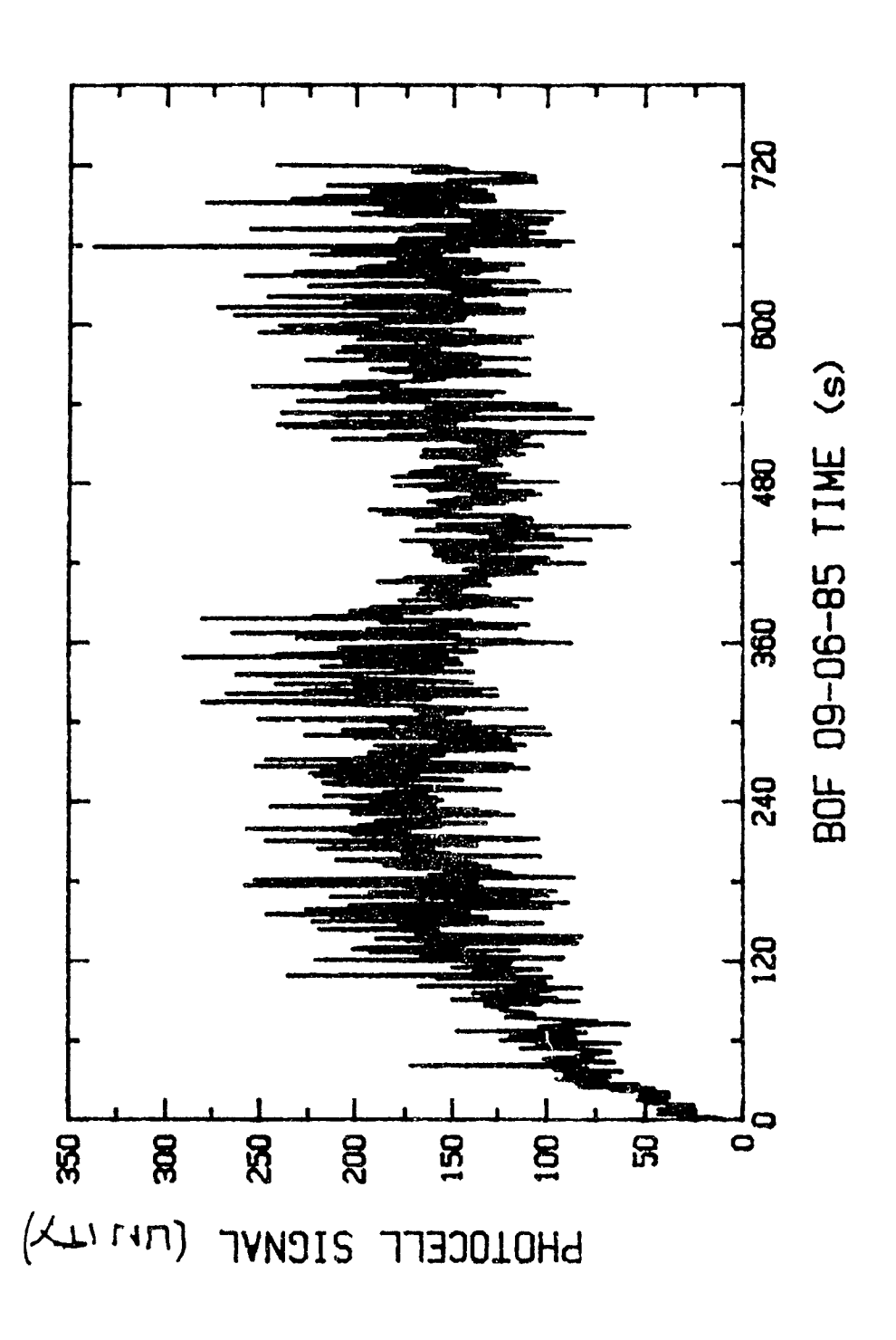
ACCELEROMETER VARIANCE

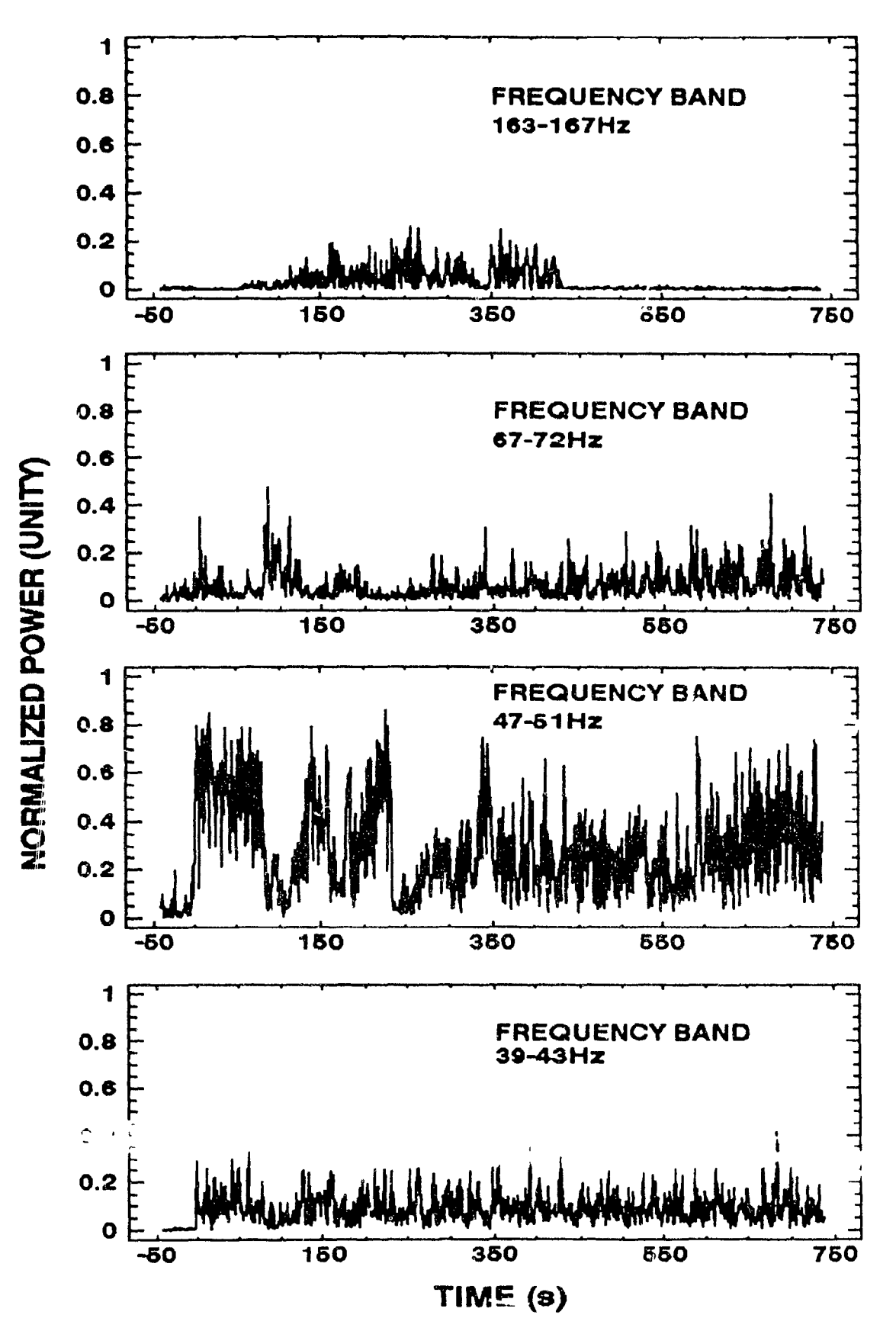




NOZZLE WATER TEMPERATURE (°C)

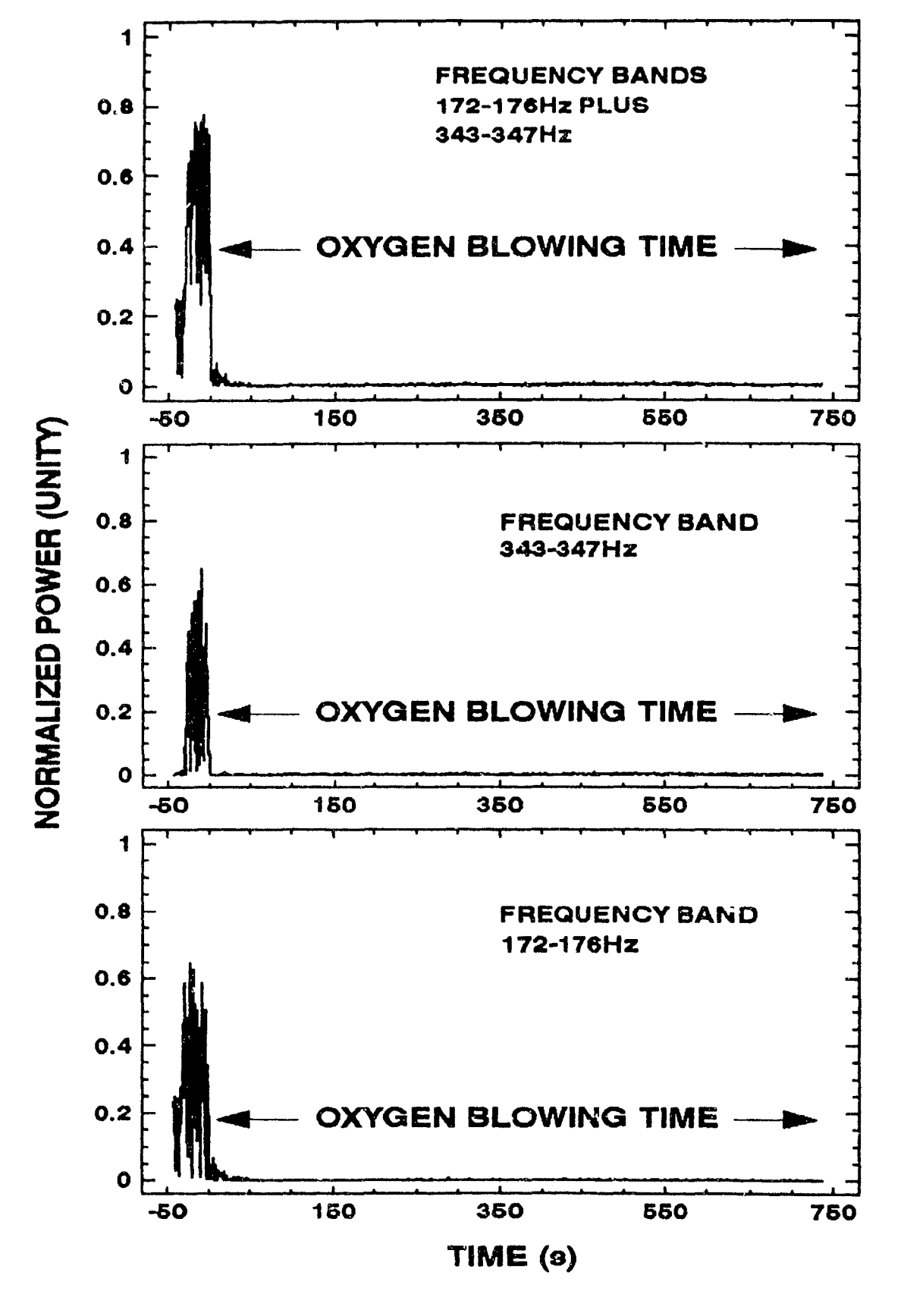


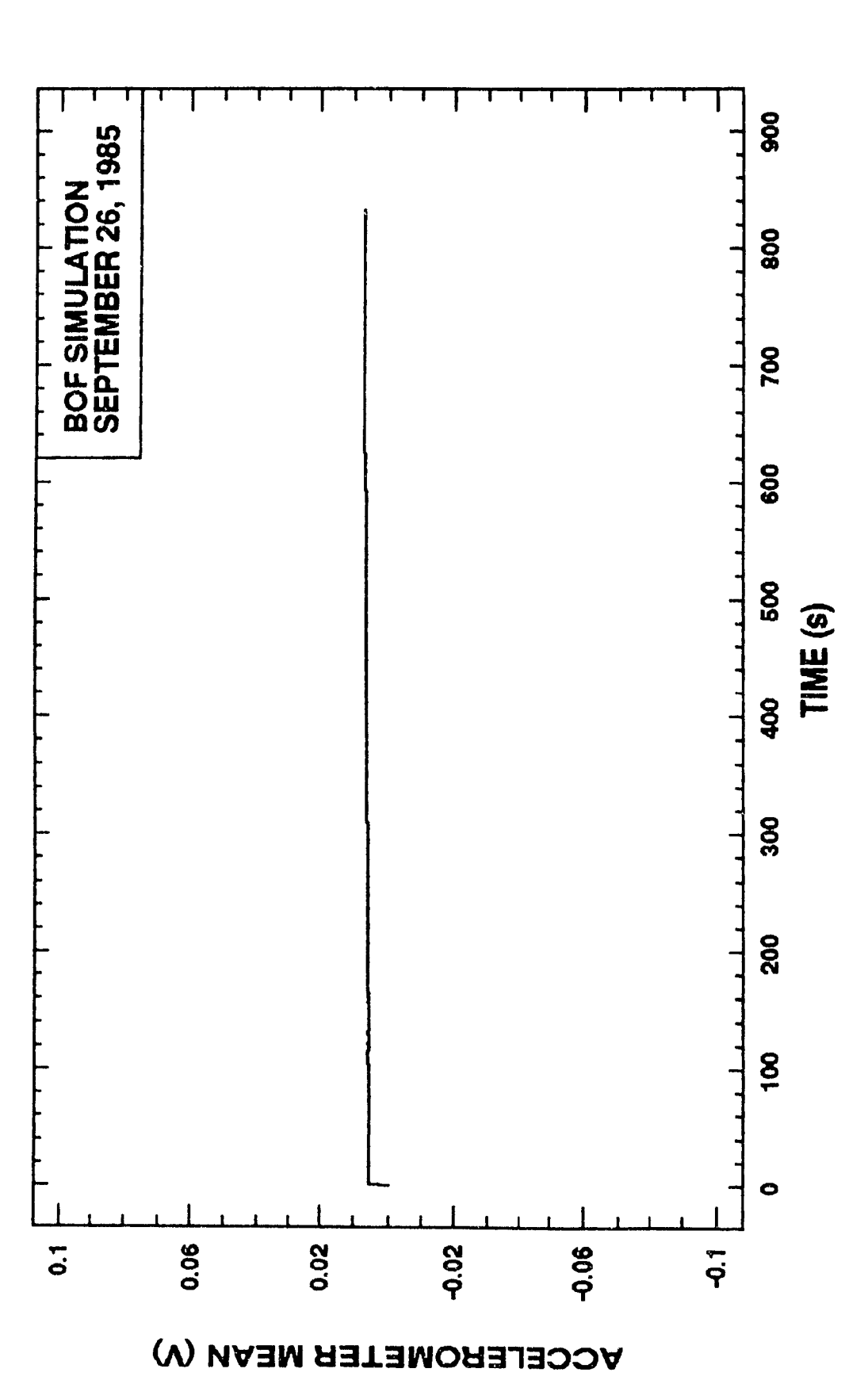




BOF SIMULATION - SEPTEMBER 6, 1985





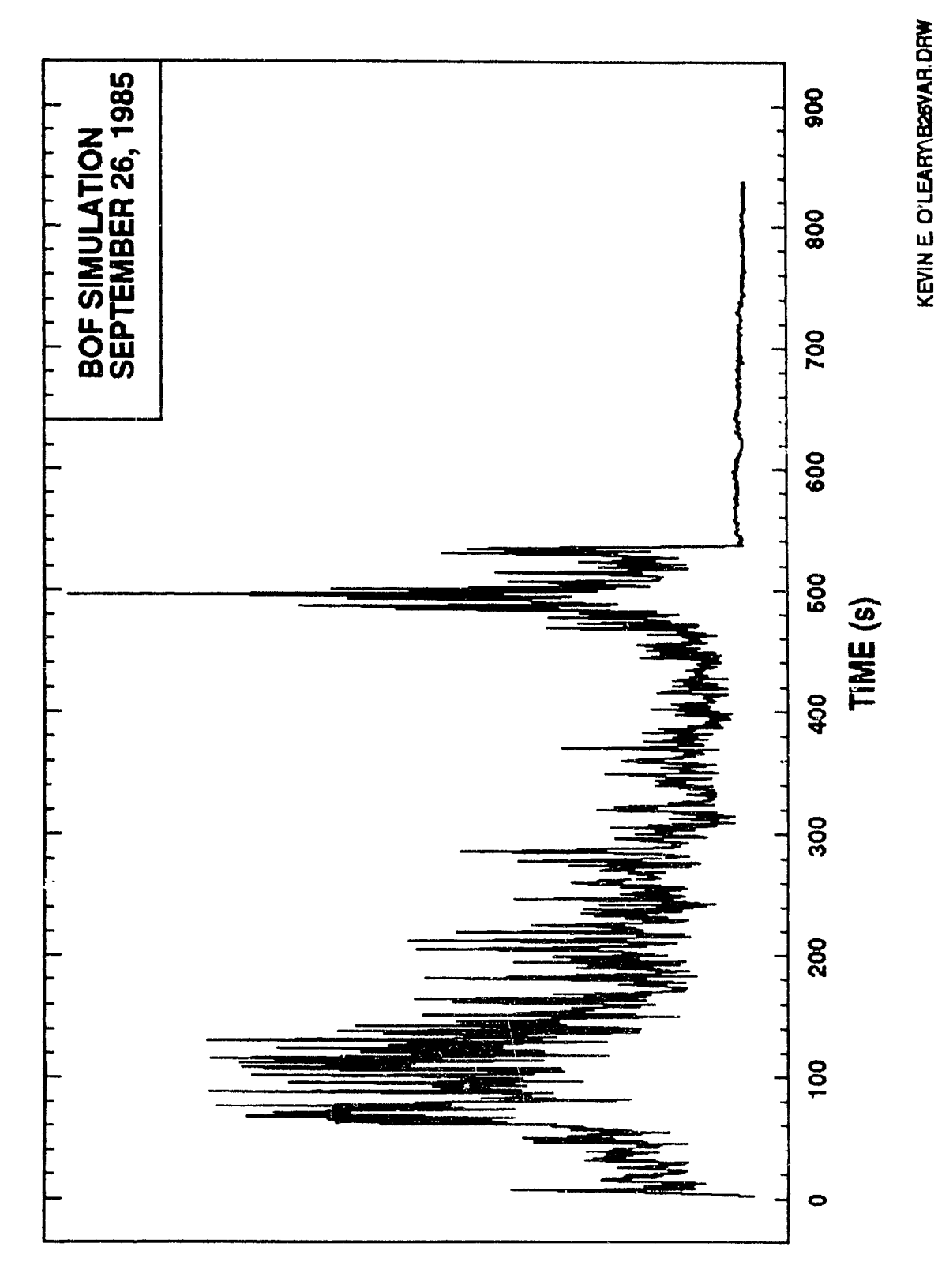


 \mathbf{f}_{i}

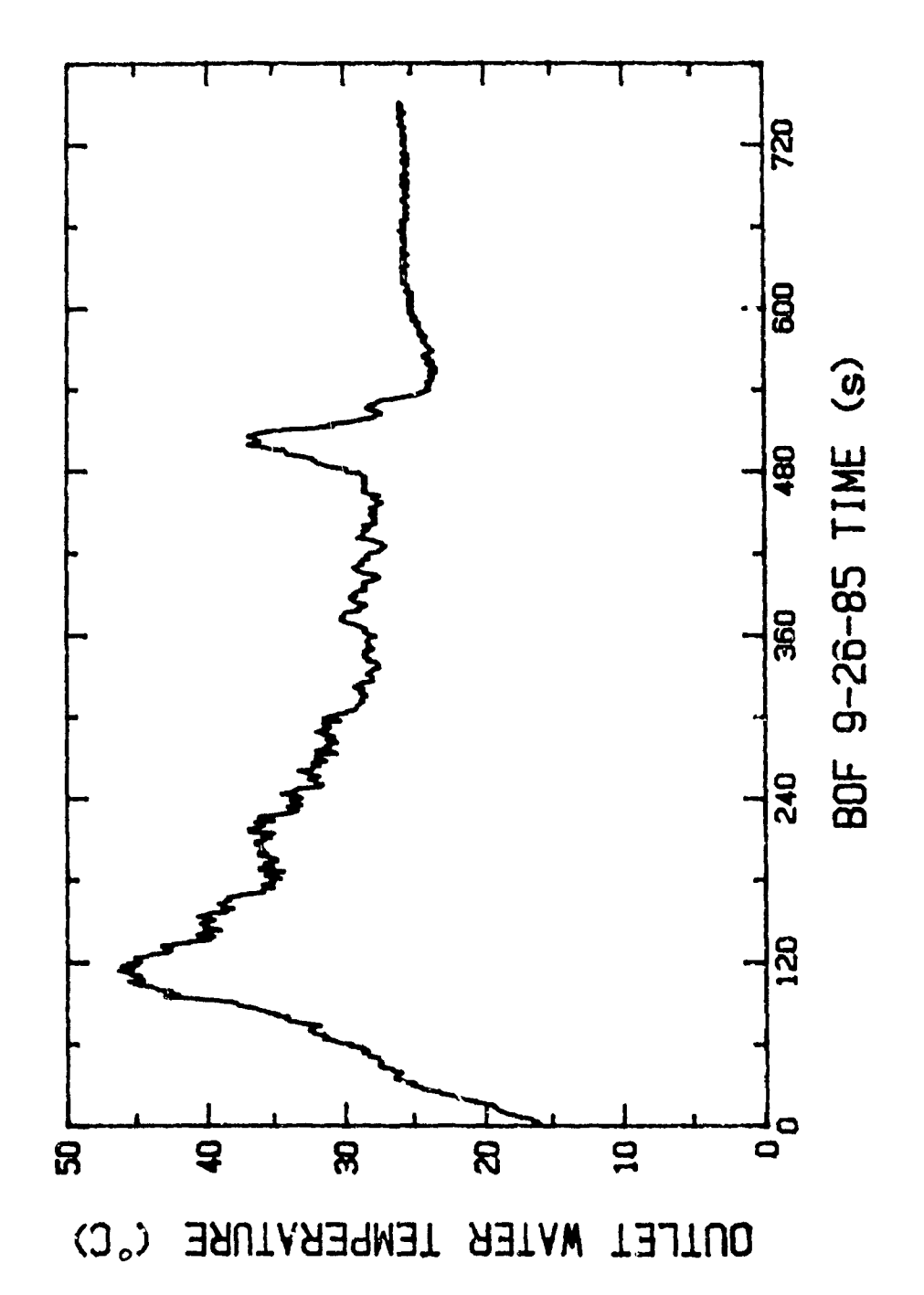
Ę

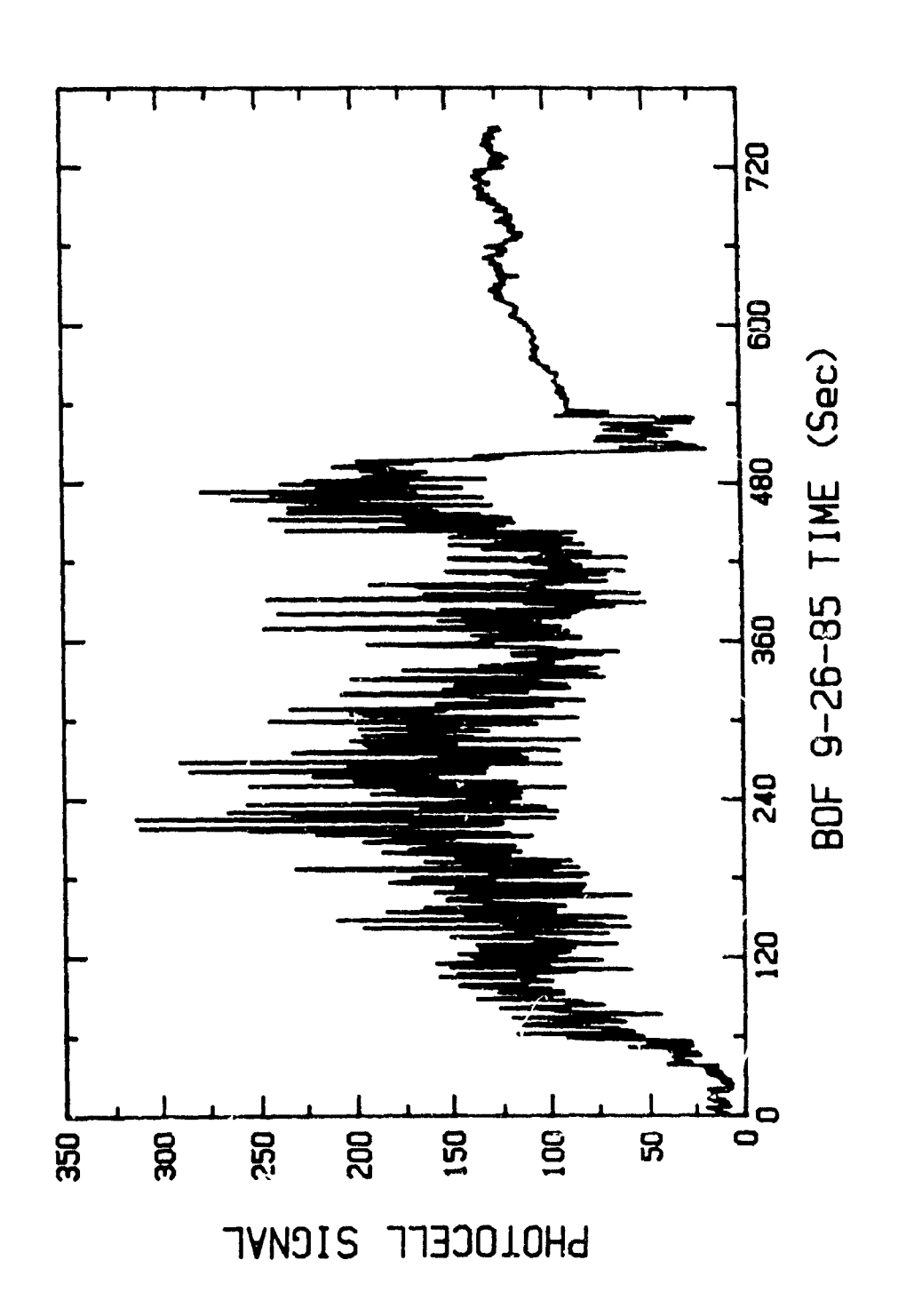
KEVIN E. O'LEARY B26XBAR. DRW

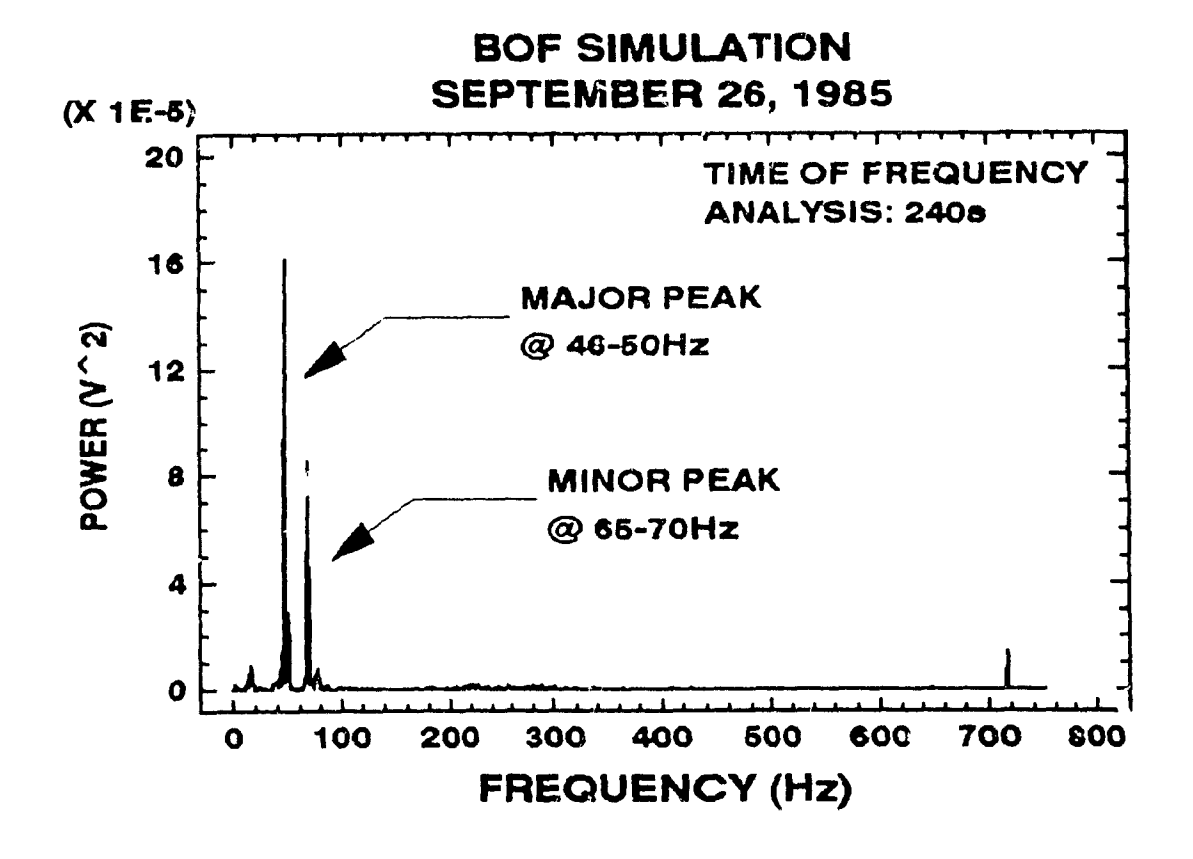
ACCELEROMETER VARIANCE

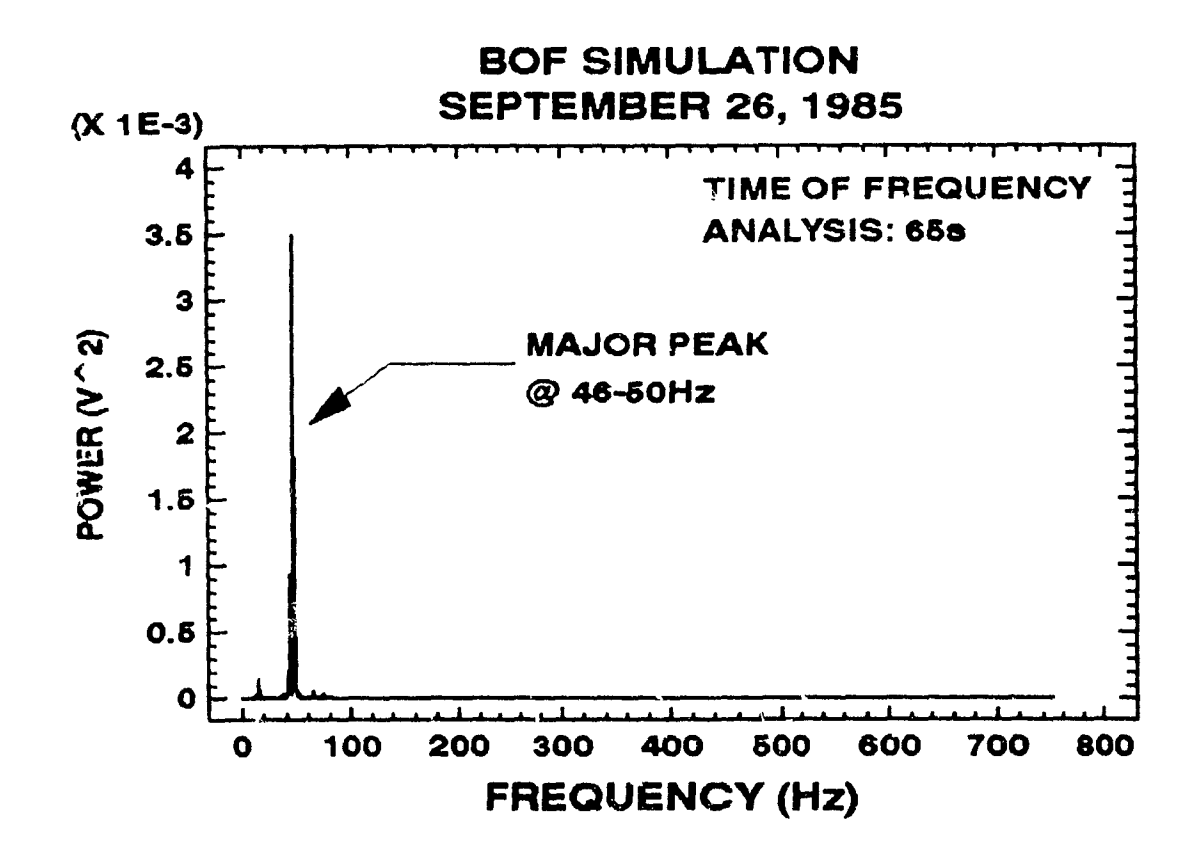


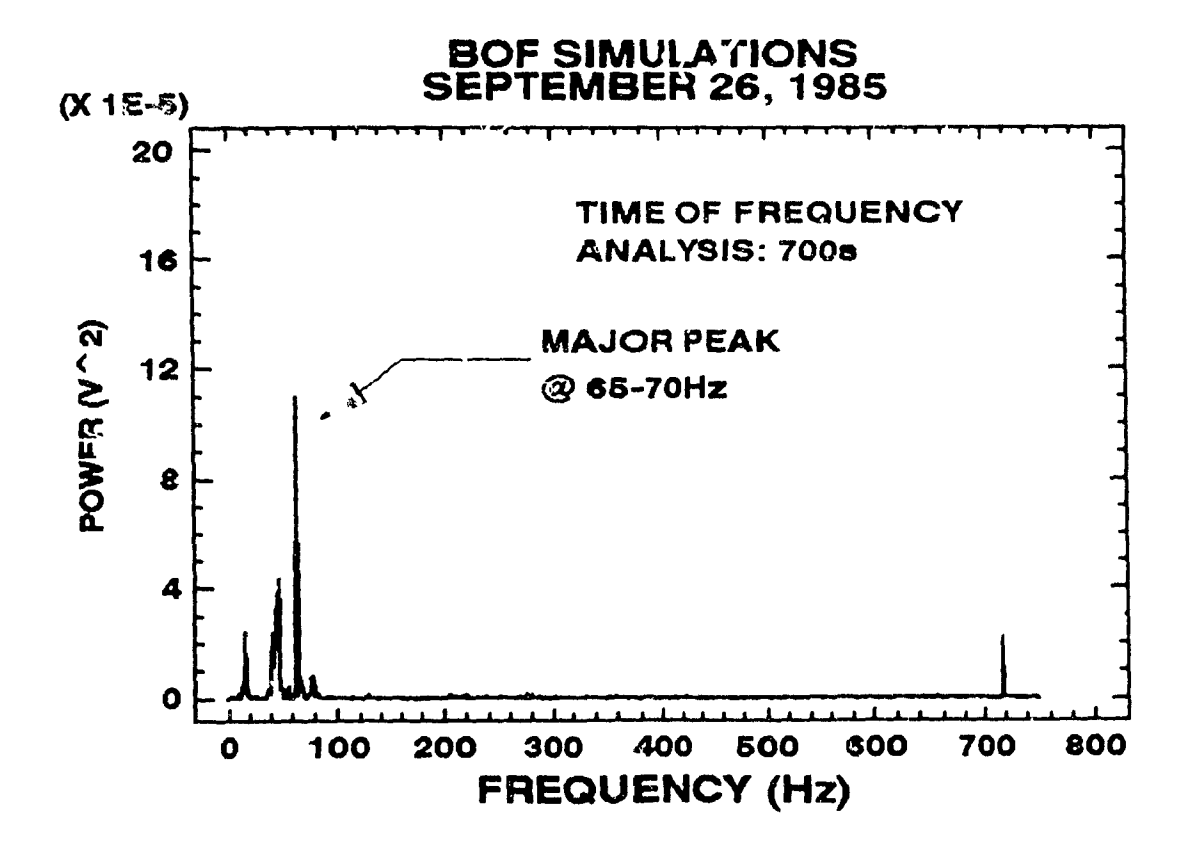
NOZZLE WATER TEMPERATURE (°C)



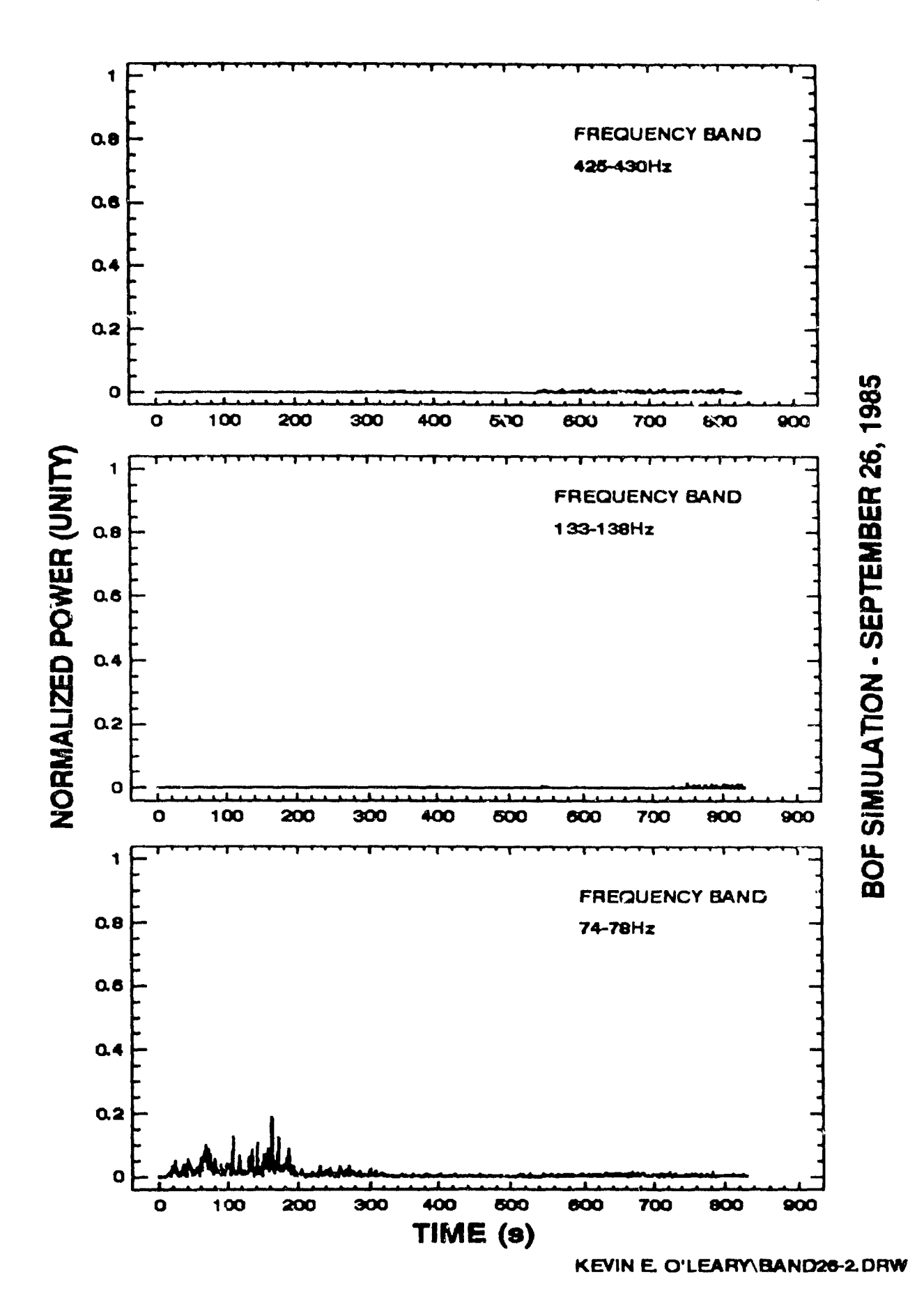




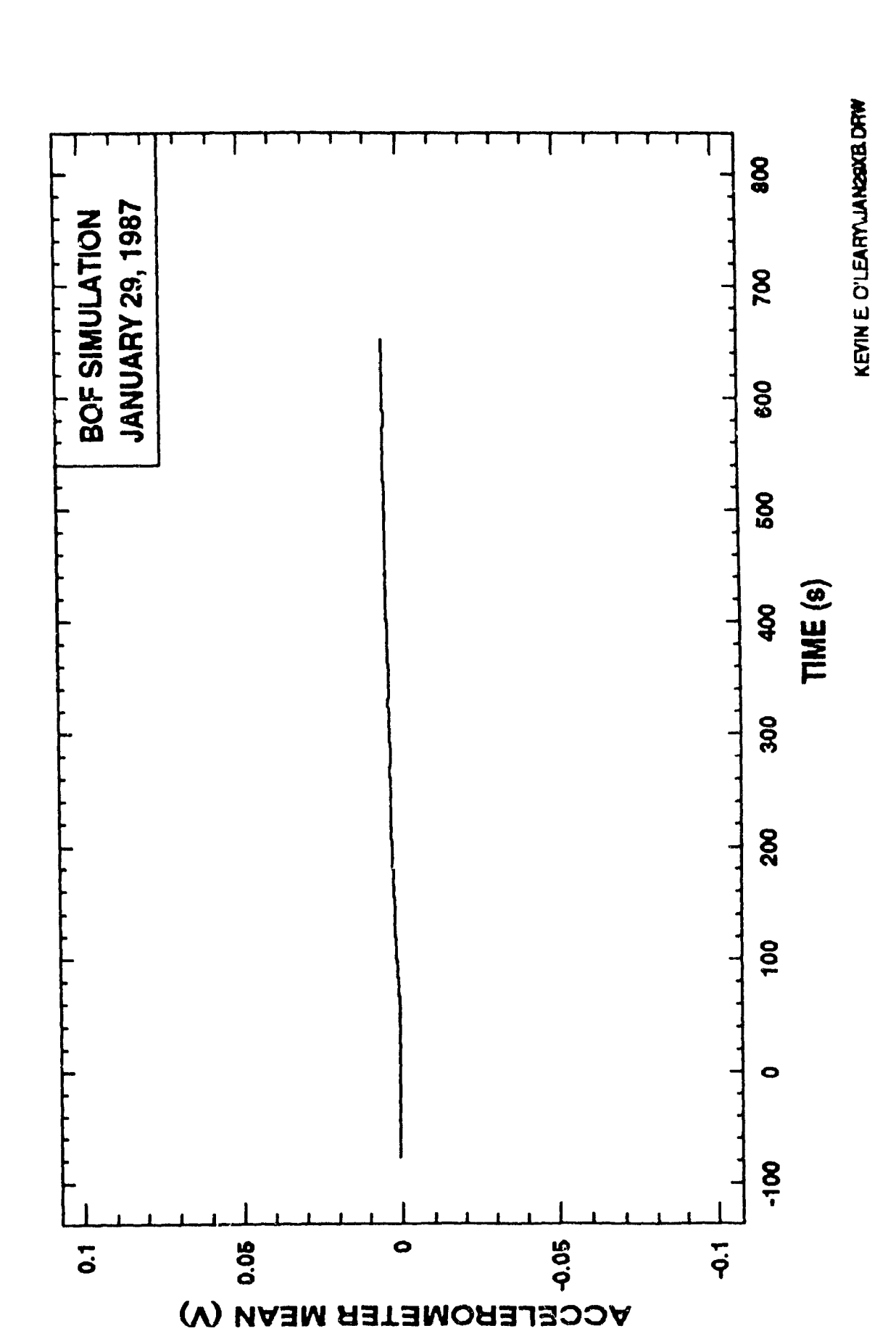


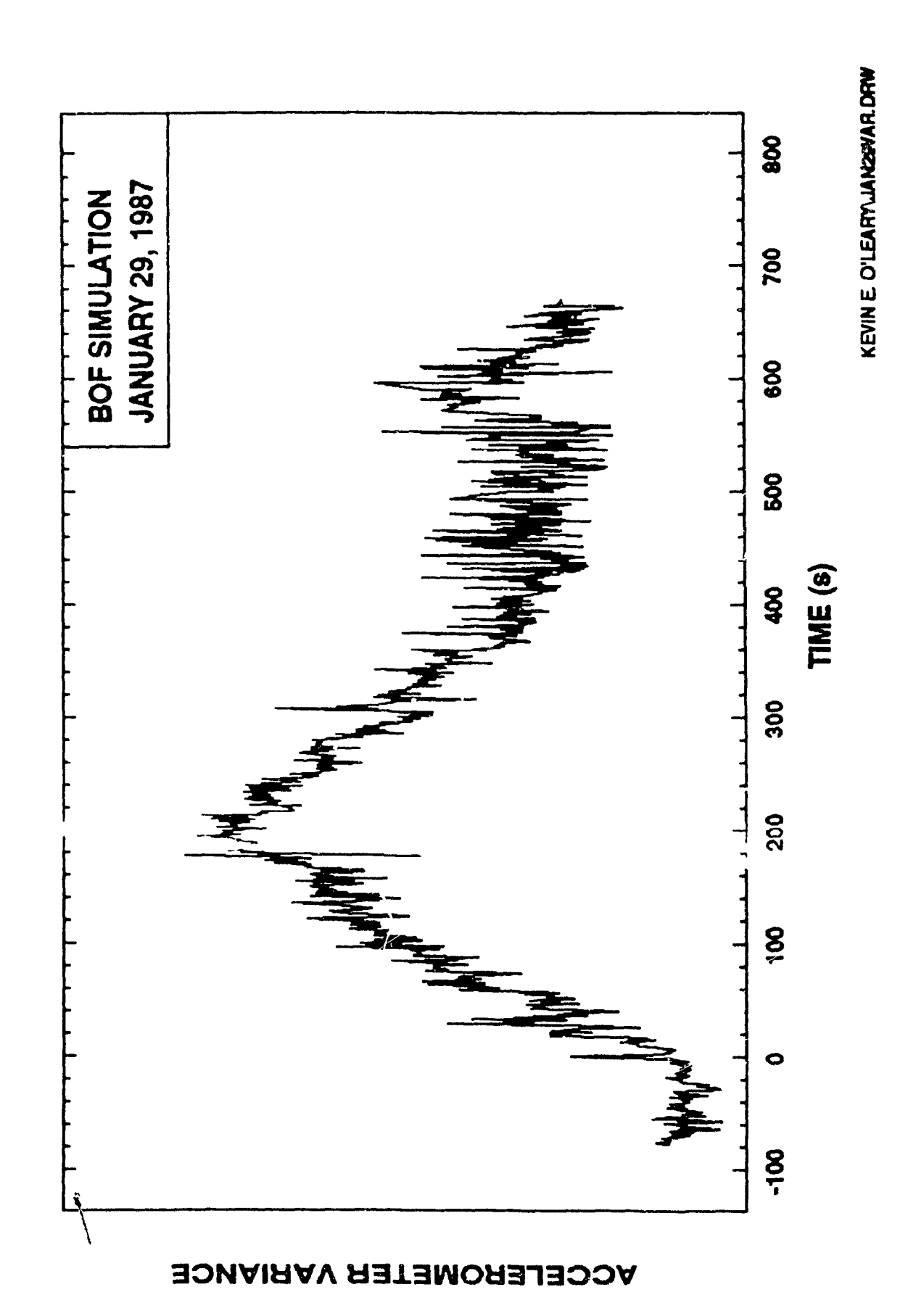


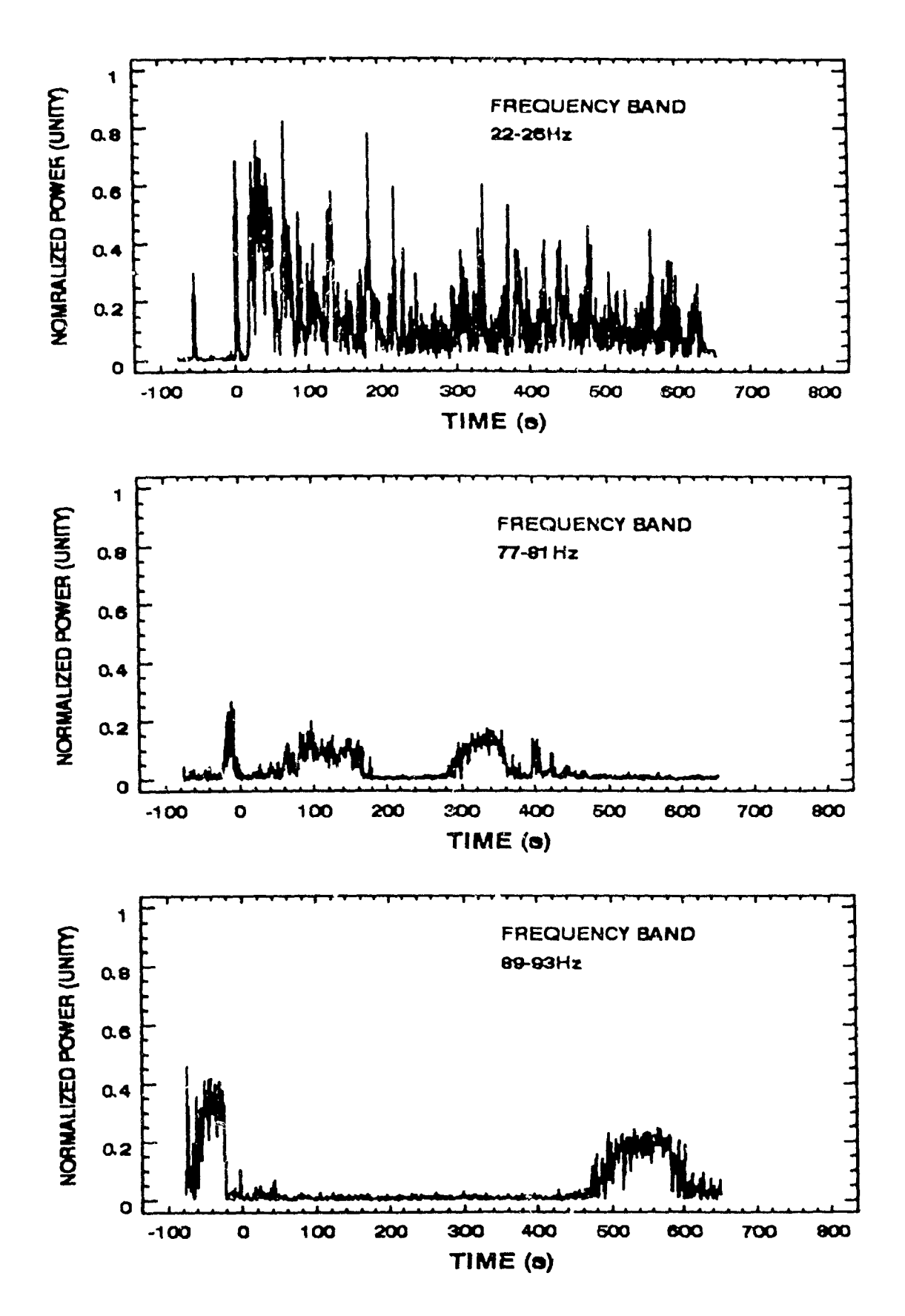
BOF SIMULATION - SEPTEMBER 26, 1985



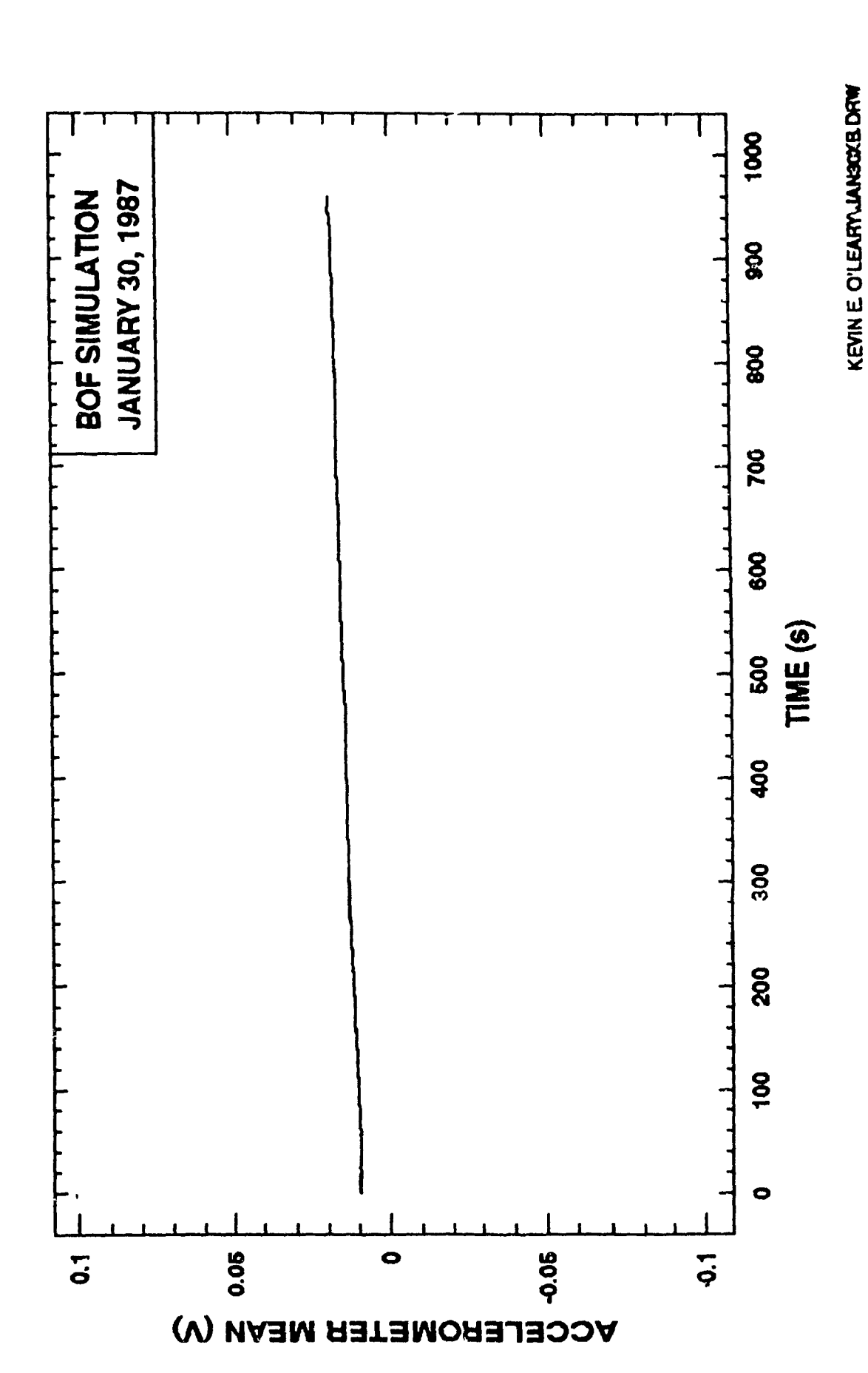
Test Code: C/1 Test Date: January 29, 1987 Operating Parameters: Hot Metal Weight: 14.1 kg Final Carbon: <u>1.01</u> %wt Free Board: <u>190 mm</u> Change in Carbon: 4.00 %wt Lance Depth: 165 mm Blown Oxygen Volume: 865 N·1 Height Above Melt: 25 mm Blowing Time: <u>720 s</u> Furnace Power: ___0 kVA_ Oxygen Flow Rate: 1.20 N·1/s Accelerometer Signal Aralysis: Sampling Frequency: 500 Hz Decay in $\partial C/\partial O$ Observed: Not Observed Time of Observation: N/A Major Frequency Bands Analyzed: 22-26Hz, 77-81Hz, and 89-93Hz

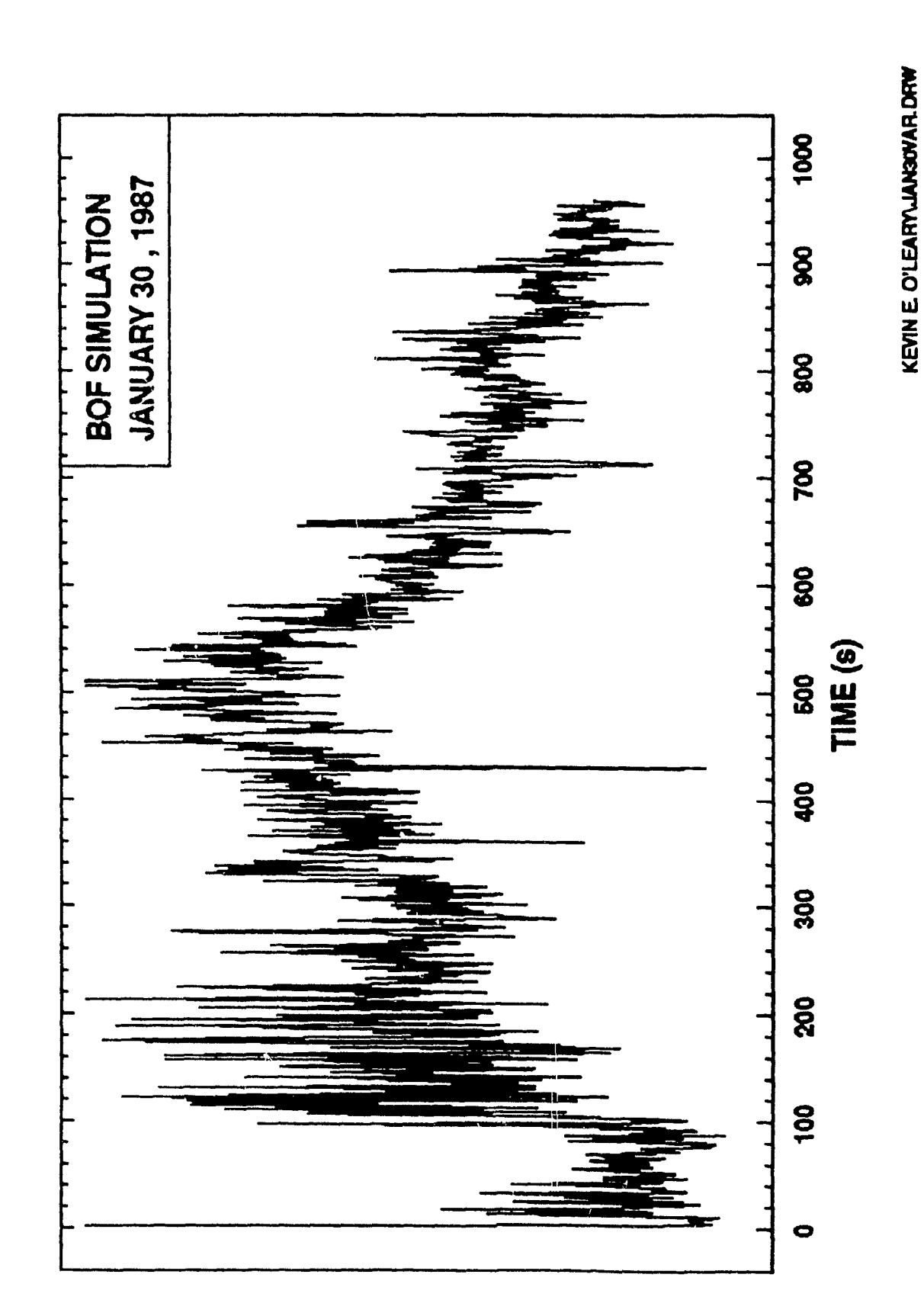


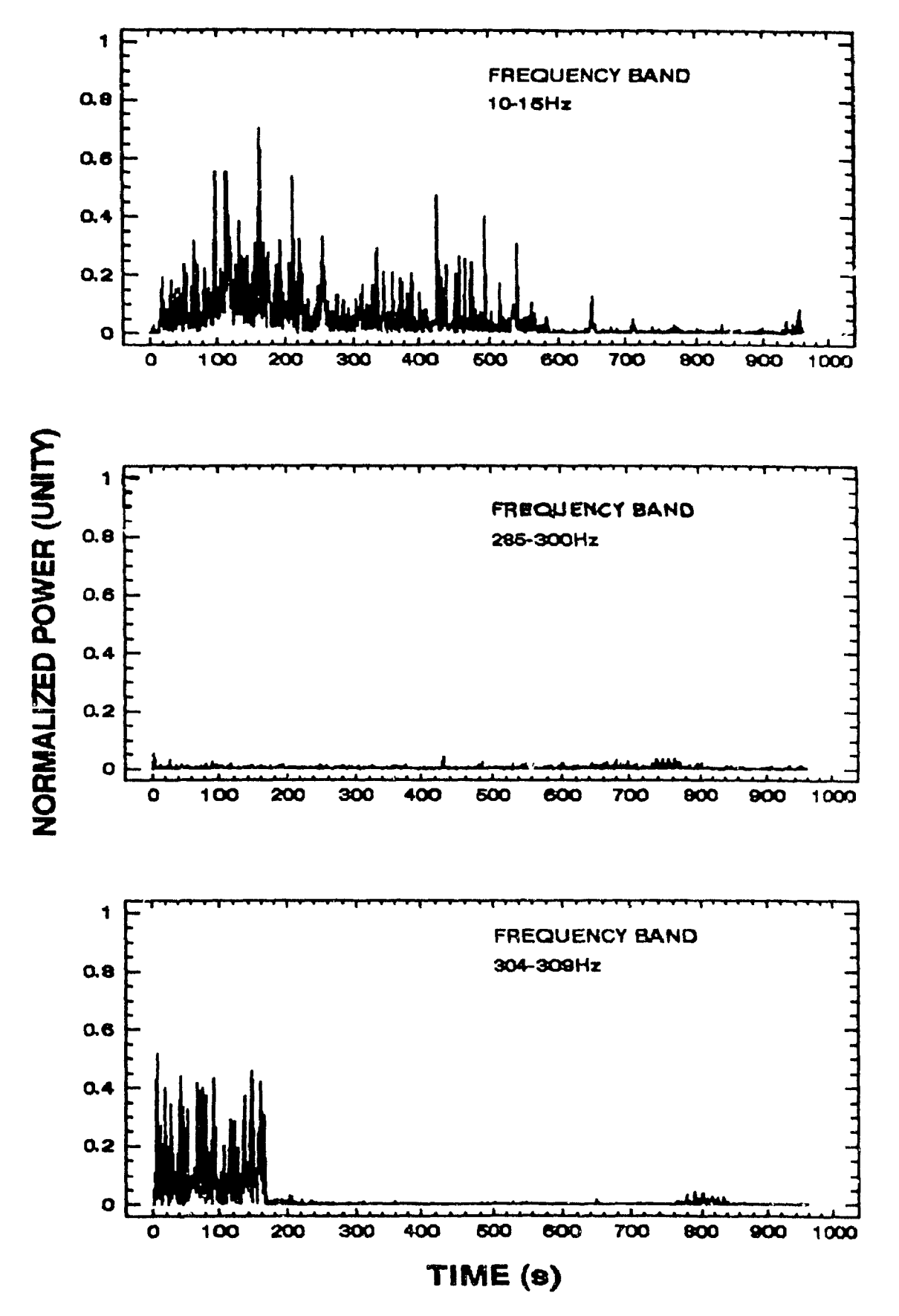




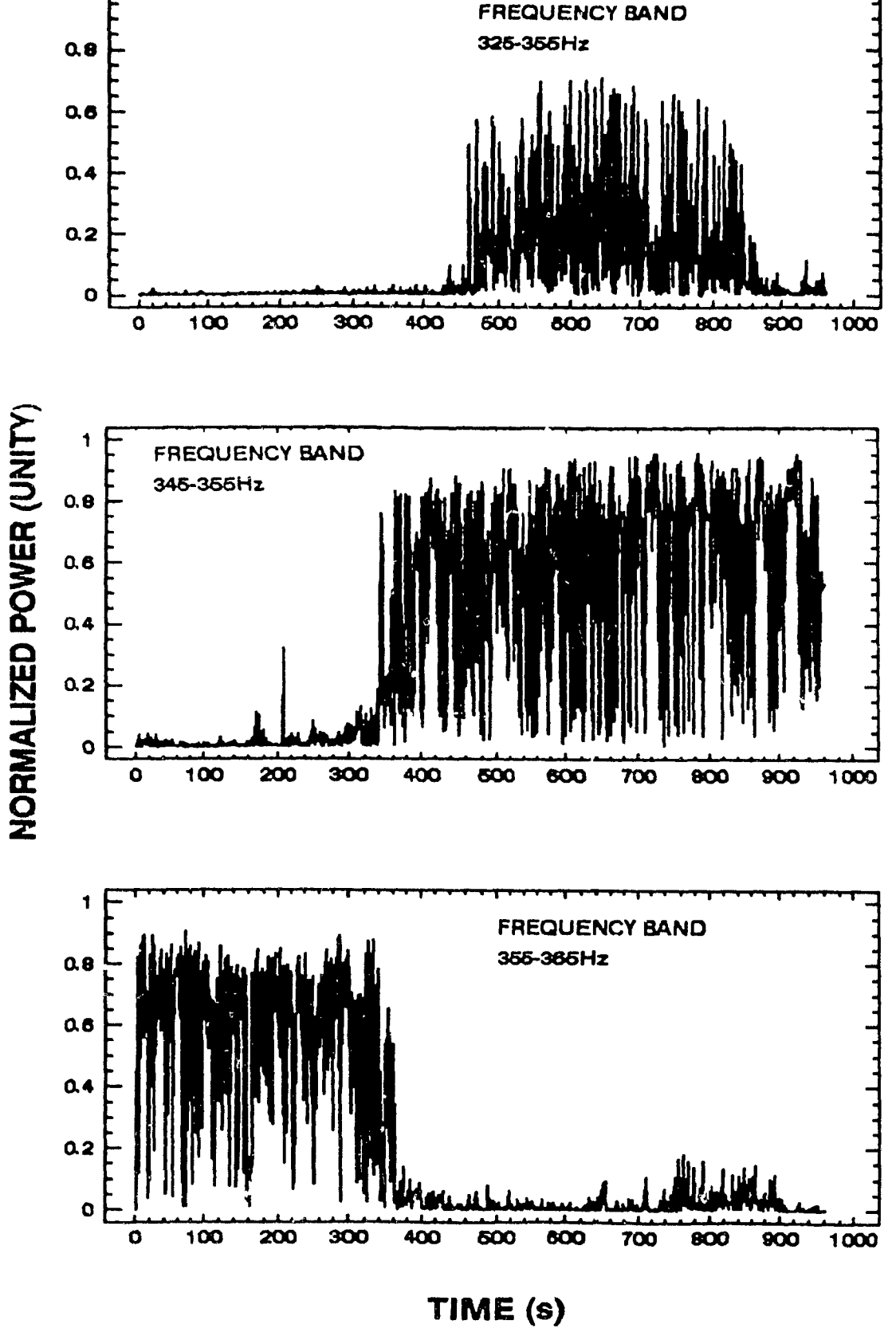
Test Code: C/2		Test Date: January 30,	1987		
Operating Parameters:	<u>.</u>				
Hot Metal Weight:	22.7 kg	Final Carbon: 1.94	8wt		
Free Board:	220 mm	Change in Carbon: 4.00	1 8wt		
Lance Depth:	195 mm	Blown Oxygen Volume: 865	N•1		
Height Above Melt:	25 mm	Blowing Time: 960	s		
Furnace Power:	0 kVA	Oxygen Flow Rate: 0.90	N•1/5		
Accelerometer Signal	Analysis:				
Sampling Frequency:		1000 Hz			
Decay in $\partial C/\partial O$ Observed: Time of Observation:		Not Observed			
		N/A			
Major Frequency Bands Analyzed		10-15Hz, 285-3Hz, 304-			
		325-355Hz, 345-355Hz, and 365Hz	7 222.		





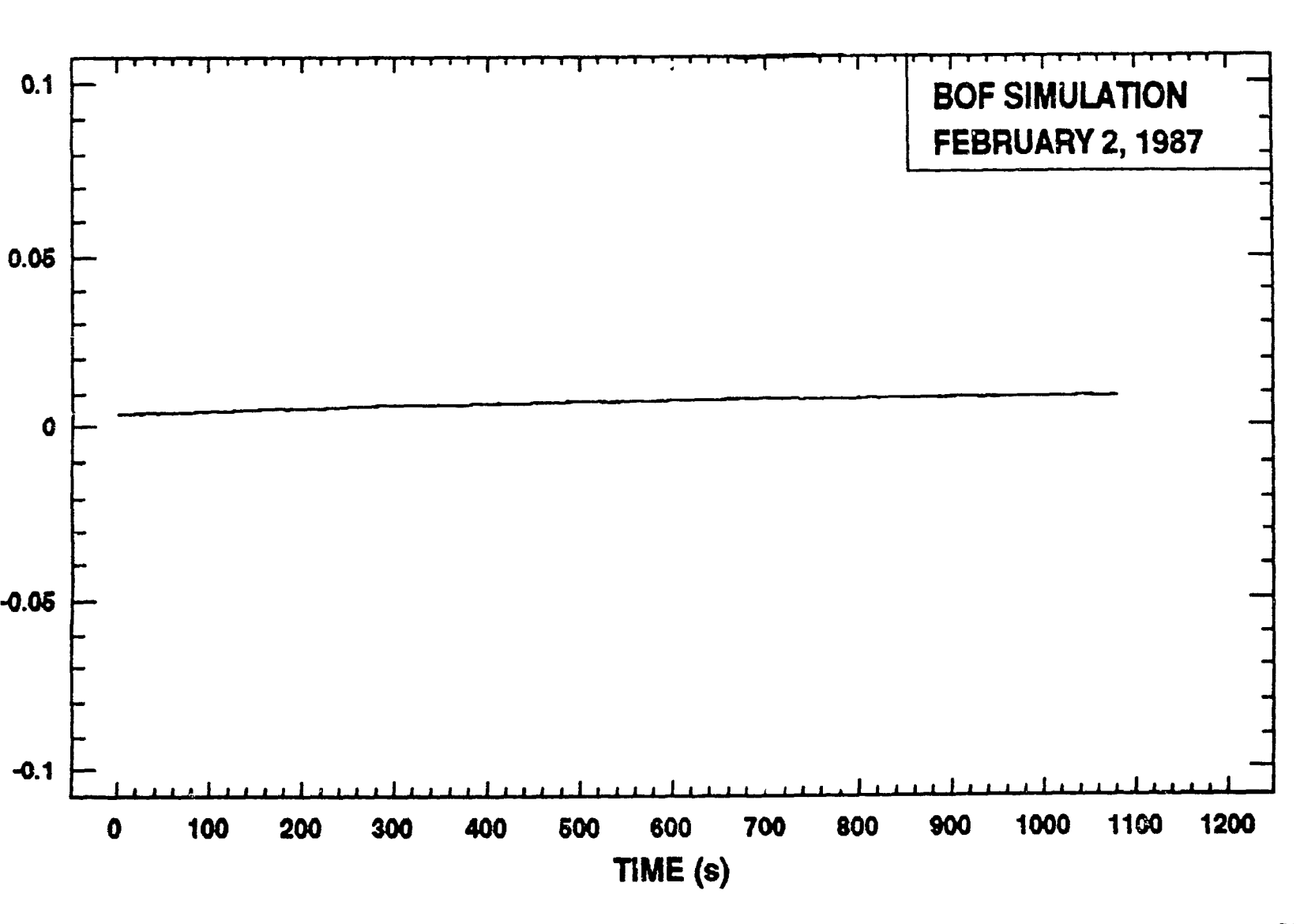


BOF SIMULATION - JANUARY 30, 1987

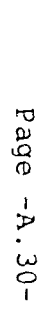


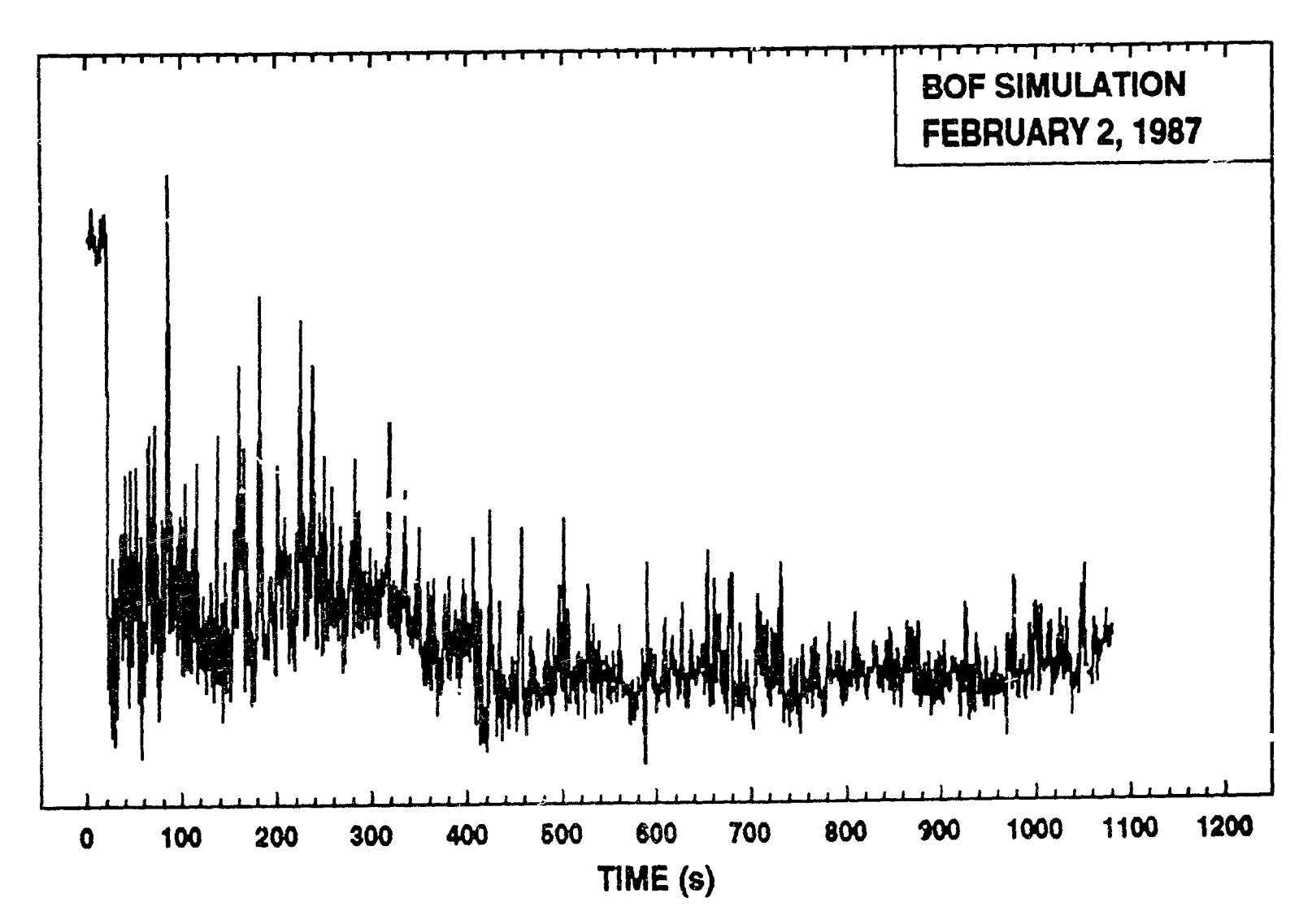
Ì

Test Code: C/3		Test	Date:	Februar	y 2,	1987
Operating Parameters:	-					
Hot Metal Weight:	23.2 kg	Fina	l Carbon:		0.44	%wt_
Free Board:	220 mm	Chan	ge in Car	bon:	4.00	₹wt
Lance Depth:	195 mm	Blow	n Oxygen	Volume:	1096	N•1
Height Above Melt:	25 mm	Blow	ing Time:		900	S
Furnace Power:	0 kVA	Охуд	en Flow R	ate:	1.22	N•1/s
Accelerometer Signal	Analysis:					
Sampling Frequency:			1000 Hz			
Decay in $\partial C/\partial O$ Observed:		<u>]</u>	Not Obser	ved		
Time of Observation:			N/A	······		
Major Frequency Bands	Analyzed:		15Hz, 290 370Hz, an			311Hz,

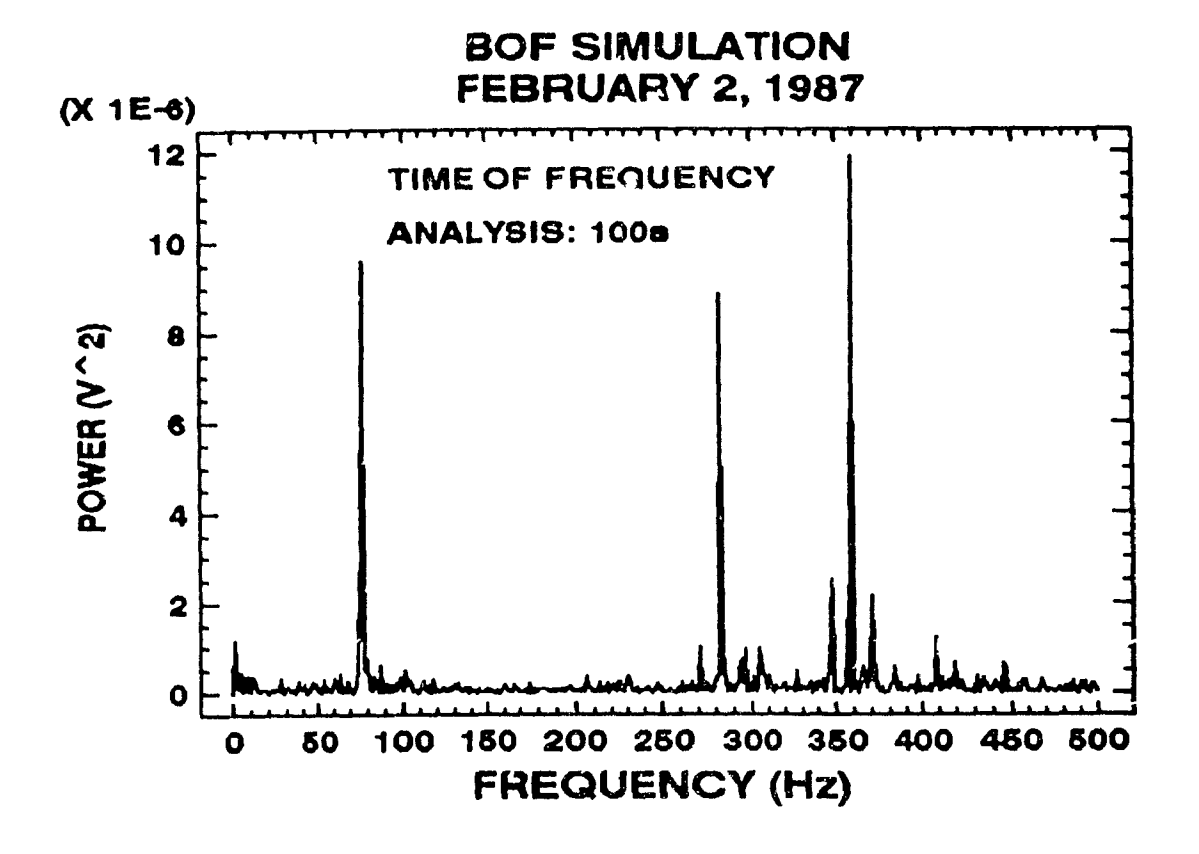


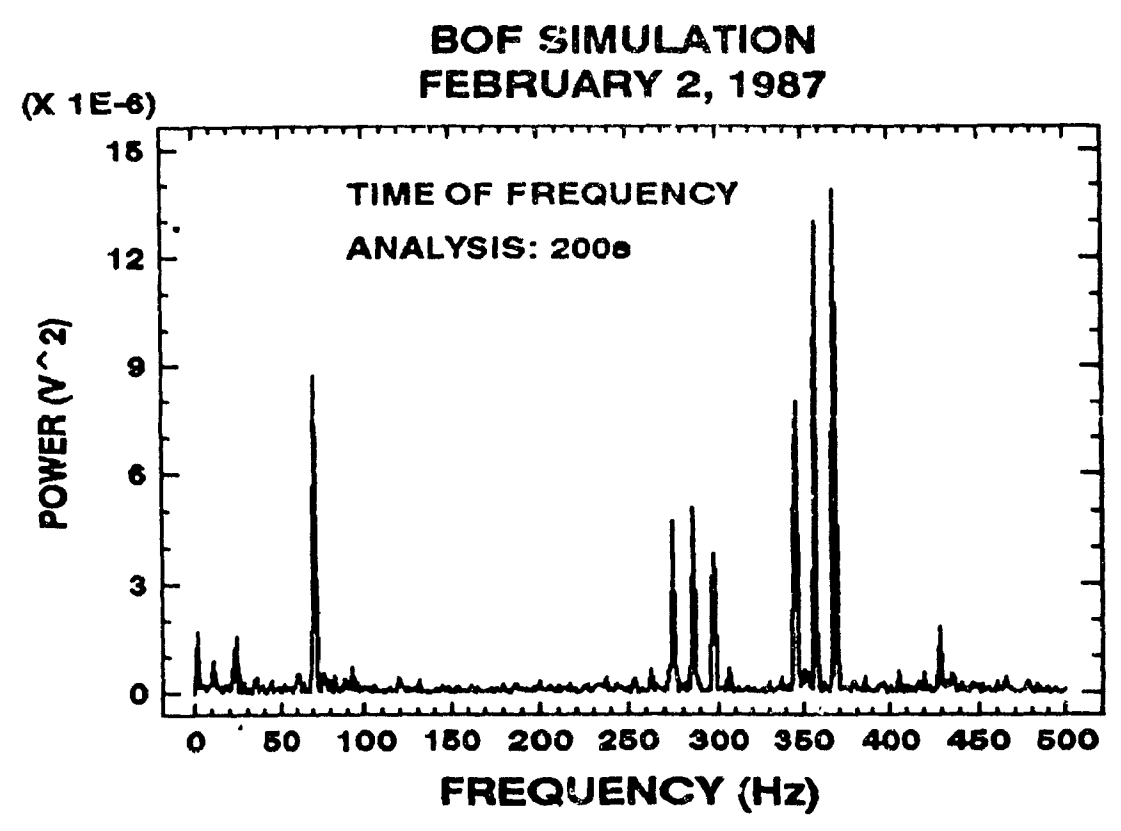
KEVIN E. O'LEARY\FEB2XBAR.DRW

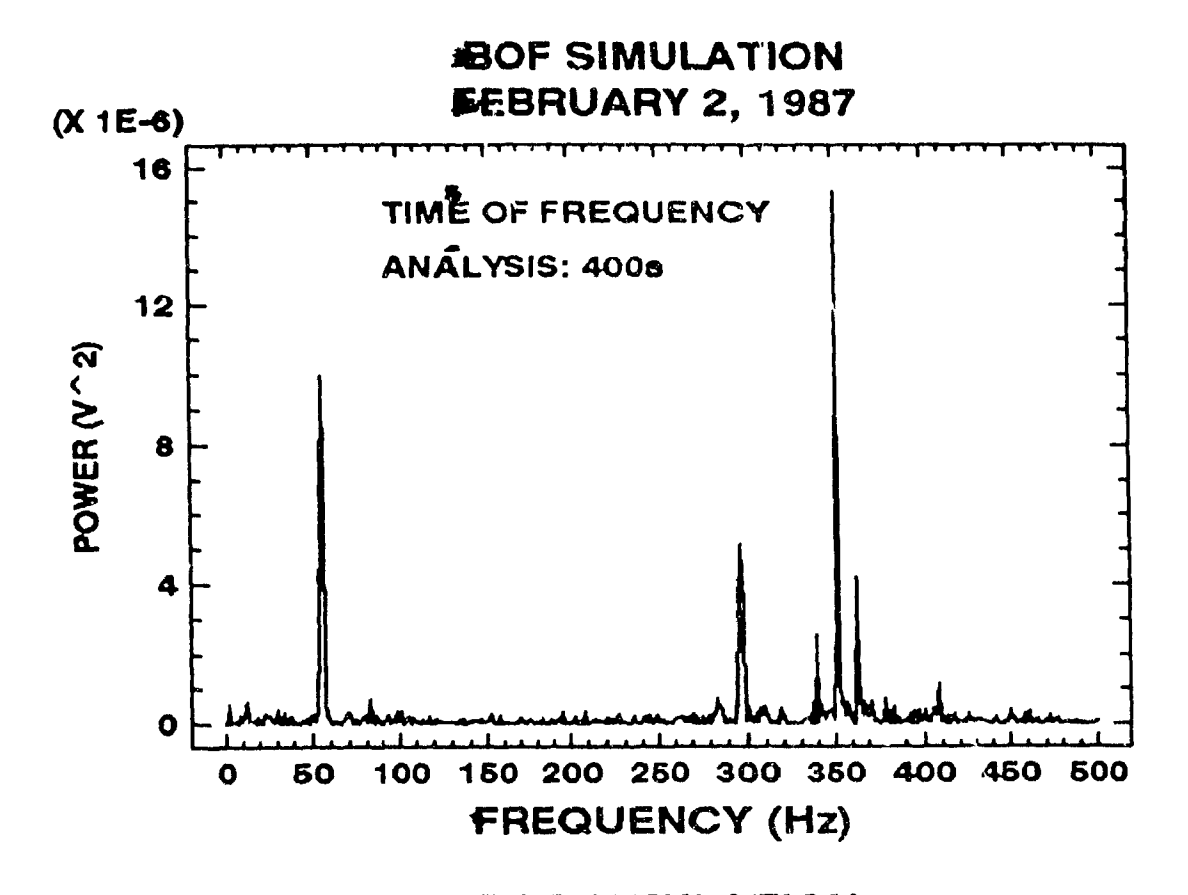


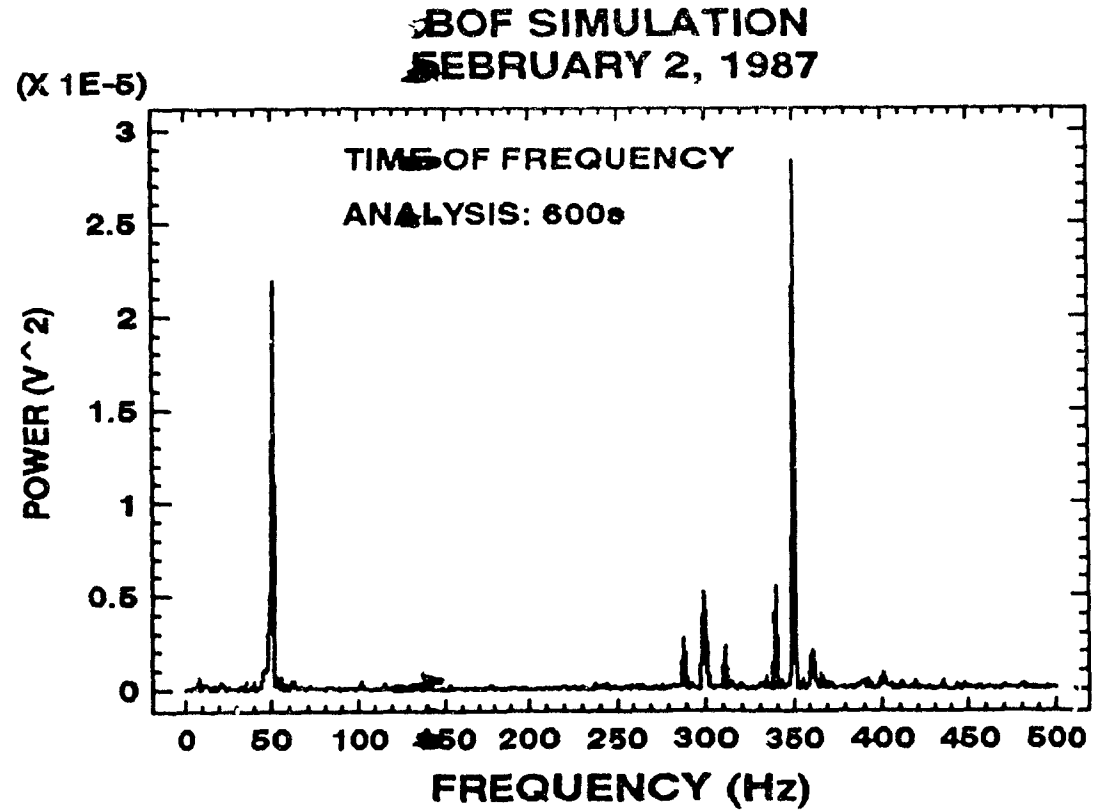


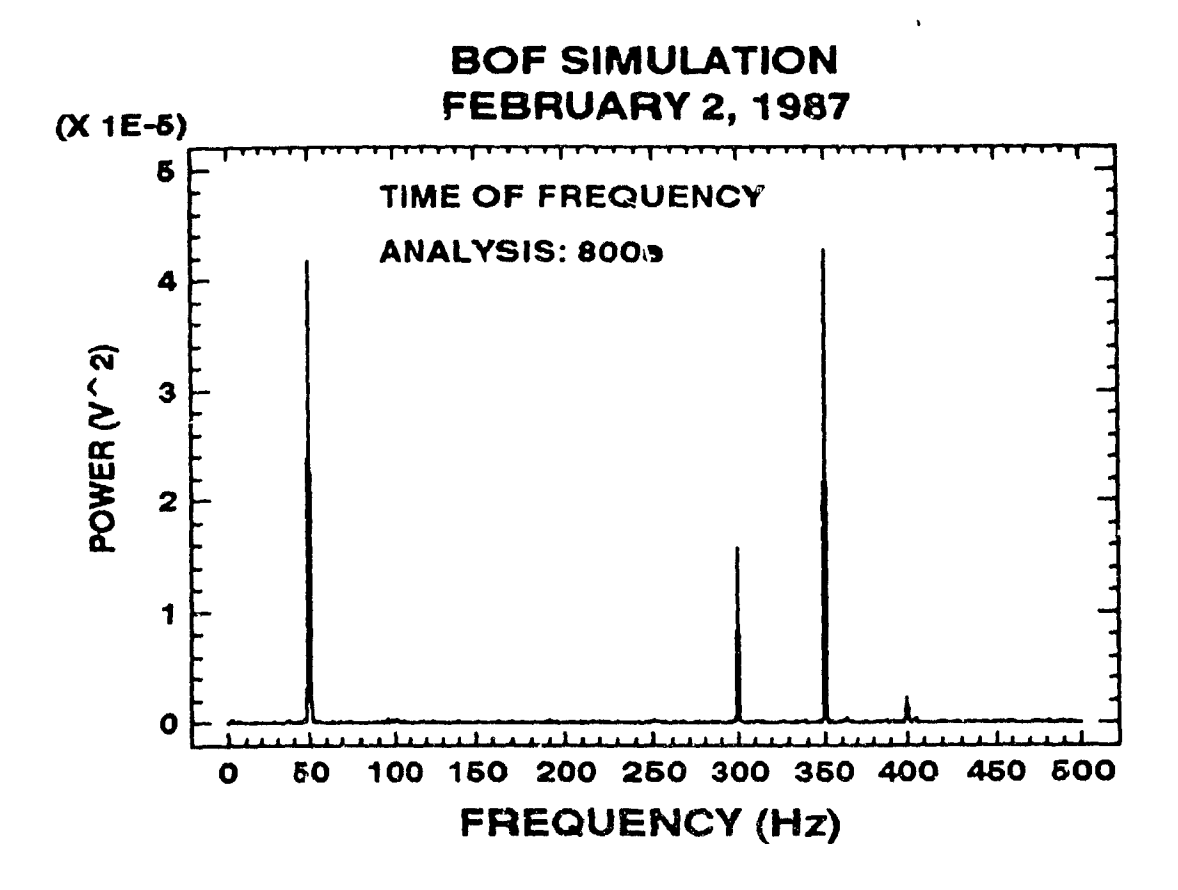
KEVIN E. O'LEARY\FEB2VAR.DRW

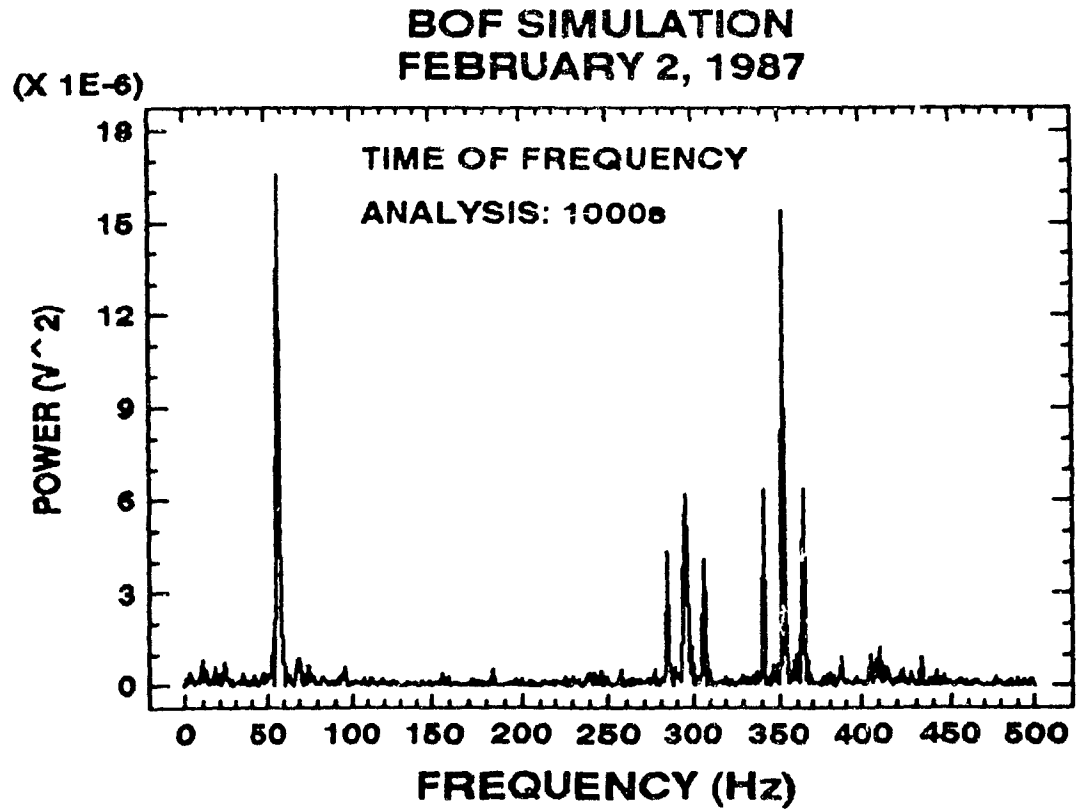


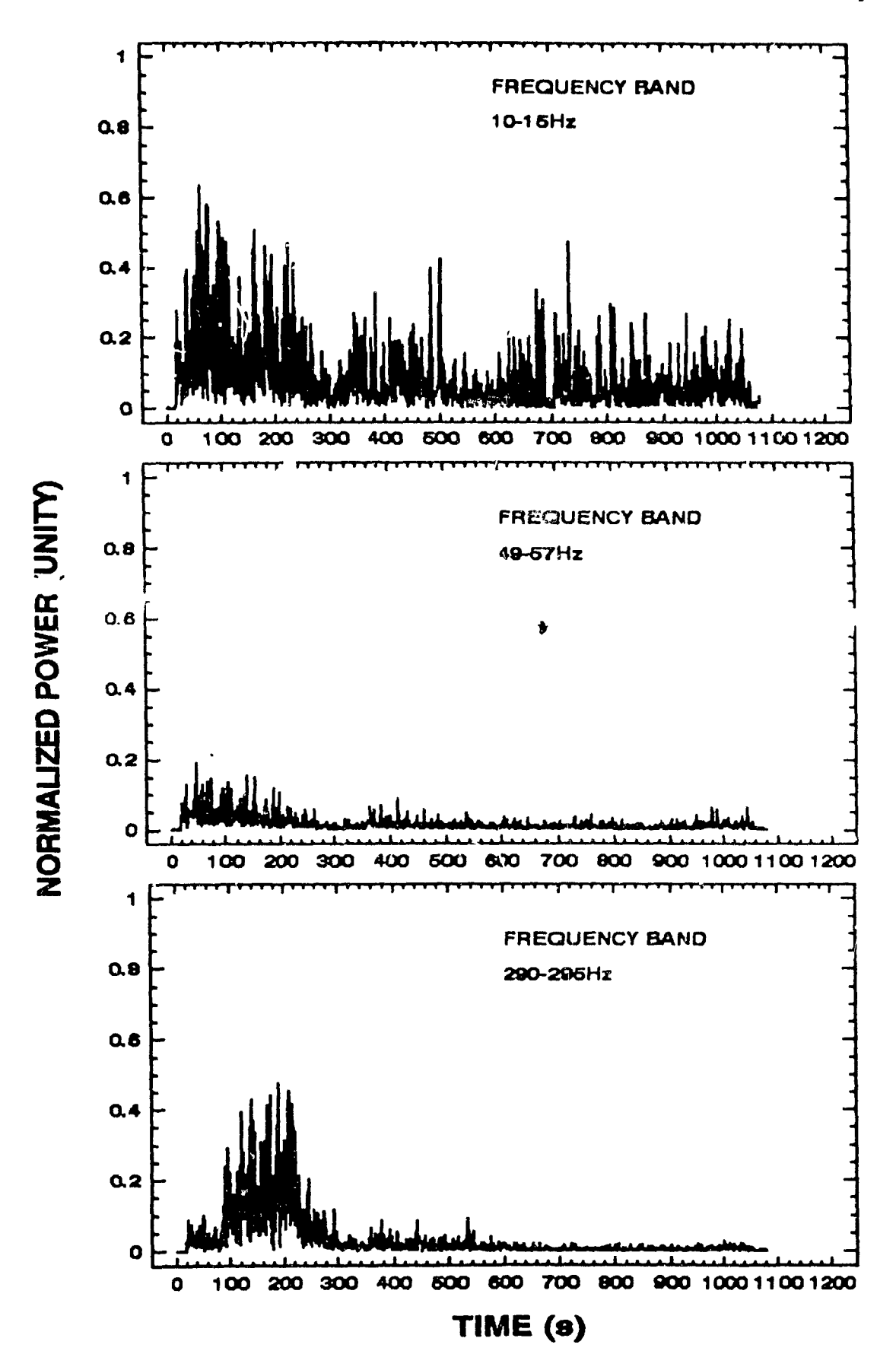


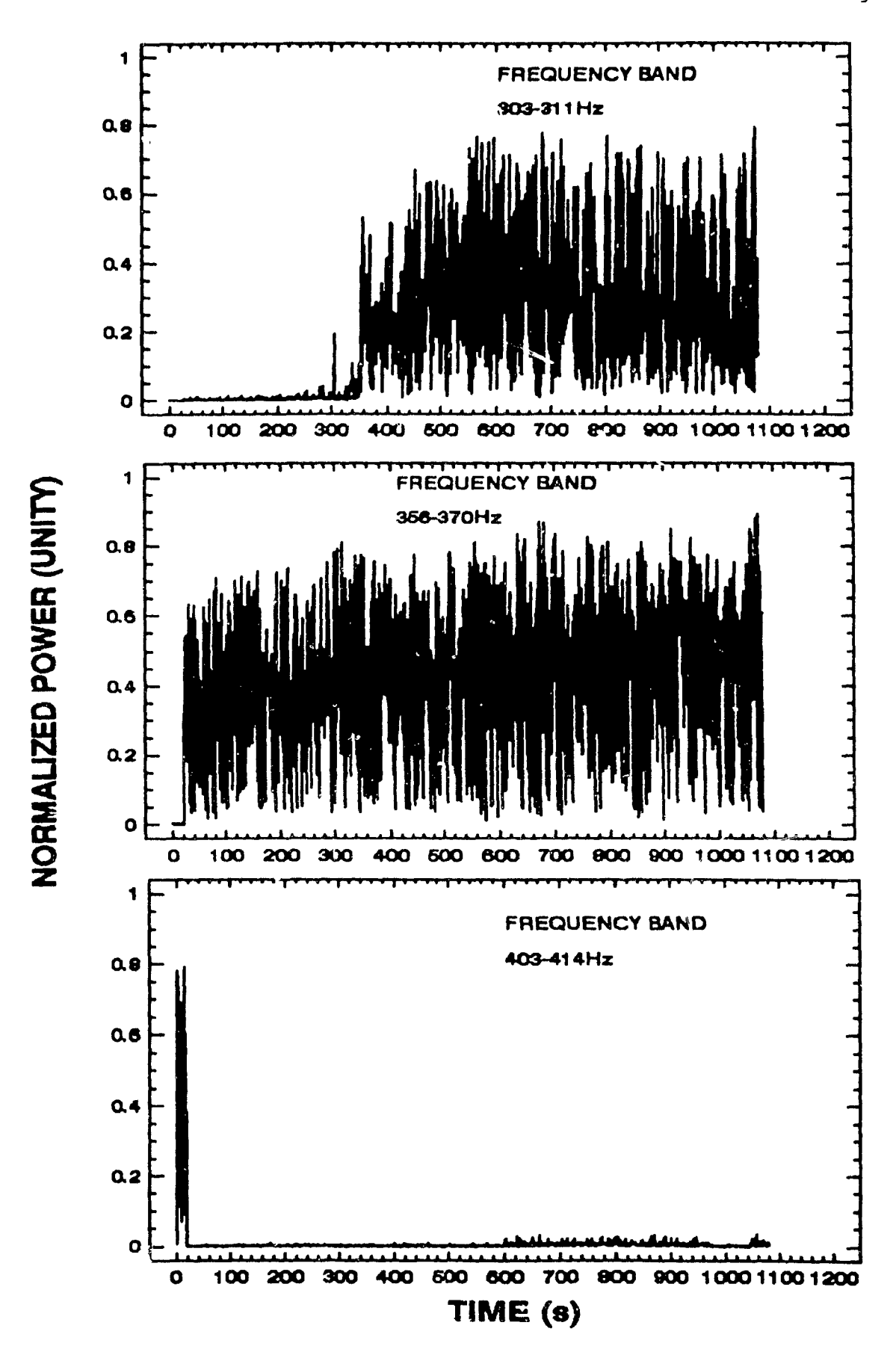




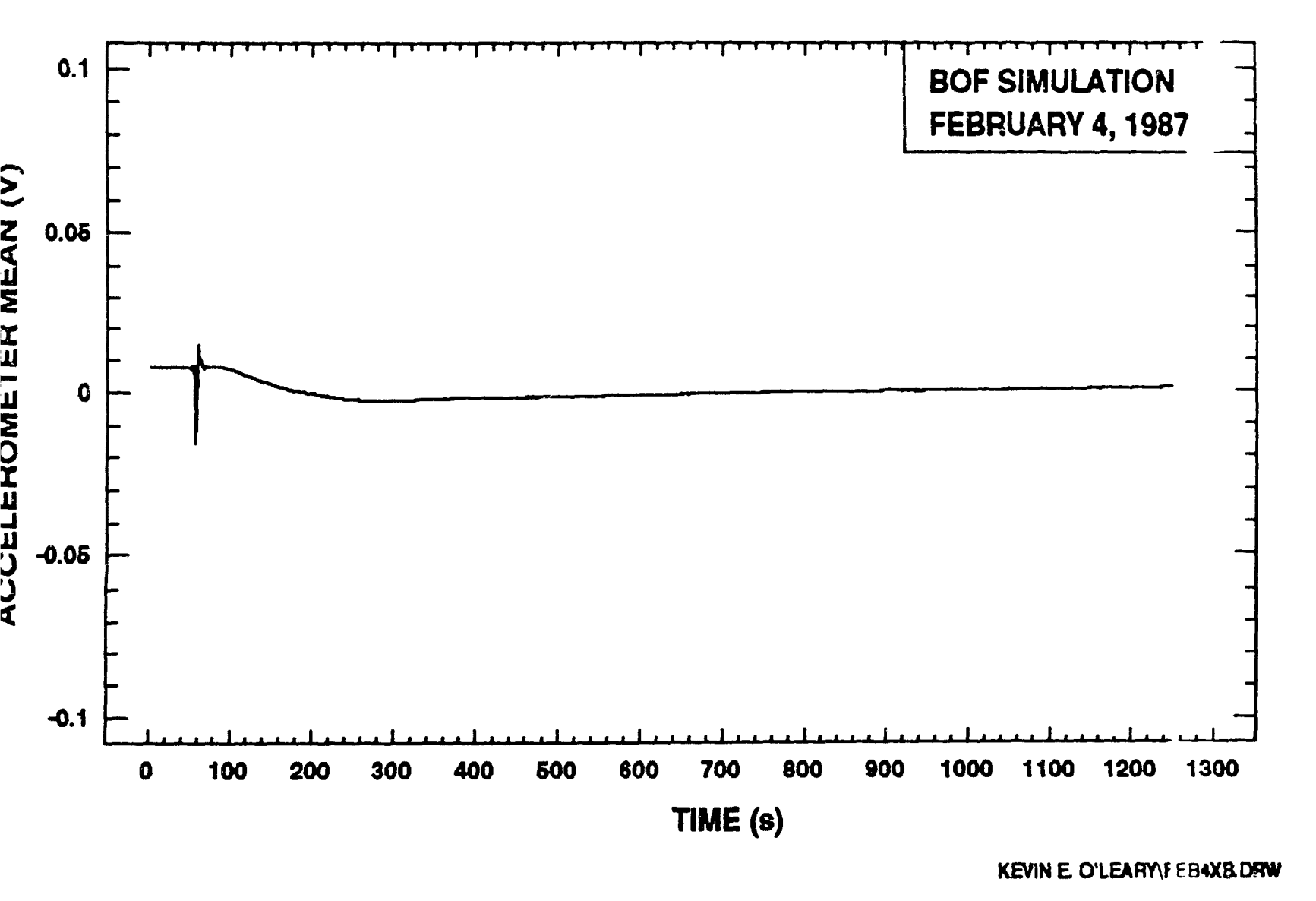






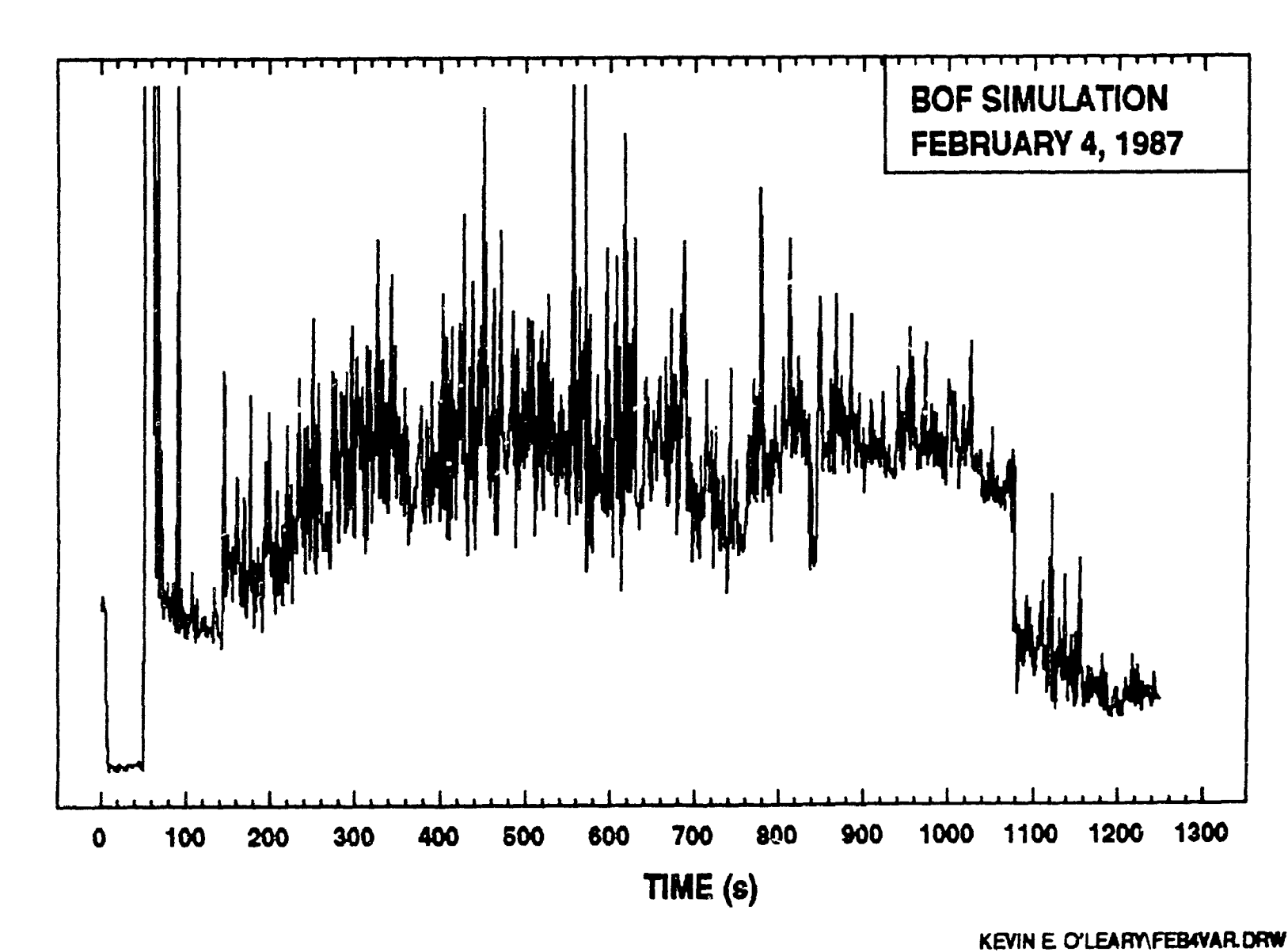


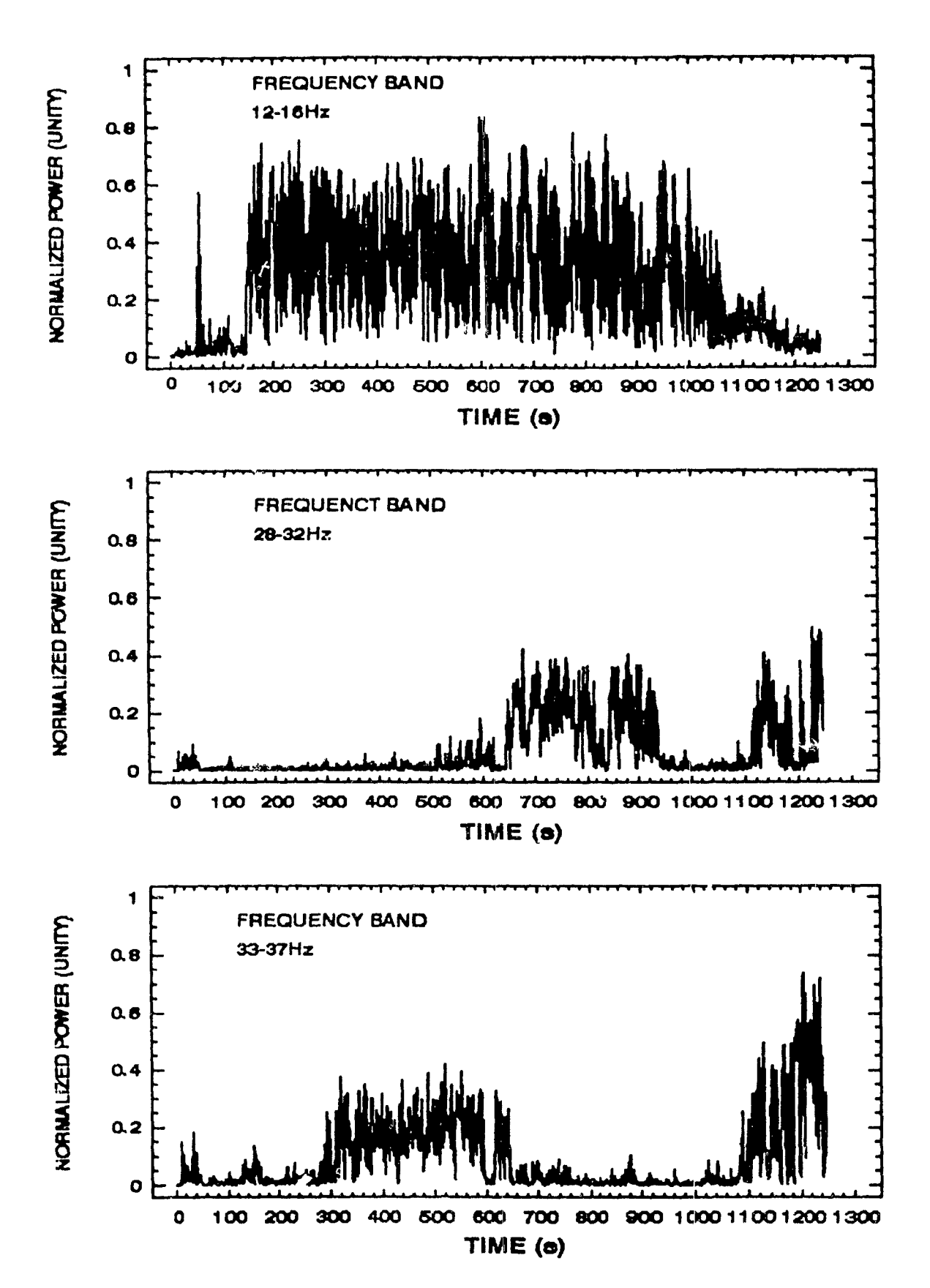
Test Code: C/4		Test Date	: Februa	ry 4, 1987	
Operating Parameters:	<u>-</u>				
Hot Metal Weight:	22.2 kg	Final Carl	bon:	0.05 %wt	
Free Board:	230 mm	Change in	Carbon:	4.00 %wt	
Lance Depth:	205 mm	Blown Oxy	gen Volume:	1009 N•1	
Height Above Melt:	25 mm	Blowing T	ıme:	1298 5	
Furnace Power:	0 kVA	Oxygen Fl	ow Rate:	ე.78 №1/s	
Accelerometer Signal	Analysis:				
Sampling Trequency:		1000 Hz			
Decay in $\partial C/\partial O$ Observed:		Obs	erved		
Time of Observation:		1	077s		
Major Frequency Bands	s Analyzed:		28-32Hz, 3 0-56Hz, and	33- <u>37Hz, 38-</u> 1 57-66Hz	

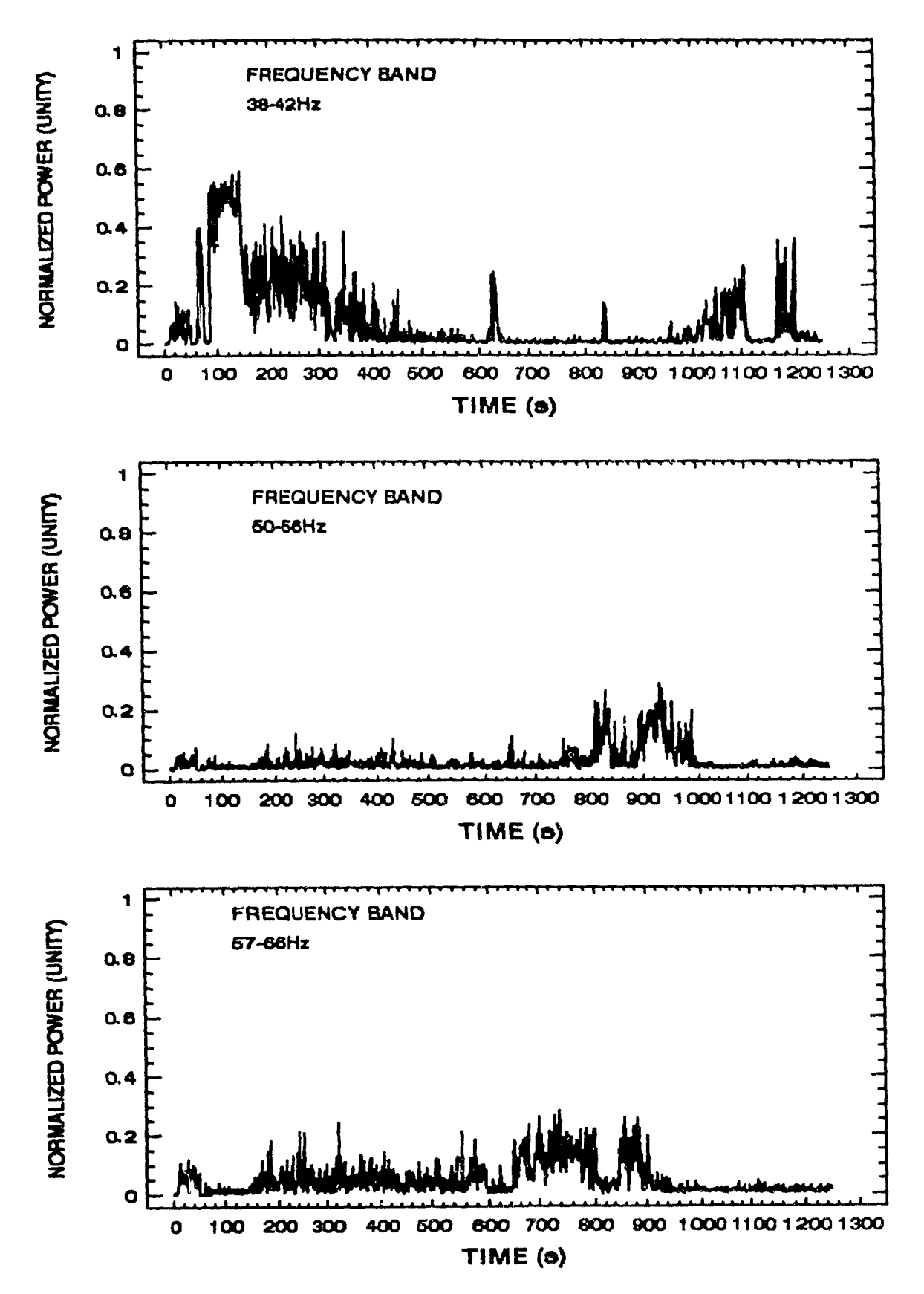


Page -A.37-





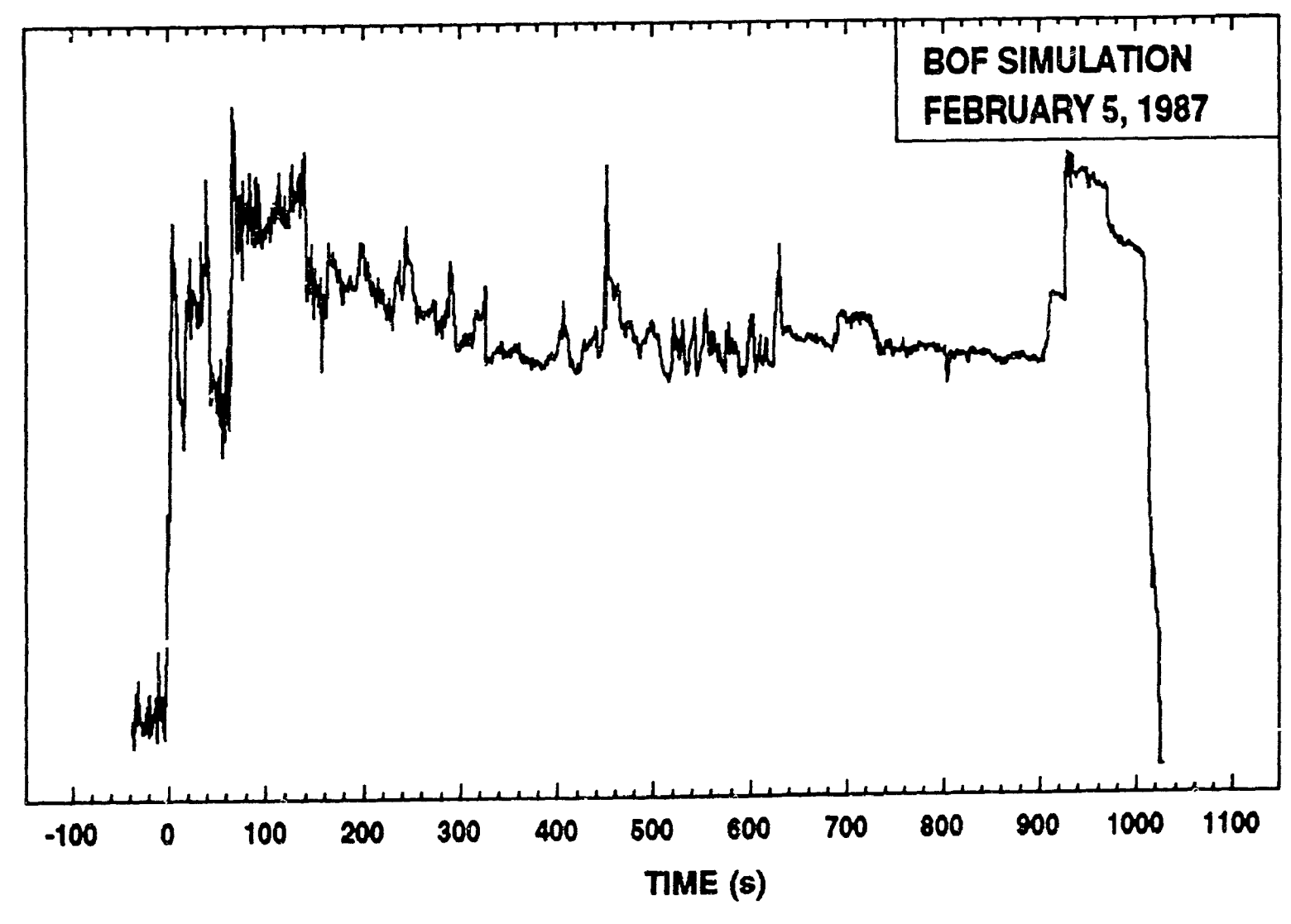




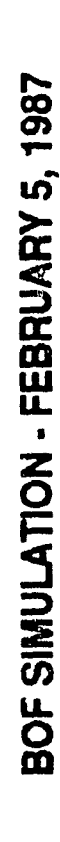
KEVIN E. O'LEARY \ FEB4A3.DRW

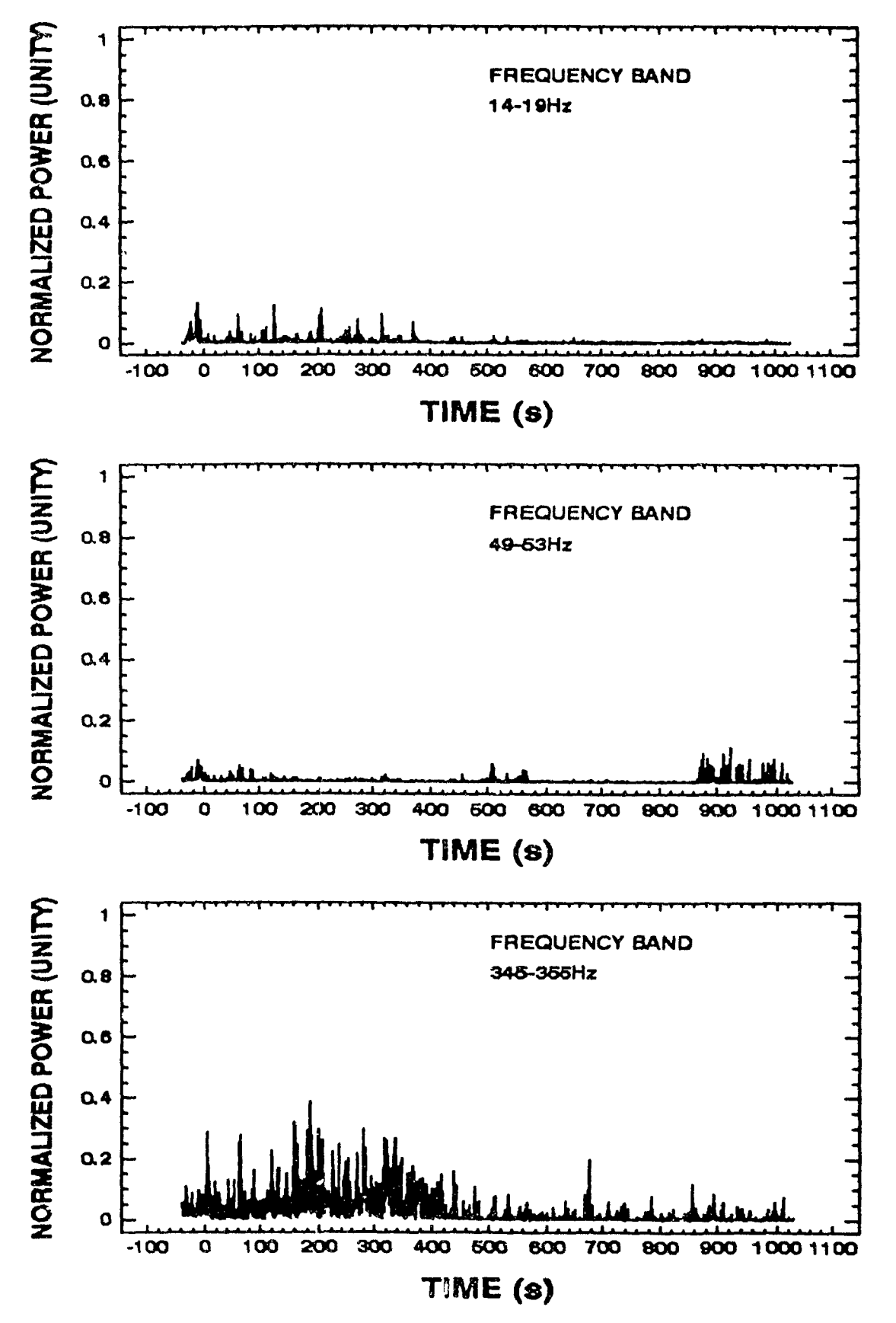
Test Code: C/5		Test Date: February 5, 1987			
Operating Parameters:					
Hot Metal Weight:	21.8 kg	Fina Carbon:	0.40 %wt		
Free Board:	235 mm	Change in Carbon:	4.00 %wt		
Lance Depth:	210 mm	Blown Oxygen Volume:	1226 N•1		
Height Above Melt:	25 mm	Blowing Time:	1050 s		
Furnace Power:	0 kVA	Oxygen Flow Rate:	1.17 N•1/s		
Accelerometer Signal	Analysis:				
Sampling Frequency:		1000 Hz			
Decay in $\partial C/\partial O$ Observed:		Observed			
Time of Observation:	_	1010s			
Major Frequency Bands Analyzed:		322-334Hz, 334-34 355Hz, and 356-365H	322-334Hz, 334-344Hz, 345 355Hz, and 356-365Hz		

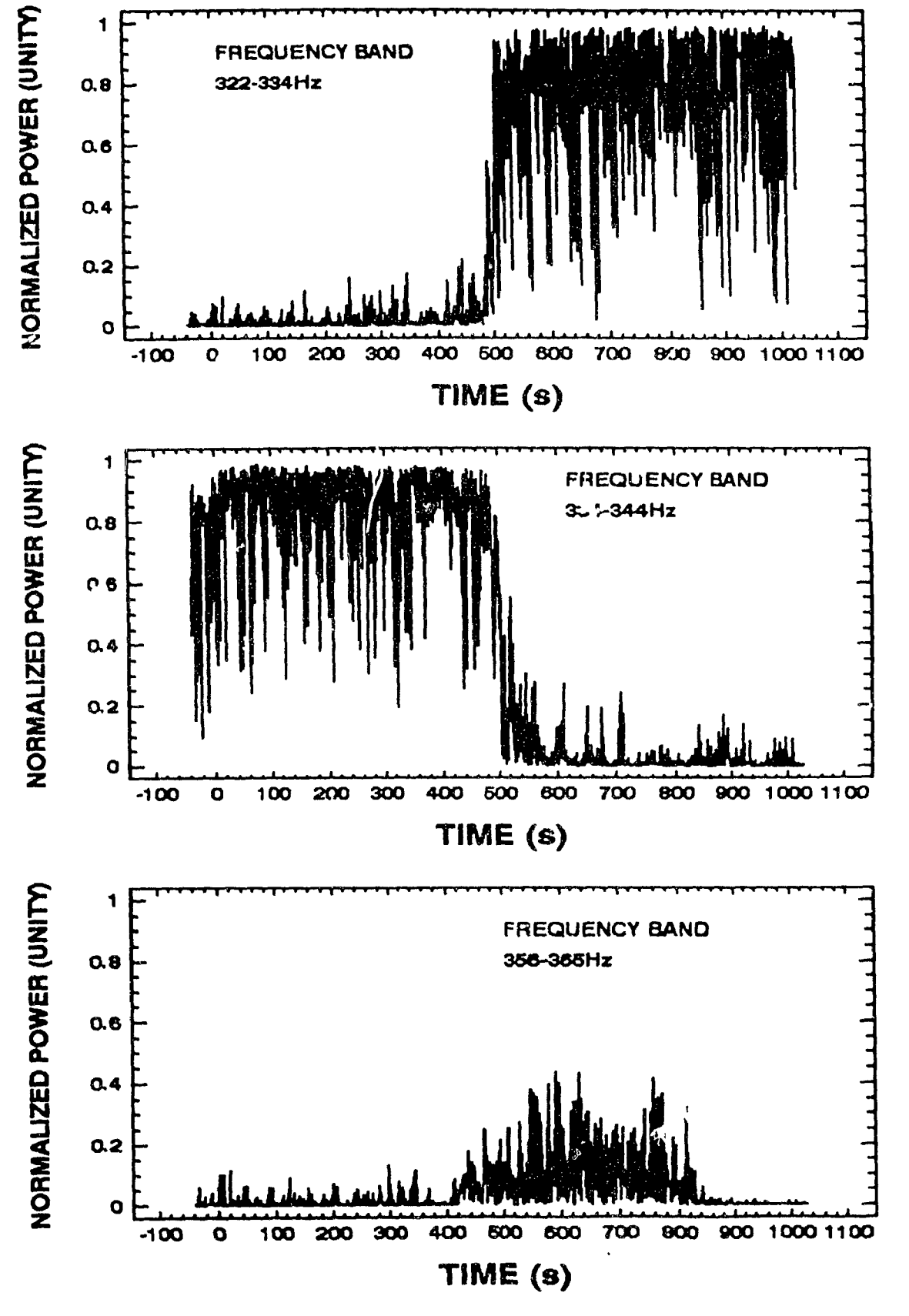
KEVIN E. O'LEARY\FEB6XBAR.DRW



KEVIN E. O'LEARY\FEB6YAR.DRW

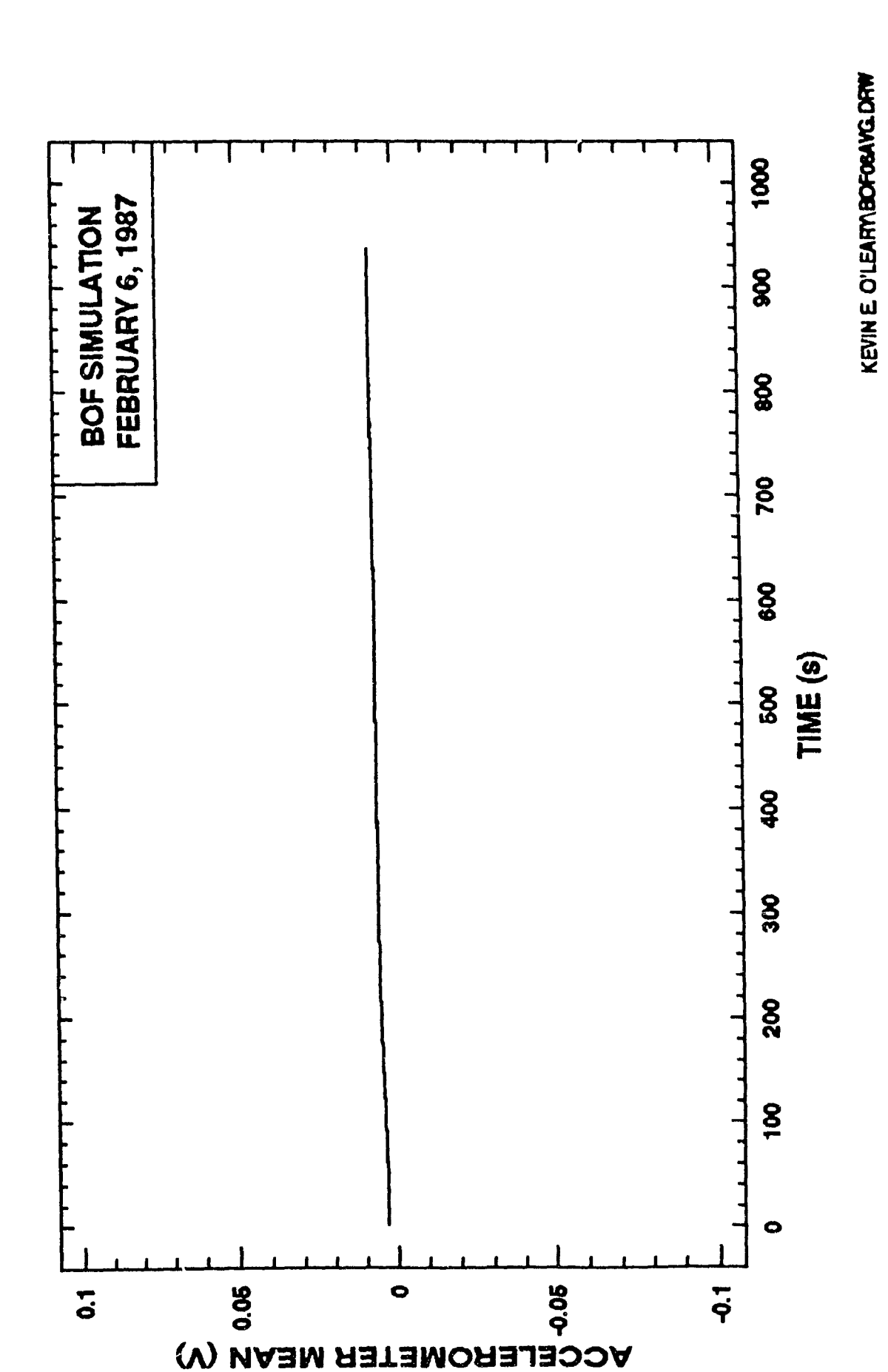




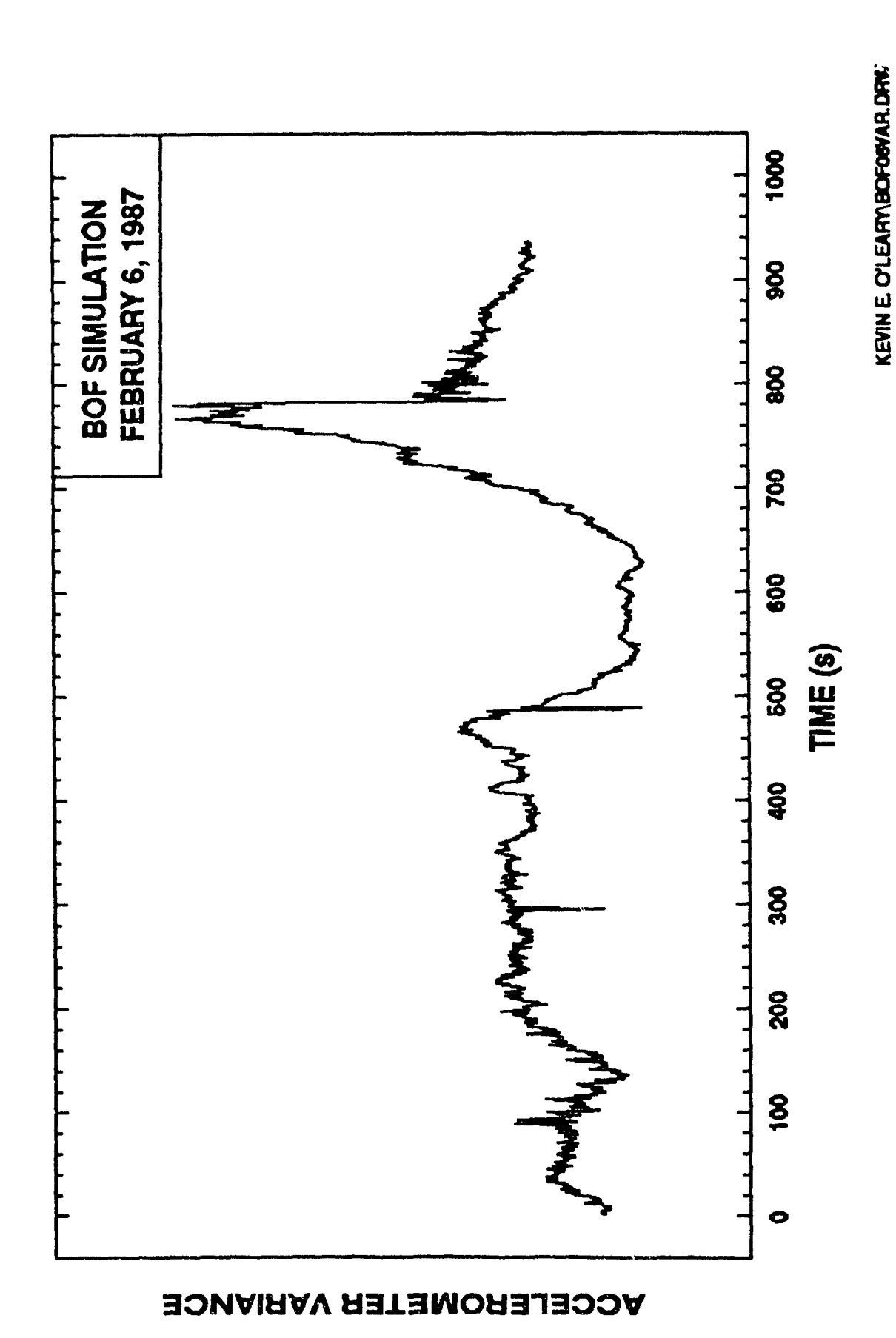


BOF SIMULATION - FEBRUARY 5, 1987

Test Code: C/6 Test Date: February 6, 1987 Operating Parameters: Final Carbon: Hot Metal Weight: <u>23.2 kg</u> 0.04 %wt Free Board: 230 mm Change in Carbon: 4.00 %wt Blown Oxygen Volume: 1154 N•1 Lance Depth: 205 mm Height Above Melt: Blowing Time: 25 mm 1080 s Furnace Power: O kVA Oxygen Flow Rate: 1.07 N·1/s Accelerometer Signal Analysis: Sampling Frequency: 1000 Hz Decay in $\partial C/\partial O$ Observed: Observed _____ Time of Observation: 780s 4-10Hz, 11-15Hz, 20-25Hz, and Major Frequency Bands Analyzed:

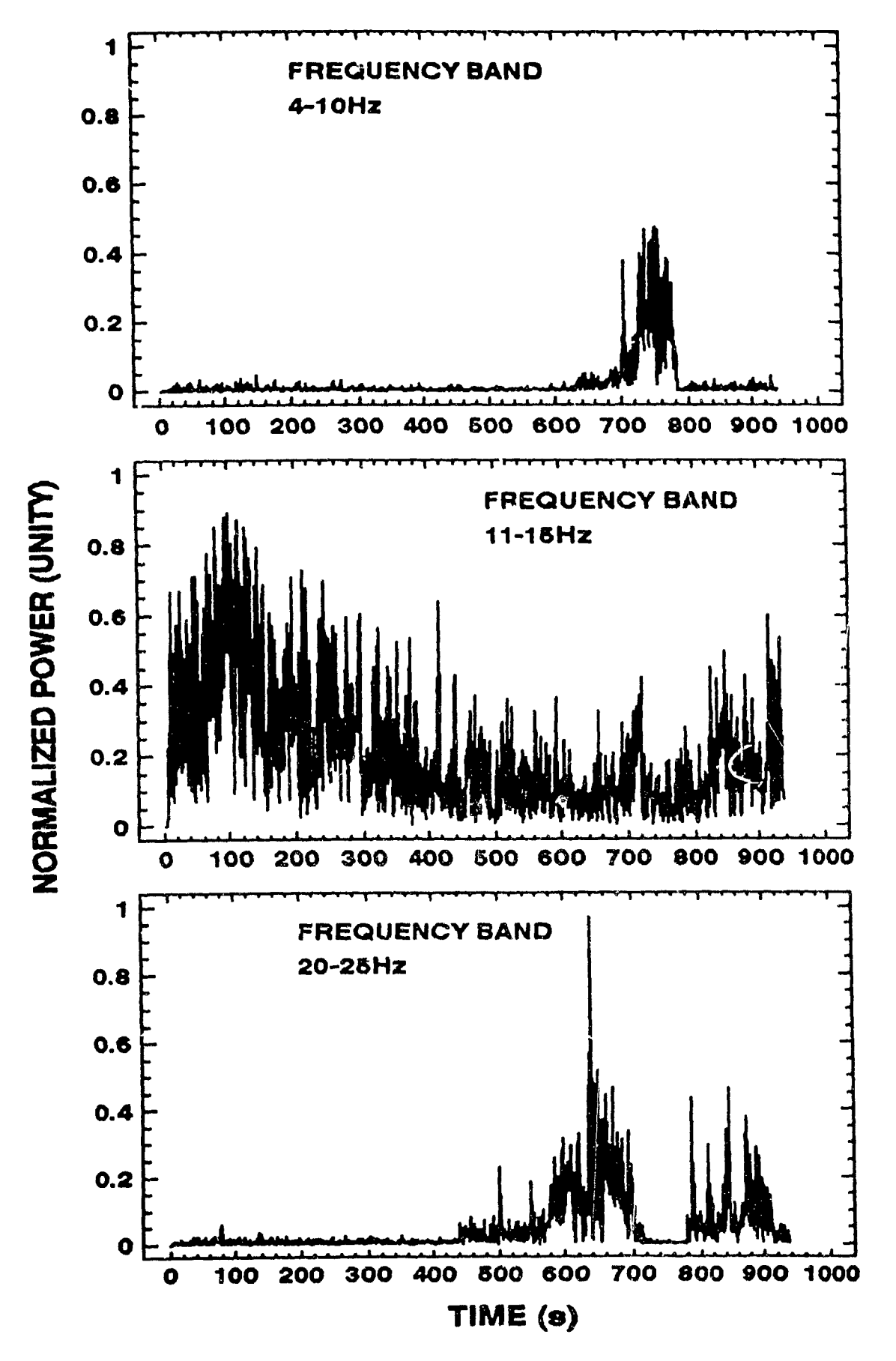


金牌.

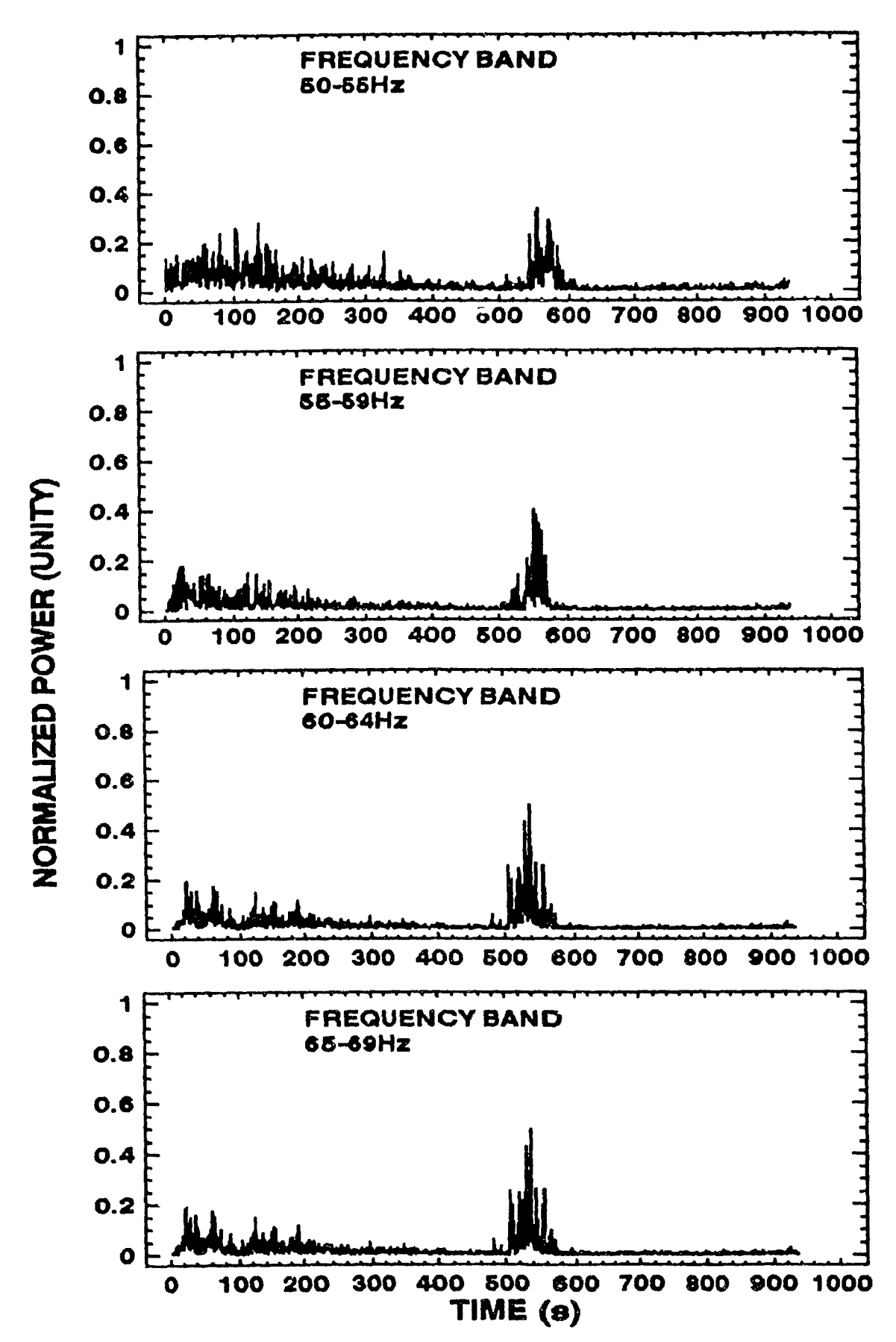


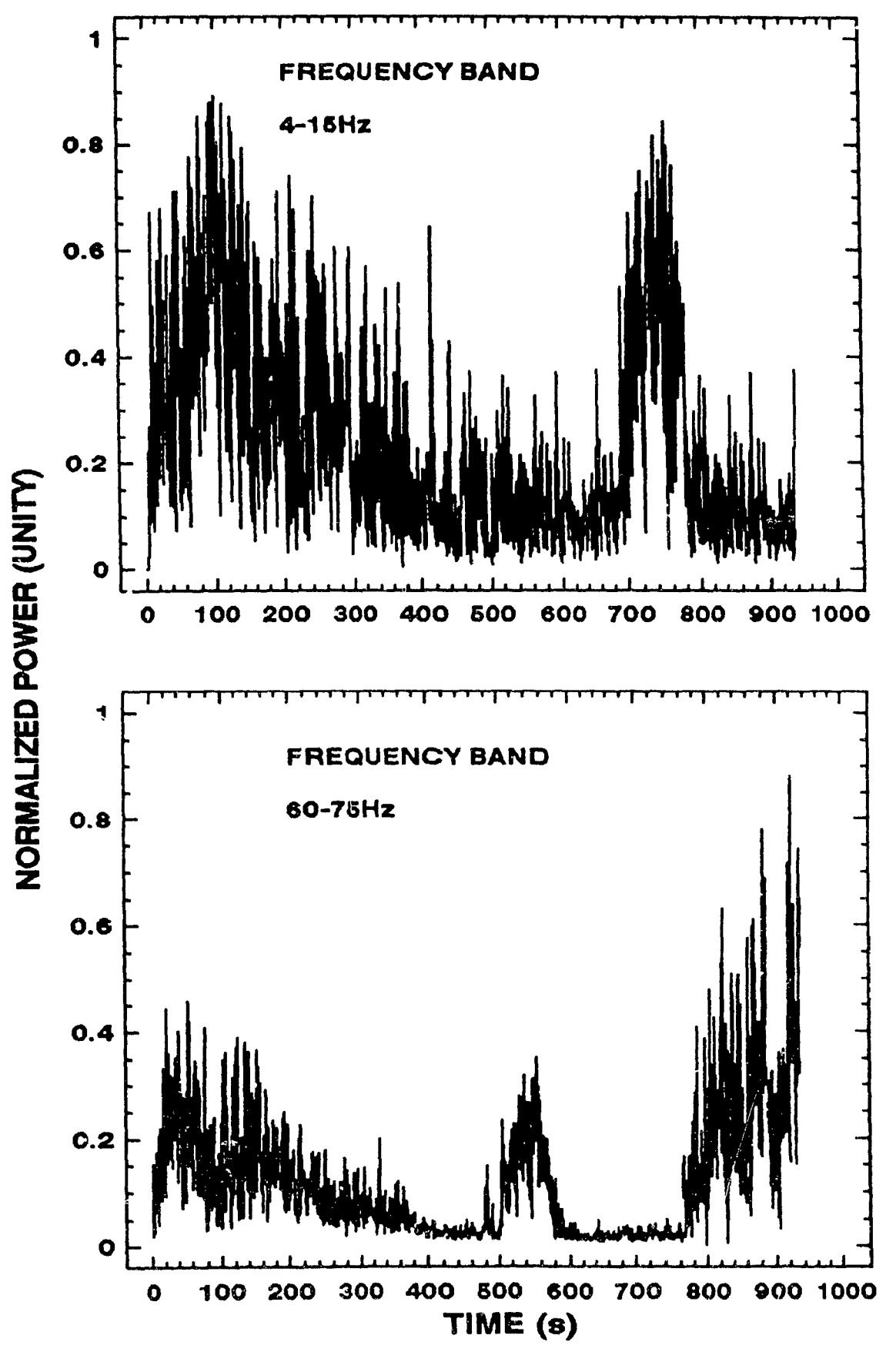
i











1

Ì

BOF SIMULATION - FEBRUARY 6, 1985

7

- 1. Durrer, R., et al, Stahl und Eisen, Vol. 85, 1965.
- 2. Durrer, R., et al, Stahl und Eisen, Vol. 86, 1966.
- 3. Hauttmann, H., Bulletin of The Research Institute of VÖEST, Linz-Donau, August, 1953.
- 4. Ed., Gaines, J.M., BOF Steelmaking, Vol 1-2, AIME, 1982.
- 5. Lankford, W.T., Samways, N.L., Craven, R.F., and McGannon, H.E., <u>The Making, Shaping, and Treating of Steel</u>, 10th Ed., AISE, 1985.
- 6. Daugherty, R.L., and Franzini, J.B., <u>Fluid Mechanics With</u> <u>Engineering Applications</u>, 7th Ed., McGraw-Hill, 1977.
- 7. Ed. Fritz, E., and Gollob, U., OBM Brochure, Eisen-Gessellschaft Maximilianshutte mbh, 1980.
- 8. Hladio, W. F., Bechtold, R. A., and /herd, T. J., "Construction and Start Up Experience of Republic Steel's First Q-BOP", Steelmaking Proc. of AIME, Vol. 6, 1970.
- 9. Hubble, D. H., and French, L. W., "Refractories for the Q-BOP Process", Steelmaking Proc of AIME, Vol. 60, 1977.
- 10. Pearce, J., "The Present Status and Future of Q-BOP Steelmaking", Steelmaking Proc. of AIME, Vol. 60, 1977.
- 11. Emi, T., Recent Progress in Basic Oxygen Steelmaking, Stahl Und Eiesen 100, Nr. 17, 1980.
- 12. Papinchok, M. J., and Weaver, T. M., "Current Status of the Q-BOP Oxygen Steelmaking Process", I&SM, October, 1978
- 13. Brotzman, K., "Progress in Increasing Scrap Rates in Converter Steelmaking", Ironmaking and Steelmaking, No. 5, 1980.
- 14. Wardrop, R.M., "L.B.E. Operations at Gary Works", Steelmaking Proc. of AIME, Vol. 68, 1985.
- 15. Webster, D.L., Greenhalgh, K.G., and Boswell, C., "Recent Developments in Process Control and Efficiency at BHP Newcastle Works BOS Shop", Steelmaking Proc. of AIME, Vol. 68, 1985.
- 16. Mullen, R.B., and Goetz, F.J., "Experience With Lance Equilibrium Bubbling and Post-Combustion at Dofasco, Inc.", Steelmaking Proc. of AIME, Vol. 68,1985.
- 17. Brotzman, K., "Improvements in Bottom Blowing by Combined Blowing Techniques and Increase of the Scrap Rate", Stahl und Eisen, Vol. 102, No. 7, 1982.

- 18. Turkdogan, E.T., and Pearson, J., J. Iron and Steel Inst., Vol. 176, 1954.
- 19. Fuwa, T., and Chipman, J., Trans. Met. Soc. AIME, Vol. 218, 1960.
- 20. Elliot, J.F., GLeiser, M., and Ramakrıshna, V., "Thermochemistry for Steelmaking", Vol 2, Addison Wesley, 1963.
- 21. Molloy, N.A., JISI, Vol. 208, 1970.

À

1

- 22. Flinn, R.A., Phelke, R.D., Glass, D.R., and Hays, P.D., Trans. of AIME, Vol. 239, 1967.
- 23. Rote, F.E., University of Michigan Ph. D. Thesis, 1968.
- 24. Shirma, S.K., Hlinka, J.W., and Kern, D.W., "The Bath Circulation, Jet Penetration and High-Temperature Reaction Zone in BOF Steelmaking', Iron and Steelmaker, July, 1977.
- 25. Meyer, H.W., Porter, W.F., Smith, G.C., and Szekely, J., Journal of Metals, July, 1968.
- 26. Norton, H.N., <u>Handbook of Transducers for Electronic Measuring Systems</u>, Prentice-Hall, 1977.
- 27. PCB Piezotronics Inc. Catalog, 1983.
- 28. Katsura, K., Isobe, K., and Itasko, J., Journal of Metals, April 1964.
- 29. Philbrook, W.O., Open Hearth Proc. of AIME, Vol. 41, 1958.
- 30. Slatosky, W.J., Trans. Met. Soc. of AIME, Vol. 221, 1961.
- 31. Boltz, D.G., Iron and Steel Engineer, Vol. 44, 1967.
- 32. Katsura, K., Isobe, K., and Itasko, J., Journal of Metals, April 1964.
- 33. Dauby, P., Back, M., Hoffman, P., and Nilles, P., CRM Metallurgical Reports, July 1968.

- 34. Fischer, M. M., 17th Annual Instrument Automation Conference, ISA Annual Conference, New York, October, 1962.
- 35. Booster, P., Steel Times, January, 1965.
- 36. Meyer, H.W., Dukelow, D.A., Fischer, M.M., IRSID International Conference on Oxygen Steelmaking, Le Toriquet-Dunkerque, September 1963.
- 37. Dummont-Pillon, J., Manqin, F., Bachet, C., and Pierrand, H., Rev. de Met., February 1963.
- 38. Fillon, J., U.S. Patent 3,181,343.
- 39. Meyer, H.W., and Glasgow, J.A., Iron and Steel Engineer, Vol. 33, 1966.
- 40. Aukrust, E., Fischer, M.M. and Porter, W.F., Symposium on Continuous Processing and Process Control, Philadelphia, Met. Soc. Conference, Vol. 49, 1966.
- 41. Kern, D. W., and Stelts, P.D., "BOF Control Utilizing an In-Furnace Liquidus Carbon and Temperature Sensor", Iron and Steel Engineer, July 1968.
- 42. Kern, D.W., Balla, D.M., and Reinhold, R.J., "Experience Using Sensor Lance on BOF's at Bethlehem Steel", Iron and Steel Engineer, March, 1980.
- 43. U.S. Patent 3,327,531 (June 27, 1967) Assigned to Bethlehem Steel Corp.
- 44. Roeser, W.F., and Winsel, H.T., "Freezing Temperatures of High-Purity Iron and of Some Steels", Research Paper RP1375, Journal of Research of the National Bureau of Standards, Vol. 26, April 1941.
- 45. Kawawa, T., "Historical Review and Present Status of BOF Computer Control System of NKK", McMaster Symposium No. 9, May 1981.
- 46. Stacy, A.D., and Griffith, E.D., "Dynamic Sensor Lance Control of BOF's at ARMCO", Steelmaking Proc. of AIME, Vol. 63, 1980.
- 47. Watson, D.R., Stacey, J.N., and Buchanan, D.J., "Start-up of Dofasco's No. 2 Meltshop", Iron and Steel Engineer, September 1981.
- 48. Boom, R., Slangen, B., Raaijen, W., and Zonneveld, P., "Developments in Sublance Design and Measurement Techniques at Hoogovens' Ijmuiden Plant", Iron and Steelmaker, March 1988.

- 49. Voll, H., "Experimental Study of the LD-AC Process Dynamics", C.R.M. Reports, No. 33, December 1972.
- 50. Anderson, D., Parkin, C.J., and du Bois, E.A., "The design and Performance of Rapid Waste Gas Sampling and Analysis Equipment for B.O.S. Steelmaking", Steelmaking Proc. of AIME, Vol. 63, 1980.
- 51. Nilles, P., and Denis, E., "Automatic Control of the Blow on Two 180 t LD Converters at Cockerill-Ougreé-Providence", C.N.R.M. Reports, No. 15, June 1968.
- 52. Voll., H., and Ramelor, D., "Fast Determination of Decarburization Rate by Fumes Temperature Measurement", C.R.M. Reports, No. 33, December 1972.
- 53. Nilles, P., and Holper, R., "Converter Noise and Off-Gas Temperature Measurements, Tools for Better BOF Control", C.R.M. Reports, No. 35, June 1973.
- 54. Klärding, J., German Patent No. 819246, October 1951.
- 55. Ramelot, D., and Claes, J., "determination of the End of Blowing for LD and OBM Processes by Means of a Sonic Meter", C.R.M. Reports, No. 54, June 1979.
- 56. Boudin, M., Jacobs, H., and Nilles, P.E., "The OBM steelworks of Forges de Thy-Marcinelle et Monceau", Iron and Steel Engineer, February 1979.
- 57. Bardenheuer, F., and Oberhauser, P.G., "Comparison of the Vibration and Sound Measurements to Control the Formation of Slag in the Basic Oxygen Converter", Stahl und Eisen, Vol. 90, No. 15, July 1970.
- 58. Grenfell, H.W., Bowen, D.J., and McQueen, C., "The role of Continuous Vessel Weighing in The Commissioning and Operation of B.S.C. Ravenscraig New No.3 B.O.F.", Steelmaking Proc of AIME, Vol. 60, 1977.
- 59. Nilles, P.E., and Dauby, B.H., "Control of the OBM/Q-BOP Process", Iron and Steel Engineer, March 1976.
- 60. Jacobs, H., Jeschin, B., Dauby, P.H., and Claes, J., "Development and Application of the LD-HC Top and Bottom Blowing Process", Iron and Steel Engineer, December 1981.
- 61. Toshihiro, E., "Recent Progress in Basic Oxygen Steelmaking", Stahl und Eisen, Vol. 100, No. 17, August 1980.
- 62. Iida, Y., Emoto, K., Ogawa, M., Masuda, Y., Ohnishi, M., and Yamada, H., "Fully Automatic Blowing Technique for Basic Oxygen Steelmaking Furnace", Trans. of ISIJ, Vol. 24, 1984.

- 63. Chnishi, M., Nagai, J., Yamamoto, T., Nakai, K., Take, H., and Tachibana, R., "Metallurgical Characteristics and Operation of Oxygen Top and Bottom Blowing at Mizushima Works", Iron and Steelmaker, August 1983.
- 64. Fradeneck, R.J., Davis, T.R. and Zackey, R.T.. "Low-cost, Dynamic Predictive Maintenance System at Bethlehem Steel", Iron and Steel Engineer, April 1984.
- 65. Kido, S., Akaji, M., Mureta, M., Takashi, N., Nitanda, M. and Kuwano H., "Hydraulic Wrapper Roll in Hot Strip Down Coiler", Iron and Steel Engineer, September 1982.
- 66. Destate, J.C., Joannes, R., Pesch, R. and Pirlet, R., "Acoustic Measurement of Rimming in Steels", C.R.M. No. 41, December 1974.
- 67. Mucciardi, M., Canadian Metallurgical Quarterly, Vol. 26, No. 4, 1987.
- 68. Krujelskis, V., and Mucciardi, M, Process Tech. Proc. of AIME, Vol. 4, 1984.
- 69. Nakaniski, K., Fujii, T., and Szekely, J., Ironmaking and Steelmaking Q., 3, 193, 1975.
- 70. Hadi, O., and Brimacombe, K., Proc. Scaninject II (1980).
- 71. Asia, S., Okamoto, T., He, J., and Muchi, I., Trans. Iron and Steel Inst. Japan, Vol. 23, 1983.
- 72. Greussier, A., Vachiery, E., Tranchant, J., and Szezesny, R., Iron and Steel Engrs, Vol. 67, No. 22, 1984.
- 73. Robinson, J., Proc. Scanniject III, 1983.
- 74. Fitzgerald, F., Steelresearch 1982/3, British Steel Corp., June 1983.
- 75. Mairy, M., Ramelot, D., and Dauby, P., "Monitoring the Lubrication in the Mold During Continuous Casting of Steel", Steelmaking Proc. of AIME, Vol. 63, 1980.
- 76. Mairy B., et al, "Mold Lubrication and Oscillation Monitoring for Optimizing continuous Casting", Steelmaking Proc. of AIME, Vol. 69, 1986.
- 77. Cheslak, F.R., Nicholls, J.A., and Sichel, M., "Cavities Formed on Liquid Surfaces by Impinging Gaseous Jets", J. Fluid Mech., Vol. 36, 1969.

- 78. Ichinoe, M., Yamamoto, S., Nagano, Y., Miyamura, K., Yamaguchi, K., and Tezuka, M., "A Study on Decarburization Reactions in Basic Oxygen Steelmaking Furnace", Proc. ICSTIS, Suppl. Trans. ISIJ, Vol. 11, 1971.
- 79. Elingham, H.T., J. Soc. Chem. Ind., pp.125-33, Vol. 63, 1944.
- 80. Richardson, F.D., and Jeffes, J.H.E., J. Iron and Steel Inst., pp 261-270, Vol. 160, 1948.